NACA TN 4362

NATIONAL ADVISORY COMMITTEE FOR AERONAUTICS

TECHNICAL NOTE 4362

FORCE AND PRESSURE MEASUREMENTS AT TRANSONIC SPEEDS FOR SEVERAL BODIES HAVING ELLIPTICAL CROSS SECTIONS

By John B. McDevitt and Robert A. Taylor

Ames Aeronautical Laboratory
Moffett Field, Calif.

NACA

Washington
September 1958

NATIONAL ADVISORY COMMITTEE FOR AERONAUTICS

TECHNICAL NOTE 4362

FORCE AND PRESSURE MEASUREMENTS AT TRANSONIC SPEEDS FOR SEVERAL BODIES HAVING ELLIPTICAL CROSS SECTIONS

By John B. McDevitt and Robert A. Taylor

SUMMARY

The measured force characteristics and surface-pressure distributions at angles of attack from 0° to 6° are presented for a series of bodies having elliptical cross sections. (The axial distributions of cross-sectional area for these bodies were identical and equal to that for a parabolic-arc body of revolution having a fineness ratio of 12.) Pressure distributions for the surrounding flow fields are also presented for the various bodies at zero angle of attack. The Mach number range varied from 0.8 to 1.2, and the Reynolds number, based on the theoretical length of the model from nose to point of closure, was approximately 24×10^6.

INTRODUCTION

In order to provide experimental data which may be used in the further understanding of the transonic-flow phenomena for simple bodies, a related series of experimental investigations has been initiated in the Ames 14-foot transonic wind tunnel.

In previous investigations (refs. 1 and 2), pressure distributions were obtained on the body surface and in surrounding flow fields for parabolic-arc bodies of revolution having fineness ratios of 10, 12, and 14, and for bodies of revolution having various axial locations of maximum cross-sectional area. In the present report, pressure distributions and force data are presented for a series of bodies having elliptical cross sections with ratios of major-to-minor axes of 1.0, 1.5, 2.0, and 3.0. All the bodies had identical axial distributions of cross-section area (equal to that for a parabolic-arc body of revolution having a fineness ratio of 12).

NOTATION

C_D drag coefficient, $\frac{\text{drag}}{q_\infty l^2}$

C_L lift coefficient, $\frac{\text{lift}}{q_\infty l^2}$

C_m pitching-moment coefficient, $\frac{\text{moment about } \xi=0.50}{q_\infty l^3}$

C_p pressure coefficient, $\frac{p-p_\infty}{q_\infty}$

d diameter of body of revolution

f fineness ratio for body of revolution, $\frac{\text{length}}{\text{maximum diameter}}$

l theoretical body length from nose to point of closure

l_b truncated body length

M_∞ free-stream Mach number

p local static pressure

p_∞ free-stream static pressure

q_∞ free-stream dynamic pressure

R body radius

Re Reynolds number based on body length l

S body cross-sectional area normalized by dividing by body length squared, $\frac{\pi R^2}{l^2}$

W body wetted area

α angle of attack, bodies pitched in plane of minor axis of elliptical cross section

ξ,η,θ cylindrical coordinate system (see sketch (a)) where ξ and η are streamwise and radial distances normalized by dividing by body length l

H body radius normalized by dividing by the body length l

λ ratio of major-to-minor axis of body cross section (see sketch (a))

ξ_{cp} center-of-pressure location, $\xi_{cp} = 0.5 - \frac{C_m}{C_L}$

$( )'$, $( )''$ first and second derivatives with respect to the normalized streamwise coordinate

Subscripts

1,2	major and minor axes of the elliptical cross sections (see sketch (a))
av	average
b	body base
f	friction
max	maximum

APPARATUS AND MODELS

Tunnel

This investigation was conducted in the Ames 14-foot transonic wind tunnel, which is a closed-return tunnel equipped with a perforated test section permitting continuous operation from subsonic to low supersonic speeds (fig. 1). Each wall of the test section contains 16 longitudinal slots with each slot containing a corrugated strip as indicated in figure 1. The ratio of accumulated slot widths (slot width minus the accumulated widths of the corrugated insets) to tunnel perimeter in a plane normal to the air stream is equal to 0.054 (usually referred to as the porosity factor). Figure 2 shows a model mounted in the tunnel test section.

Models

The four models considered in this investigation constituted a series of progressively flattened bodies having elliptical cross sections. The ratios of major-to-minor axes included in the series were λ = 1.0, 1.5, 2.0, and 3.0 (see fig. 3). All bodies had identical axial distributions of cross-sectional area. The body of revolution (λ = 1.0) had a fineness ratio of ~~12.~~ The normalized radii of the λ = 1.0 body (parabolic arc) are given by the equation

$$H(\xi) = 4H_{max}(\xi - \xi^2) \qquad (1)$$

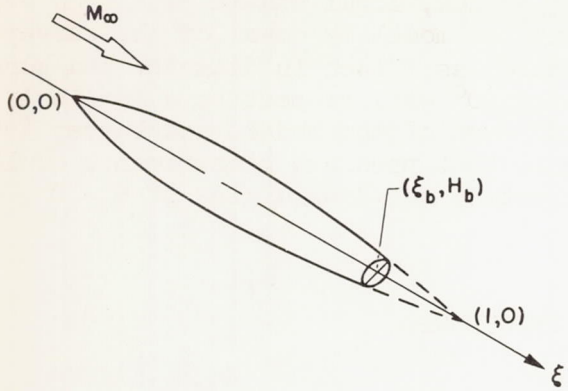

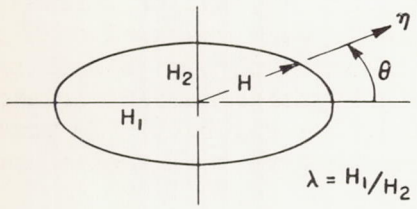

Sketch (a)

where the coordinate system (dimensionless with respect to the body length) is illustrated in sketch (a).

The normalized radii of the flattened bodies are given by

$$H(\xi) = \frac{\sqrt{\lambda}\,\tilde{H}(\xi)}{\sqrt{\cos^2\theta+\lambda^2\sin^2\theta}} \qquad (2)$$

where $\tilde{H}$ is the normalized radius of a body of revolution having identical cross-sectional area. In the present case, all the bodies have the same axial distribution of cross-sectional area and hence $\tilde{H}$ is equal to the normalized radius of the parabolic-arc body of revolution (eq. (1)).

The bodies were truncated at $\xi_b = 0.854$ (fig. 3) so that the base areas were equal to 25 percent of the maximum cross-section area. The geometric characteristics of the models are tabulated below. Additional normalized body parameters are shown in figure 4.

λ	$R_{1_{max}}$, in.	$R_{2_{max}}$, in.	l_b, in.	$\frac{l^2}{W}$
1.0	3.00	3.00	61.45	6.04
1.5	3.68	2.45	61.45	5.90
2.0	4.24	2.12	61.45	5.72
3.0	5.19	1.73	61.45	4.90

INSTRUMENTATION

The aerodynamic forces and moments were measured by a strain-gage balance enclosed within the model. Multiple-tube manometers using tetrabromoethane (specific gravity = 2.96) were photographed to record the pressure data.

Body surface-pressure data were obtained by the use of nine longitudinal rows of static-pressure orifices located at meridian angles of $\theta = 0^\circ$, $\pm5^\circ$, $\pm15^\circ$, $\pm40^\circ$, and $\pm90^\circ$. Additional orifices were located at the model base and in the cavity between the body and sting support in order to measure base pressures.

With the models at zero angle of attack, local static pressures were measured in the flow field surrounding the model by means of the survey tube shown in figure 5. The survey tube was 1 inch in diameter and contained static-pressure orifices located 90° with respect to a vertical plane passing through the longitudinal axes of the models and survey tube. The models were rotated on the sting so that pressure measurements could be made in planes corresponding to constant meridian angles of $\theta = 0°$, 40°, and 90°.

TESTS AND PROCEDURES

The force characteristics and body surface-pressure distribution were obtained at model angles of attack equal to 0°, 2°, 4°, and 6°. Pressures in the external flow fields surrounding the models were measured only at zero model angle of attack. The tests were conducted through a Mach number range of 0.80 to 1.20, with a corresponding Reynolds number variation of 23.4×10^6 to 24.6×10^6 (based on model length), see figure 6. To promote transition near the model nose, No. 60 carborundum grit was cemented over the first inch of the model.

The experimental data were not corrected for tunnel-wall interference effects. Considerations of the testing procedure and the data-reduction forces indicate that the free-stream Mach numbers are repeatable within approximately ±0.002, the angle of attack is accurate within approximately ±0.10°, and the pressure-coefficient data are repeatable within approximately ±0.005. An additional error in pressure coefficient is due to transverse flow, induced by body curvature, at the survey tube. This error is negligible except for the survey-tube position nearest the body. However, the absolute value of this error is believed to be always less than 0.005.

The force and pressure data were obtained simultaneously and reduced to standard coefficient form. The theoretical body length l is used in defining the force and moment coefficients,

$$C_D = \frac{\text{drag}}{q_\infty l^2}$$

$$C_L = \frac{\text{lift}}{q_\infty l^2}$$

$$C_m = \frac{\text{moment about } \xi=0.5}{q_\infty l^3}$$

The drag coefficient is defined by the following relationship:

$$C_D = C_{D_{sp}} + C_{D_{bp}} + C_{D_f}$$

where

$$C_{D_{sp}} = \int_0^{\xi_b} \int_0^{2\pi} C_p HH' d\xi \, d\theta$$

$$C_{D_{bp}} = \int_0^{\xi_b} \int_0^{2\pi} C_{p_b} \eta \, d\eta \, d\theta$$

$$C_{D_f} = \frac{D_f}{q_\infty l^2}$$

The pressure drag of the body, $C_{D_{sp}} + C_{D_{bp}}$, was calculated (at zero angle of attack) by means of numerical integrations using measured pressure distributions. In the present tests it was found that the pressure coefficient was essentially constant over the base surface so that an average base pressure coefficient could be used; that is,

$$C_{D_{bp}} \approx -(C_{p_b})_{av} S_b$$

The skin-friction coefficient, C_{D_f}, was estimated by the use of the charts of reference 3.

DATA PRESENTATION

The data presented in this report consist of body surface pressures and longitudinal forces at angles of attack from 0° to 6° and pressure distributions in the surrounding flow fields for the models at zero angle of attack.

Pressure Data

The measured pressure distributions for the models at zero angle of attack are presented in figures 7 to 10 and the measured surface-pressure distributions at positive angles of attack are presented in figures 11 to 14. The survey tube was used to obtain pressure distributions in planes corresponding to meridian angles of 0°, 40°, and 90°. (The data have not been faired in regions where shock waves are believed to exist.) The variations of body-pressure coefficient with meridian angles θ for various axial stations are presented in figures 15 and 16 for the bodies having values of λ equal to 2 and 3, respectively.

Force Data

The basic lift, drag, and pitching-moment data for the series of bodies having ratios of major-to-minor axes, λ of 1.0, 1.5, 2.0, and 3.0,

are presented in figures 17 to 20. The drag coefficients have been adjusted to represent free-stream static pressure at the base of each model. (The average base drag coefficients, $C_{D_{bp}}$, are tabulated in table I.) Cross plots of longitudinal force characteristics as a function of Mach number and axis ratio λ are presented in figures 21 to 29.

The variations of lift coefficient with Mach number for constant angle of attack are presented in figure 21. The effects of changes in the parameter λ at a Mach number of unity are summarized in figure 22.

The variations of drag coefficient with Mach number for constant angles of attack are presented in figure 23, and the drag coefficient variations with λ are summarized in figure 24 for three representative Mach numbers. Cross plots of the lift-drag ratio as a function of Mach number and λ are presented in figures 25 and 26. In figure 27, the drag coefficients obtained from force measurements are compared with those calculated from pressure-distribution measurements at zero angle of attack. In addition, the estimated friction-drag coefficients (ref. 3) and measured base drag coefficients are presented.

Locations of the center of pressure ξ_{cp} (with respect to model nose) are presented in figure 30 for angles of attack from 2° to 6°.

Ames Aeronautical Laboratory
National Advisory Committee for Aeronautics
Moffett Field, Calif., June 17, 1958

REFERENCES

1. Taylor, Robert A., and McDevitt, John B.: Pressure Distributions at Transonic Speeds for Parabolic-Arc Bodies of Revolution Having Fineness Ratios of 10, 12, and 14. NACA TN 4234, 1958.

2. McDevitt, John B., and Taylor, Robert A.: Pressure Distributions at Transonic Speeds for Slender Bodies Having Various Axial Locations of Maximum Diameter. NACA TN 4280, 1958.

3. Lee, Dorothy B., and Faget, Maxime A.: Charts Adapted From Van Driest's Turbulent Flat-Plate Theory for Determining Values of Turbulent Aerodynamic Friction and Heat Transfer Coefficients. NACA TN 3811, 1956.

TABLE I.- TABULATION OF BASE DRAG COEFFICIENT

M_∞	α, deg	$\lambda = 1.0$	$\lambda = 1.5$	$\lambda = 2.0$	$\lambda = 3.0$
0.90	0	-0.000060	-0.000089	-0.000077	-0.000008
	2	-.000060	-.000095	-.000079	-.000005
	4	-.000053	-.000092	-.000073	-.000002
	6	-.000050	-.000079	-.000076	.000011
.975	0	-.000106	-.000127	-.000109	-.000053
	2	-.000094	-.000115	-.000095	-.000023
	4	-.000079	-.000115	-.000095	-.000023
	6	-.000070	-.000124	-.000098	-.000013
1.00	0	-.000106	-.000141	-.000121	-.000050
	2	-.000109	-.000138	-.000121	-.000051
	4	-.000109	-.000135	-.000118	-.000051
	6	-.000103	-.000135	-.000124	-.000030
1.025	0	-.000126	-.000152	-.000149	-.000004
	2	-.000112	-.000178	-.000140	0
	4	-.000097	-.000146	-.000126	-.000011
	6	-.000086	-.000132	-.000109	-.000014
1.10	0	-.000003	-.000022	-.000024	.000049
	2	.000006	-.000024	-.000005	.000048
	4	.000011	-.000008	-.000003	.000074
	6	.000019	.000006	.000022	.000085
1.20	0	.000045	.000008	.000034	.000094
	2	.000058	.000014	.000032	.000089
	4	.000058	.000016	.000029	.000105
	6	.000068	.000047	.000040	.000123

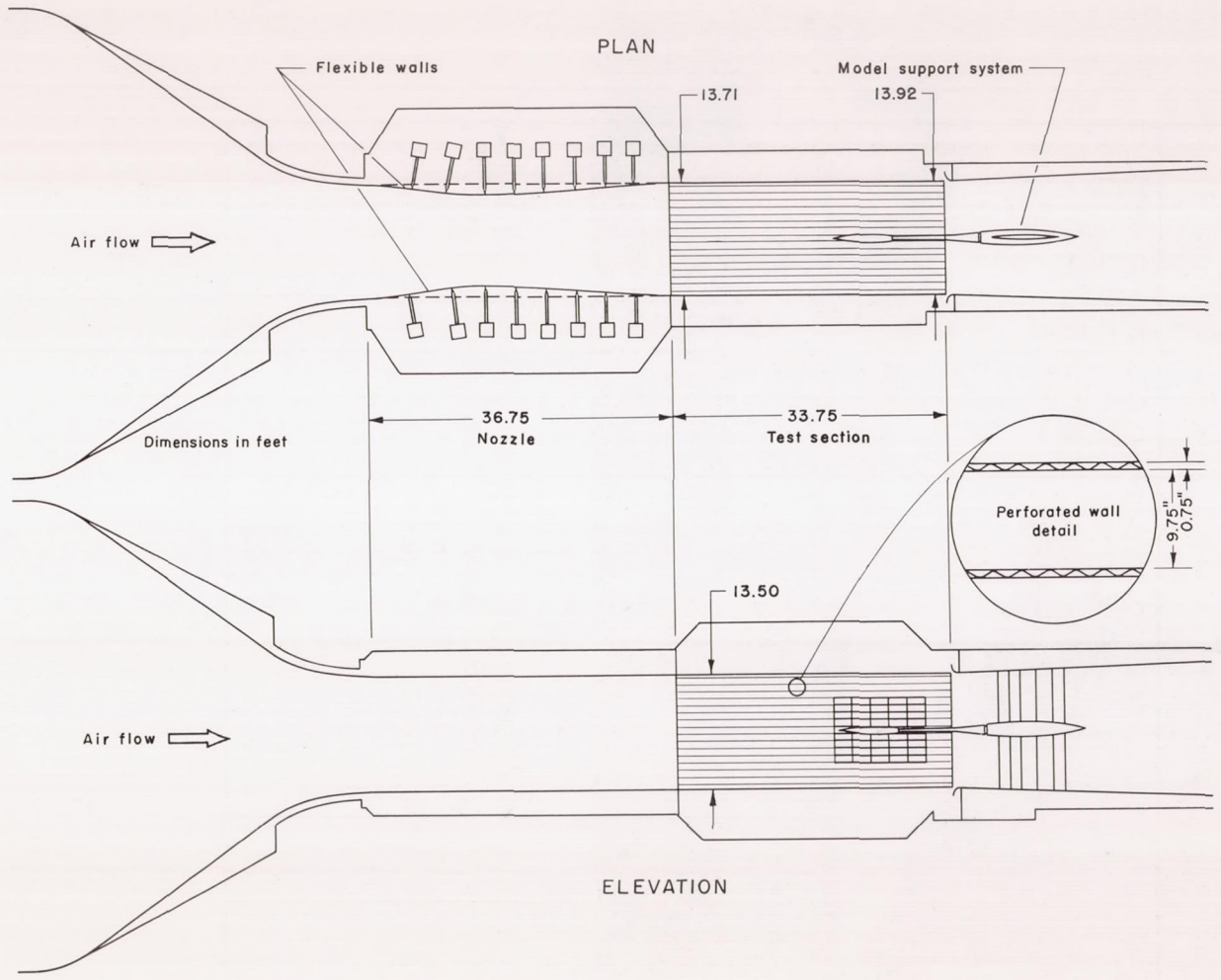

Figure 1.- General arrangement of the test section of the Ames 14-foot transonic wind tunnel.

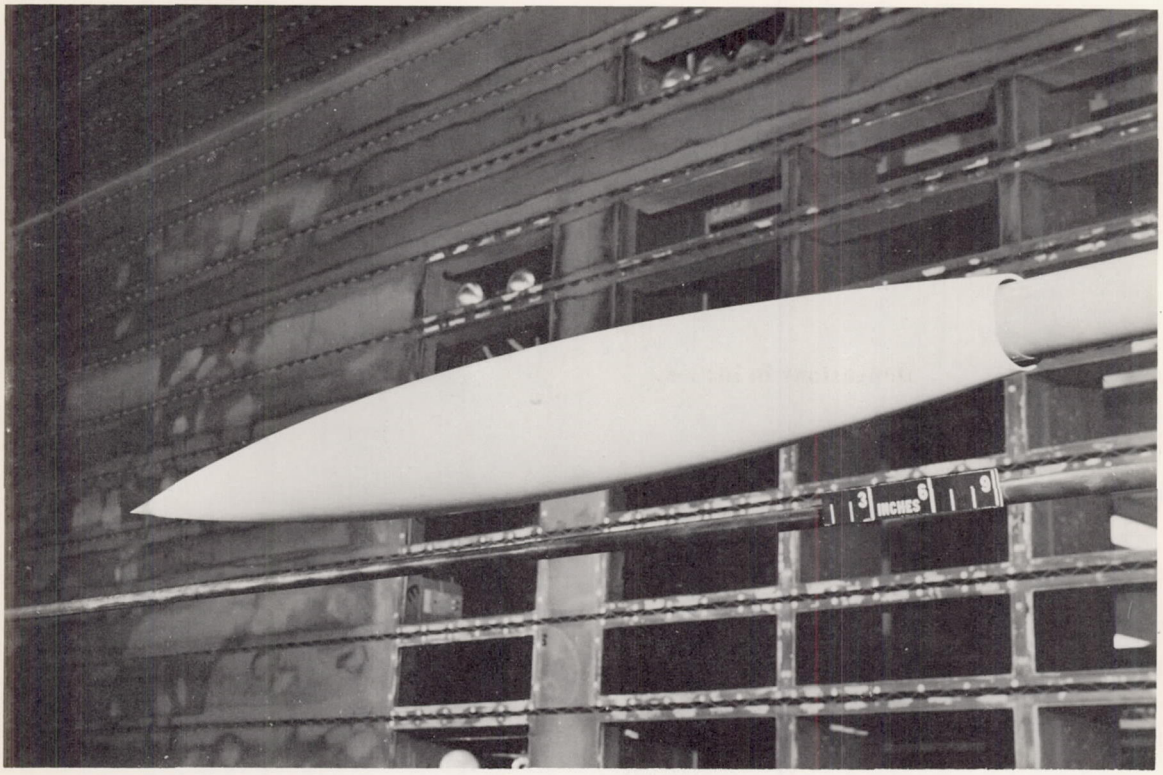

A-21864

Figure 2.- Photograph of a body of revolution and the survey tube mounted in the test section of the Ames 14-foot transonic wind tunnel.

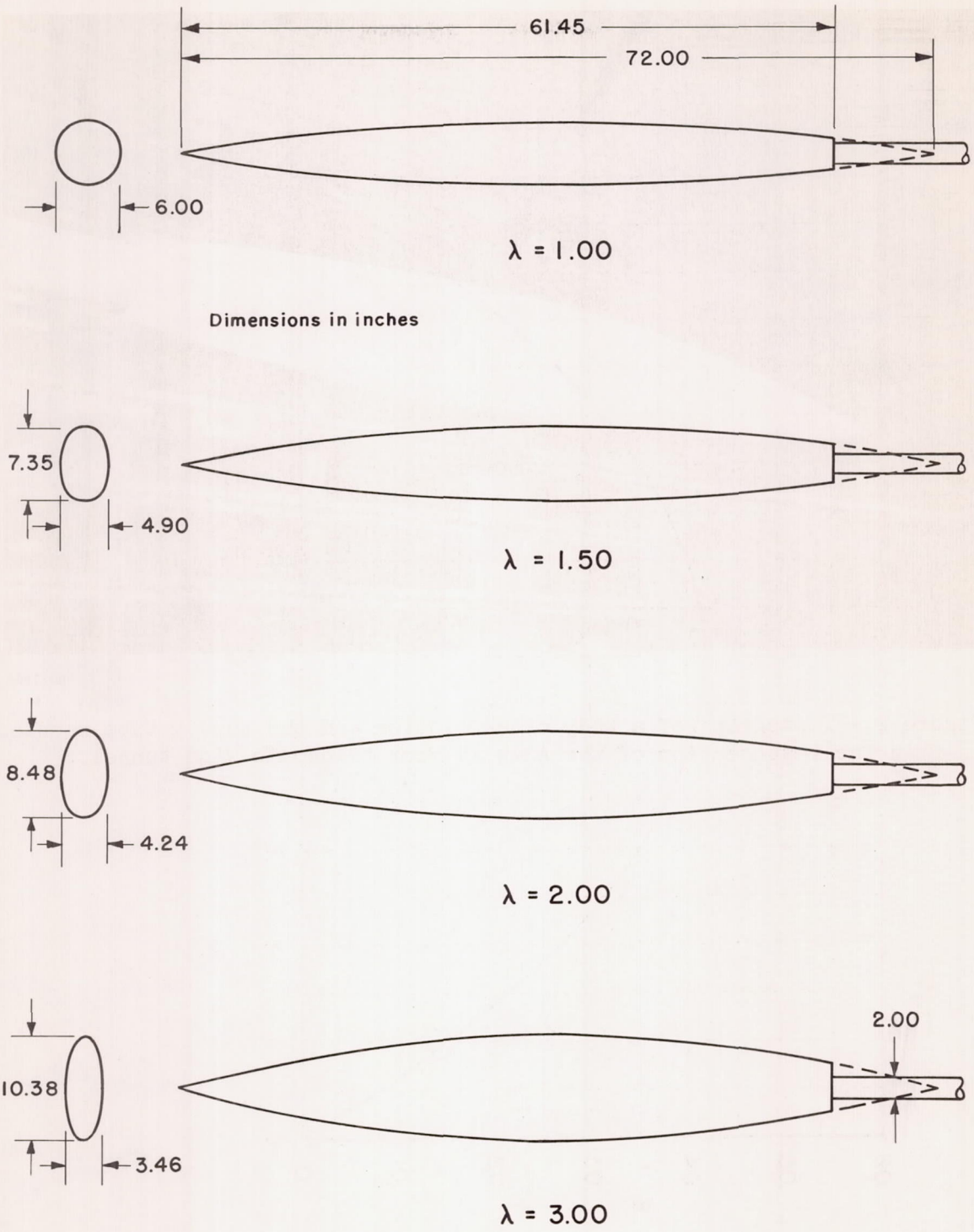

Figure 3.- Geometrical details of the models.

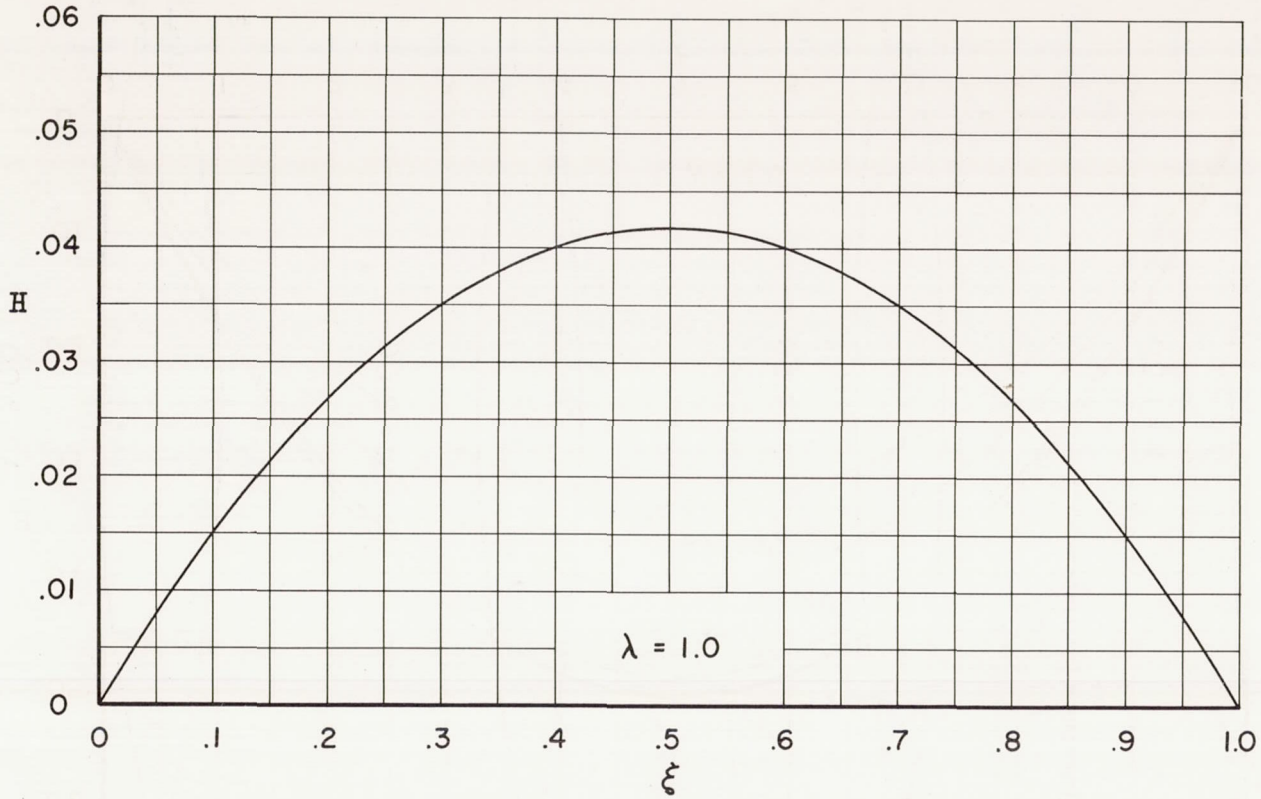

(a) Variation of H with ξ; $\lambda = 1.0$.

Figure 4.- Model geometry.

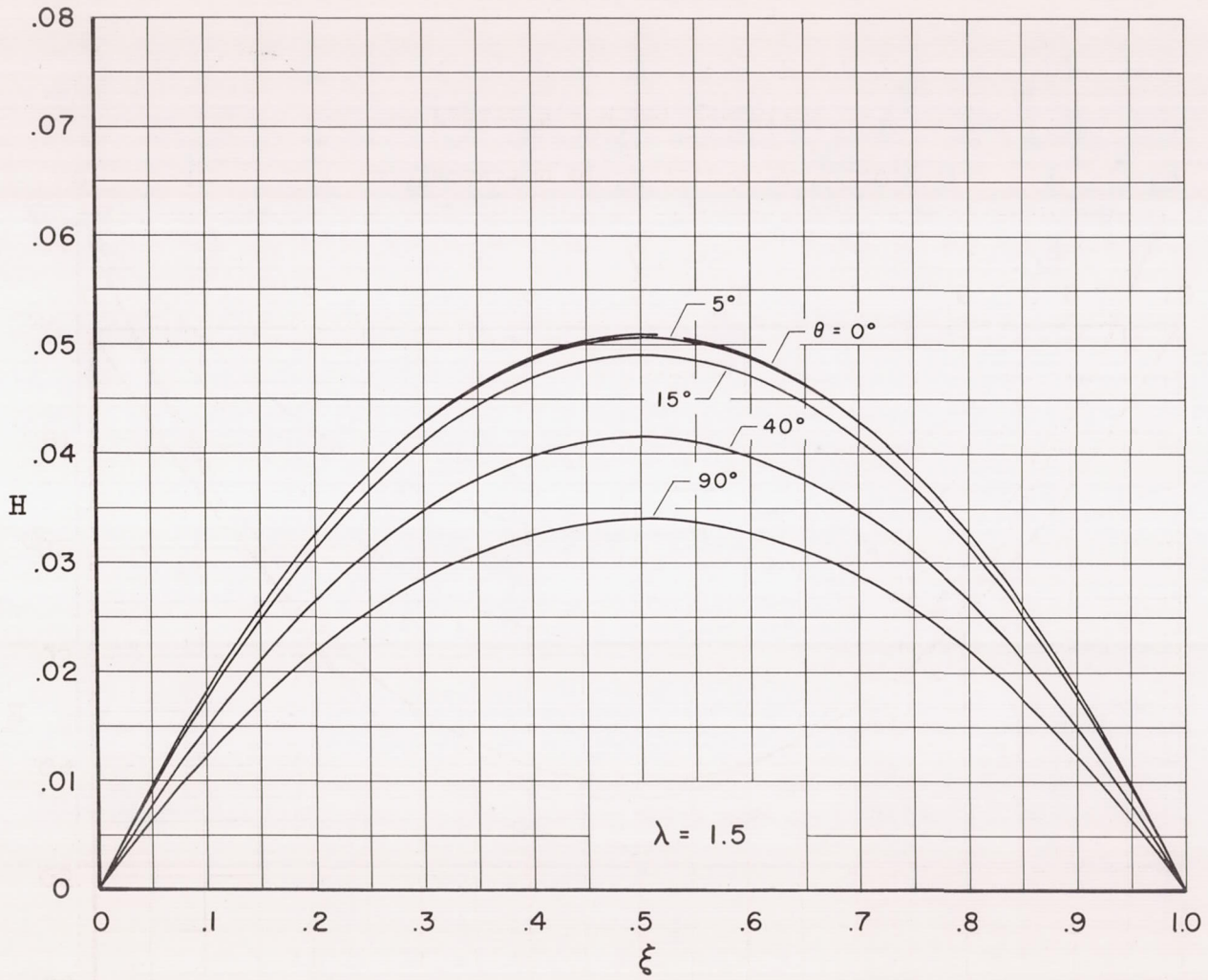

(b) Variation of H with ξ; λ = 1.5.

Figure 4.- Continued.

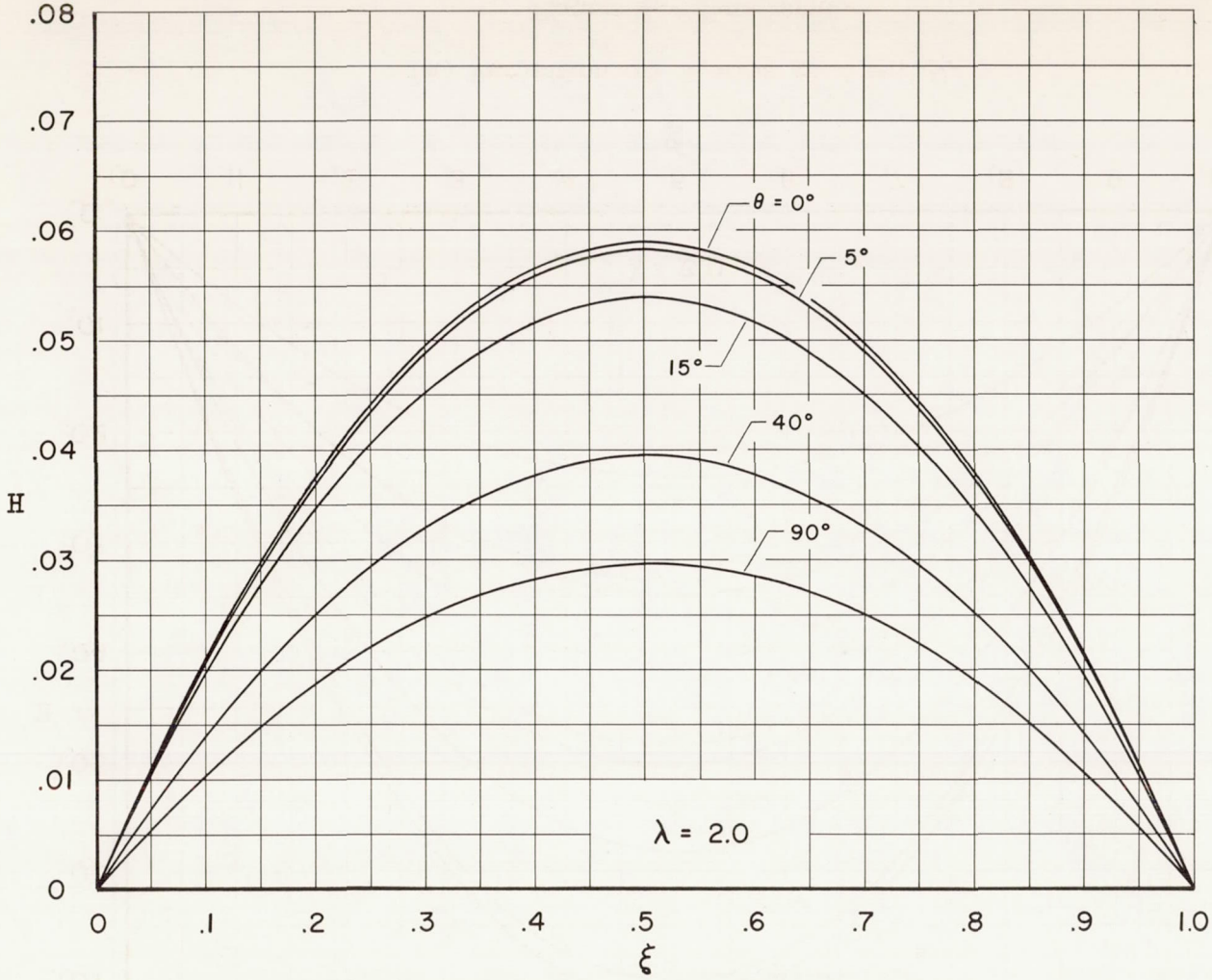

(c) Variation of H with ξ; $\lambda = 2.0$.

Figure 4.- Continued.

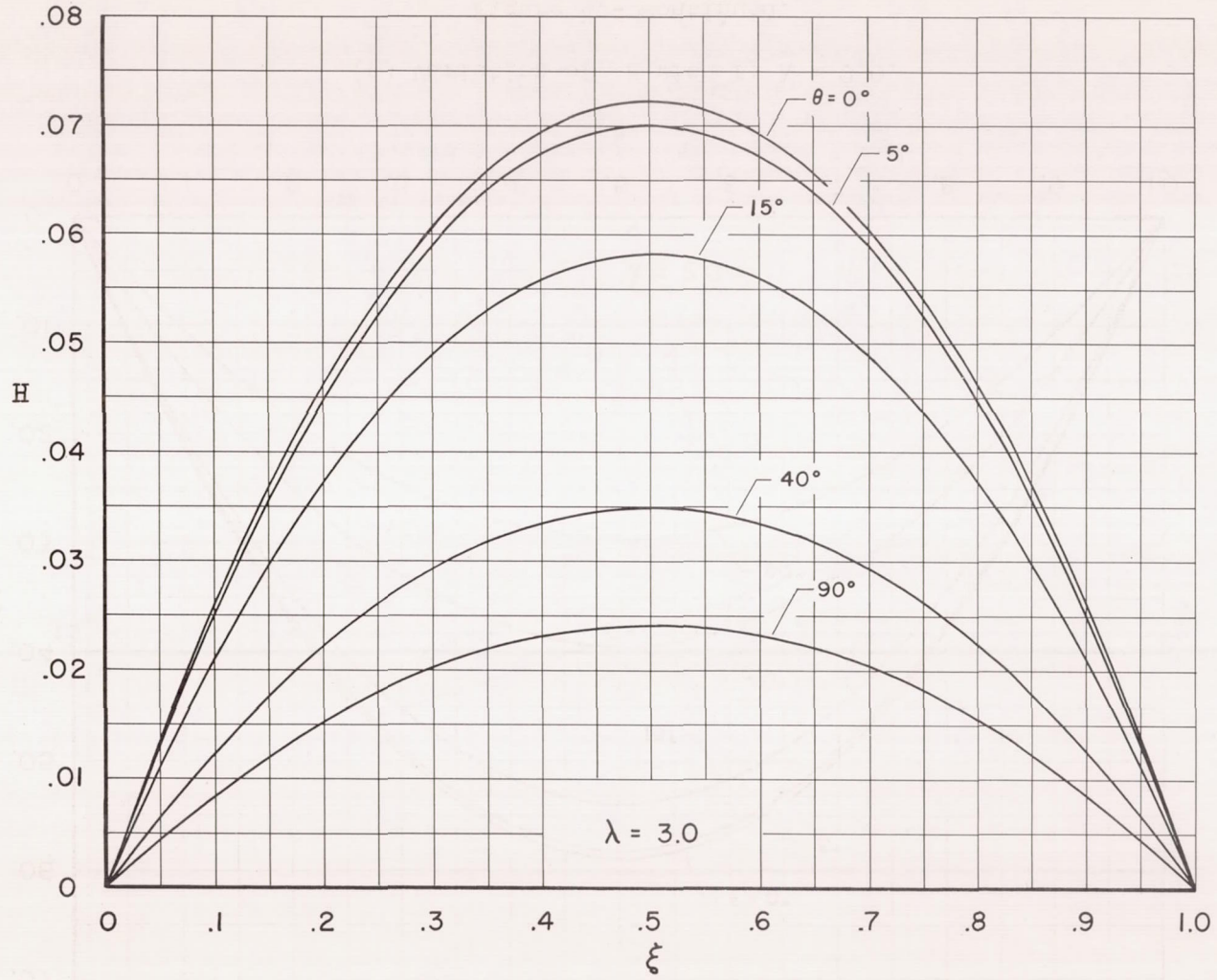

(d) Variation of H with ξ; $\lambda = 3.0$.

Figure 4.- Continued.

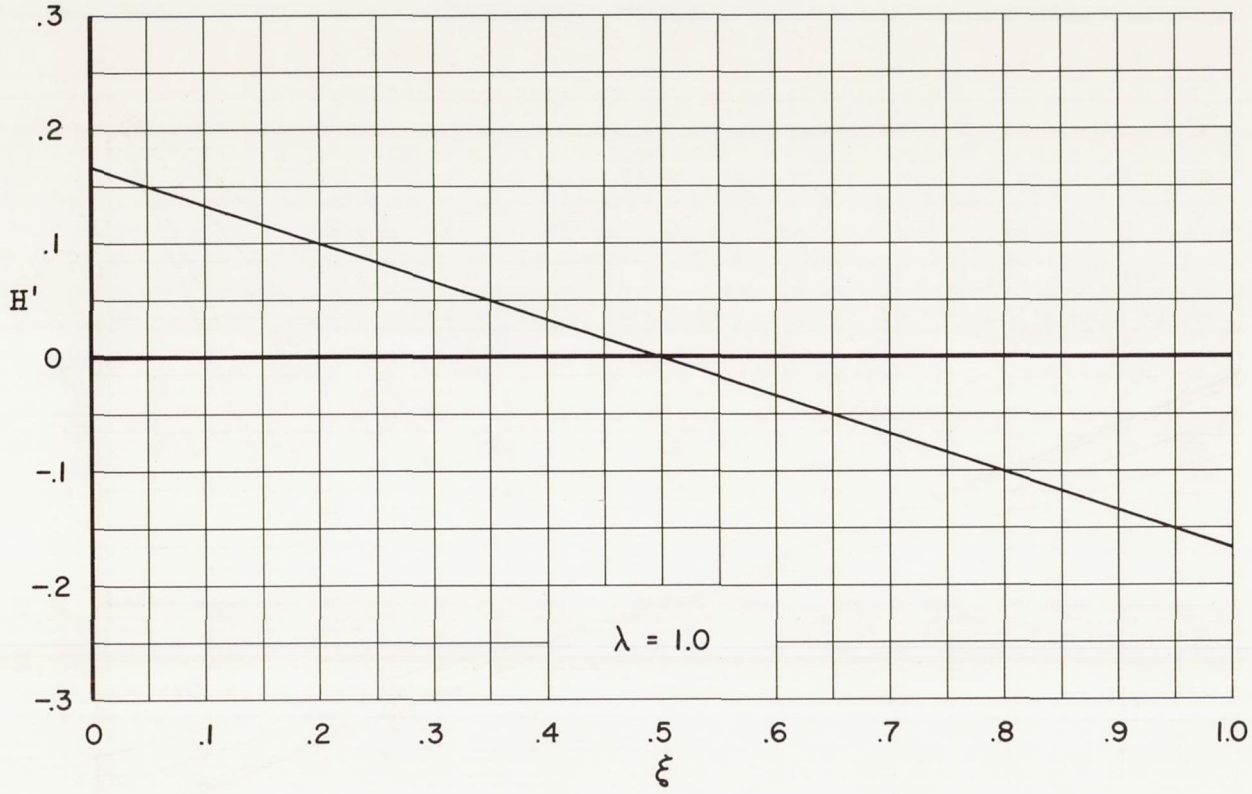

(e) Variation of H' with ξ; $\lambda = 1.0$.

Figure 4.- Continued.

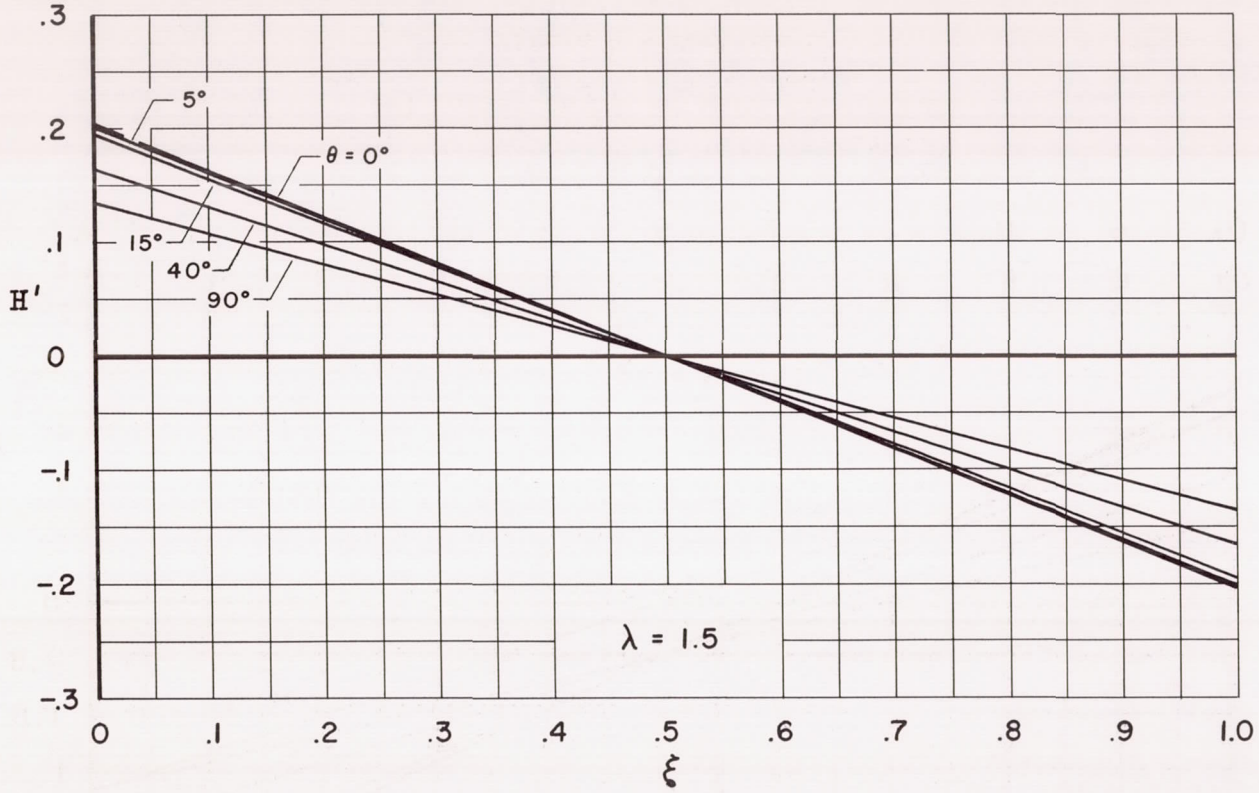

(f) Variation of H' with ξ; $\lambda = 1.5$.

Figure 4.- Continued.

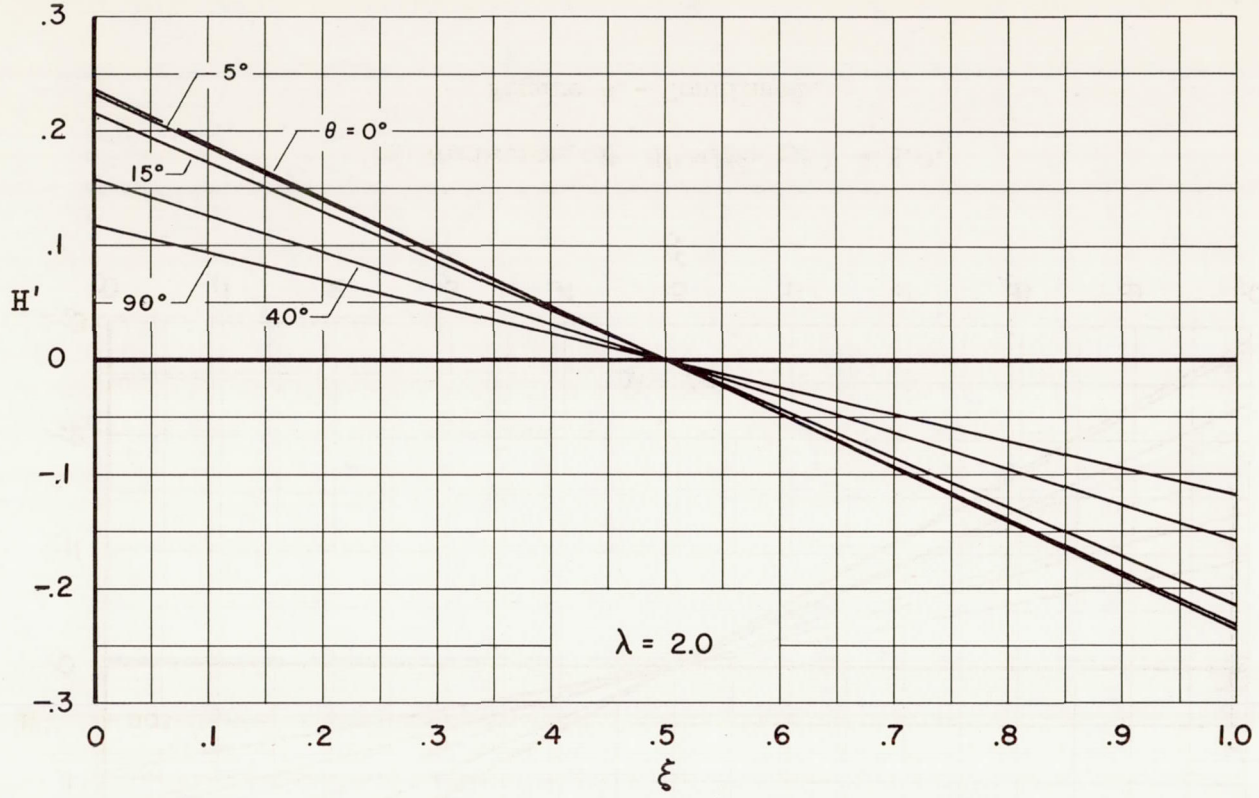

(g) Variation of H' with ξ; $\lambda = 2.0$.

Figure 4.- Continued.

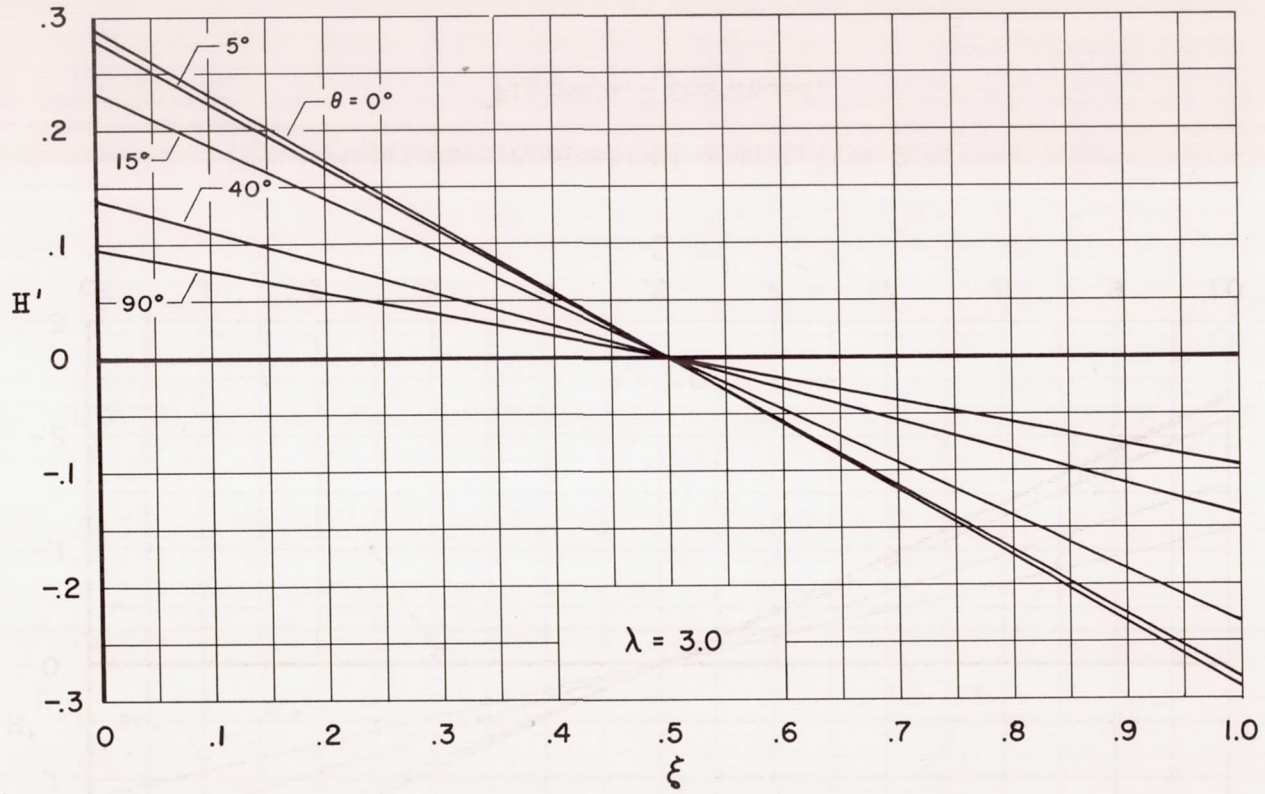

(h) Variation of H' with ξ; $\lambda = 3.0$.

Figure 4.- Continued.

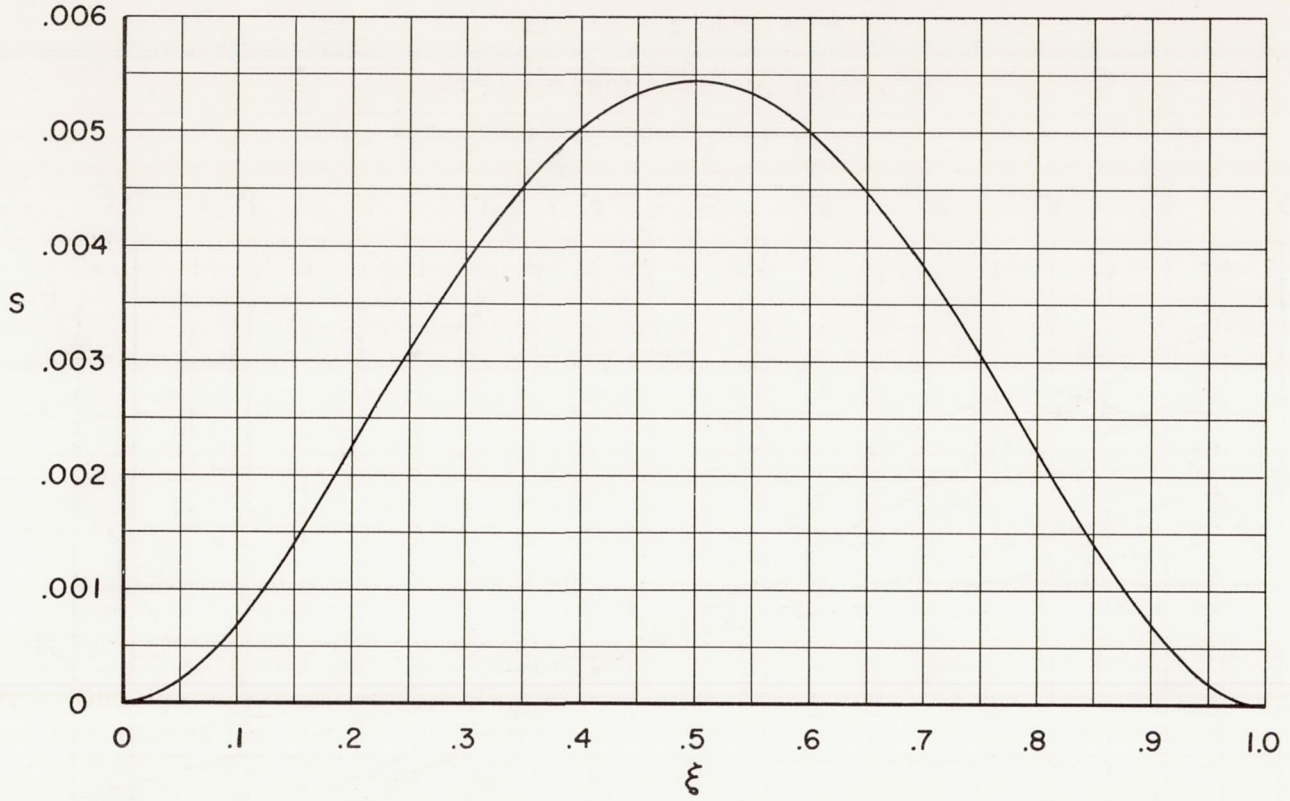

(i) Variation of S with ξ; λ = 1.0, 1.5, 2.0, and 3.0.

Figure 4.- Continued.

(j) Variation of S' with ξ.

Figure 4.- Concluded.

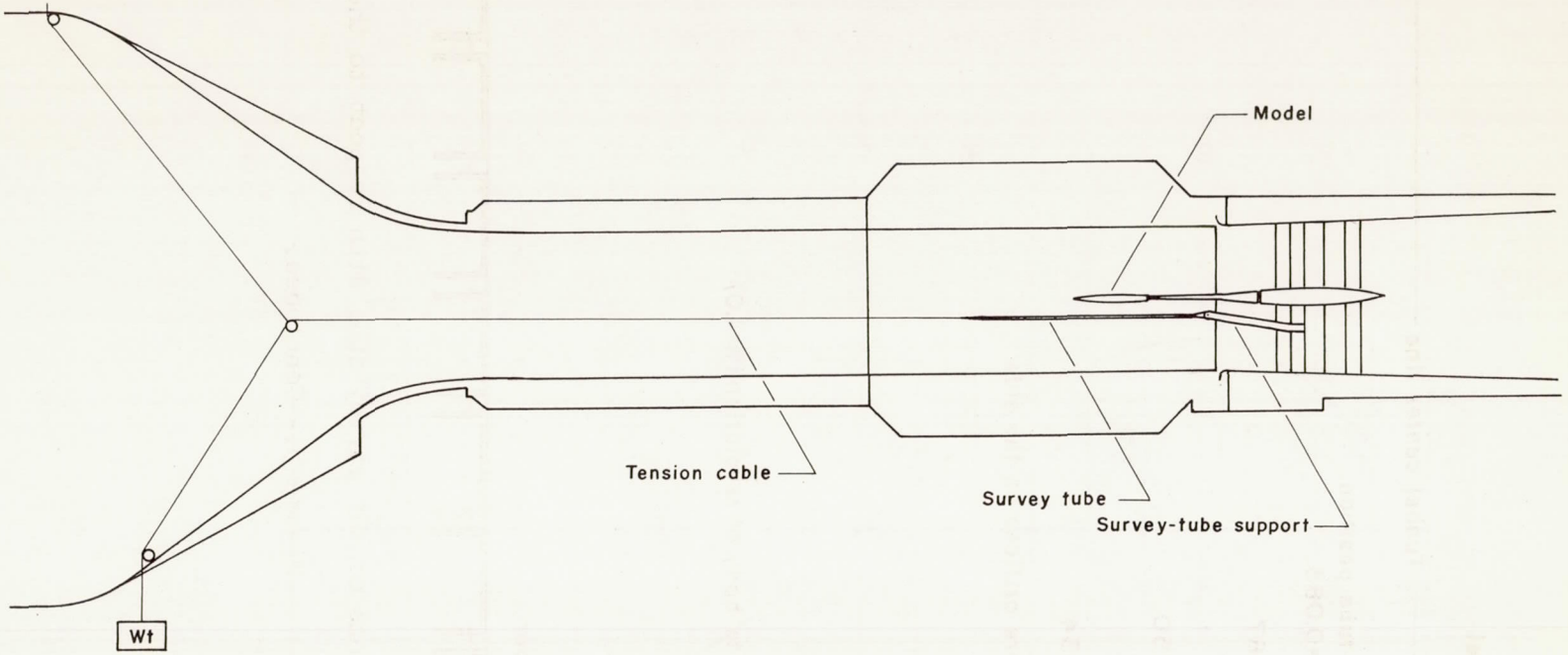

(a) Survey-tube support system.

Figure 5.- Schematic drawings of the model and survey tube.

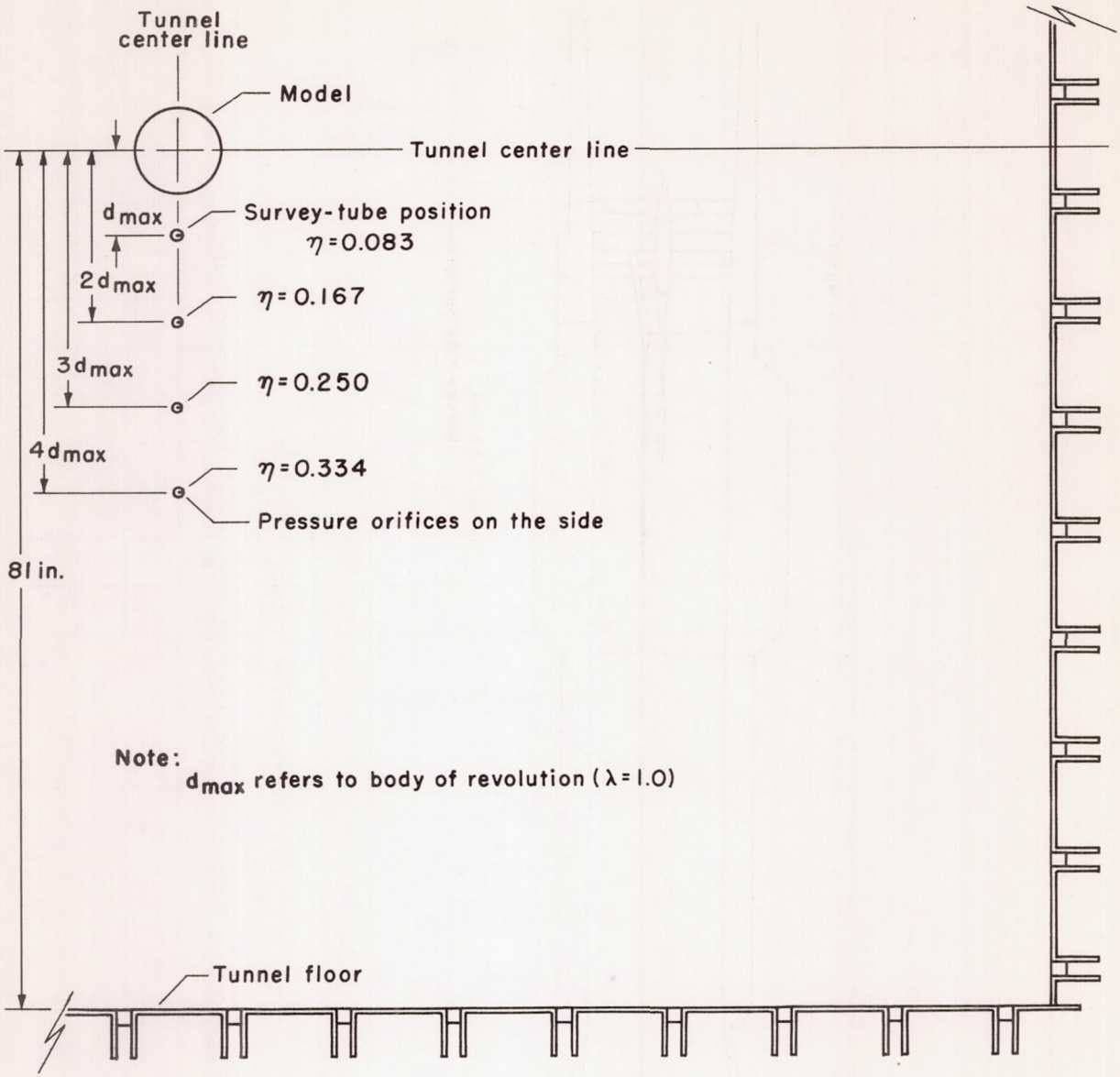

(b) Relative positions of the survey tube with respect to the model.

Figure 5.- Concluded.

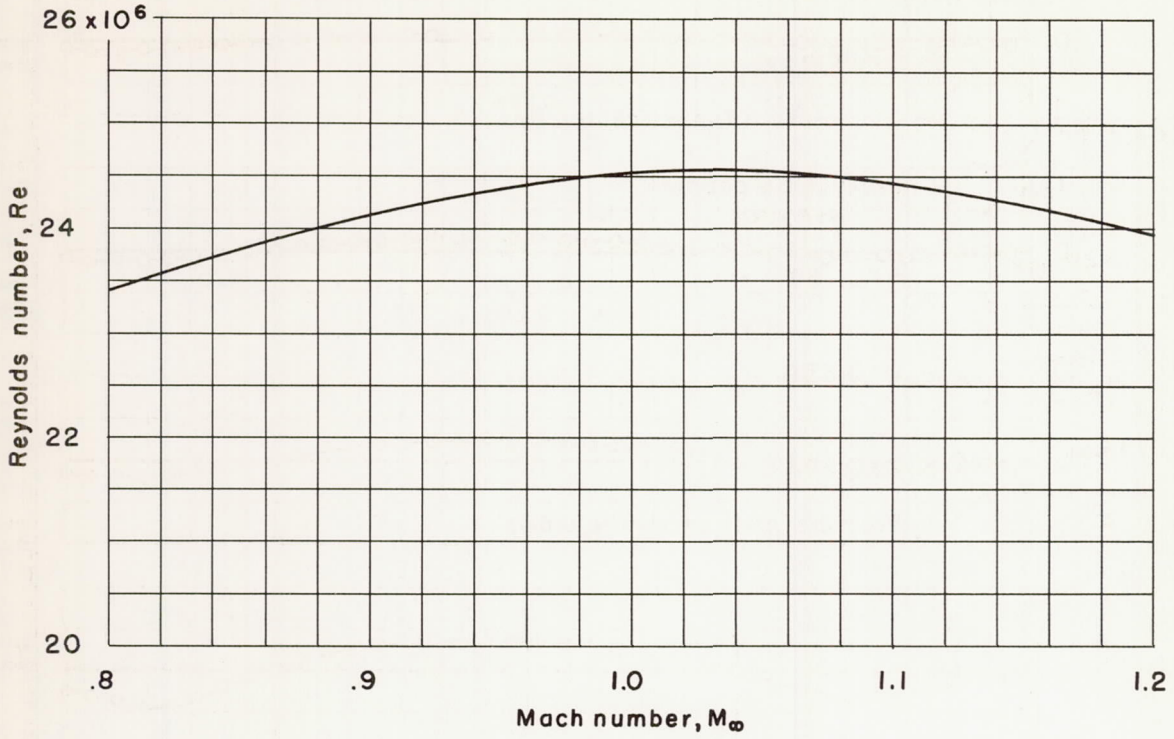

Figure 6.- Variation of Mach number with Reynolds number based on body length.

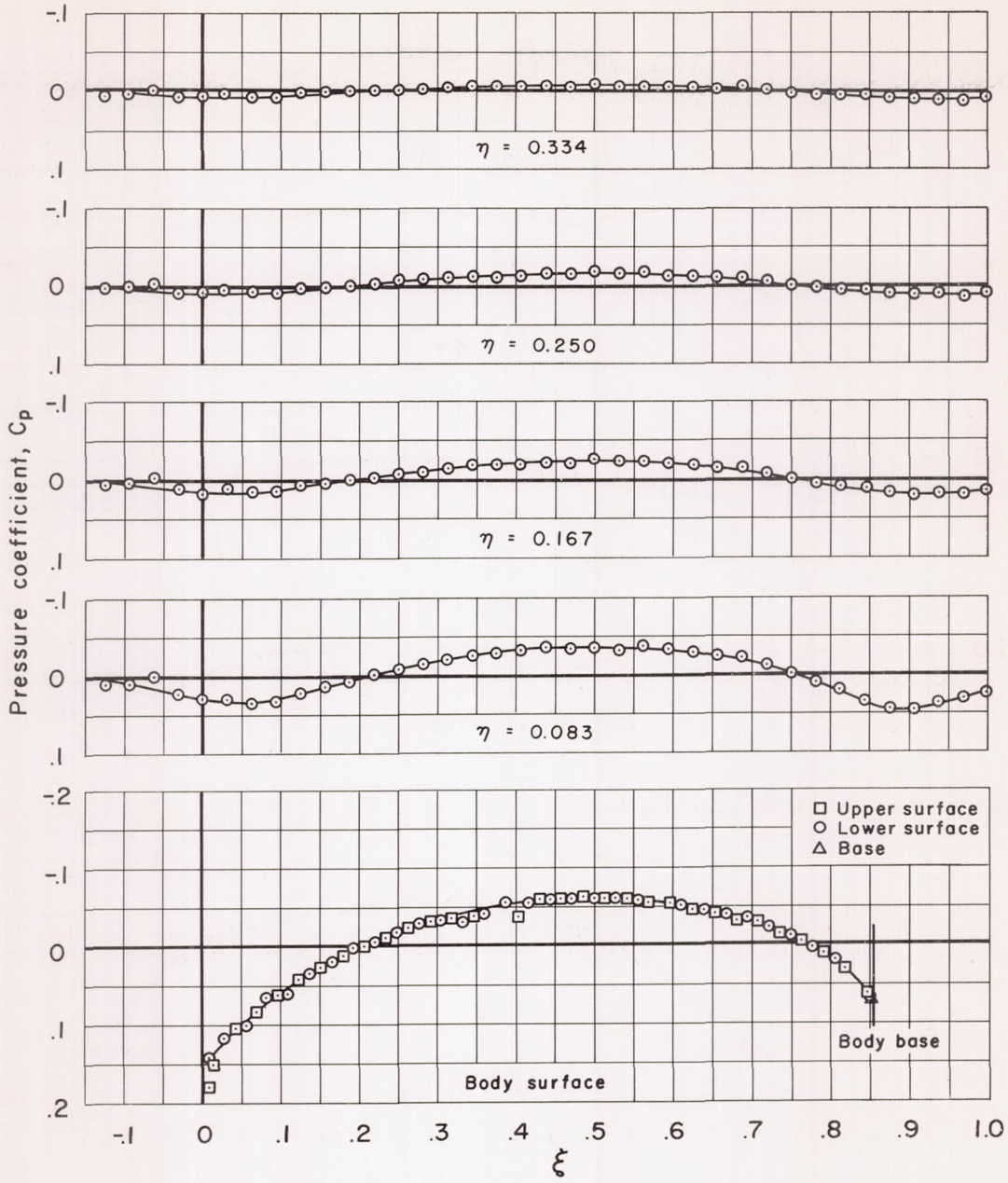

(a) $M_\infty = 0.80$, $\lambda = 1.0$

Figure 7.- Measured pressure distributions for the body of revolution.

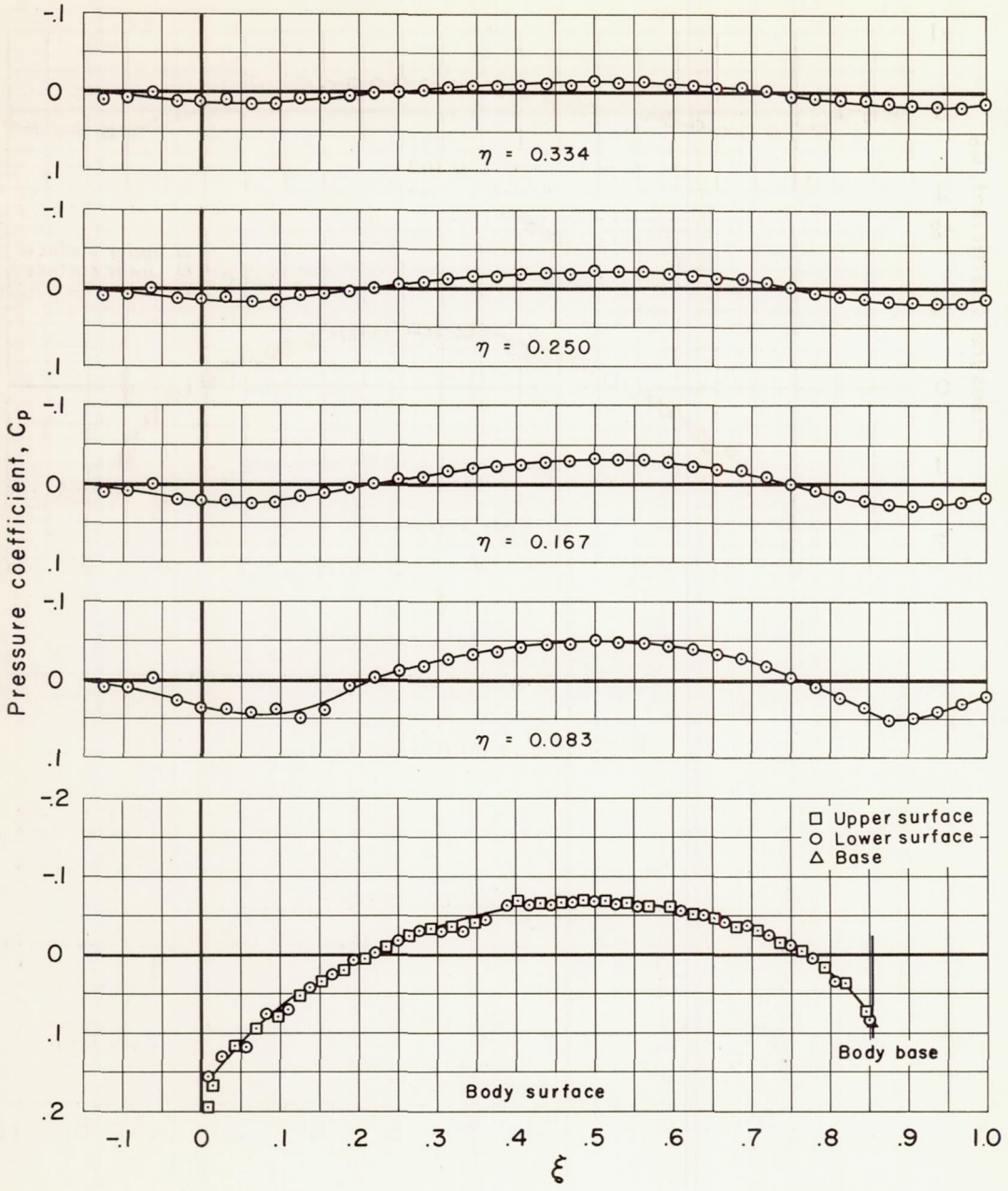

(b) $M_\infty = 0.90$, $\lambda = 1.0$

Figure 7.- Continued.

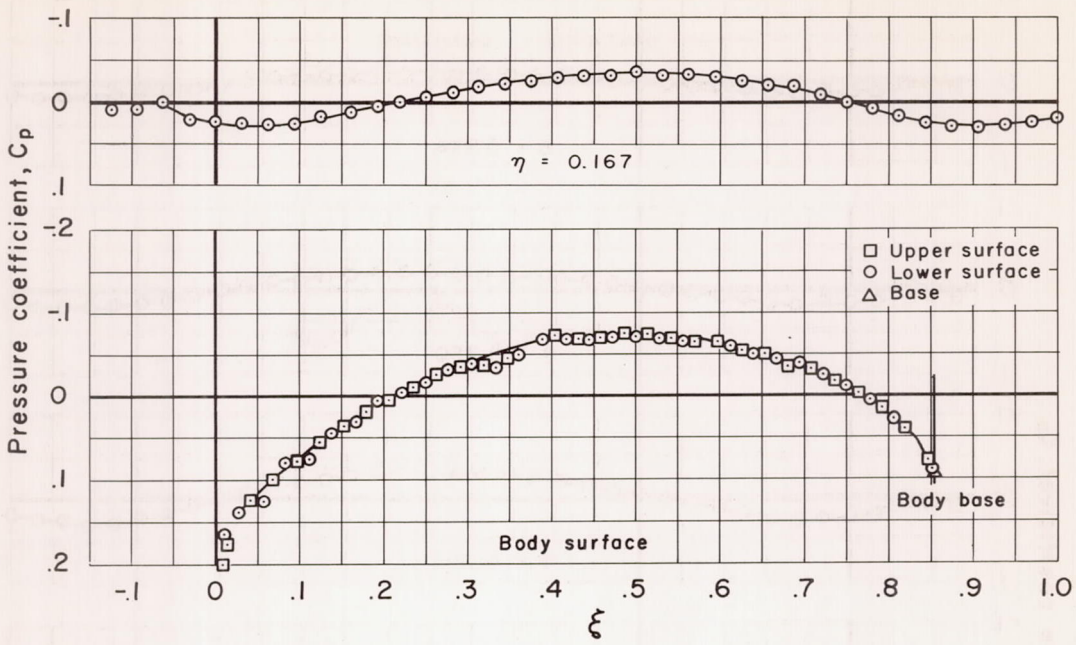

(c) $M_\infty = 0.925$, $\lambda = 1.0$

Figure 7.- Continued.

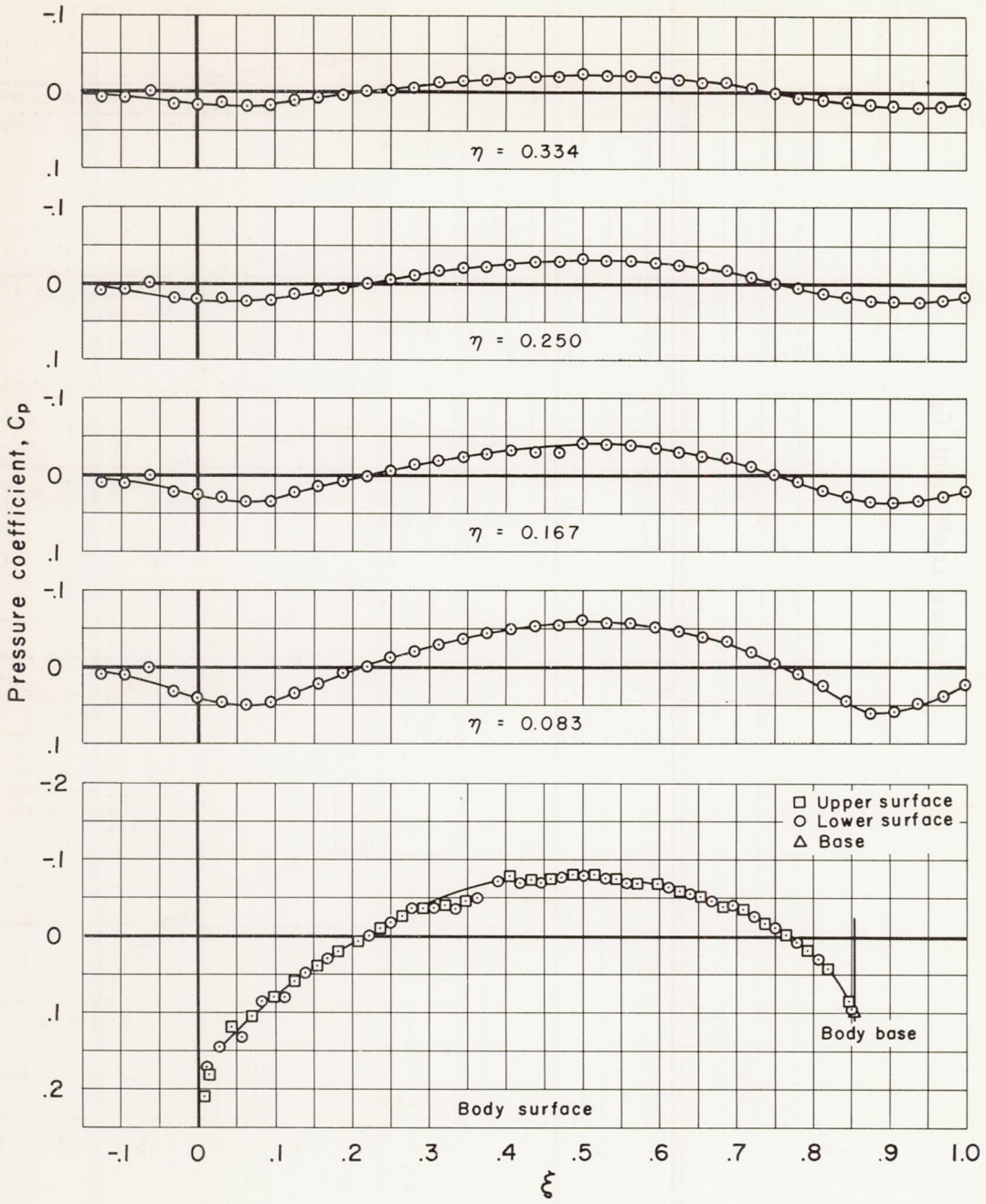

(d) $M_\infty = 0.95$, $\lambda = 1.0$

Figure 7.- Continued.

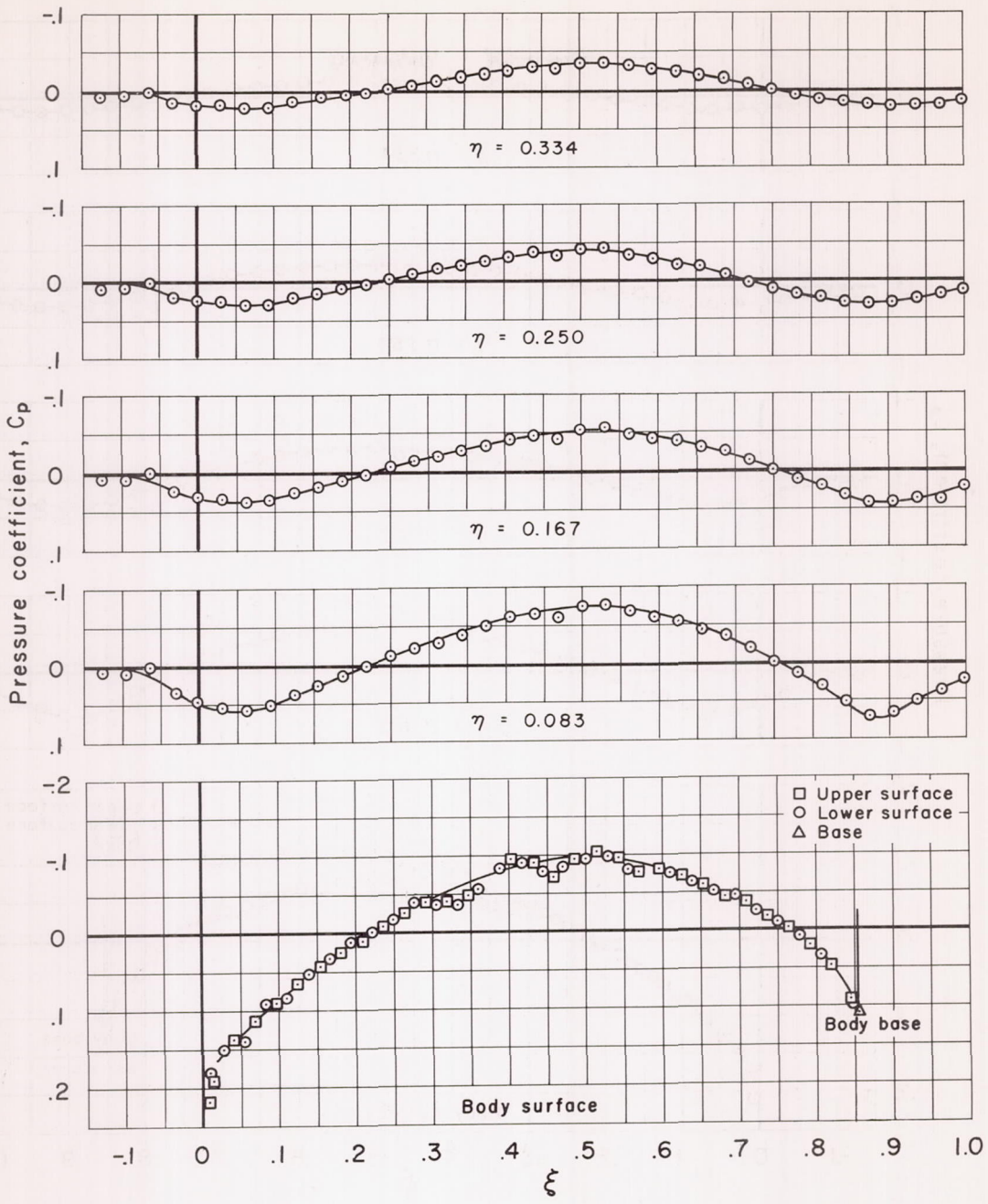

(e) $M_\infty = 0.975$, $\lambda = 1.0$

Figure 7.- Continued.

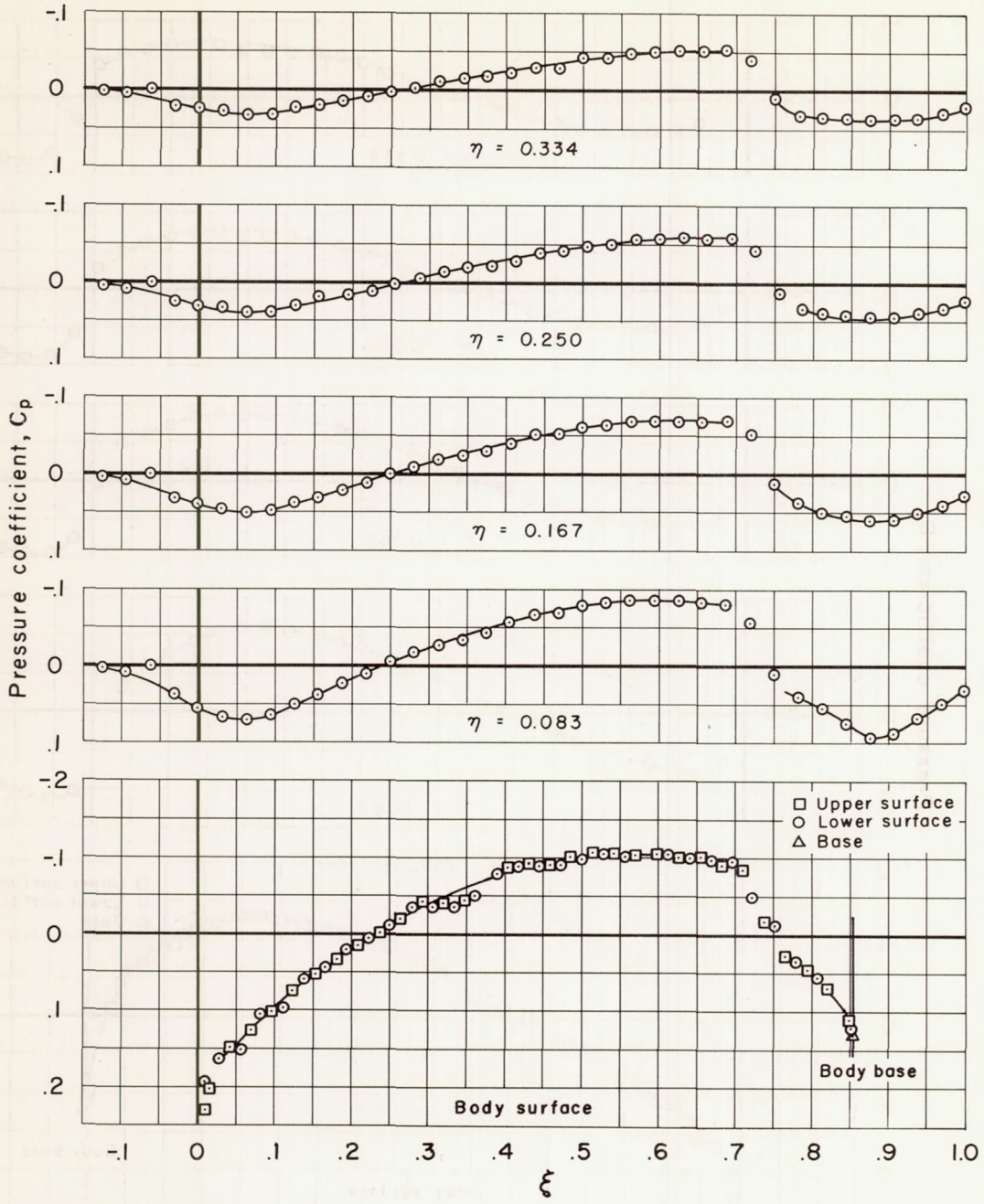

(f) $M_\infty = 1.00$, $\lambda = 1.0$

Figure 7.- Continued.

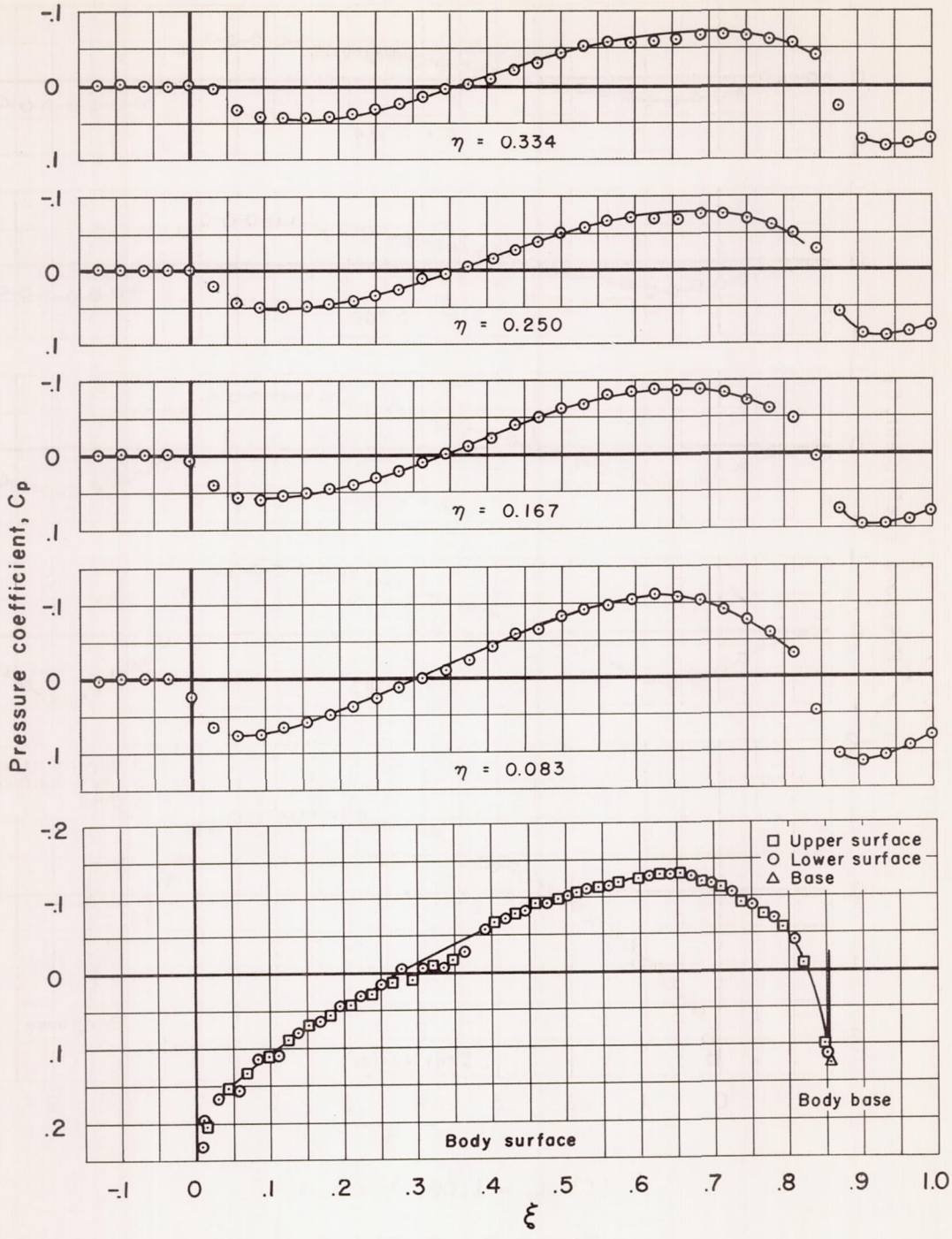

(g) $M_\infty = 1.025$, $\lambda = 1.0$

Figure 7.- Continued.

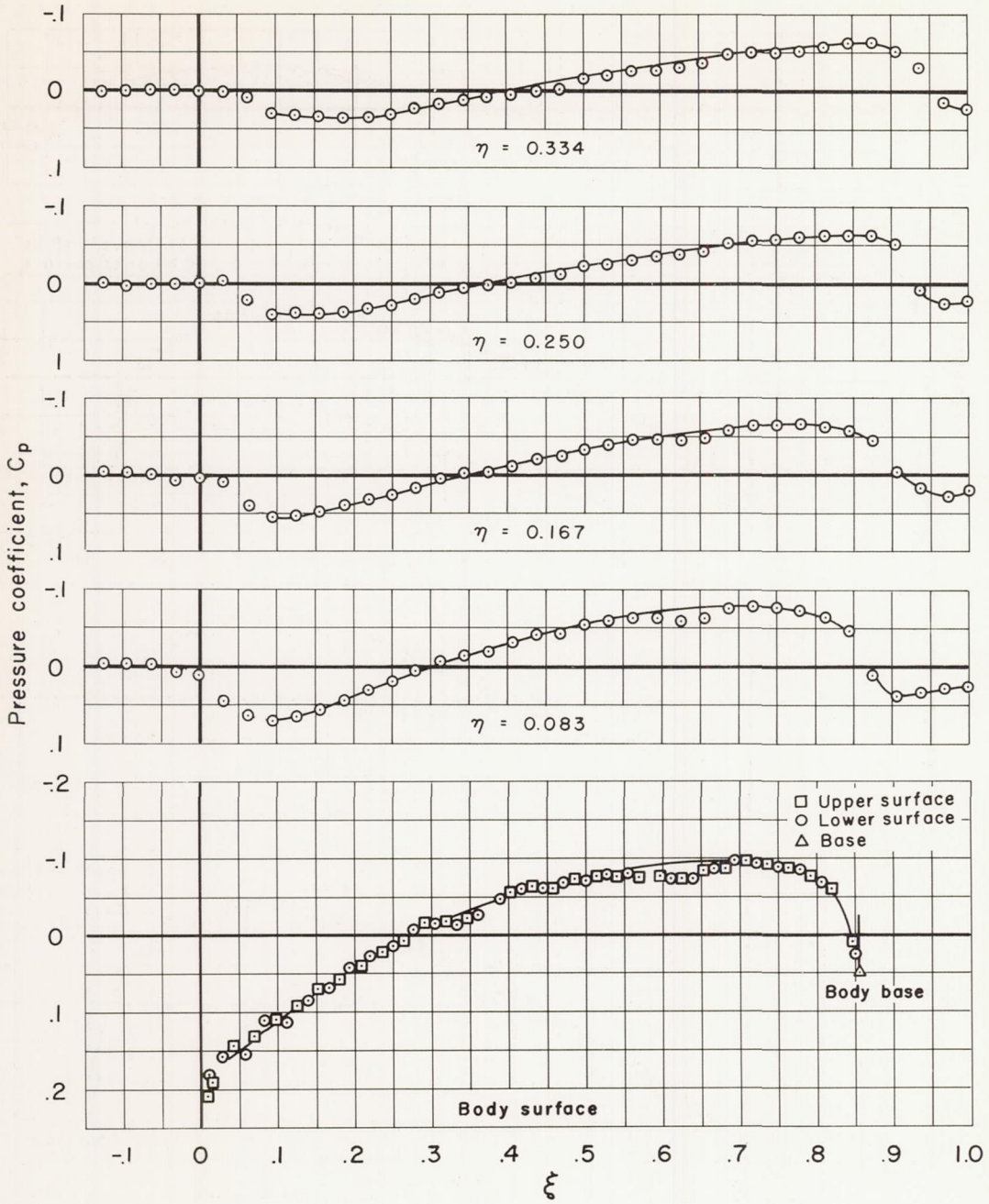

(h) $M_\infty = 1.05$, $\lambda = 1.0$

Figure 7.- Continued.

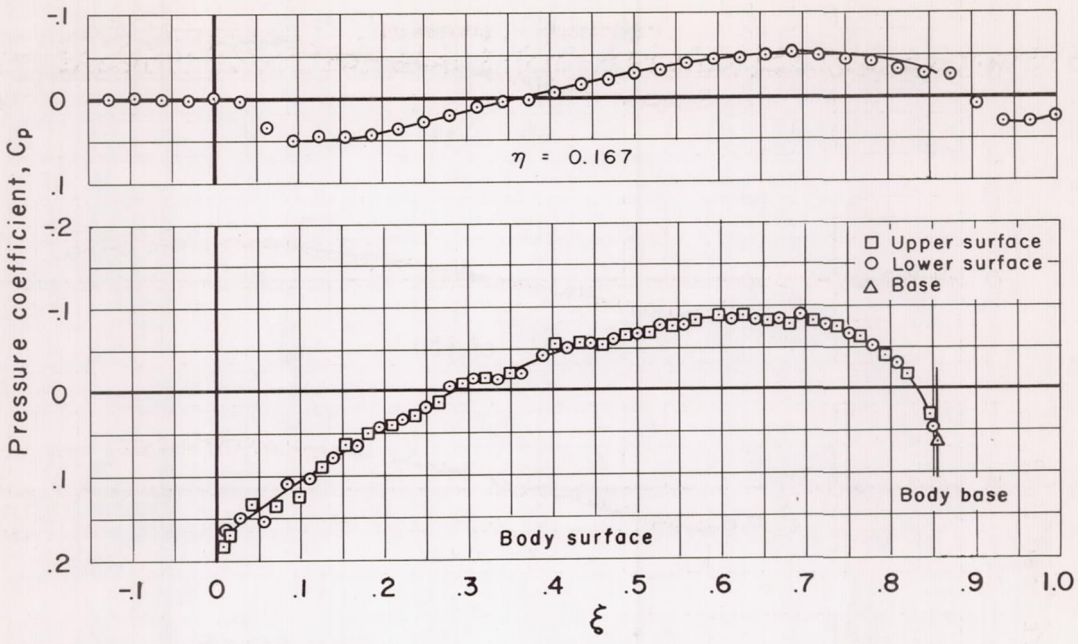

(i) $M_\infty = 1.075$, $\lambda = 1.0$

Figure 7.- Continued.

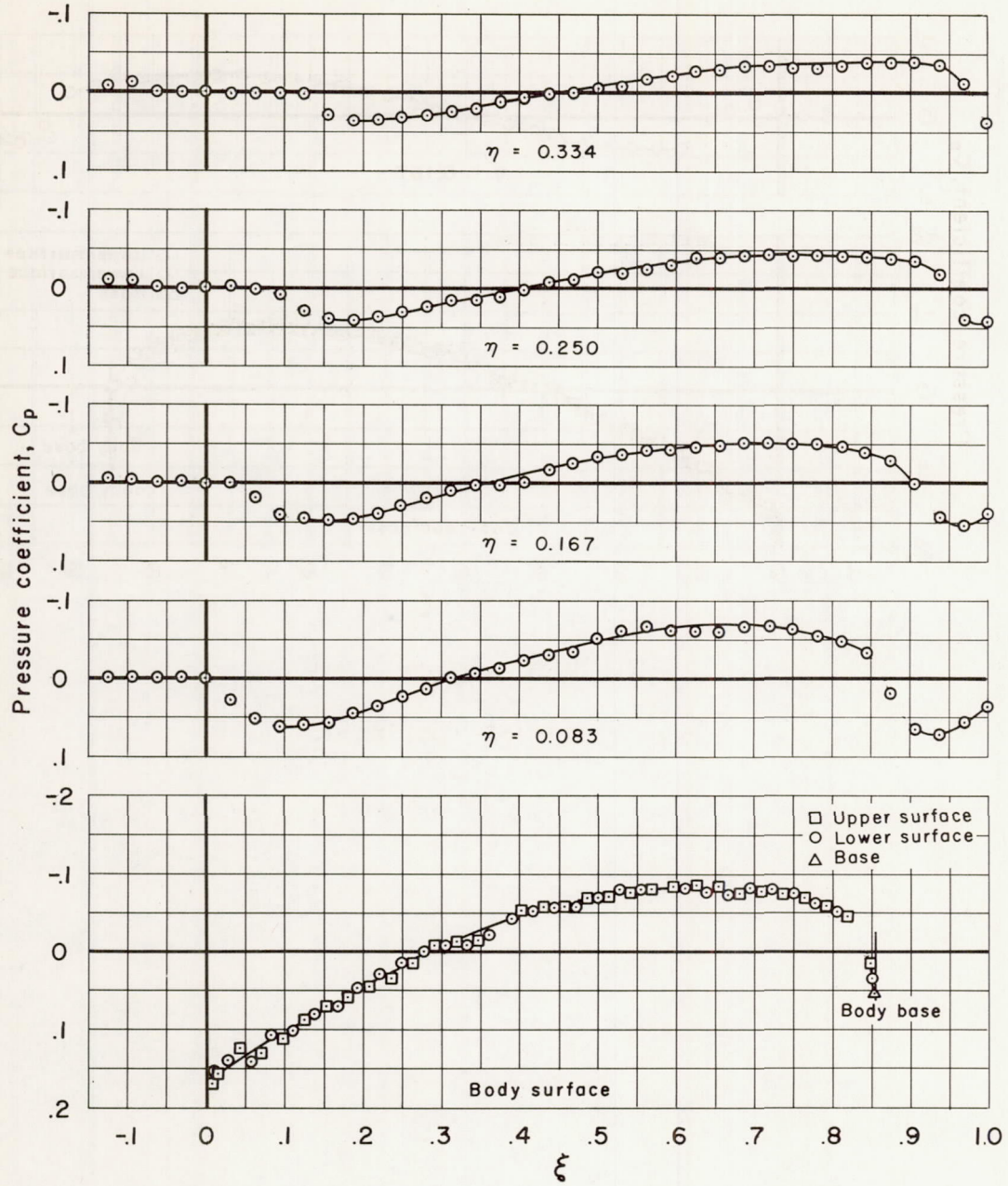

(j) $M_\infty = 1.10$, $\lambda = 1.0$

Figure 7.- Continued.

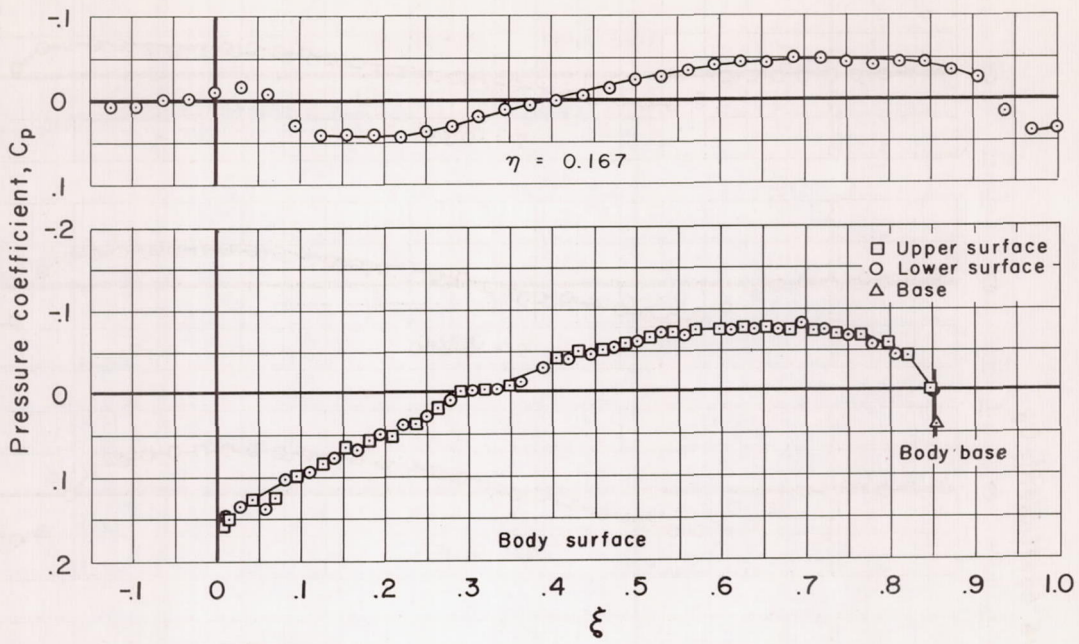

(k) $M_\infty = 1.15$, $\lambda = 1.0$

Figure 7.- Continued.

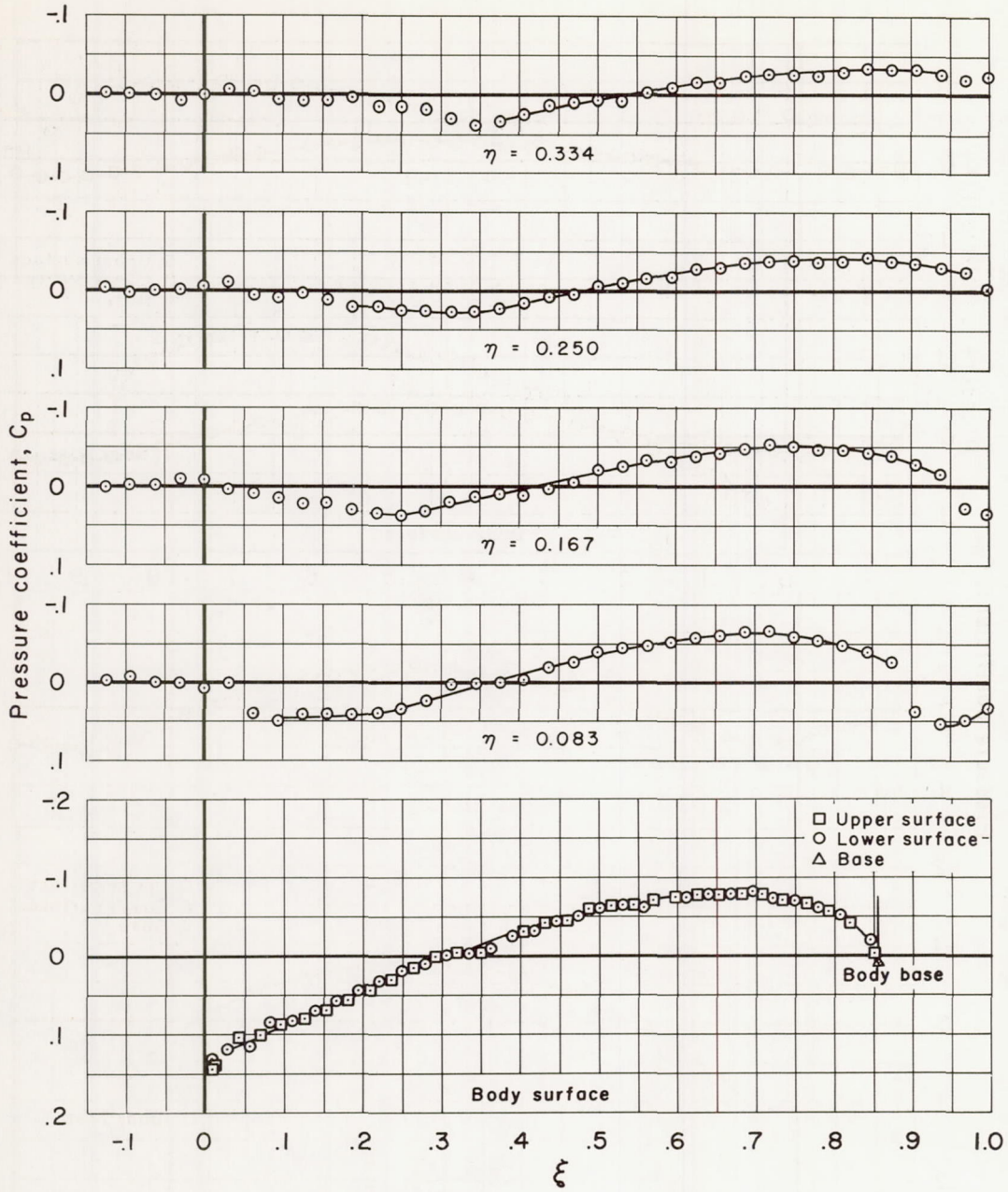

(l) $M_\infty = 1.20$, $\lambda = 1.0$

Figure 7.- Concluded.

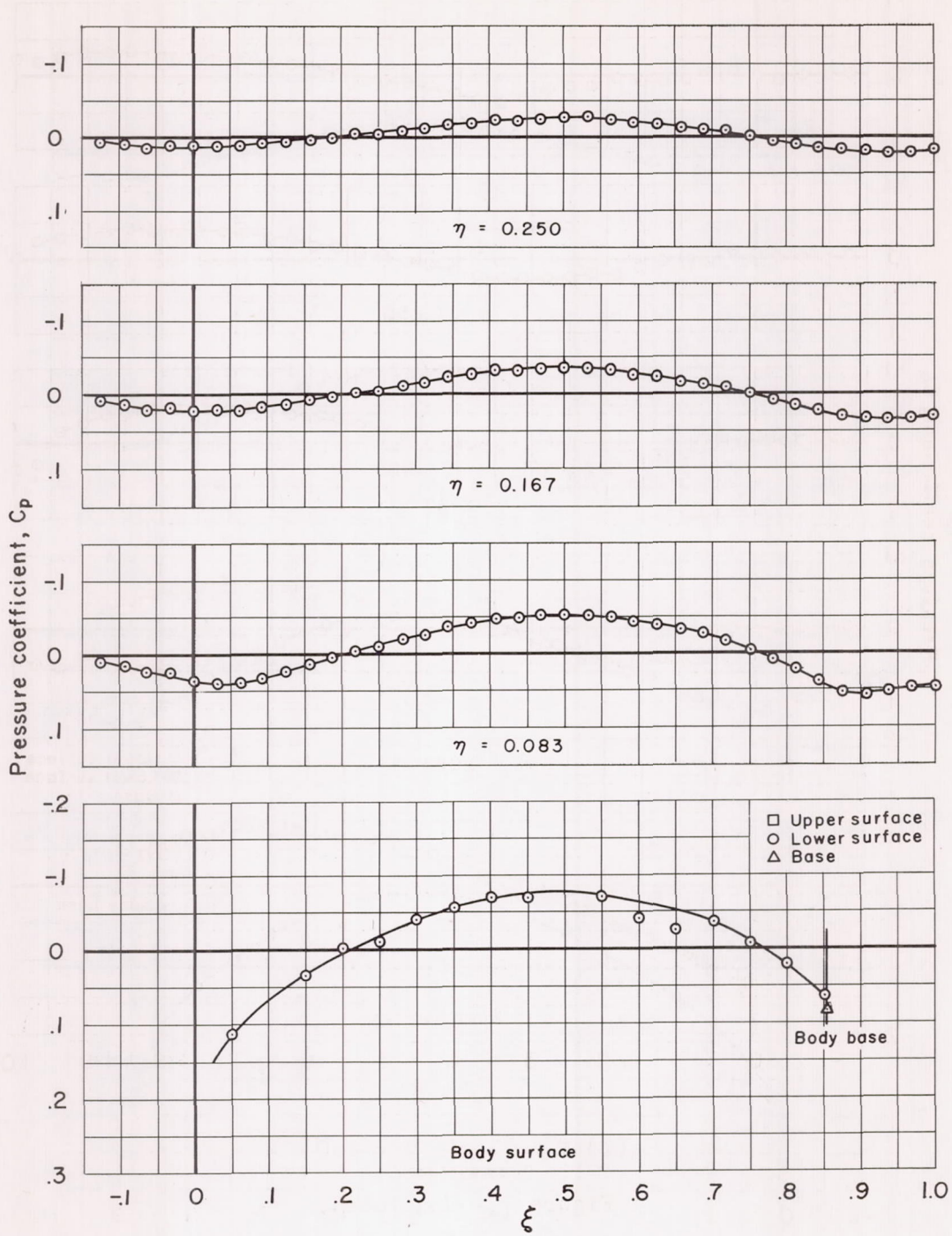

(a) $M_\infty = 0.90$, $\lambda = 1.5$, $\theta = 0^\circ$

Figure 8.- Measured pressure distributions for the body having an axis ratio of 1.5; $\alpha = 0^\circ$.

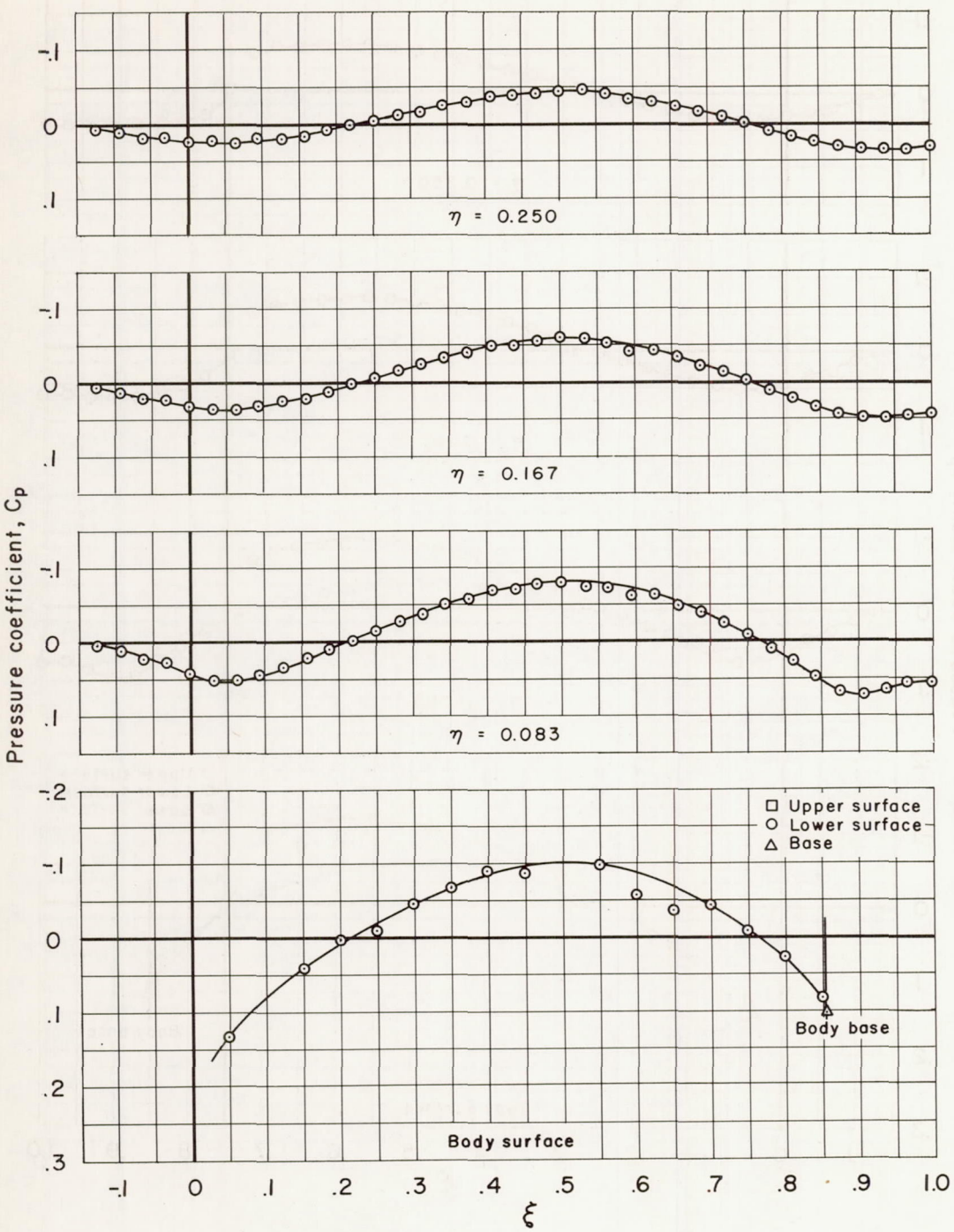

(b) $M_\infty = 0.975$, $\lambda = 1.5$, $\theta = 0^\circ$

Figure 8.- Continued.

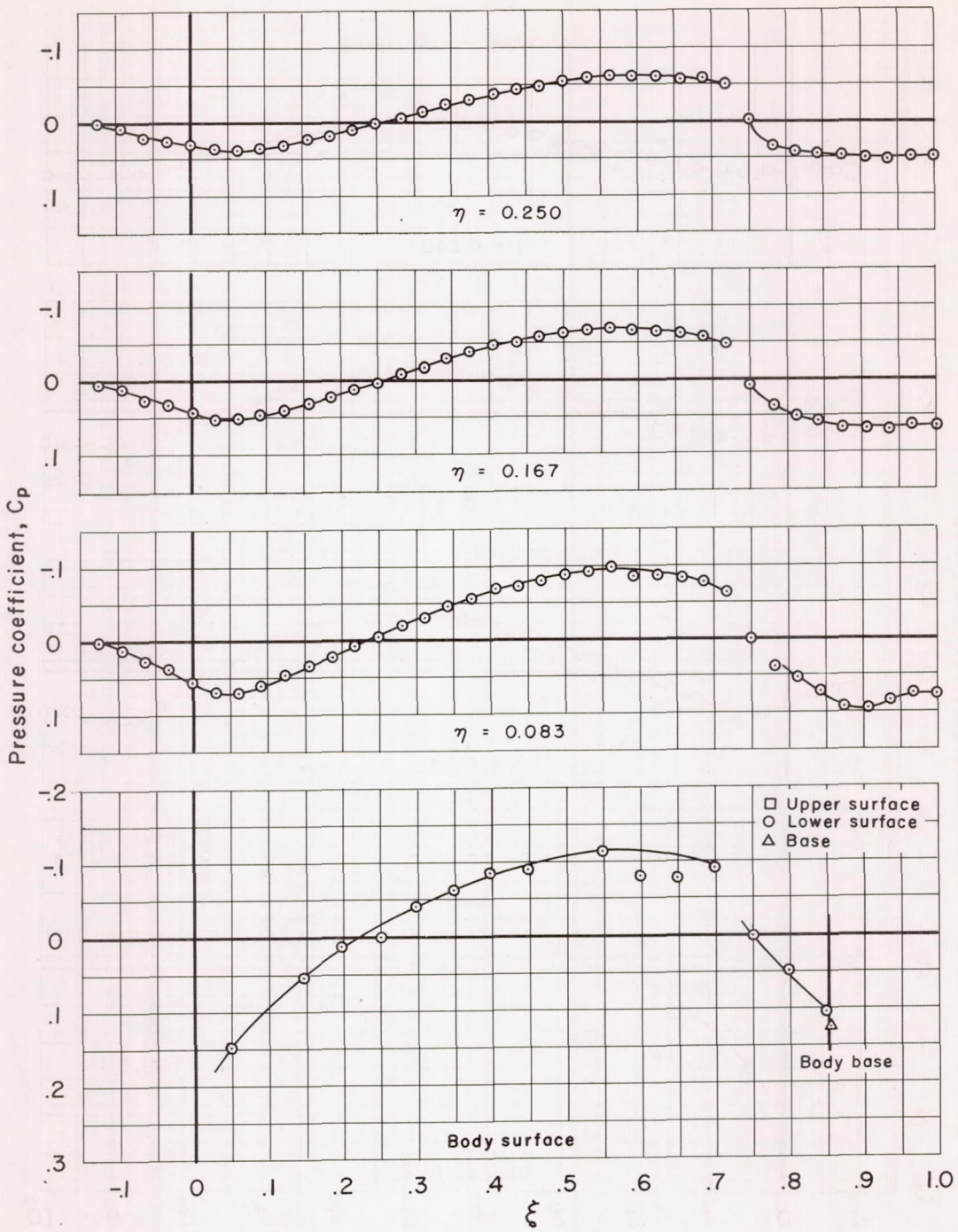

(c) $M_\infty = 1.00$, $\lambda = 1.5$, $\theta = 0^\circ$

Figure 8.- Continued.

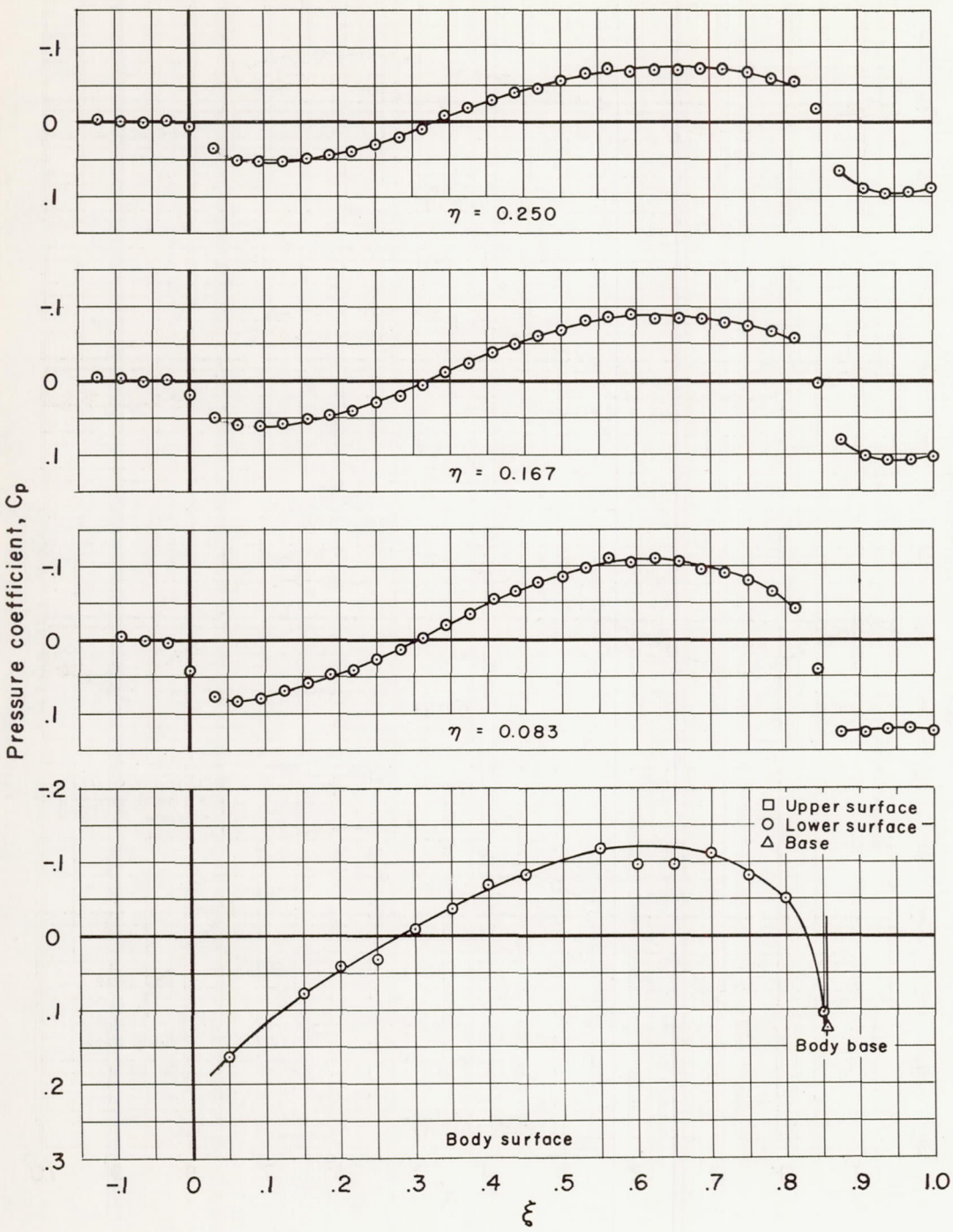

(d) $M_\infty = 1.025$, $\lambda = 1.5$, $\theta = 0^\circ$

Figure 8.- Continued.

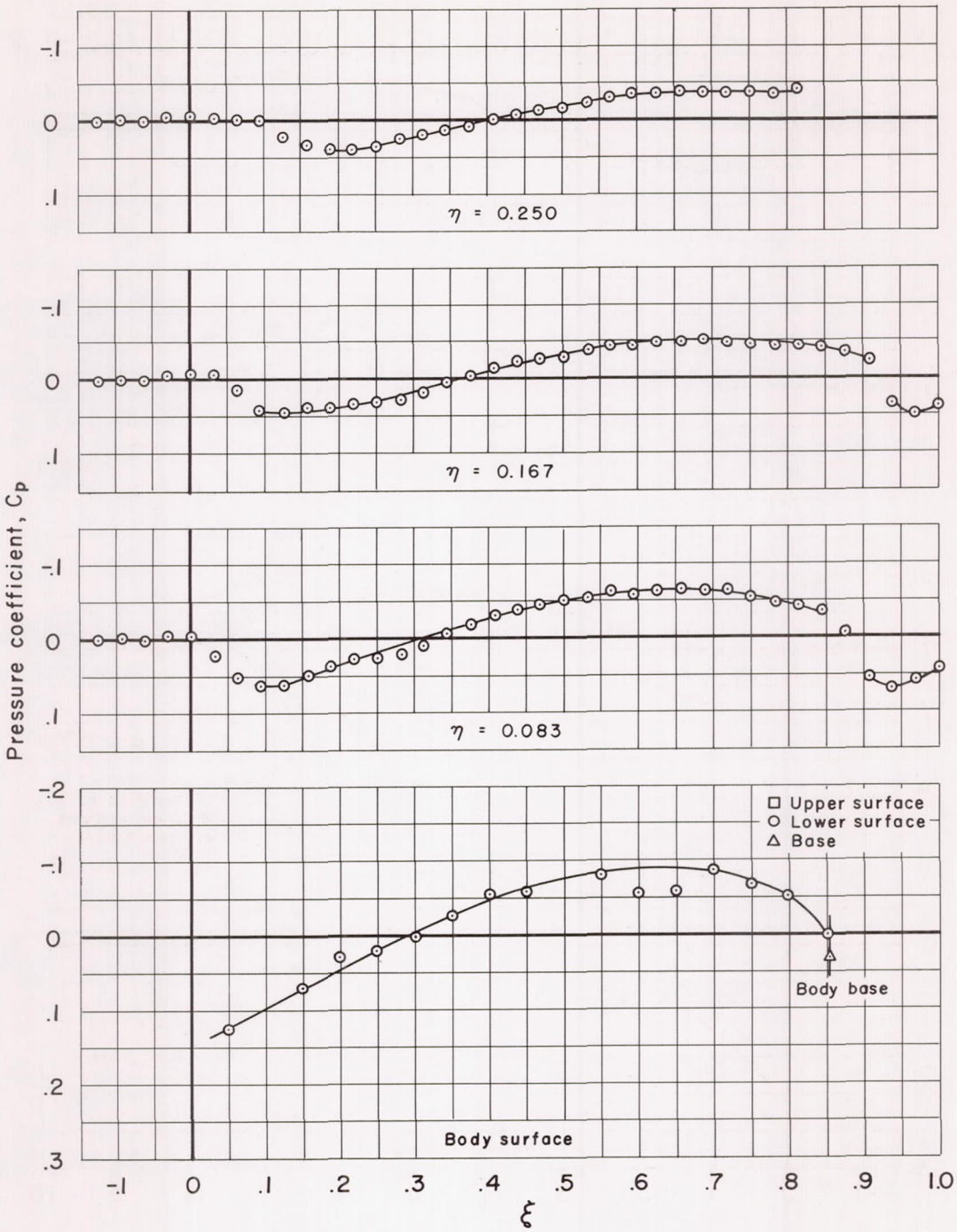

(e) $M_\infty = 1.10$, $\lambda = 1.5$, $\theta = 0^\circ$

Figure 8.- Continued.

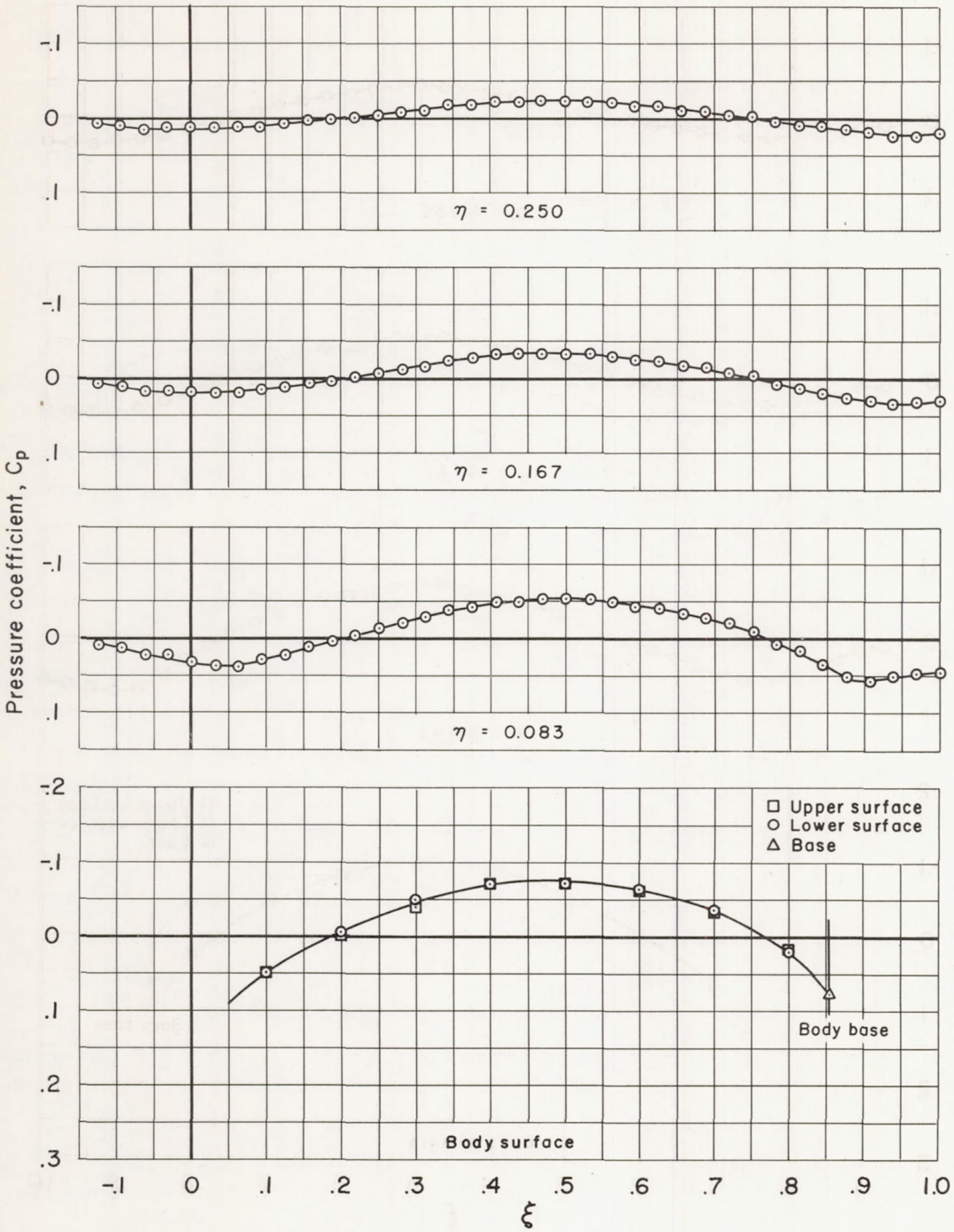

(f) $M_\infty = 0.90$, $\lambda = 1.5$, $\theta = 40^\circ$ and -40°

Figure 8.- Continued.

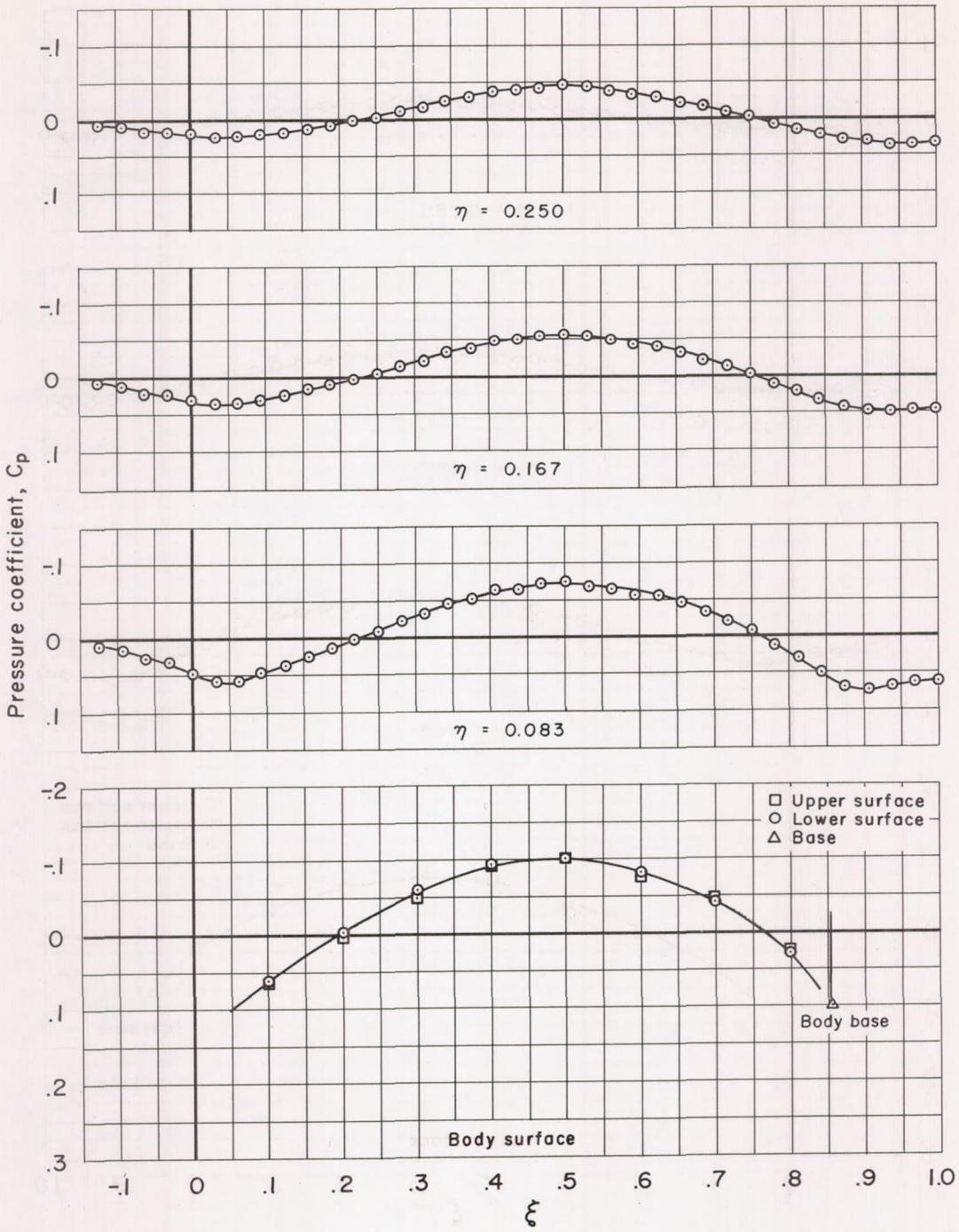

(g) $M_\infty = 0.975$, $\lambda = 1.5$, $\theta = 40^\circ$ and -40°

Figure 8.- Continued.

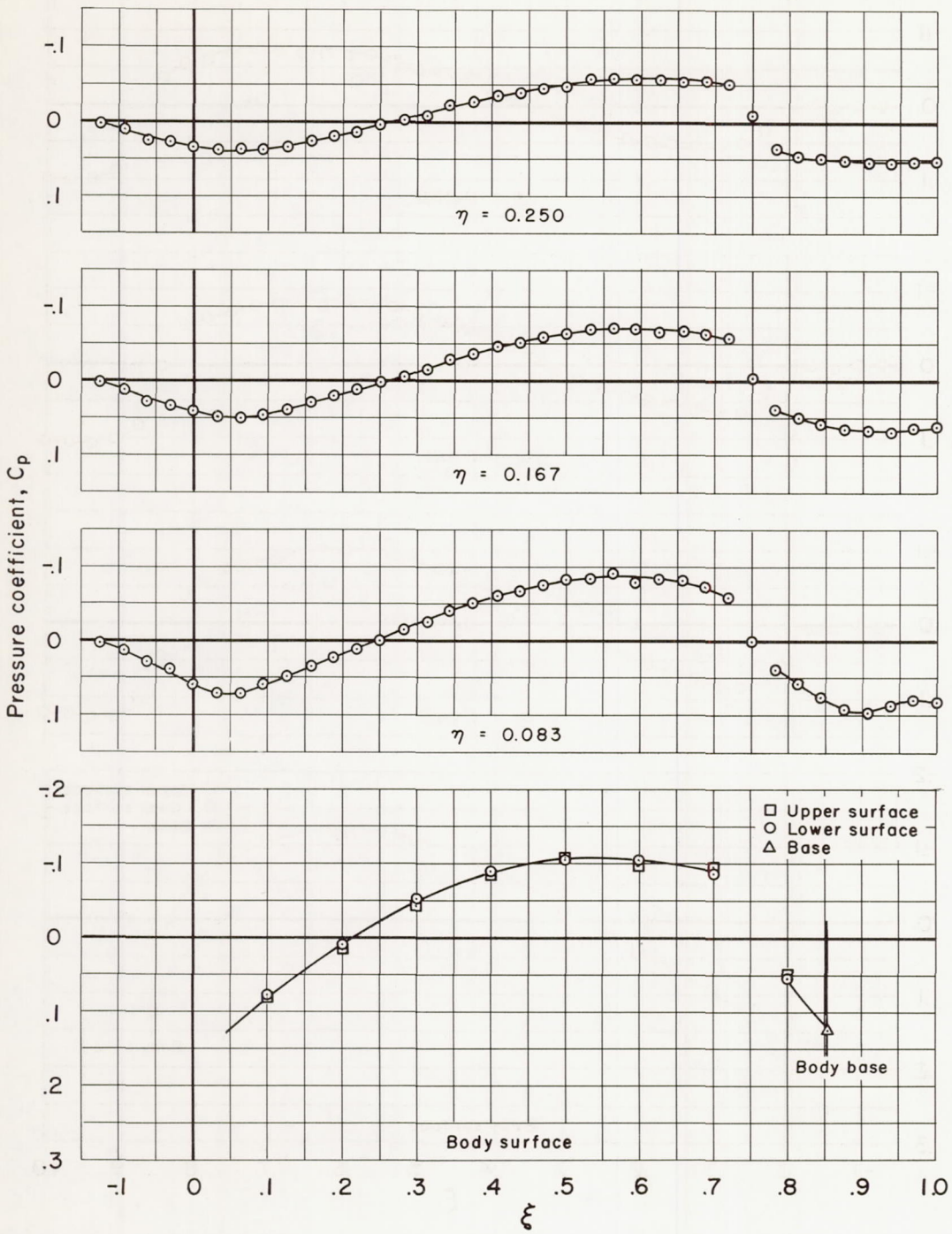

(h) $M_\infty = 1.00$, $\lambda = 1.5$, $\theta = 40^\circ$ and -40°

Figure 8.- Continued.

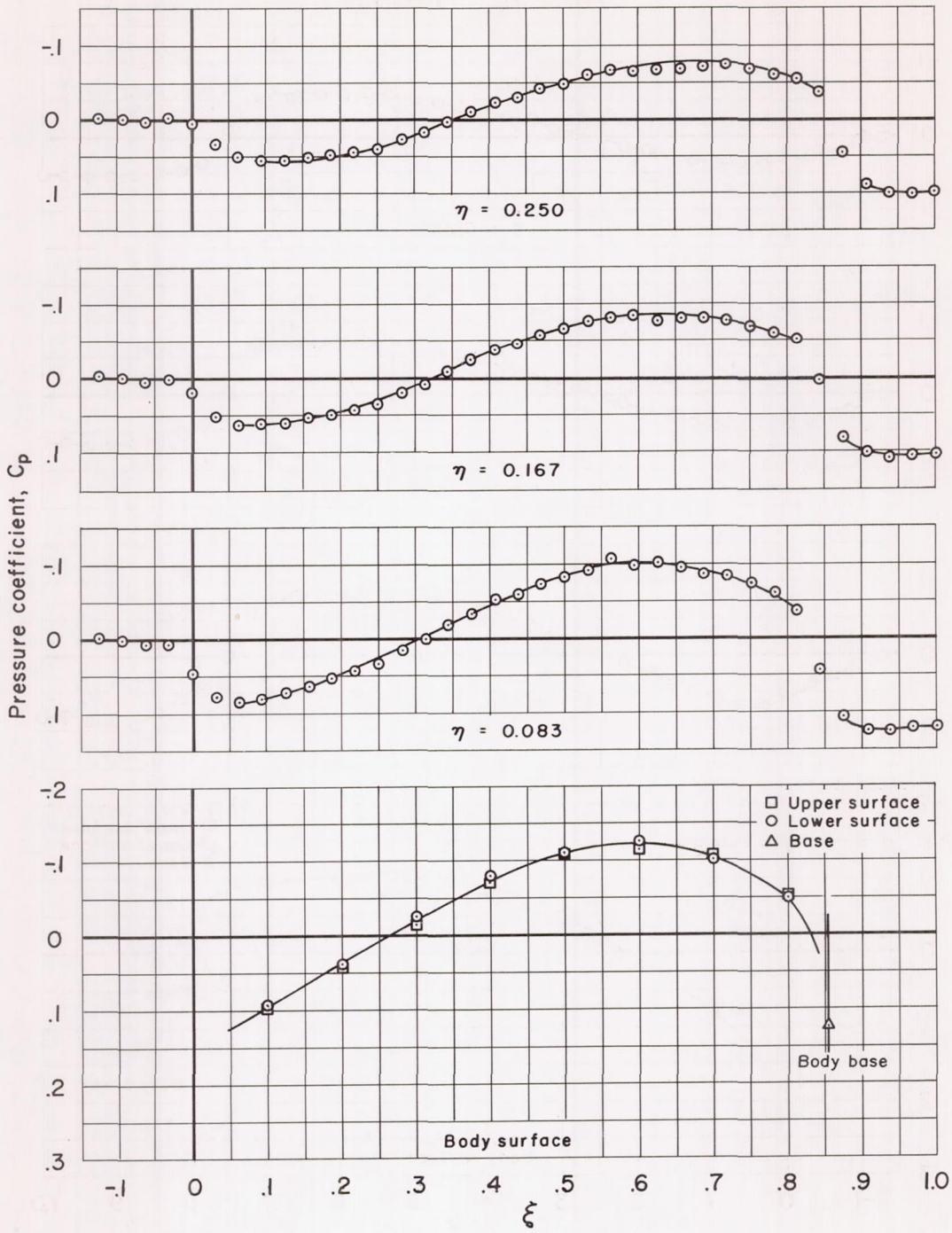

(i) $M_\infty = 1.025$, $\lambda = 1.5$

Figure 8.- Continued.

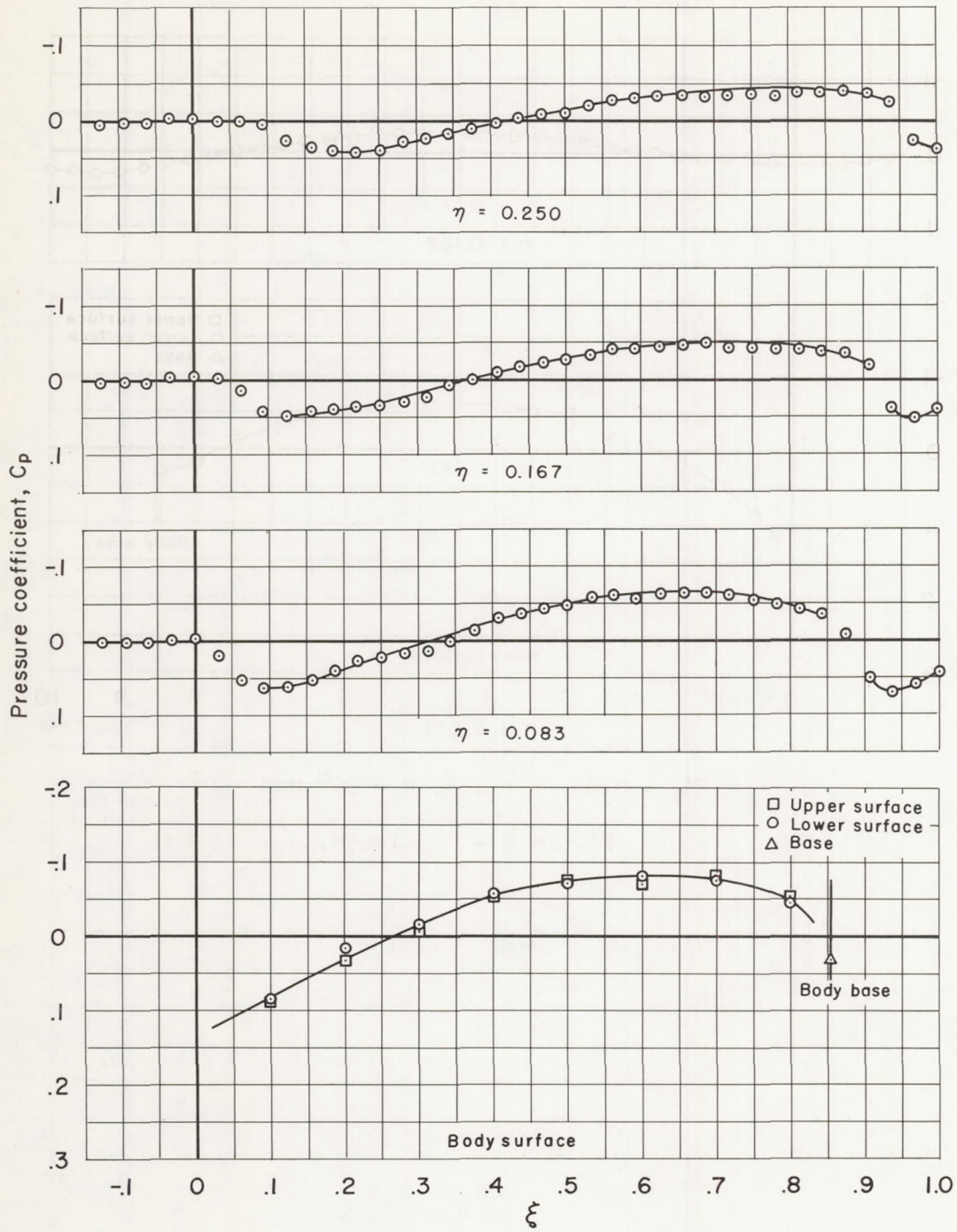

(j) M_∞ = 1.10, λ = 1.5, θ = 40° and -40°

Figure 8.- Continued.

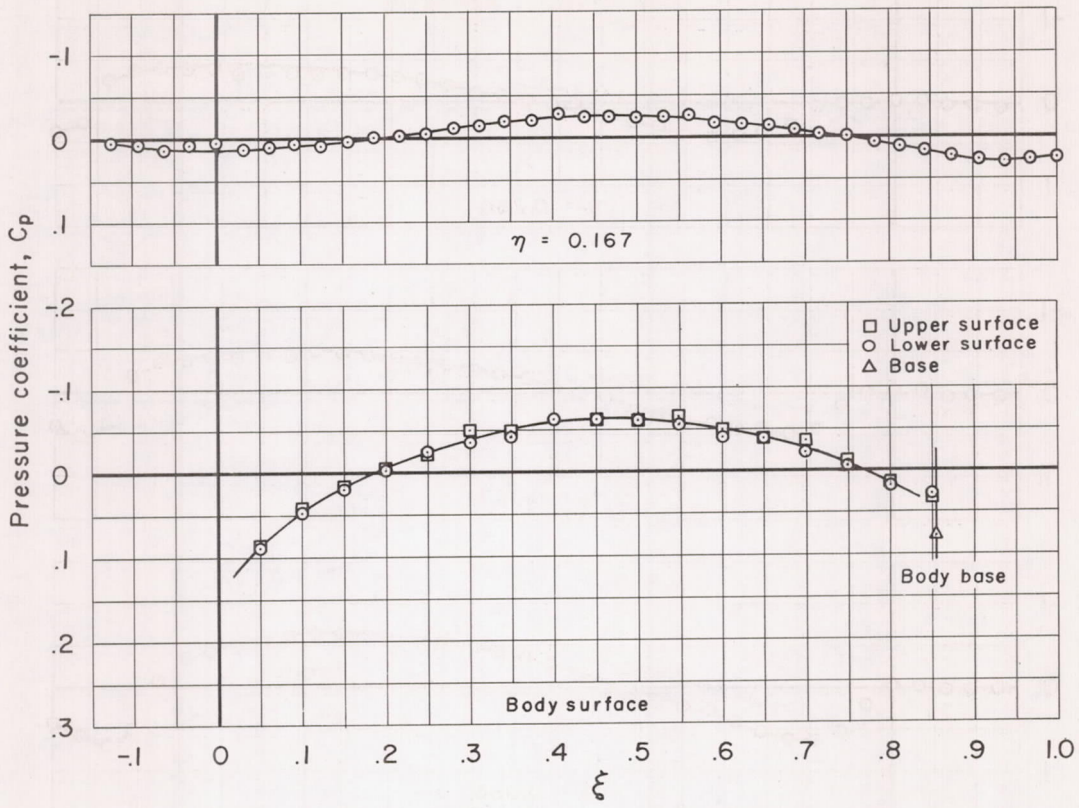

(k) $M_\infty = 0.80$, $\lambda = 1.5$, $\theta = 90^\circ$ and -90°

Figure 8.- Continued.

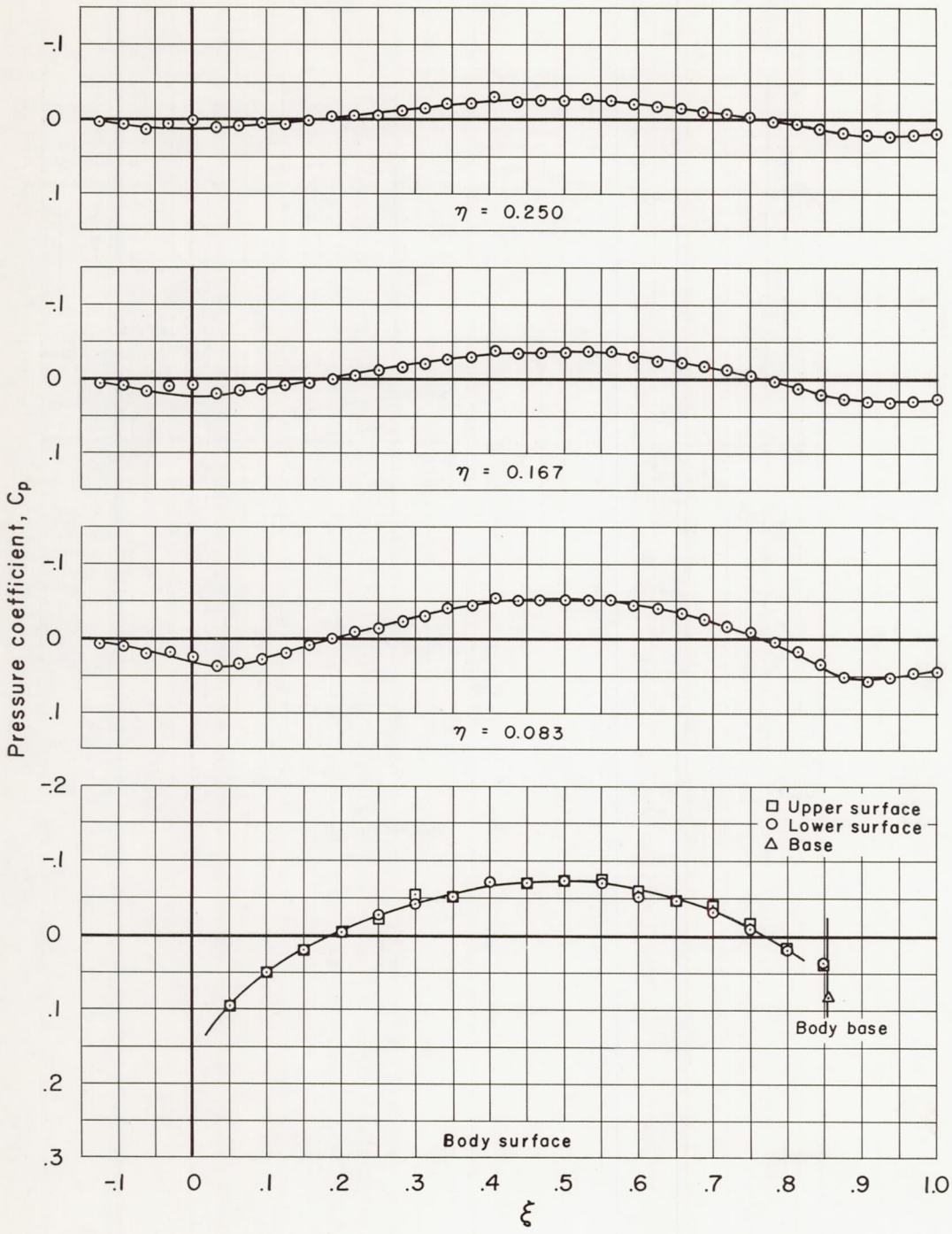

(l) $M_\infty = 0.90$, $\lambda = 1.5$, $\theta = 90^\circ$ and -90°

Figure 8.- Continued.

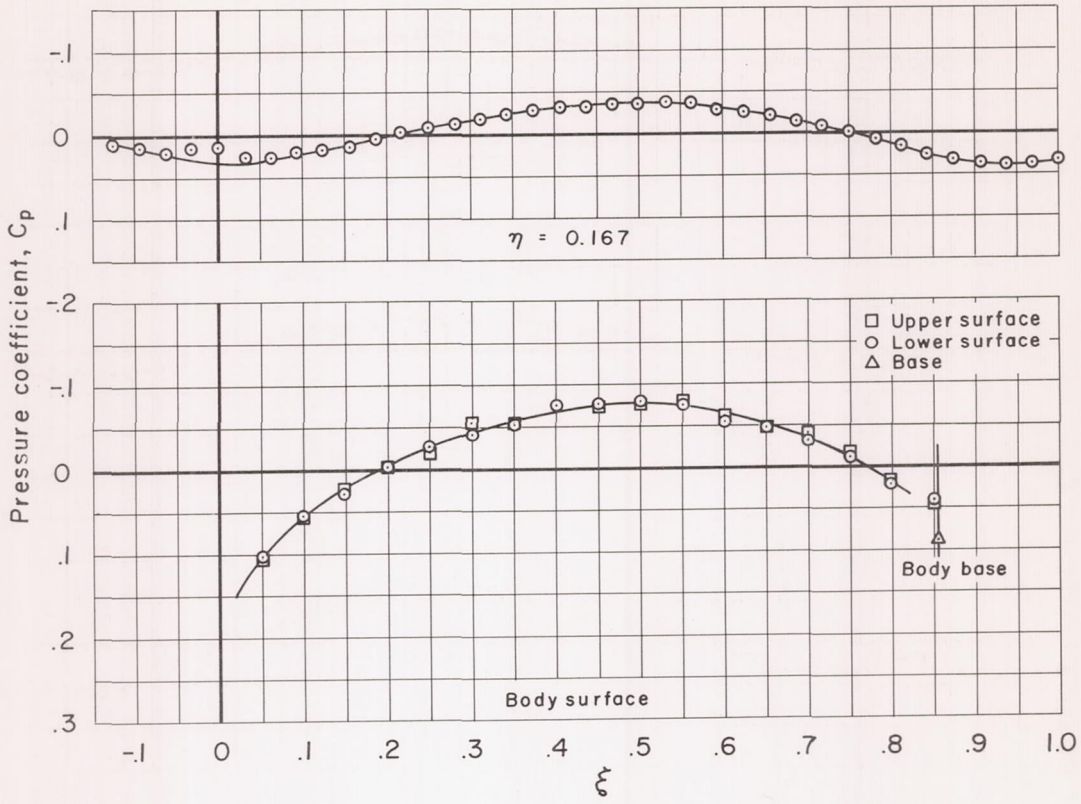

(m) $M_\infty = 0.925$, $\lambda = 1.5$, $\theta = 90^\circ$ and -90°

Figure 8.- Continued.

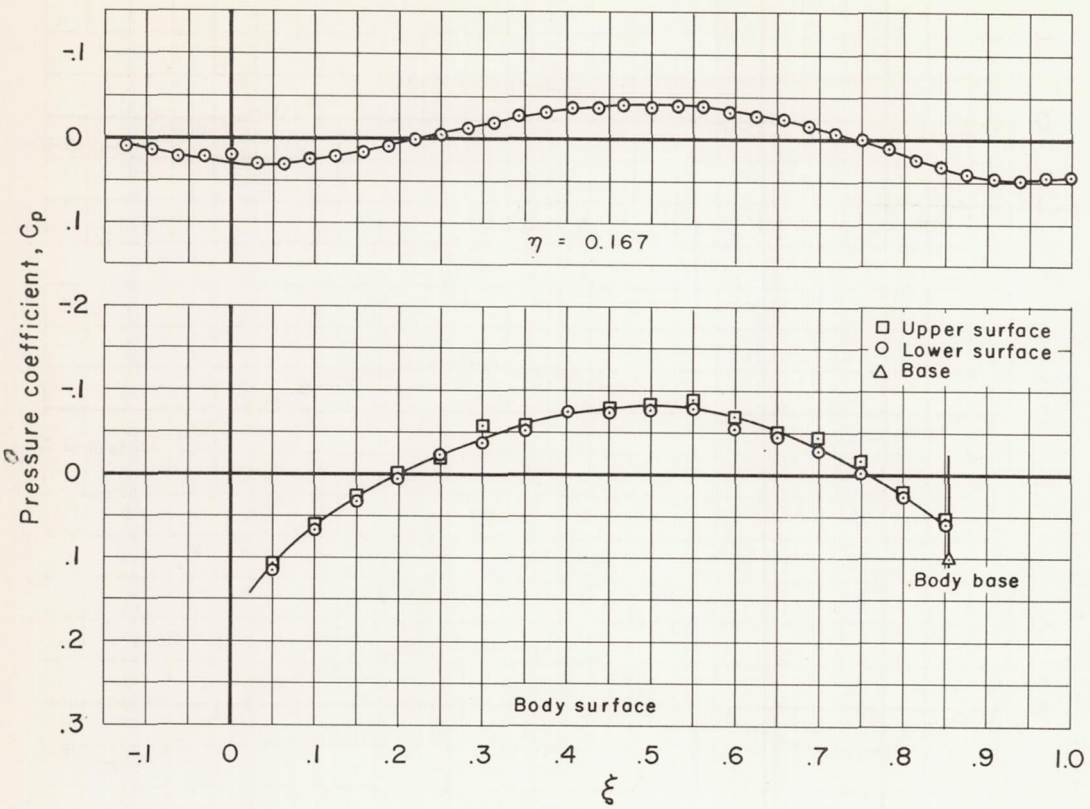

(n) $M_\infty = 0.95$, $\lambda = 1.5$, $\theta = 90^\circ$ and -90°

Figure 8.- Continued.

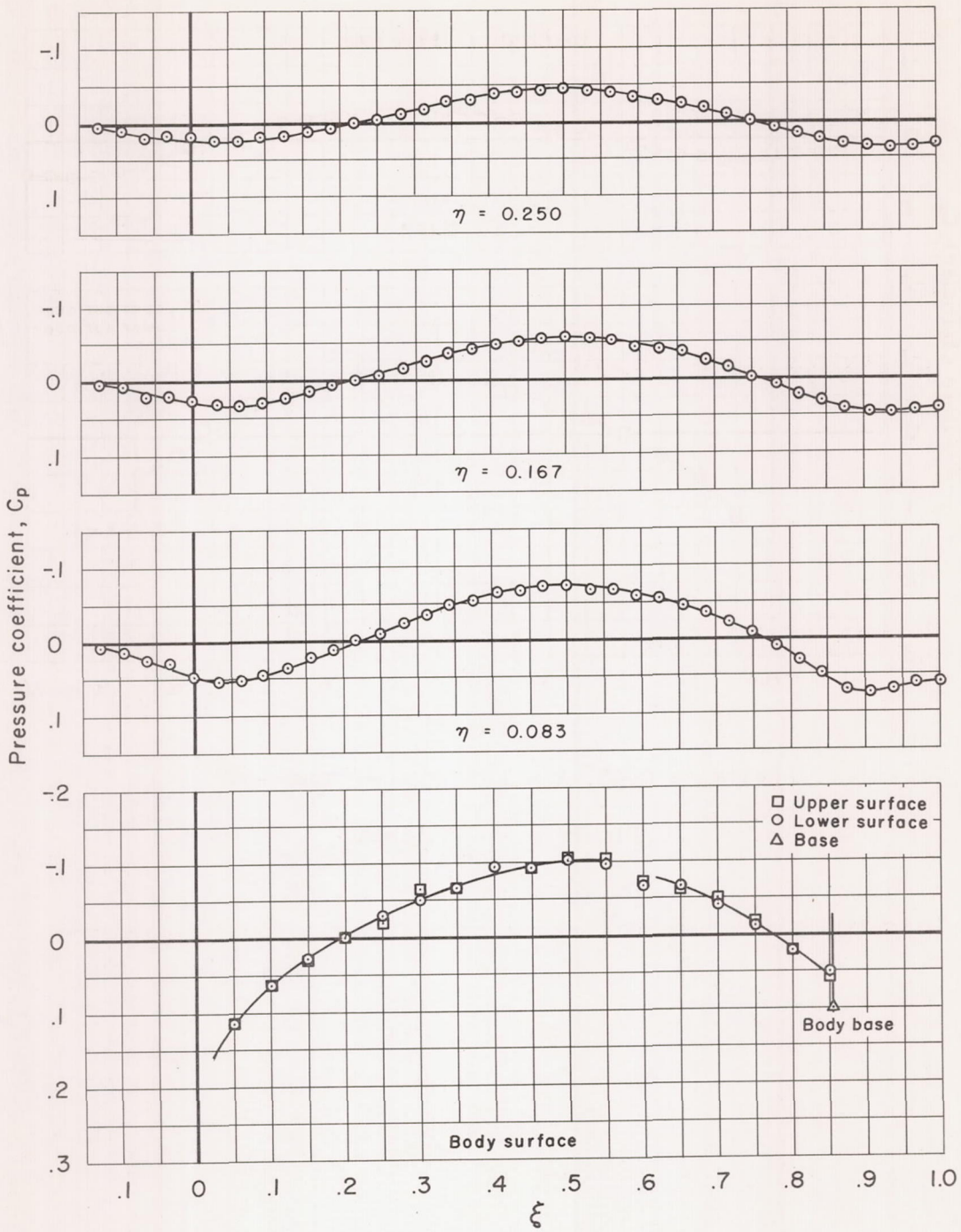

(o) $M_\infty = 0.975$, $\lambda = 1.5$, $\theta = 90^\circ$ and -90°

Figure 8.- Continued.

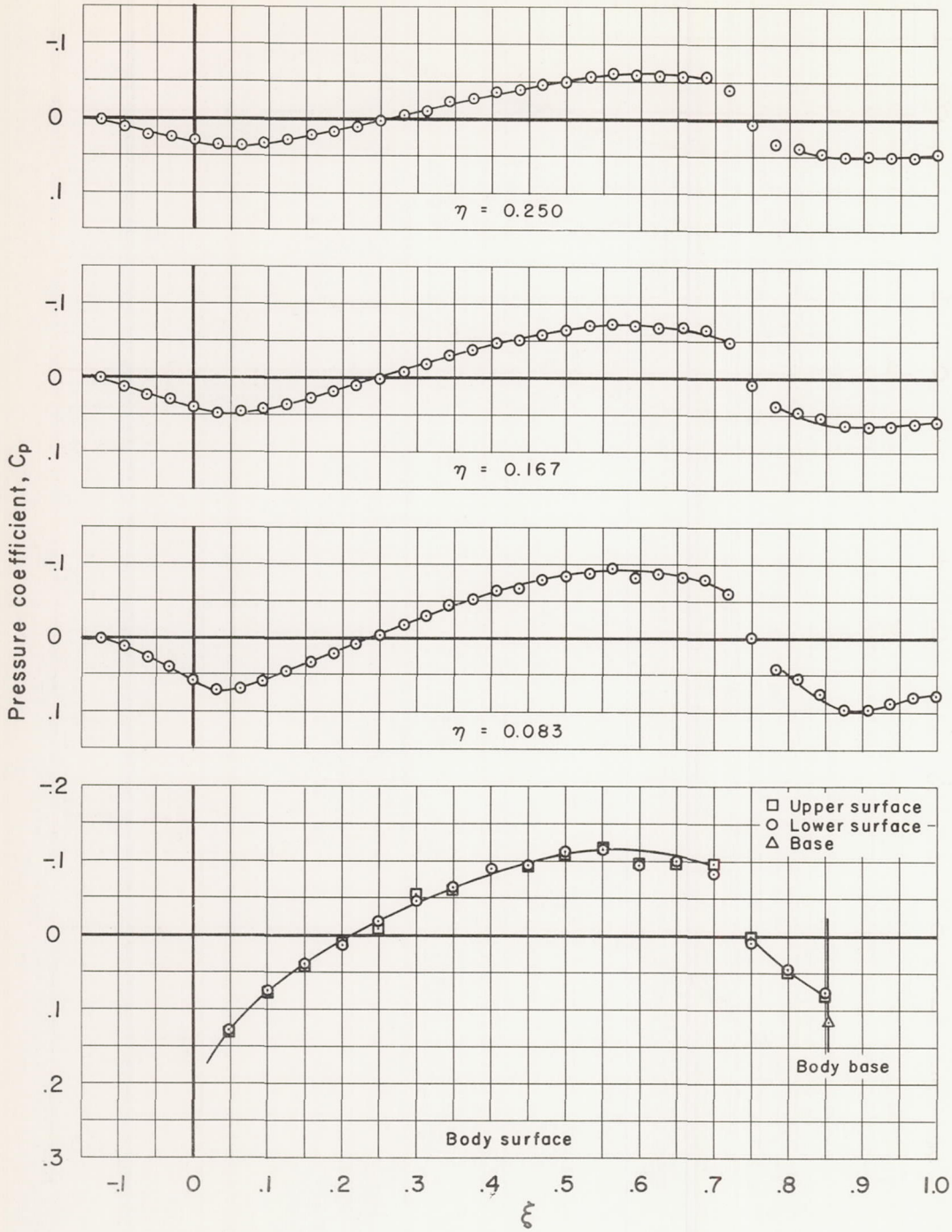

(p) $M_\infty = 1.00$, $\lambda = 1.5$, $\theta = 90^\circ$ and -90°

Figure 8.- Continued.

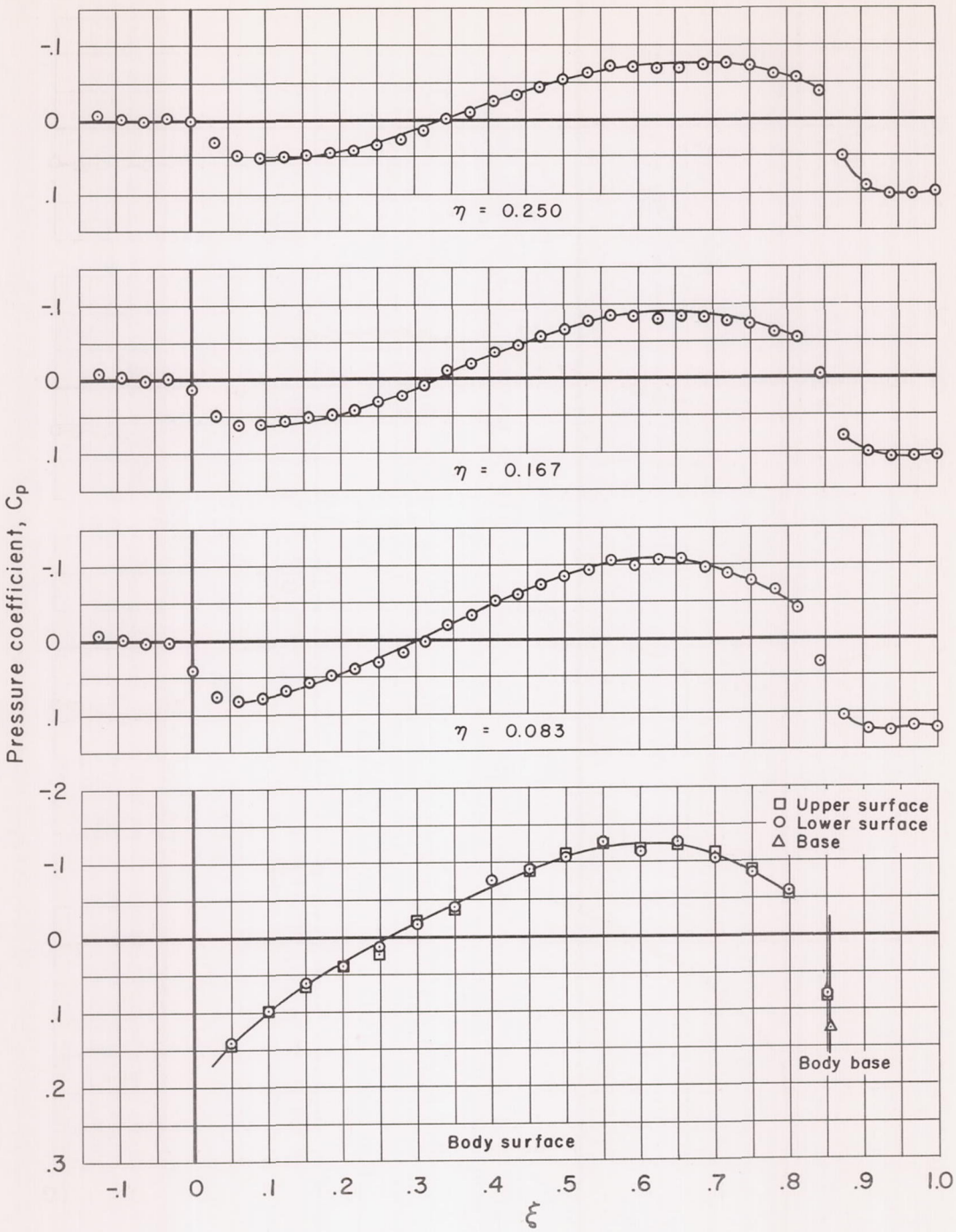

(q) $M_\infty = 1.025$, $\lambda = 1.5$, $\theta = 90^\circ$ and -90°

Figure 8.- Continued.

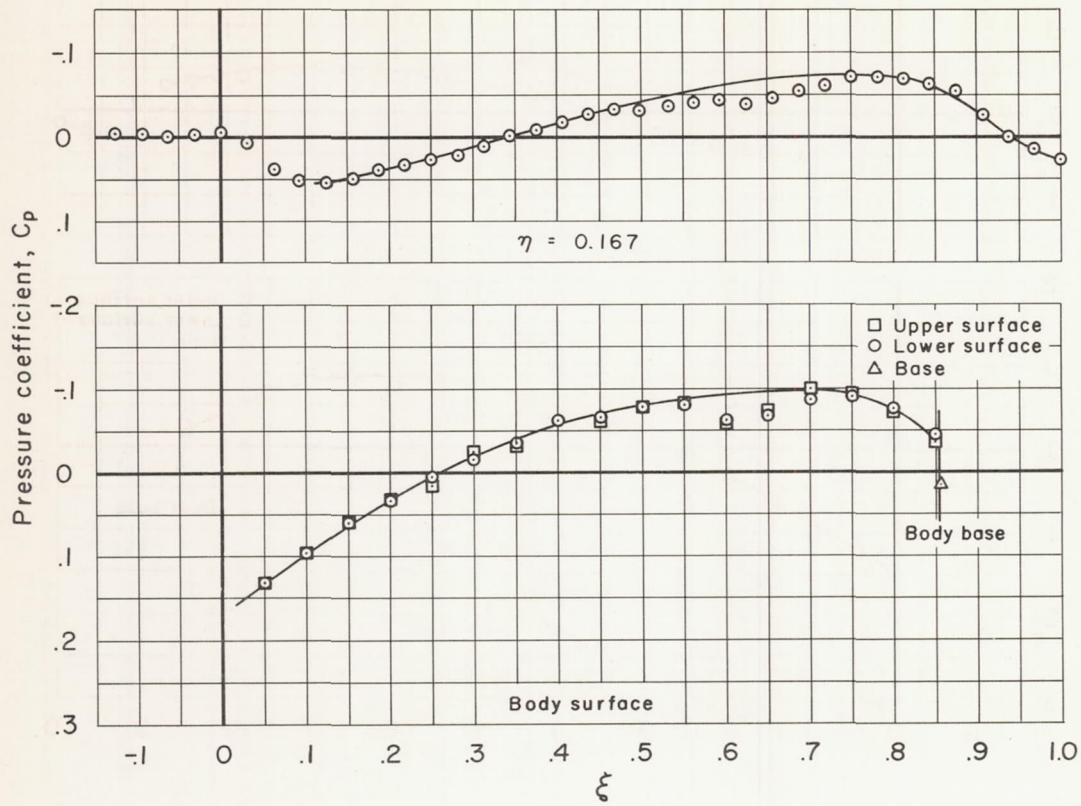

(r) $M_\infty = 1.05$, $\lambda = 1.5$, $\theta = 90^\circ$ and -90°

Figure 8.- Continued.

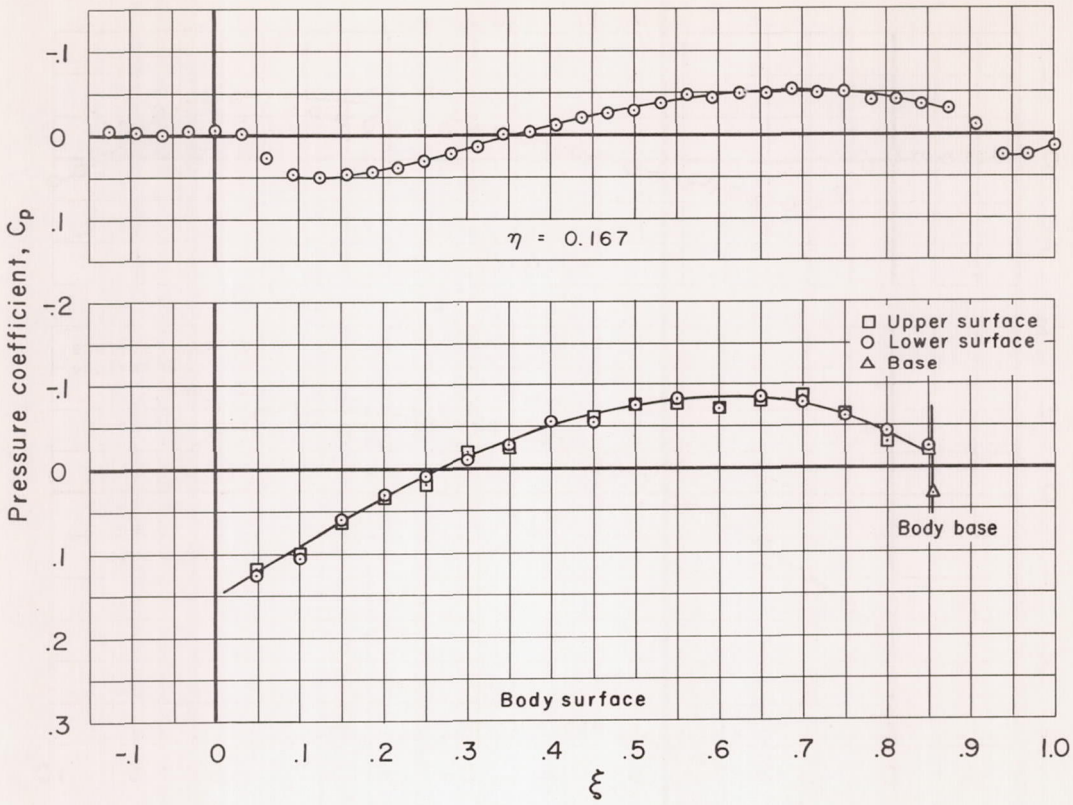

(s) $M_\infty = 1.075$, $\lambda = 1.5$, $\theta = 90^\circ$ and -90°

Figure 8.- Continued.

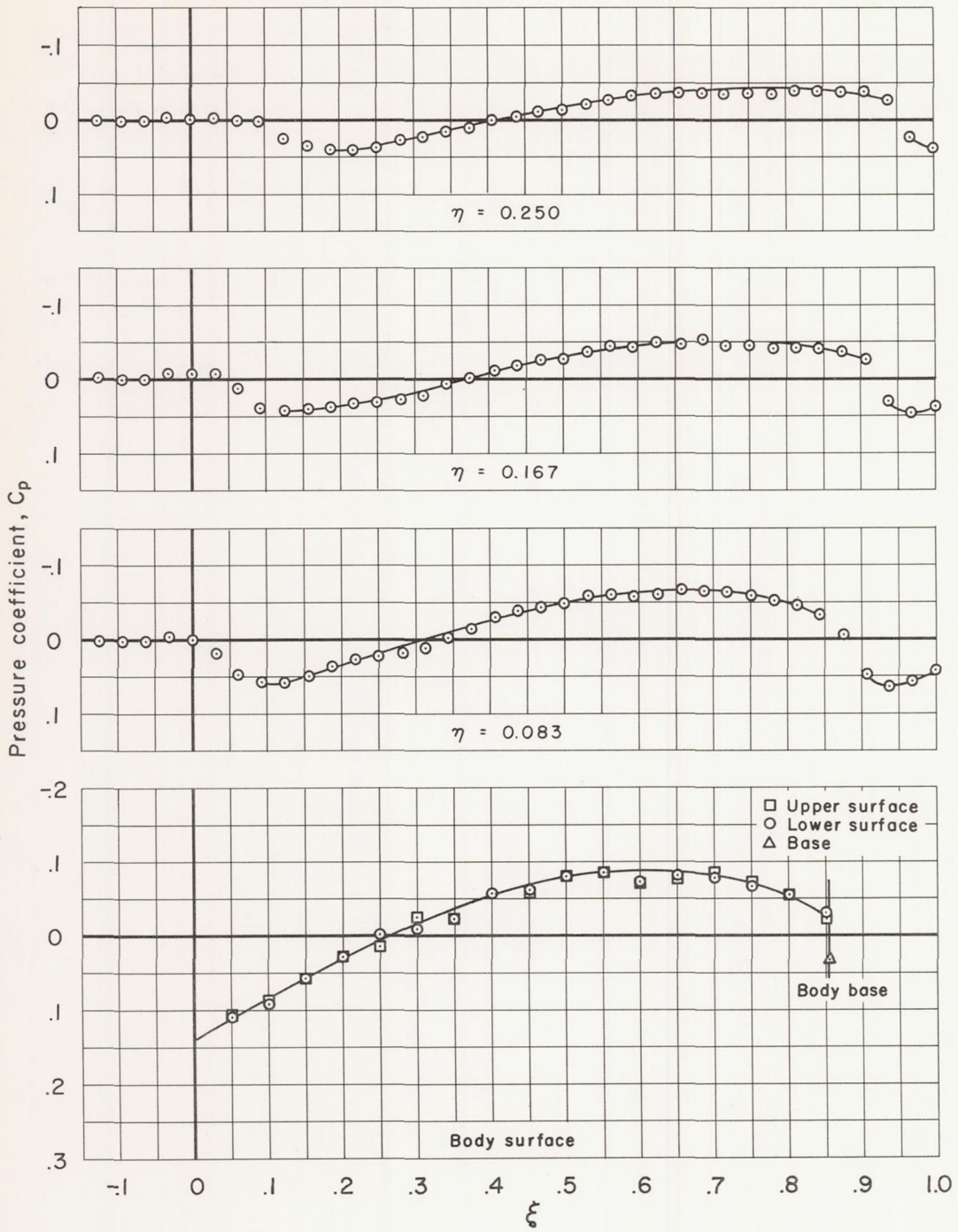

(t) $M_\infty = 1.10$, $\lambda = 1.5$, $\theta = 90^\circ$ and -90°

Figure 8.- Continued.

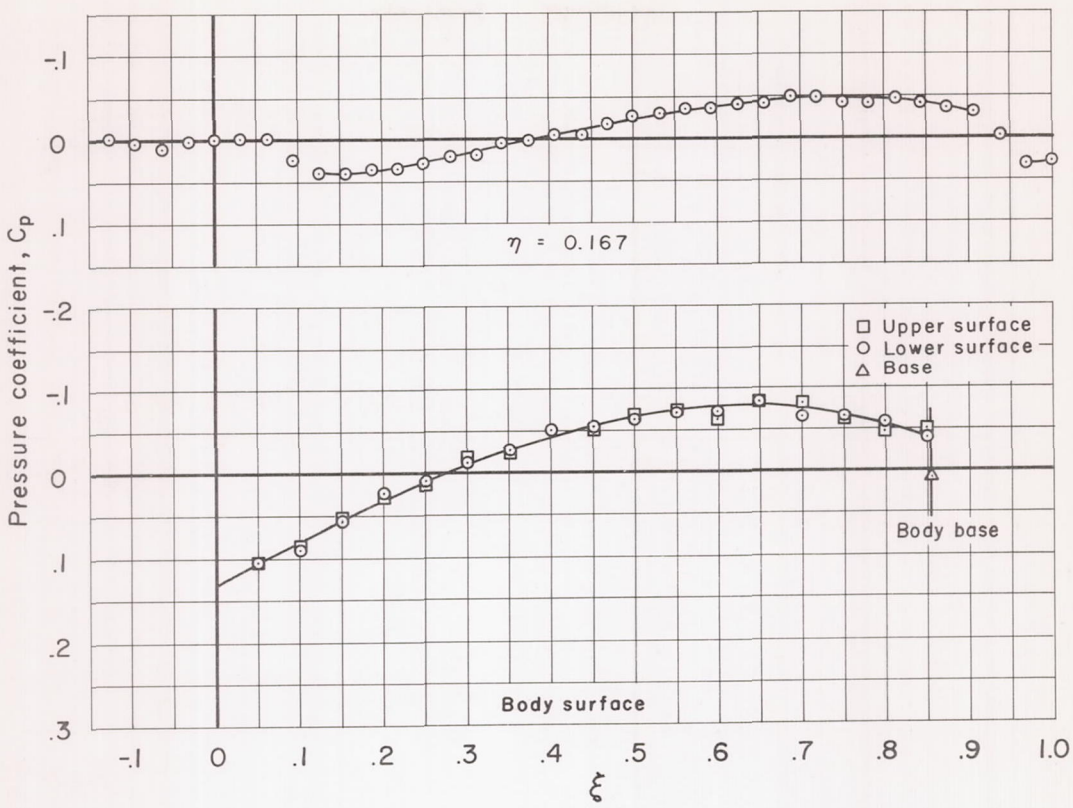

(u) $M_\infty = 1.15$, $\lambda = 1.5$, $\theta = 90^\circ$ and -90°

Figure 8.- Continued.

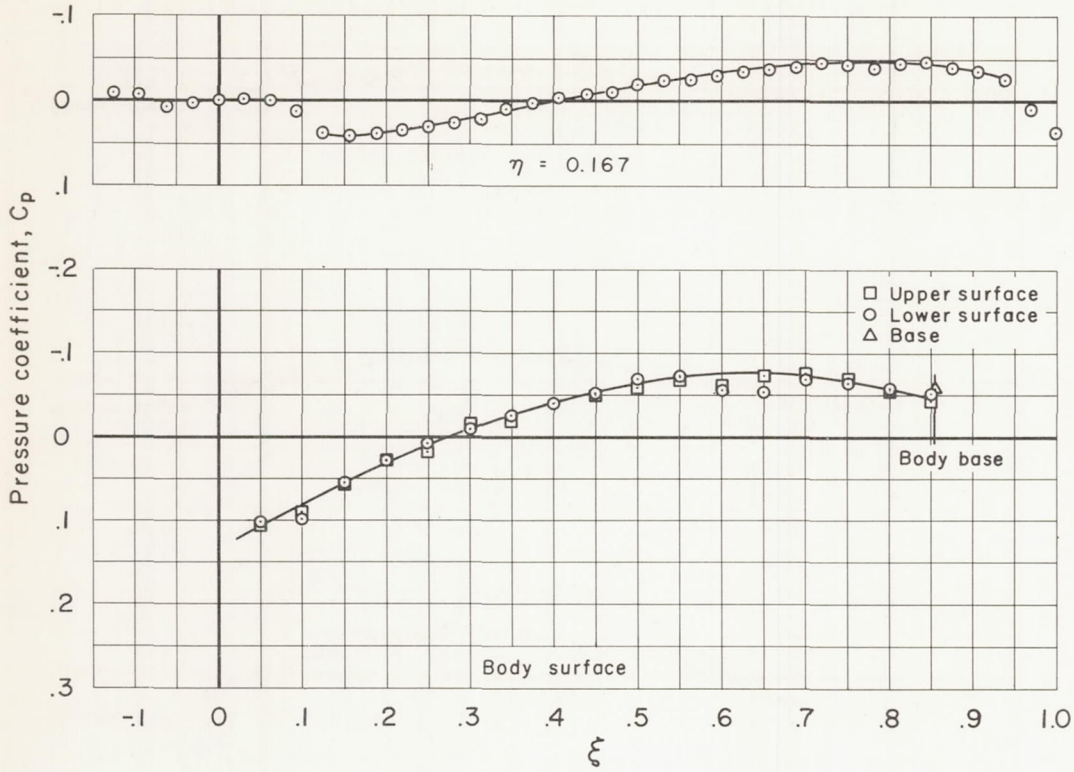

(v) $M_\infty = 1.20$, $\lambda = 1.5$, $\theta = 90^\circ$ and -90°

Figure 8.- Concluded.

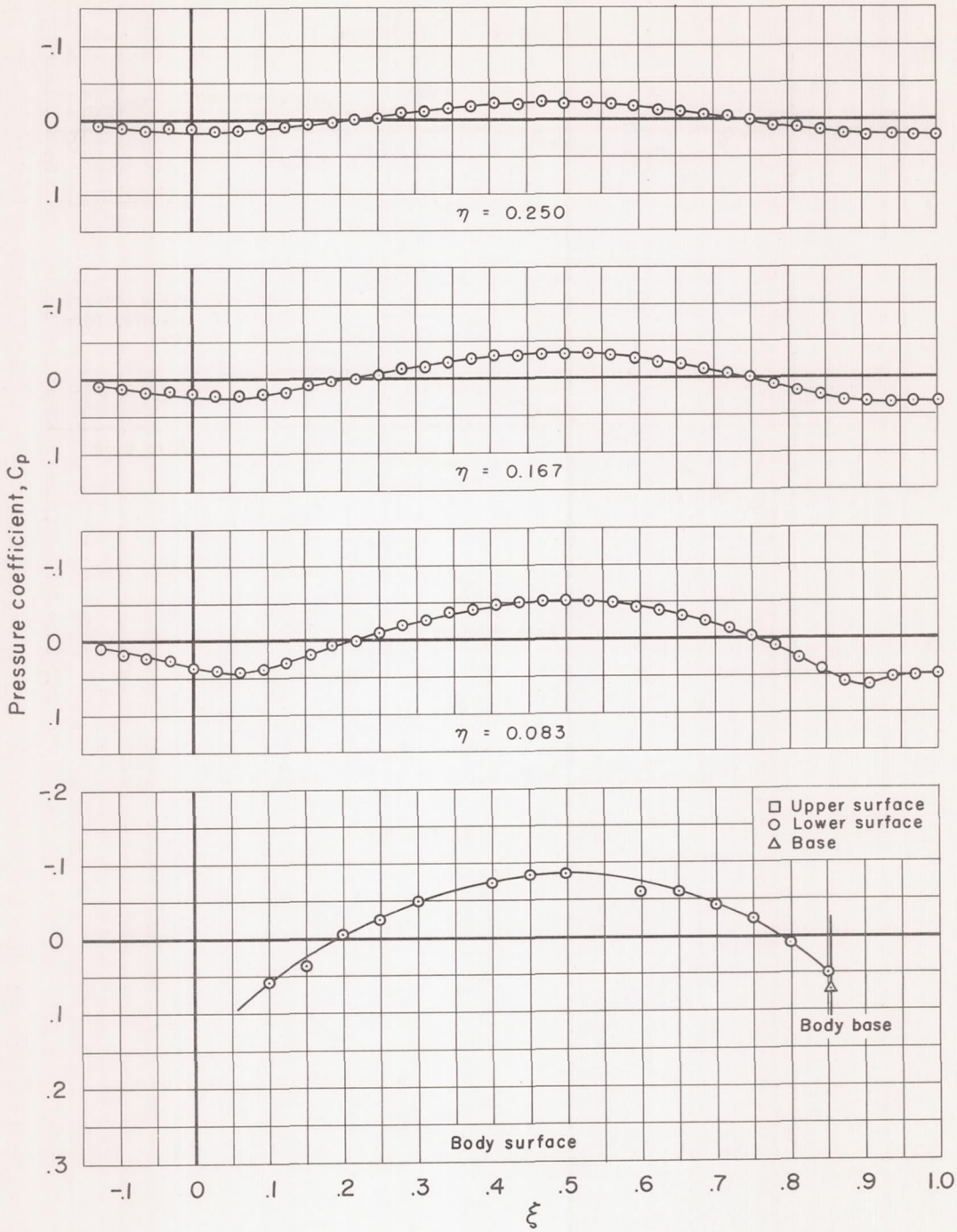

(a) $M_\infty = 0.90$, $\lambda = 2.0$, $\theta = 0^\circ$

Figure 9.- Measured pressure distributions for the body having an axis ratio of 2.0; $\alpha = 0^\circ$.

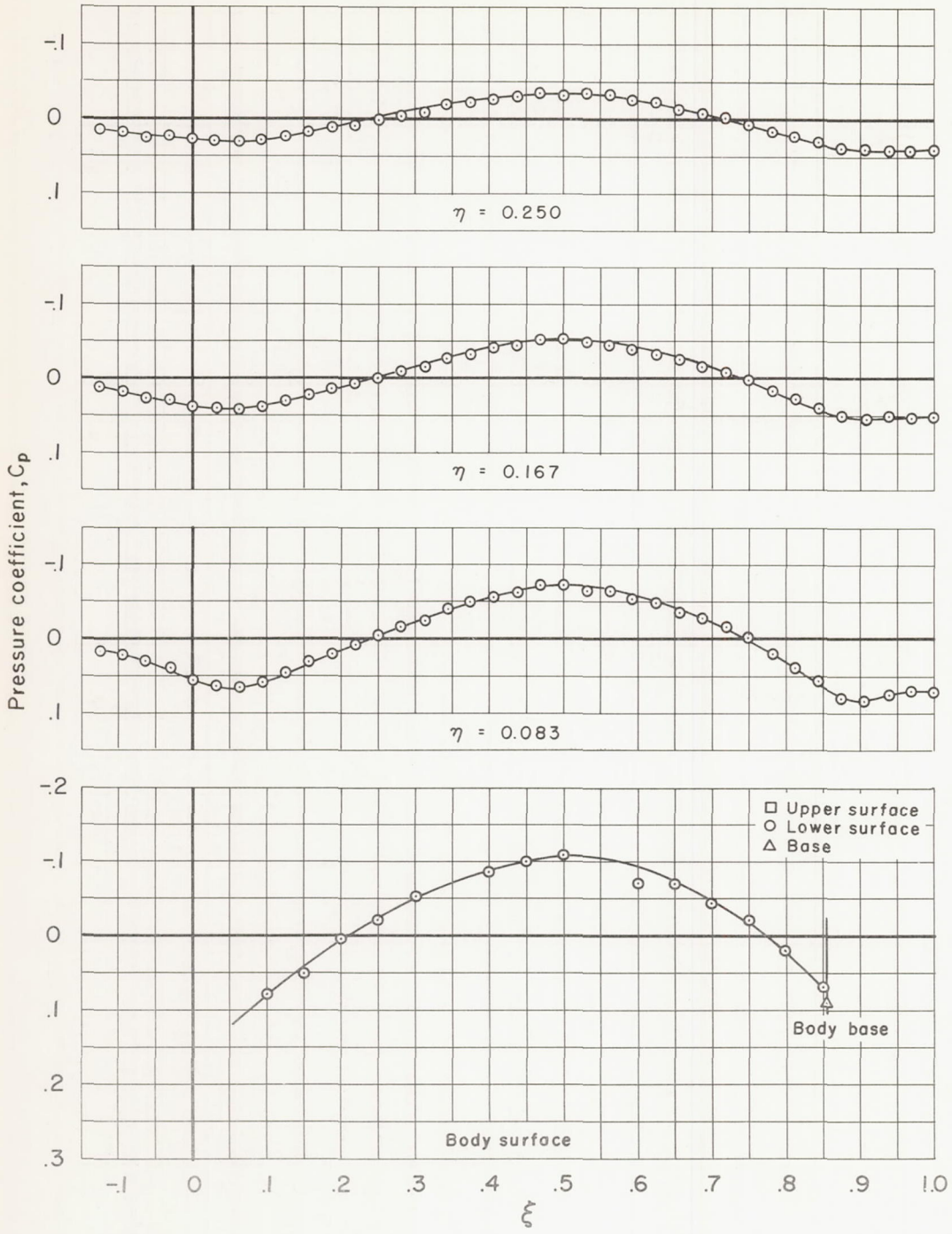

(b) $M_\infty = 0.975$, $\lambda = 2.0$, $\theta = 0^\circ$

Figure 9.- Continued.

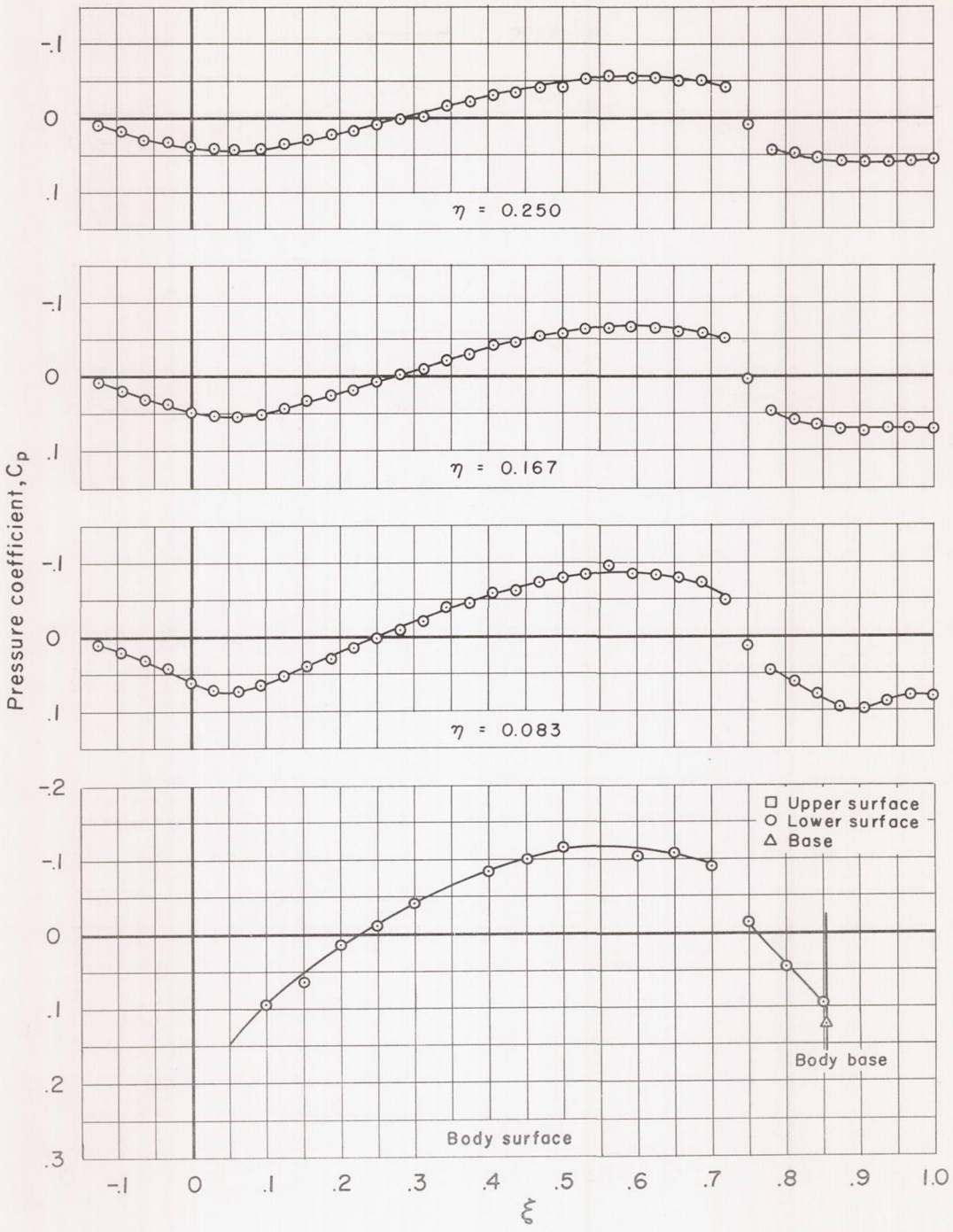

(c) $M_\infty = 1.00$, $\lambda = 2.0$, $\theta = 0^\circ$

Figure 9.- Continued.

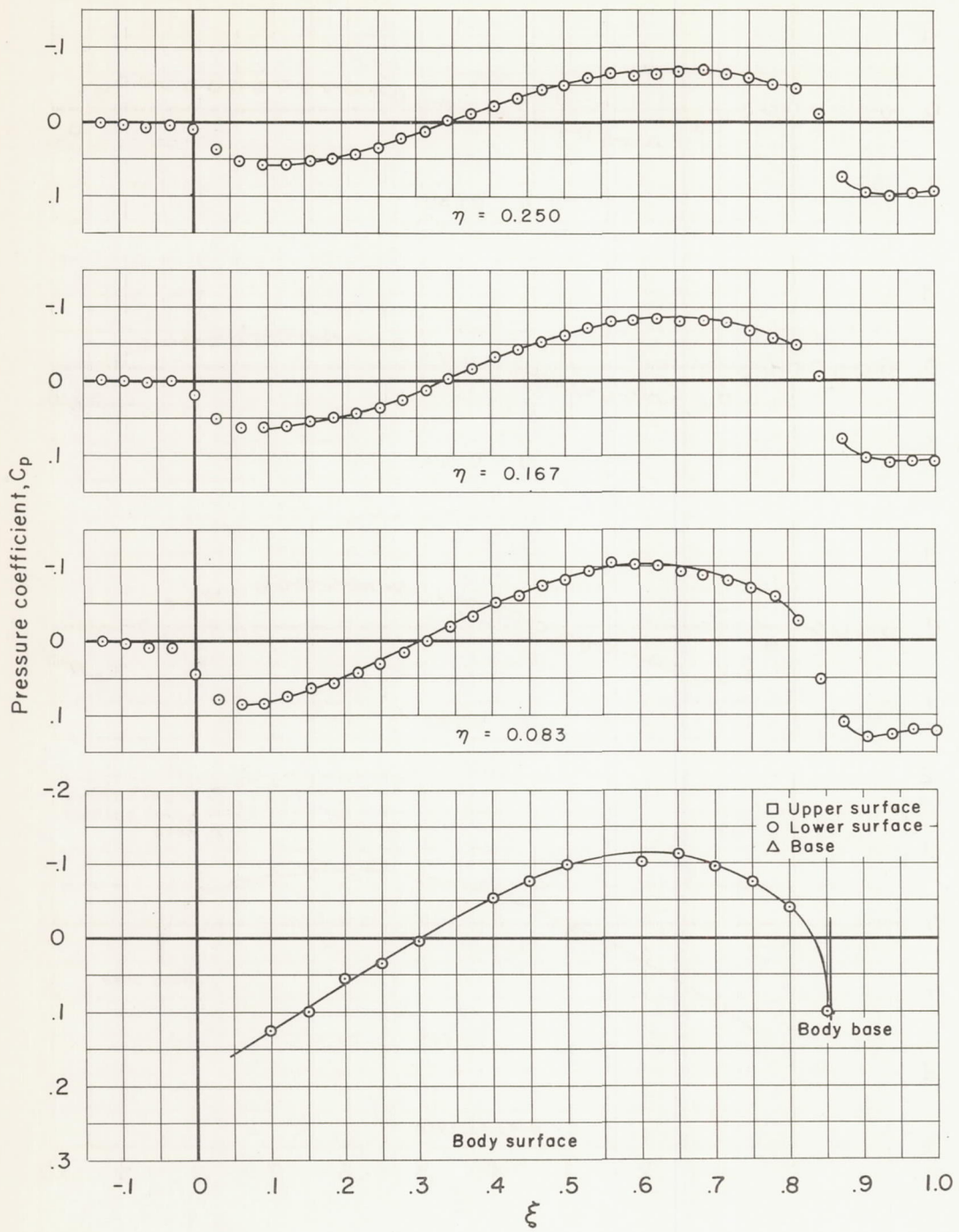

(d) $M_\infty = 1.025$, $\lambda = 2.0$, $\theta = 0^\circ$

Figure 9.- Continued.

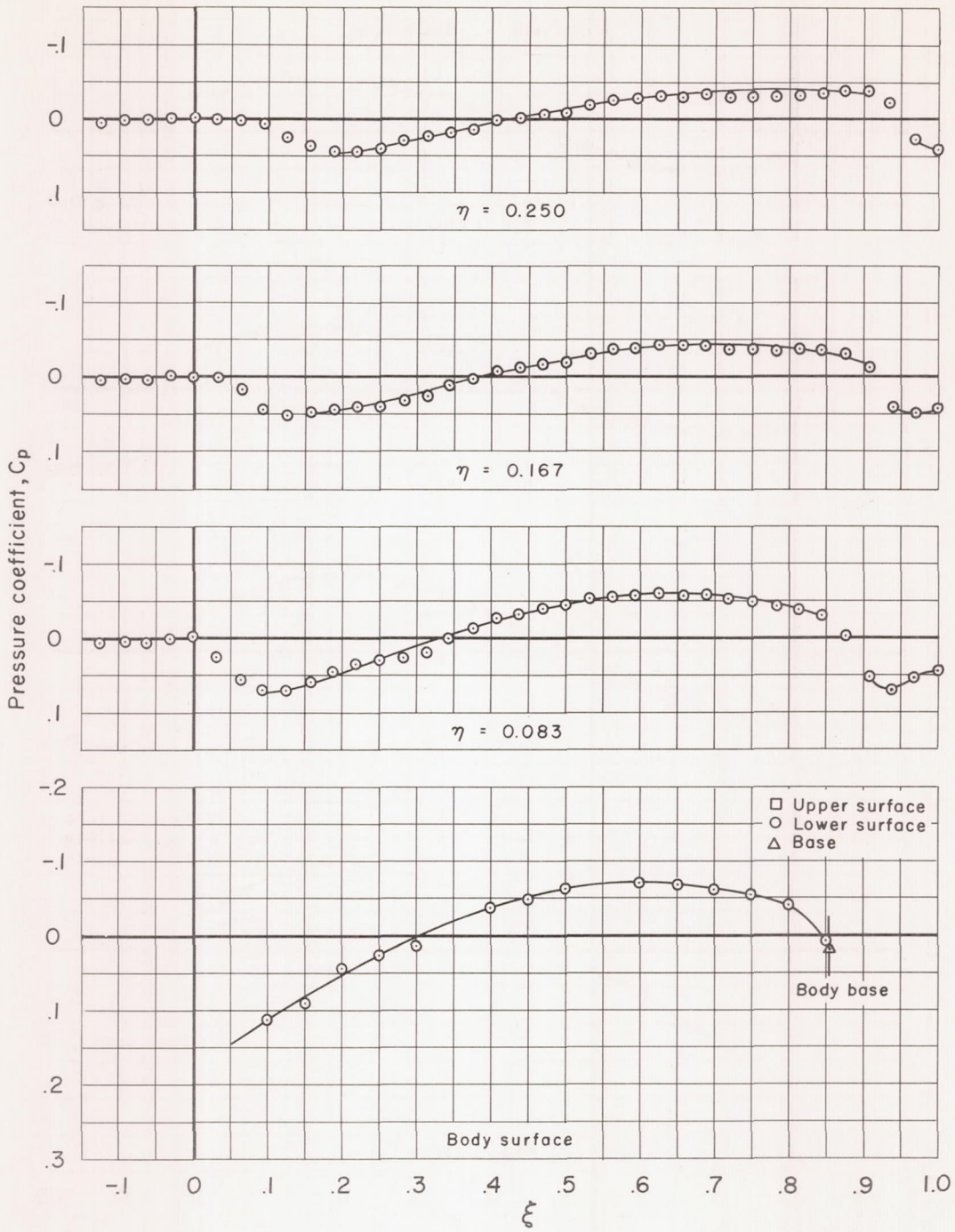

(e) $M_\infty = 1.10$, $\lambda = 2.0$, $\theta = 0^\circ$

Figure 9.- Continued.

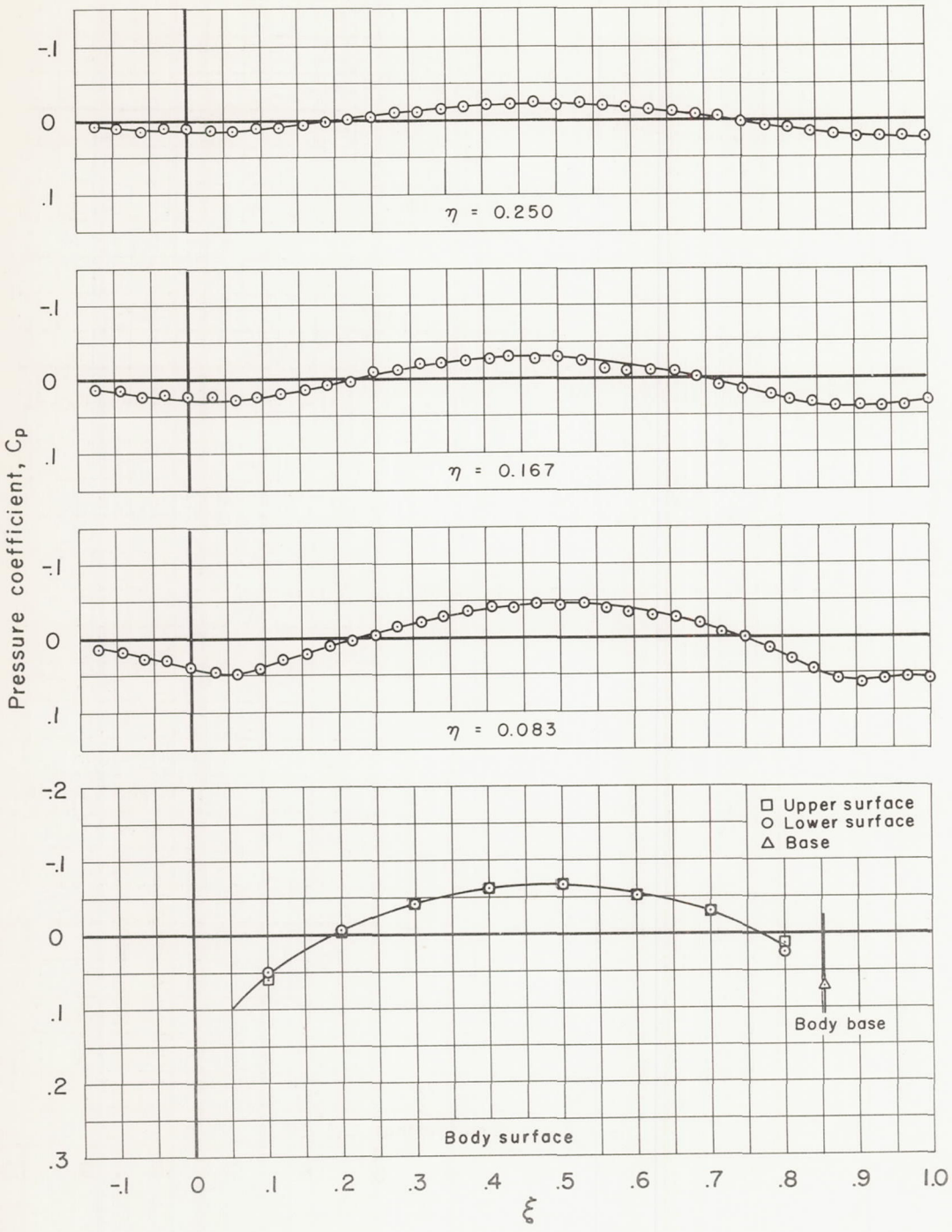

(f) $M_\infty = 0.90$, $\lambda = 2.0$, $\theta = 40^\circ$ and -40°

Figure 9.- Continued.

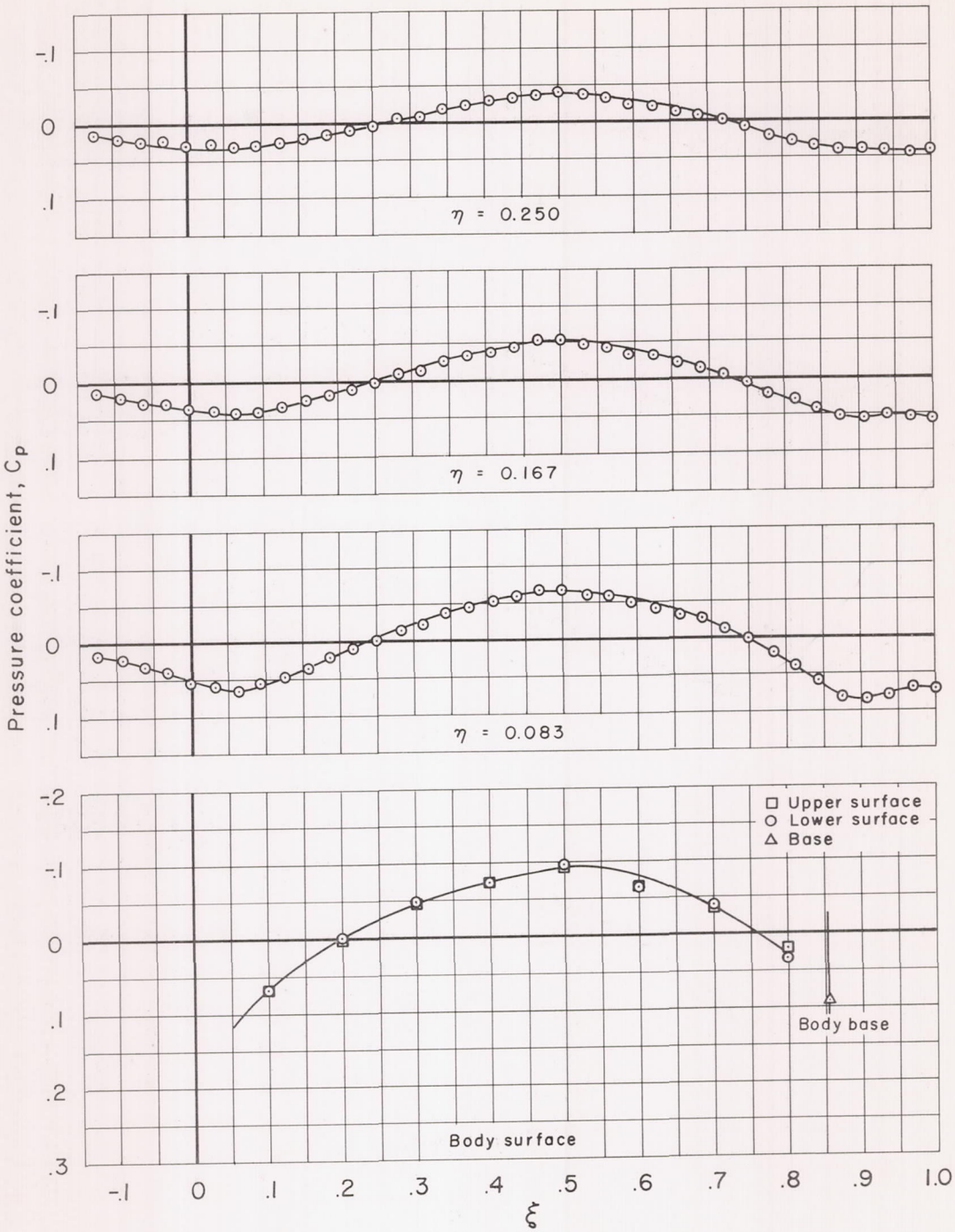

(g) $M_\infty = 0.975$, $\lambda = 2.0$, $\theta = 40^\circ$ and -40°

Figure 9.- Continued.

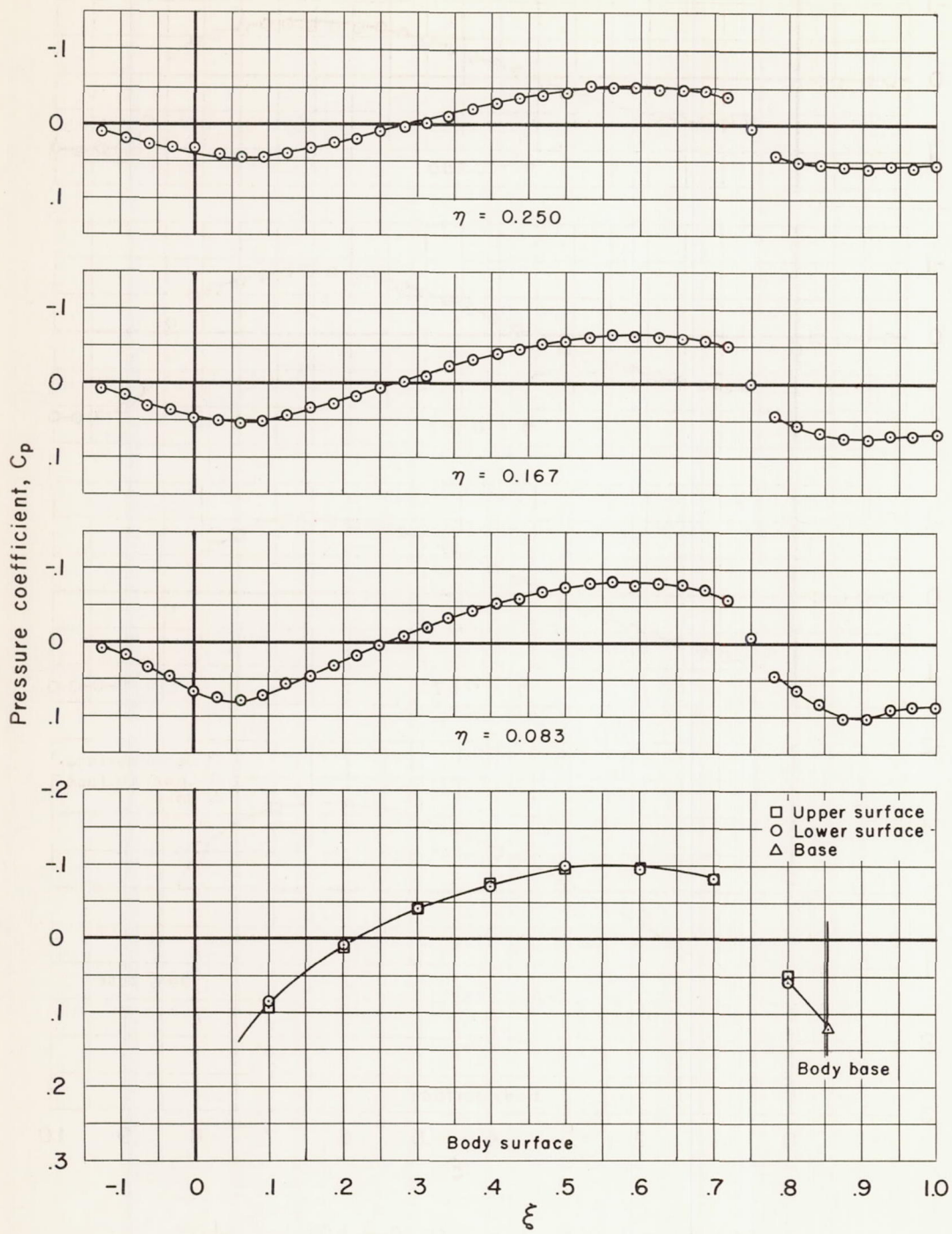

(h) $M_\infty = 1.00$, $\lambda = 2.0$, $\theta = 40^\circ$ and -40°

Figure 9.- Continued

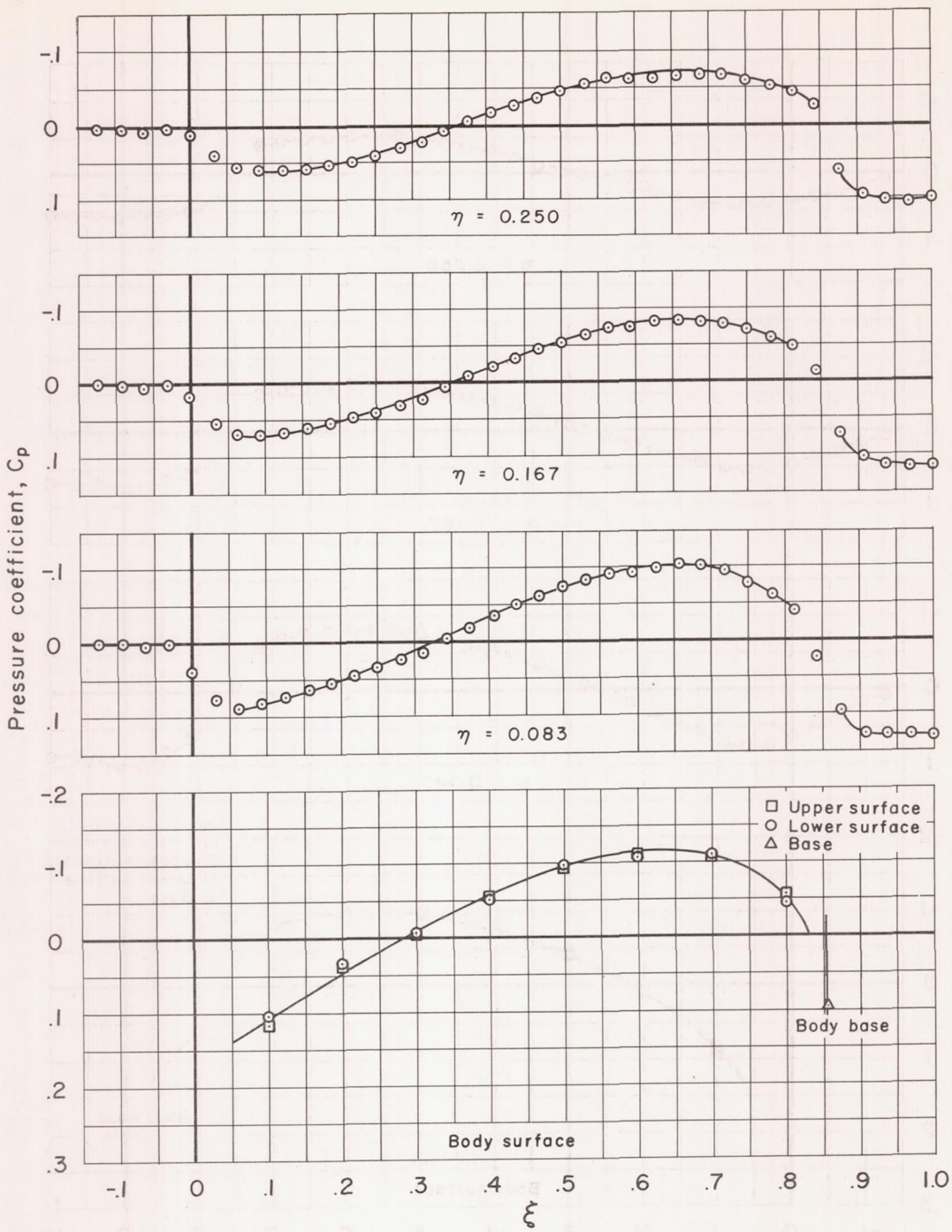

(i) $M_\infty = 1.025$, $\lambda = 2.0$, $\theta = 40^\circ$ and -40°

Figure 9.- Continued.

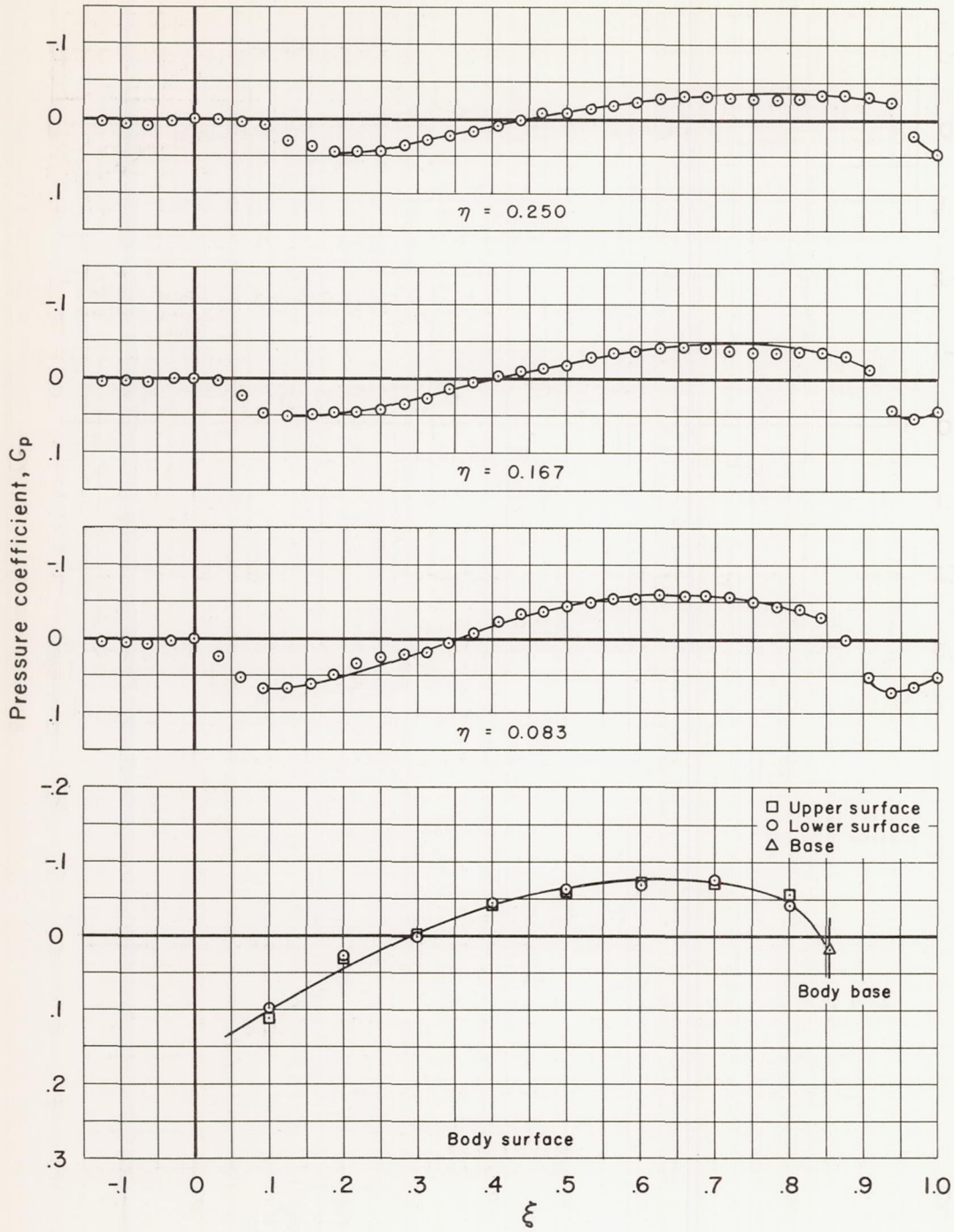

(j) M_∞ = 1.10, λ = 2.0, θ = 40° and -40°

Figure 9.- Continued.

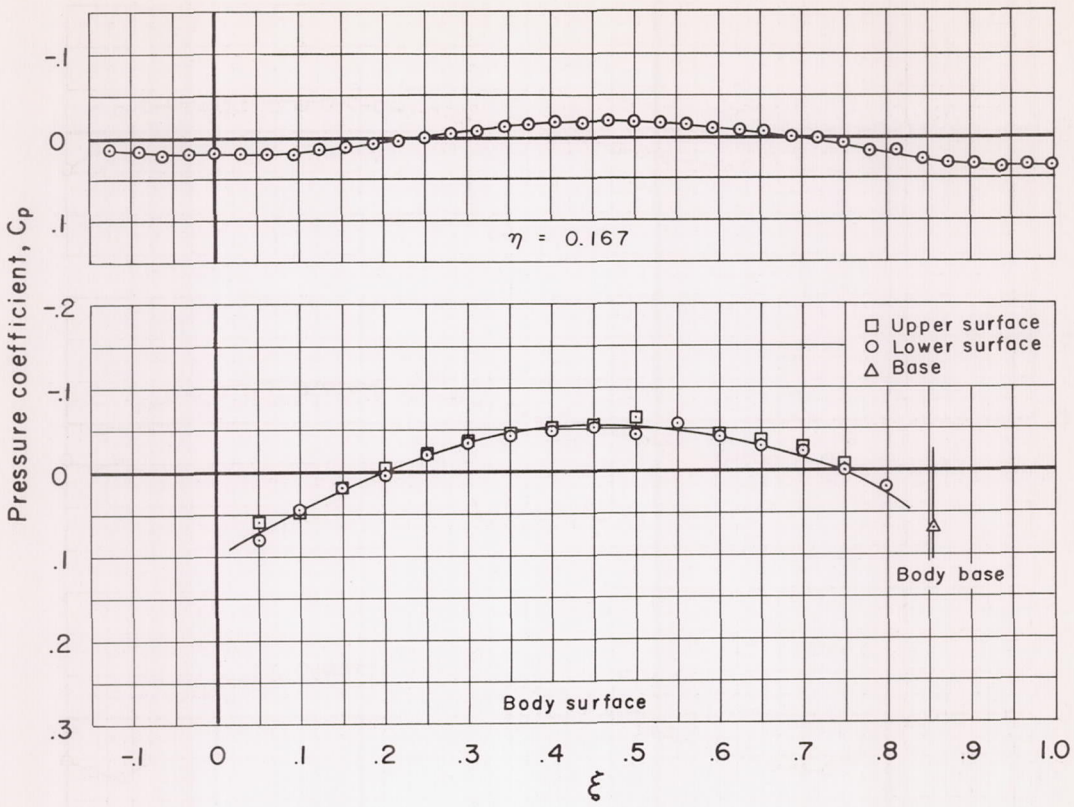

(k) $M_\infty = 0.80$, $\lambda = 2.0$, $\theta = 90^\circ$ and -90°

Figure 9.- Continued.

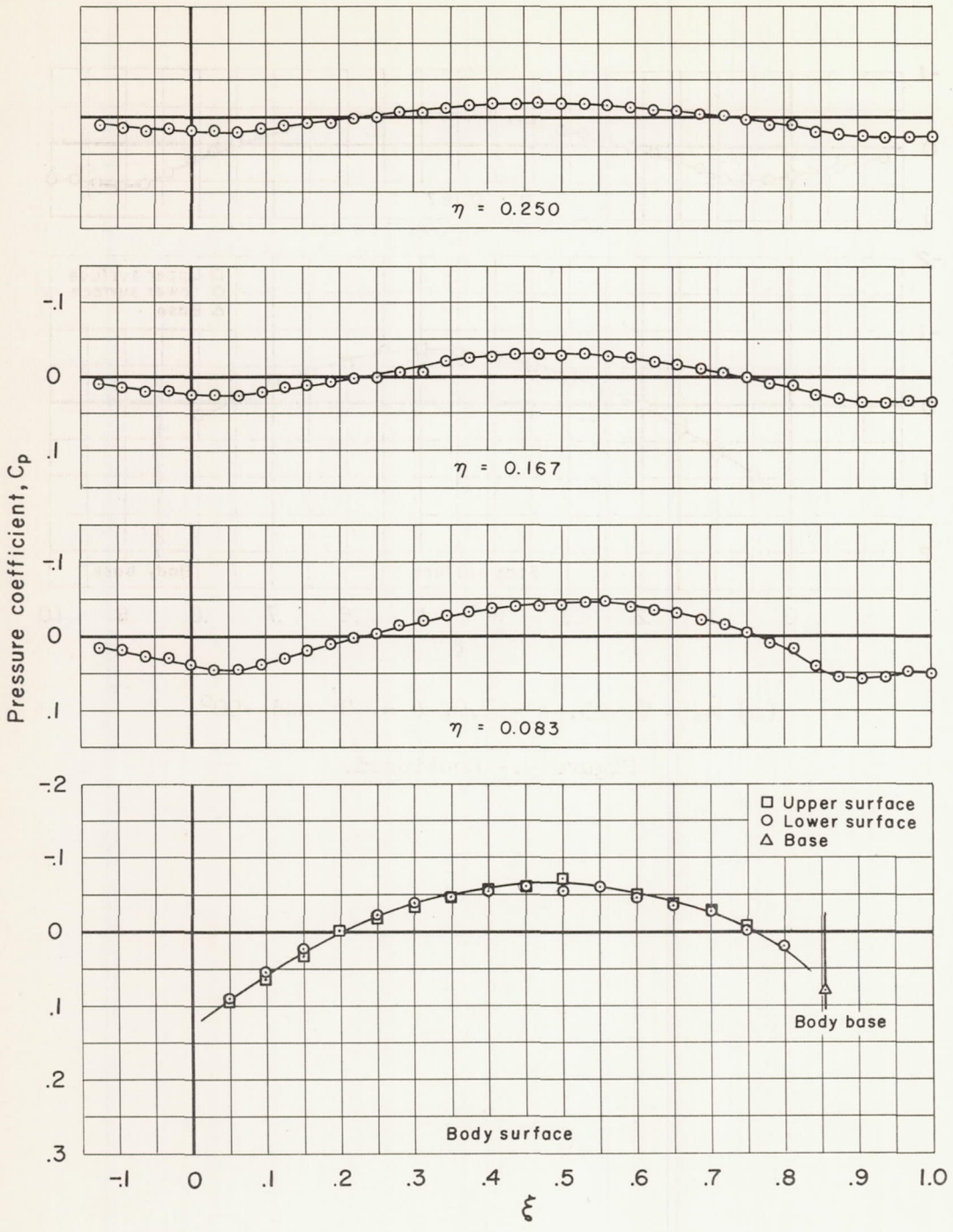

(l) $M_\infty = 0.90$, $\lambda = 2.0$, $\theta = 90^\circ$ and -90°

Figure 9.- Continued.

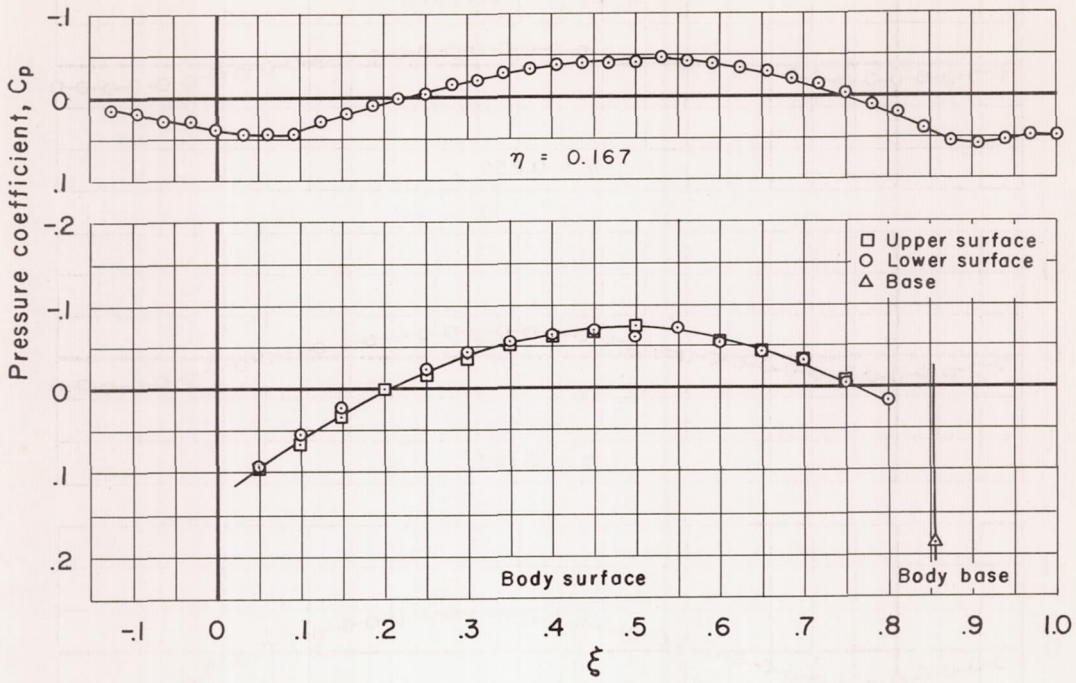

(m) $M_\infty = 0.925$, $\lambda = 2.0$, $\theta = 90^\circ$ and -90°

Figure 9.- Continued.

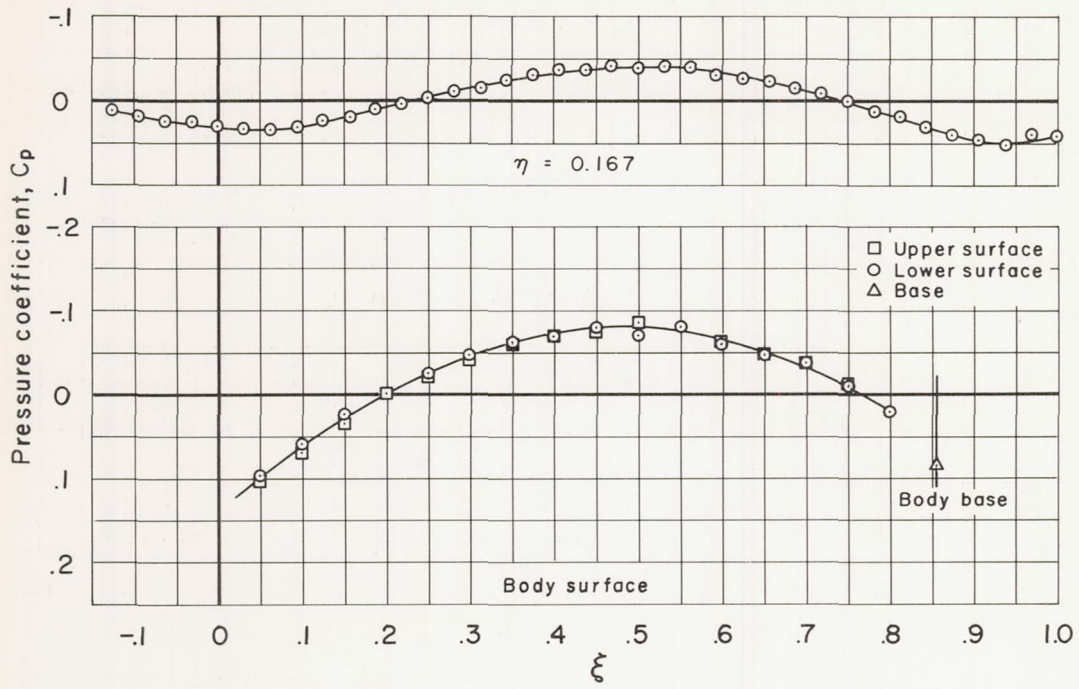

(n) $M_\infty = 0.95$, $\lambda = 2.0$, $\theta = 90^\circ$ and -90°

Figure 9.- Continued.

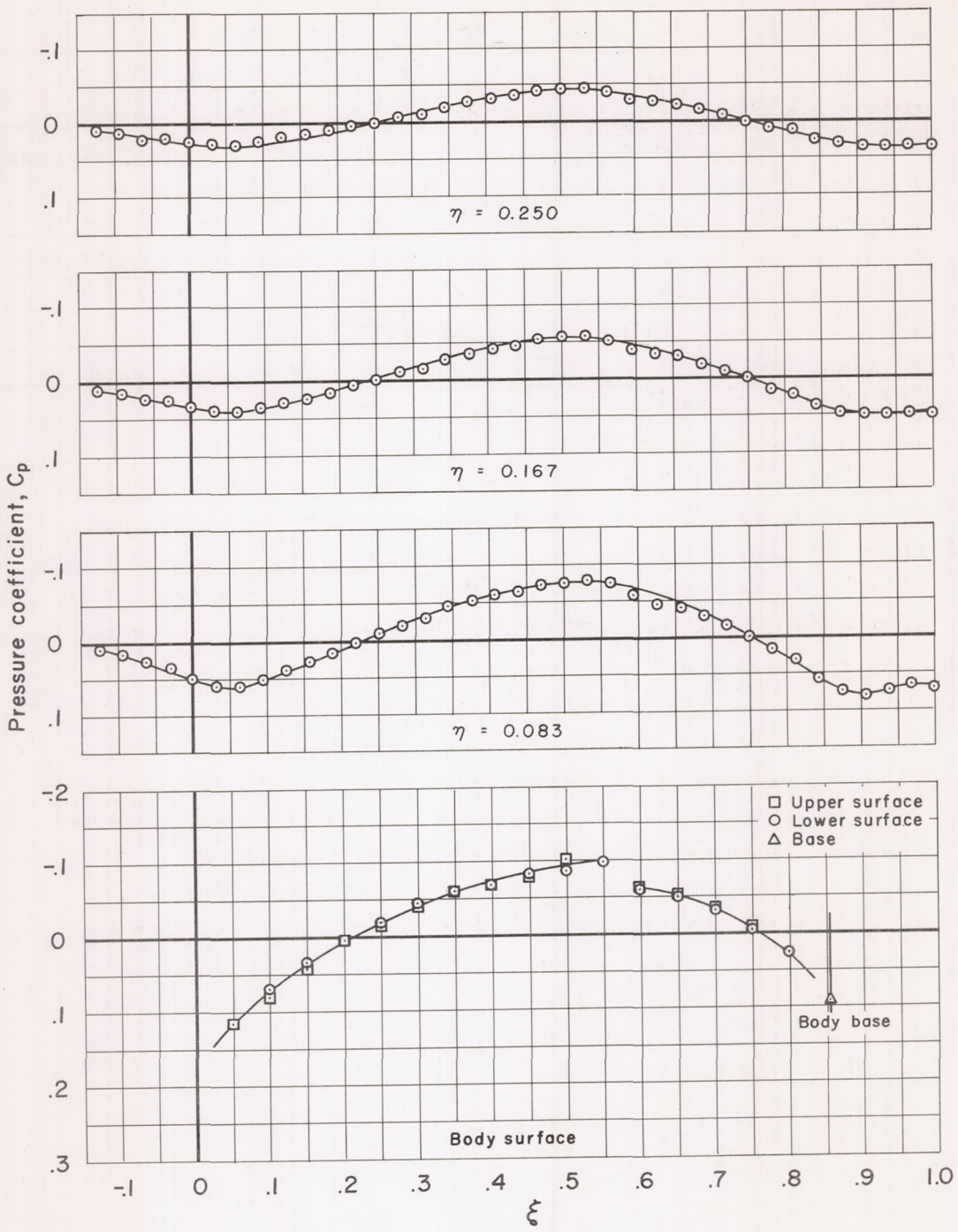

(o) $M_\infty = 0.975$, $\lambda = 2.0$, $\theta = 90^\circ$ and -90°

Figure 9.- Continued.

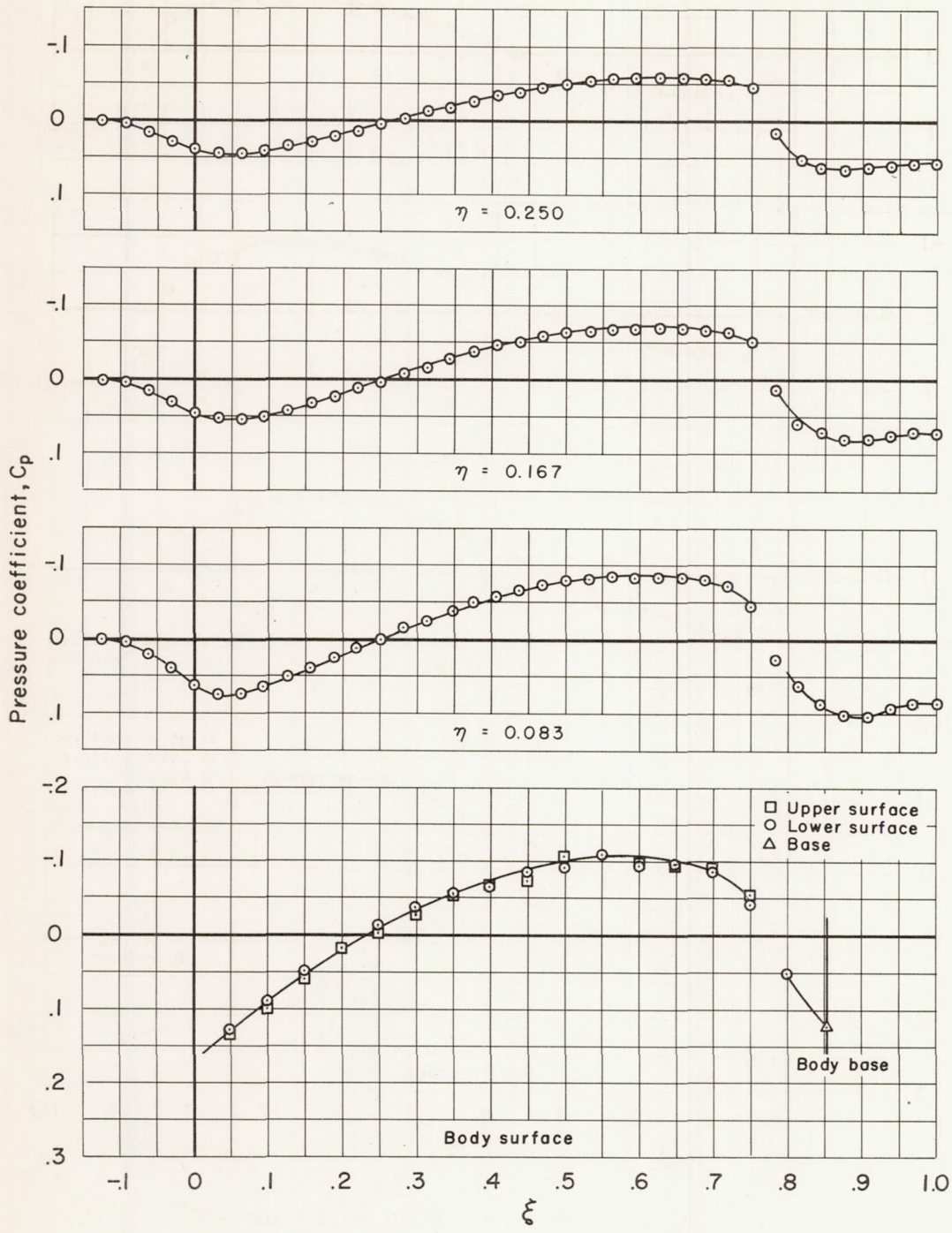

(p) $M_\infty = 1.00$, $\lambda = 2.0$, $\theta = 90^\circ$ and -90°

Figure 9.- Continued.

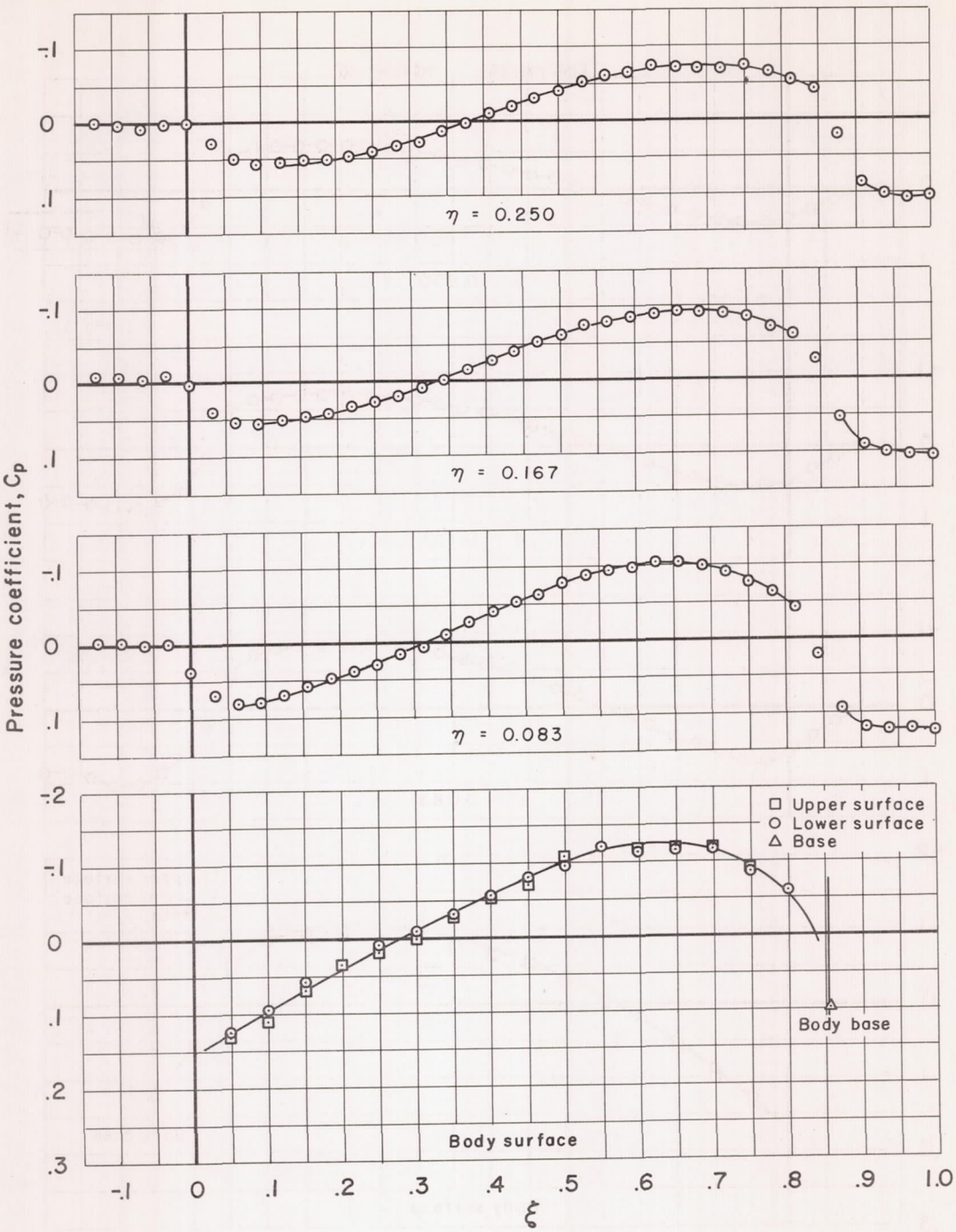

(q) $M_\infty = 1.025$, $\lambda = 2.0$, $\theta = 90^\circ$ and -90°

Figure 9.- Continued.

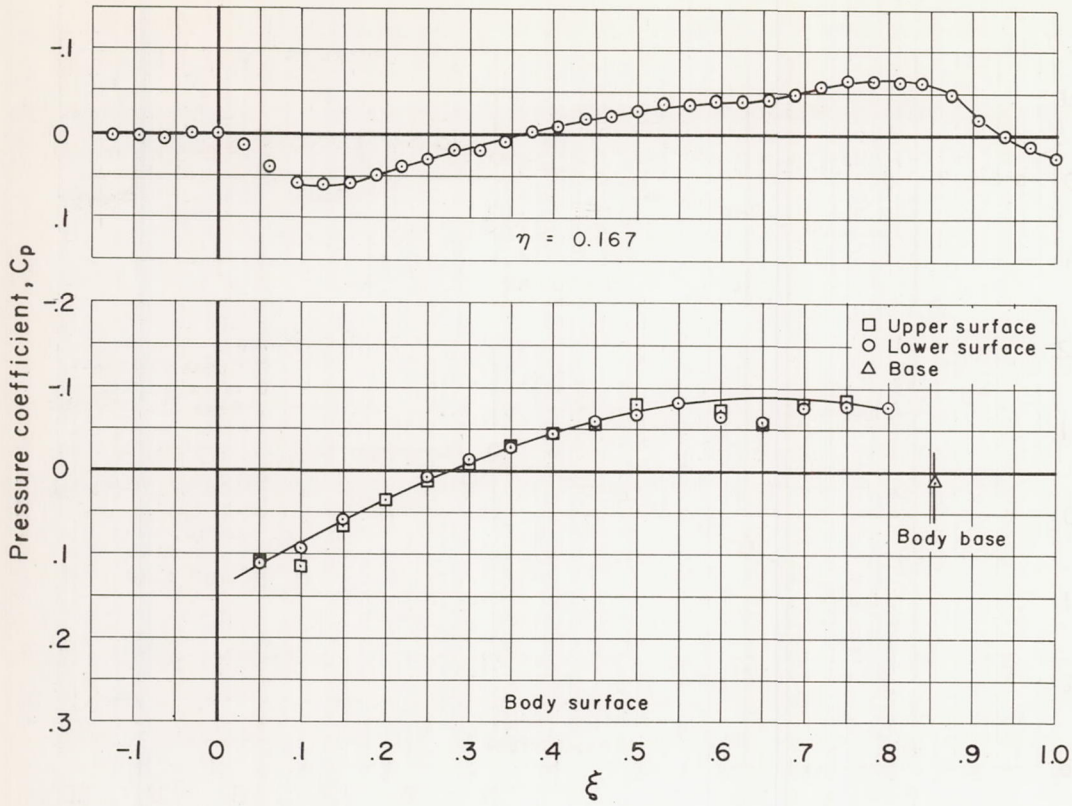

(r) $M_\infty = 1.050$, $\lambda = 2.0$, $\theta = 90^\circ$ and -90°

Figure 9.- Continued.

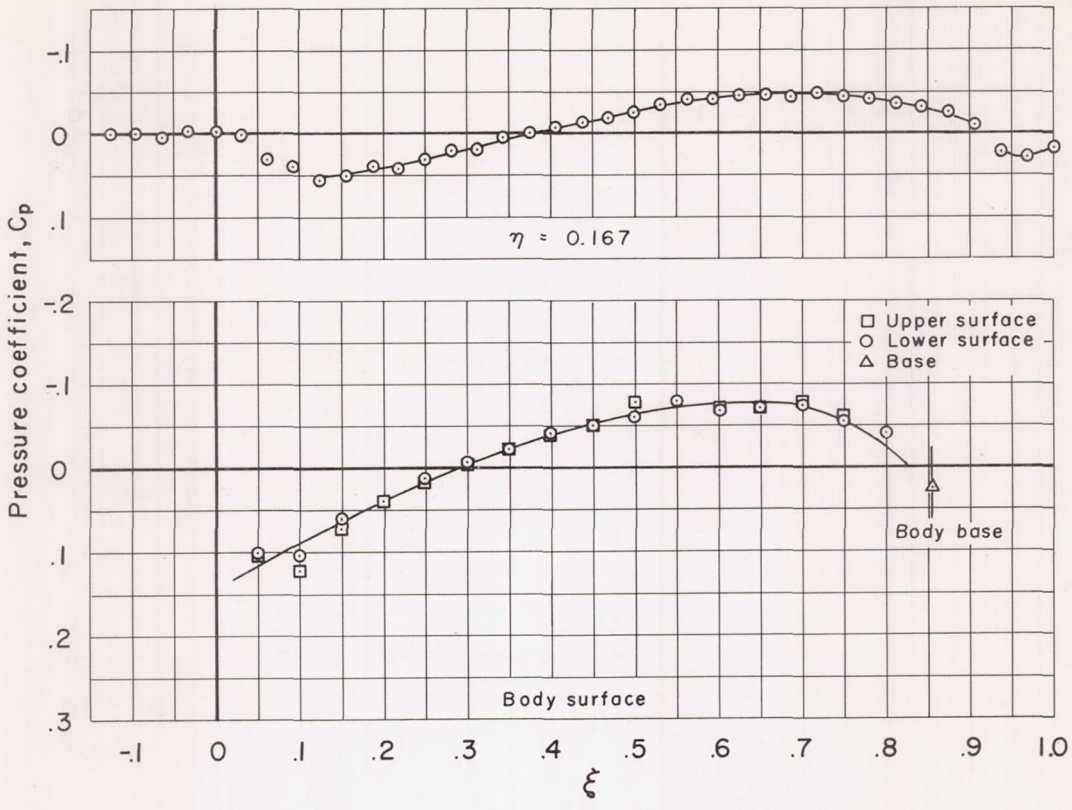

(s) $M_\infty = 1.075$, $\lambda = 2.0$, $\theta = 90^\circ$ and -90°

Figure 9.- Continued.

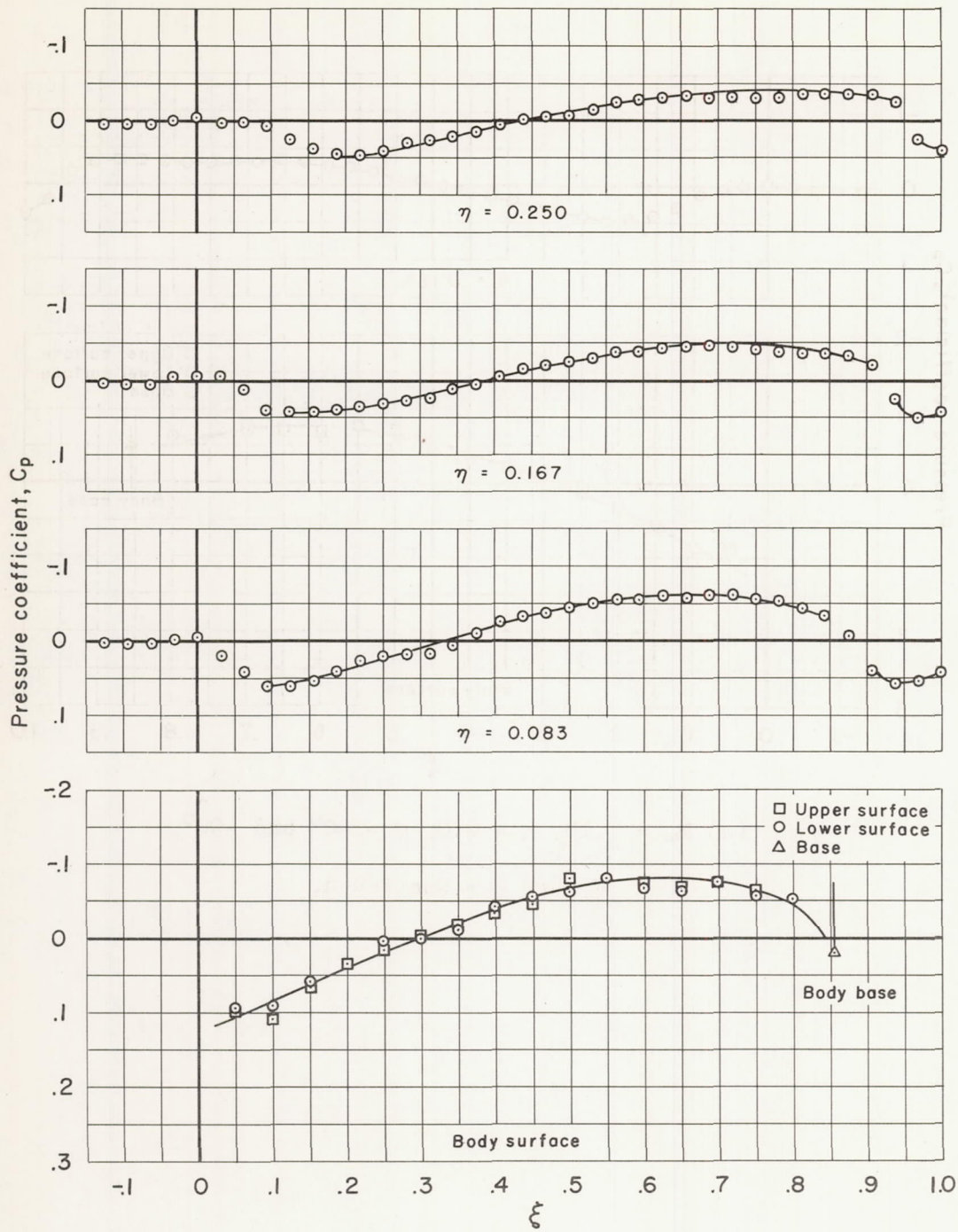

(t) $M_\infty = 1.10$, $\lambda = 2.0$, $\theta = 90^\circ$ and -90°

Figure 9.- Continued.

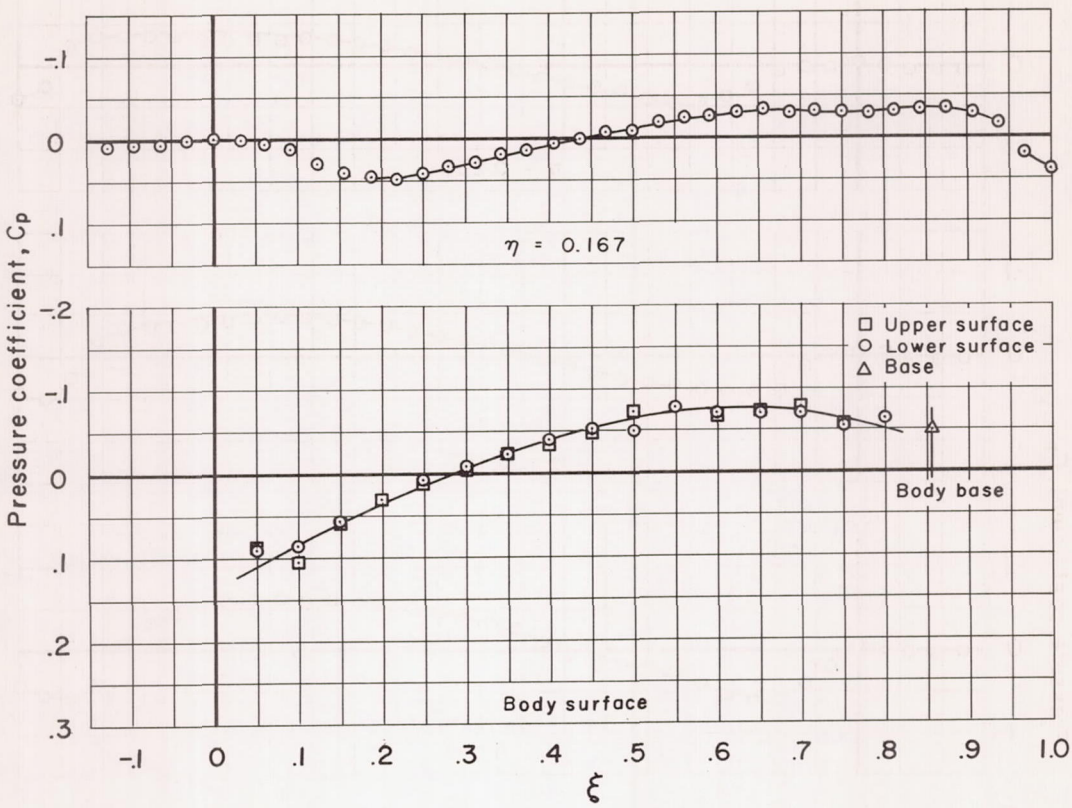

(u) $M_\infty = 1.15$, $\lambda = 2.0$, $\theta = 90^\circ$ and -90°

Figure 9.- Continued.

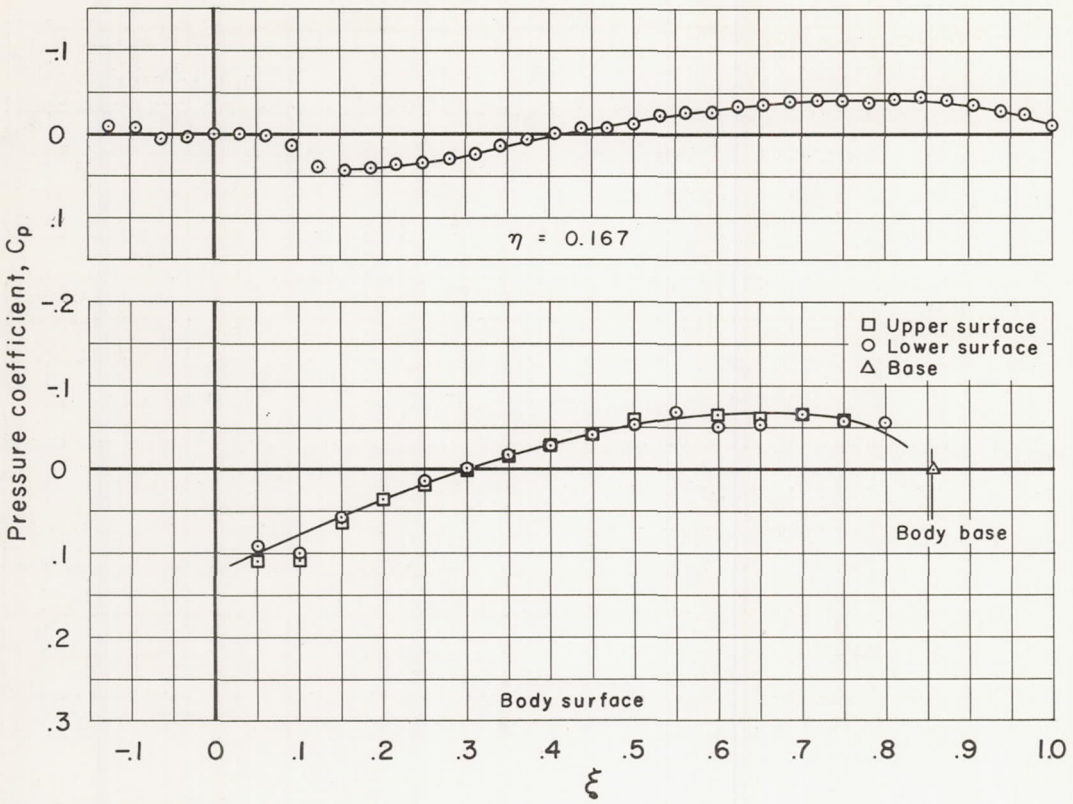

(v) $M_\infty = 1.20$, $\lambda = 2.0$, $\theta = 90^\circ$ and -90°

Figure 9.- Concluded.

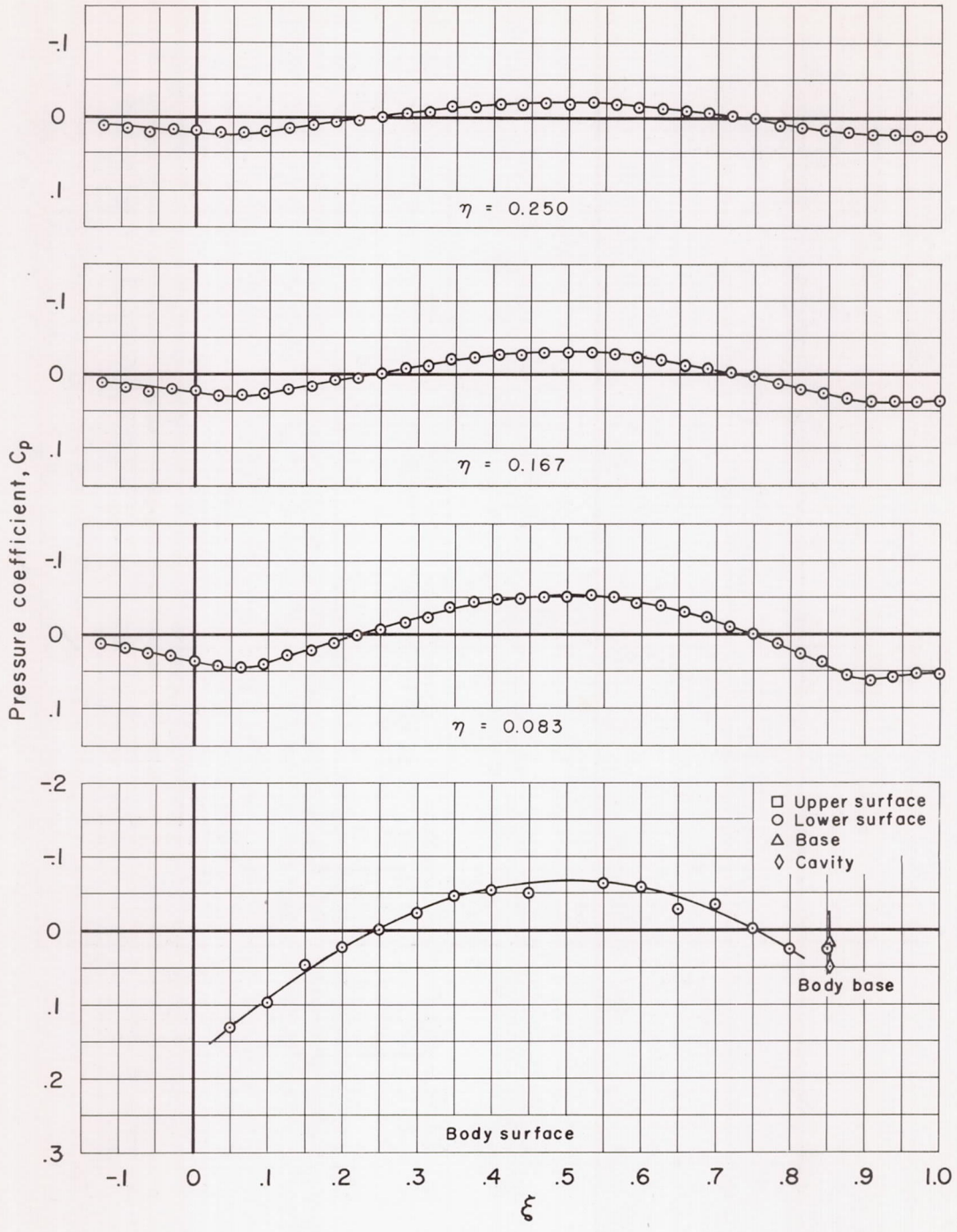

(a) $M_\infty = 0.90$, $\lambda = 3.0$, $\theta = 0^\circ$

Figure 10.- Measured pressure distributions for the body having an axis ratio of 3.0.

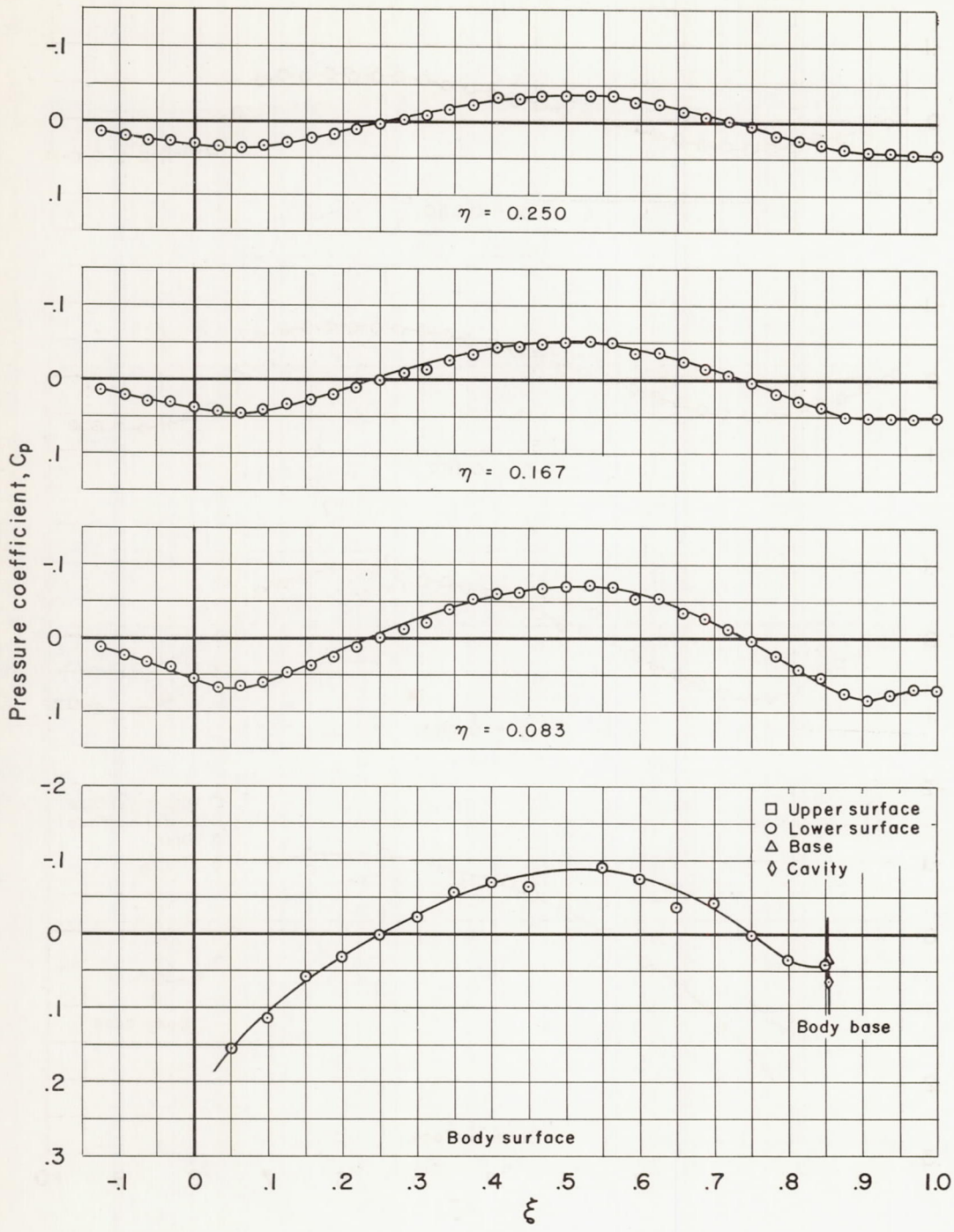

(b) $M_\infty = 0.975$, $\lambda = 3.0$, $\theta = 0^\circ$

Figure 10.- Continued.

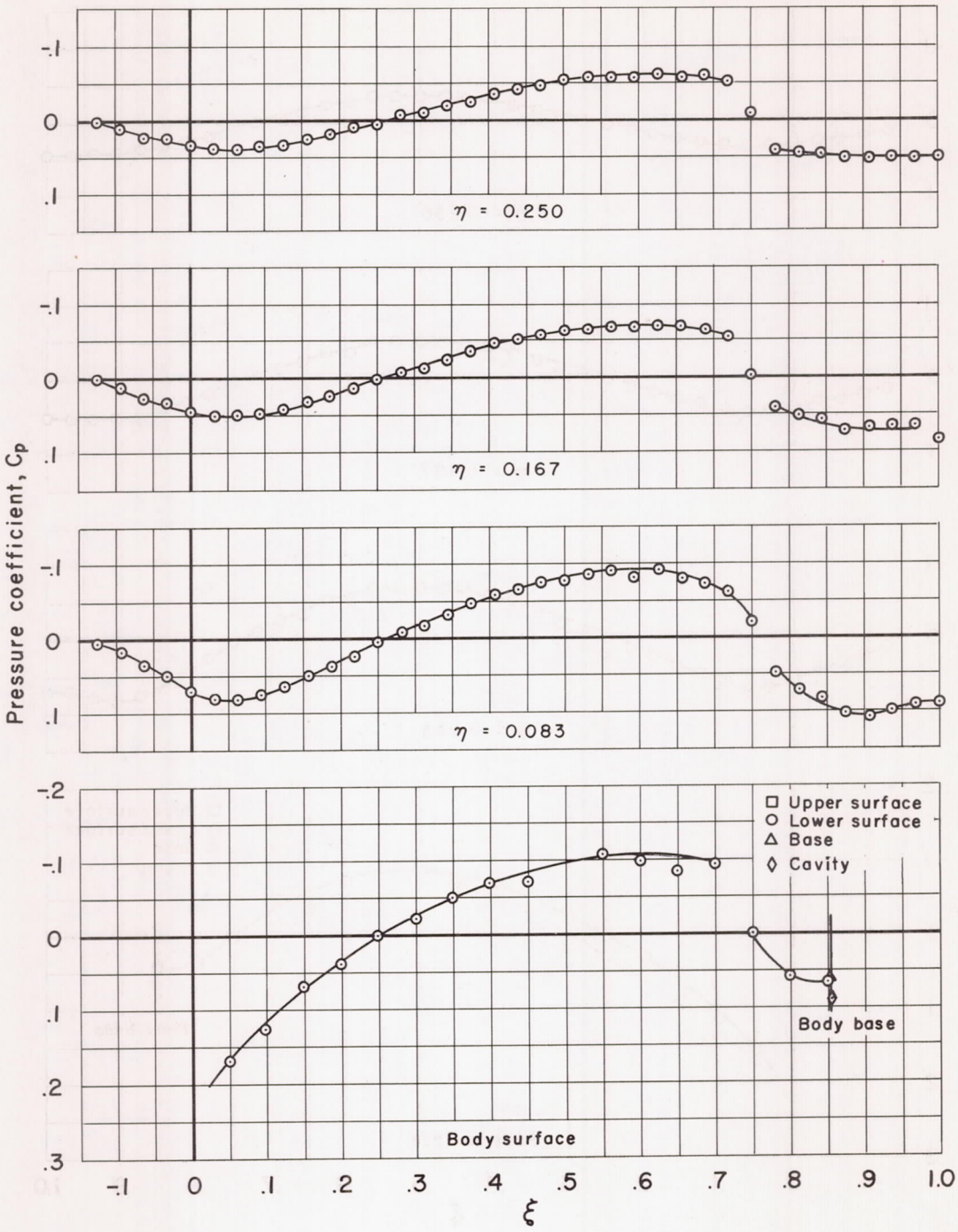

(c) $M_\infty = 1.00$, $\lambda = 3.0$, $\theta = 0^\circ$

Figure 10.- Continued.

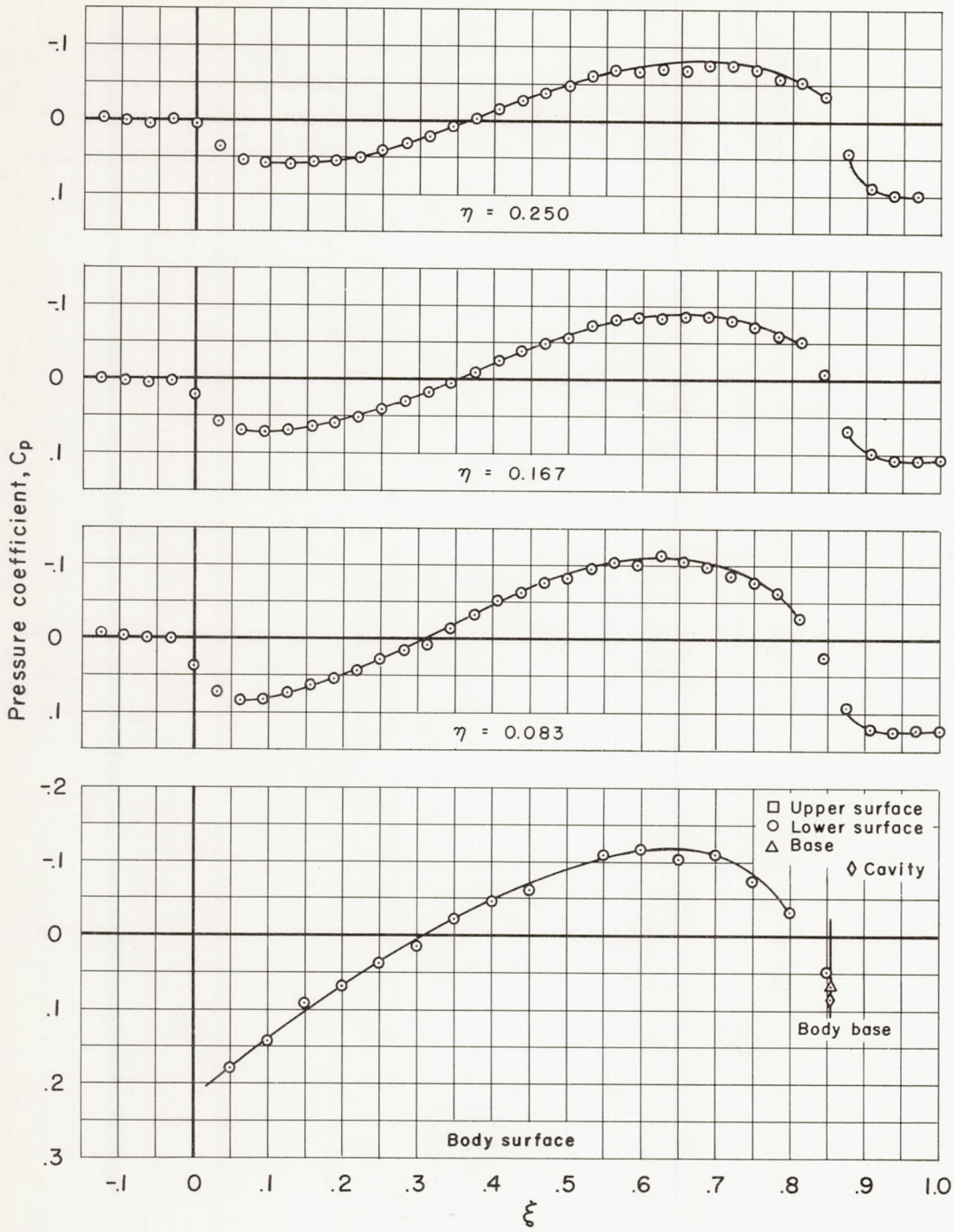

(d) $M_\infty = 1.025$, $\lambda = 3.0$, $\theta = 0^\circ$

Figure 10.- Continued.

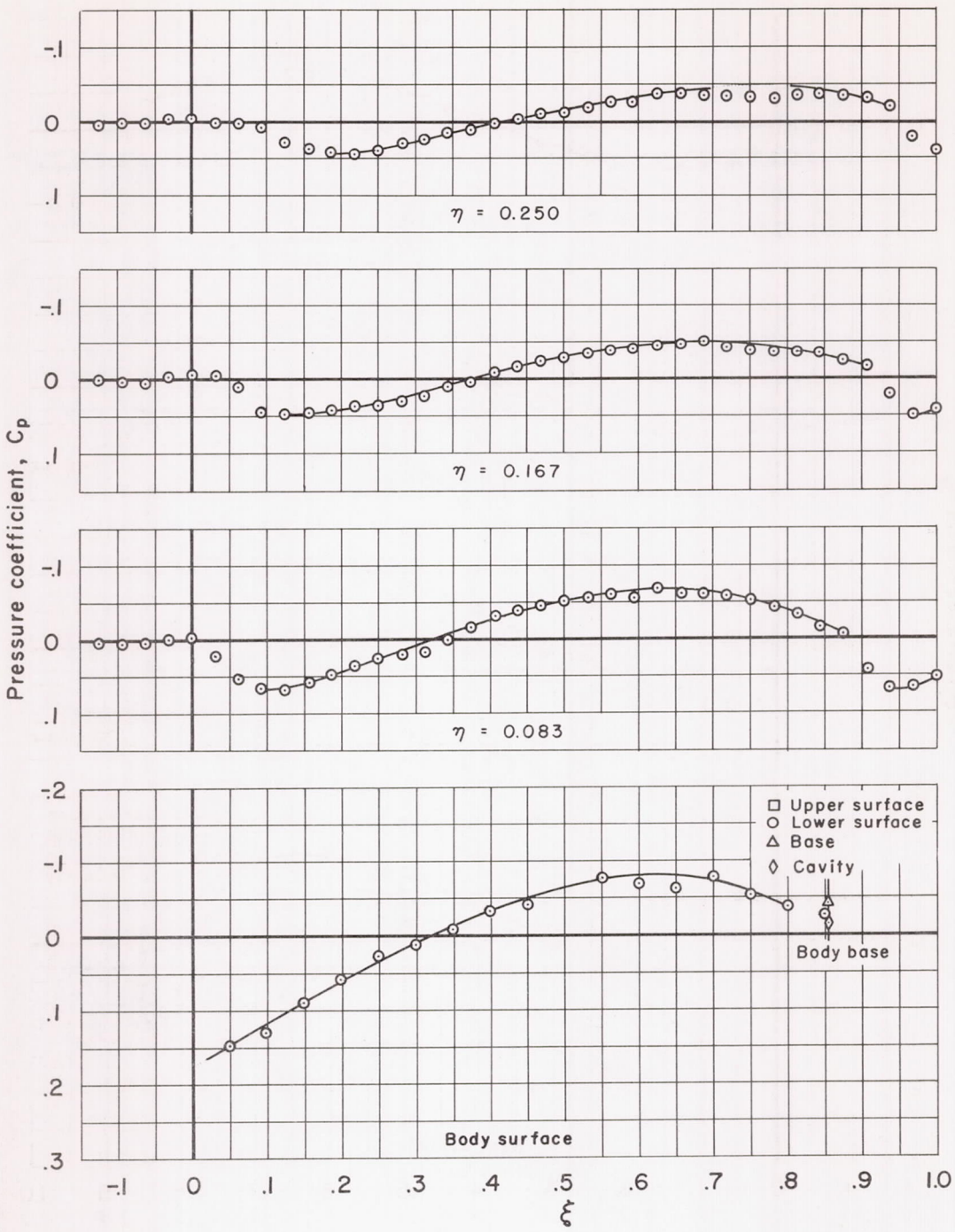

(e) $M_\infty = 1.10$, $\lambda = 3.0$, $\theta = 0^\circ$

Figure 10.- Continued.

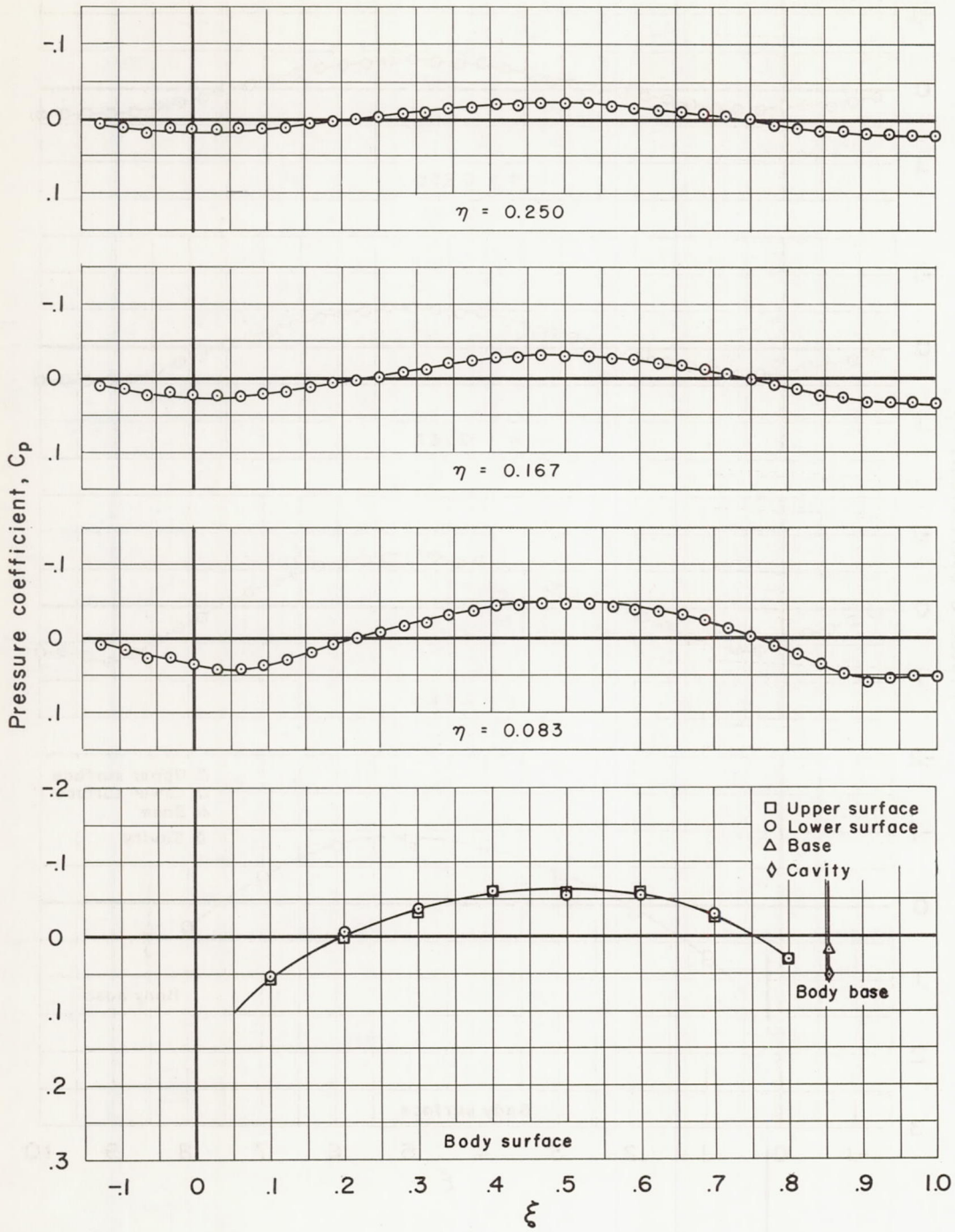

(f) $M_\infty = 0.90$, $\lambda = 3.0$, $\theta = 40^\circ$ and -40°

Figure 10.- Continued.

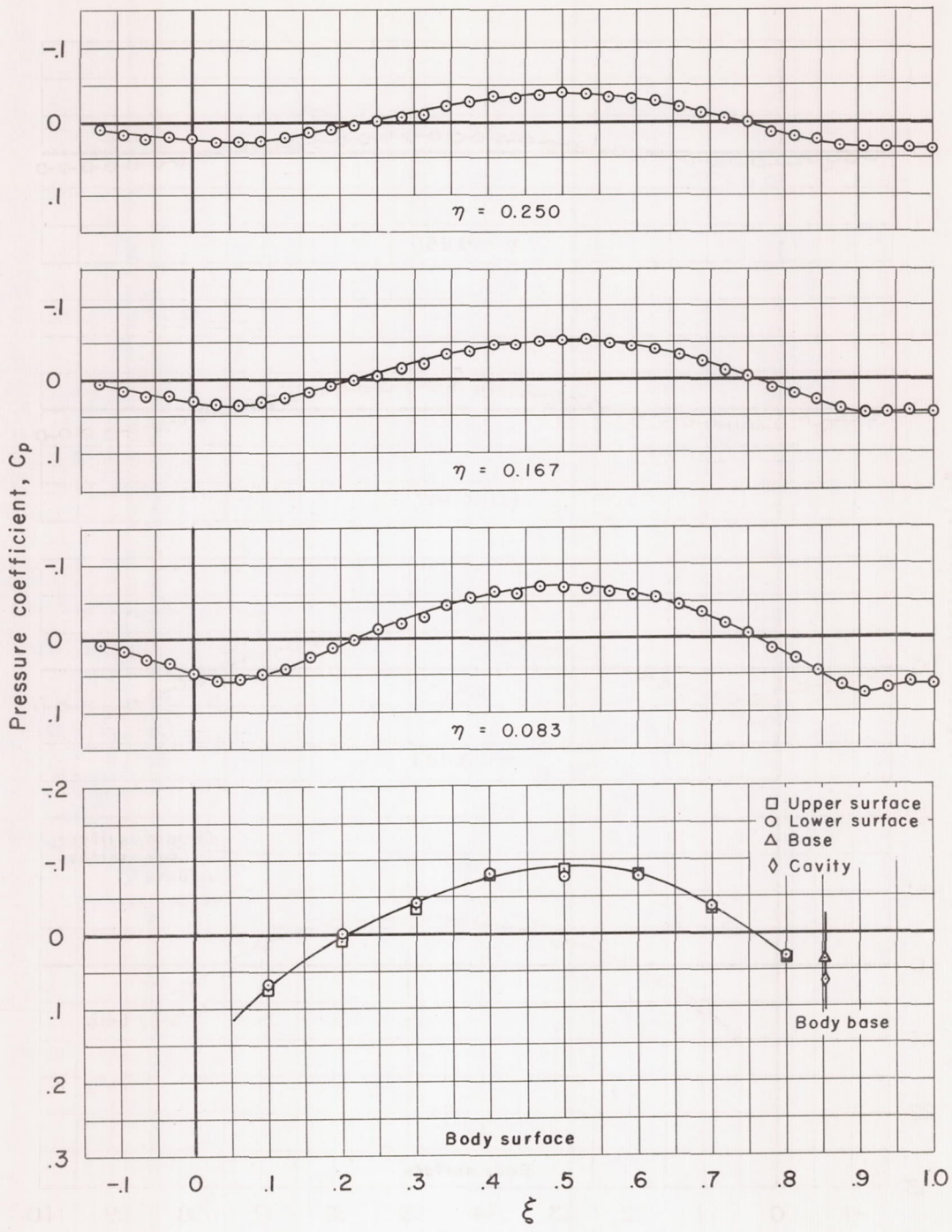

(g) $M_\infty = 0.975$, $\lambda = 3.0$, $\theta = 40^\circ$ and -40°

Figure 10.- Continued.

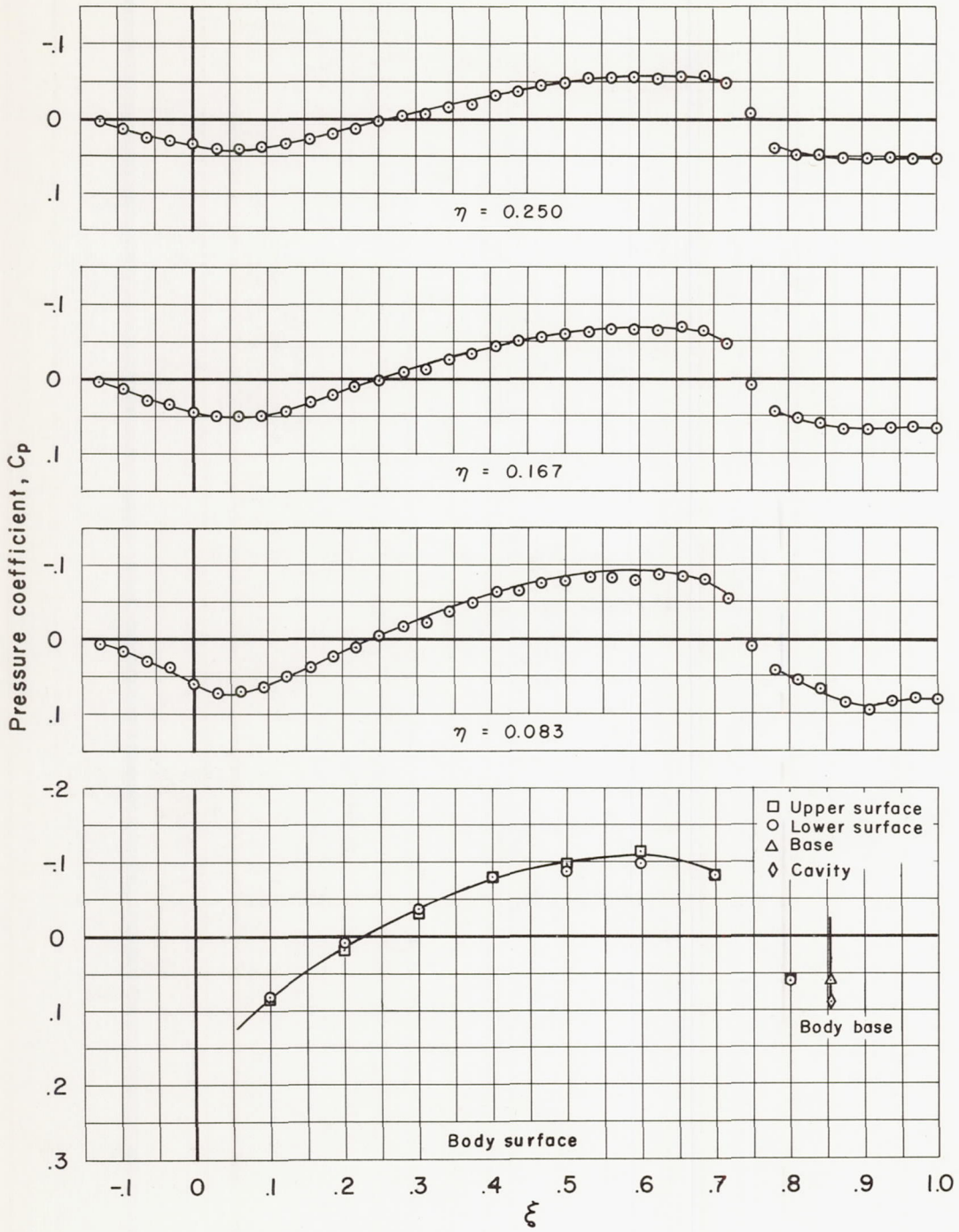

(h) $M_\infty = 1.00$, $\lambda = 3.0$, $\theta = 40^\circ$ and -40°

Figure 10.- Continued.

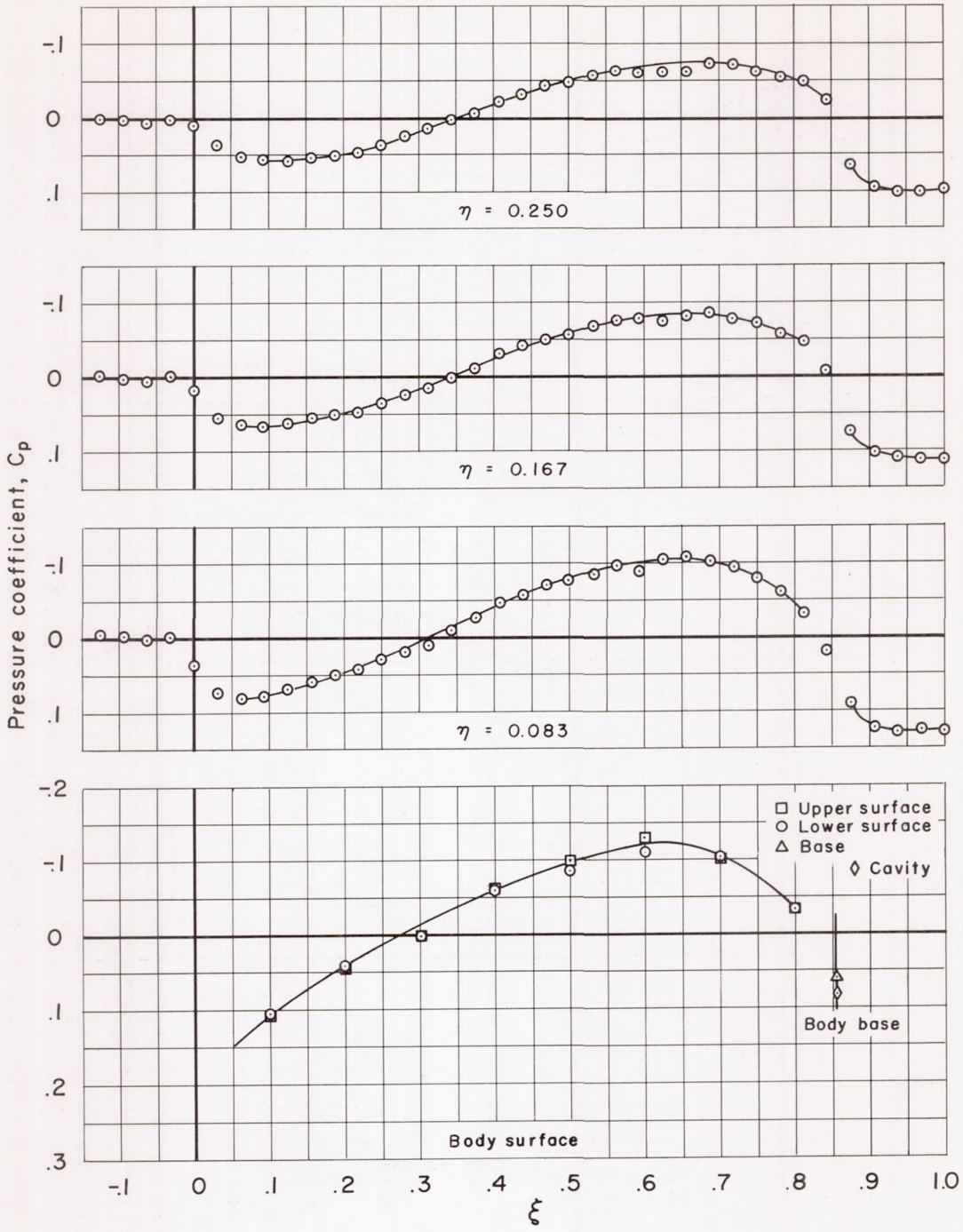

(i) $M_\infty = 1.025$, $\lambda = 3.0$, $\theta = 40^\circ$ and -40°

Figure 10.- Continued.

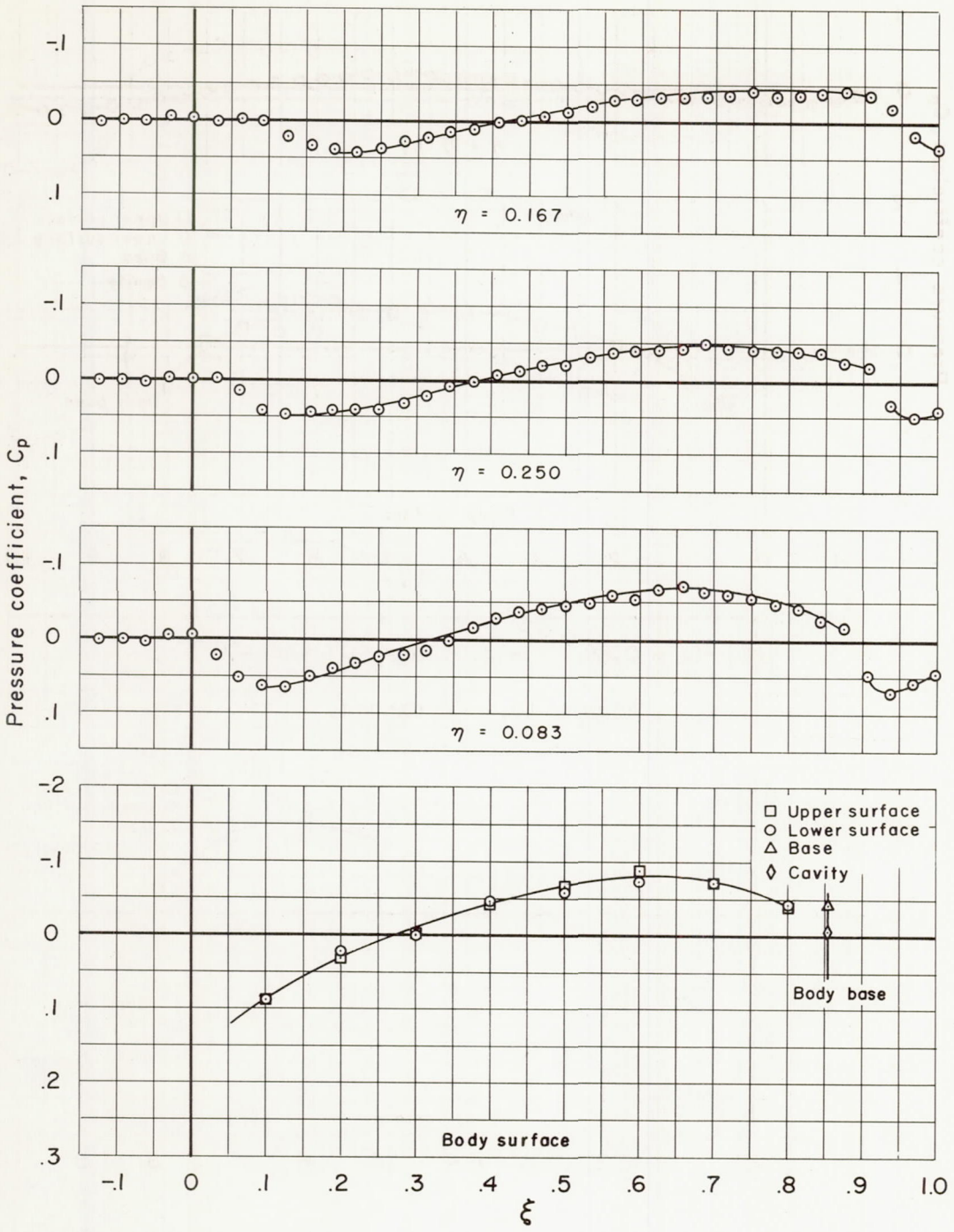

(j) M_∞ = 1.10, λ = 3.0, θ = 40° and -40°

Figure 10.- Continued.

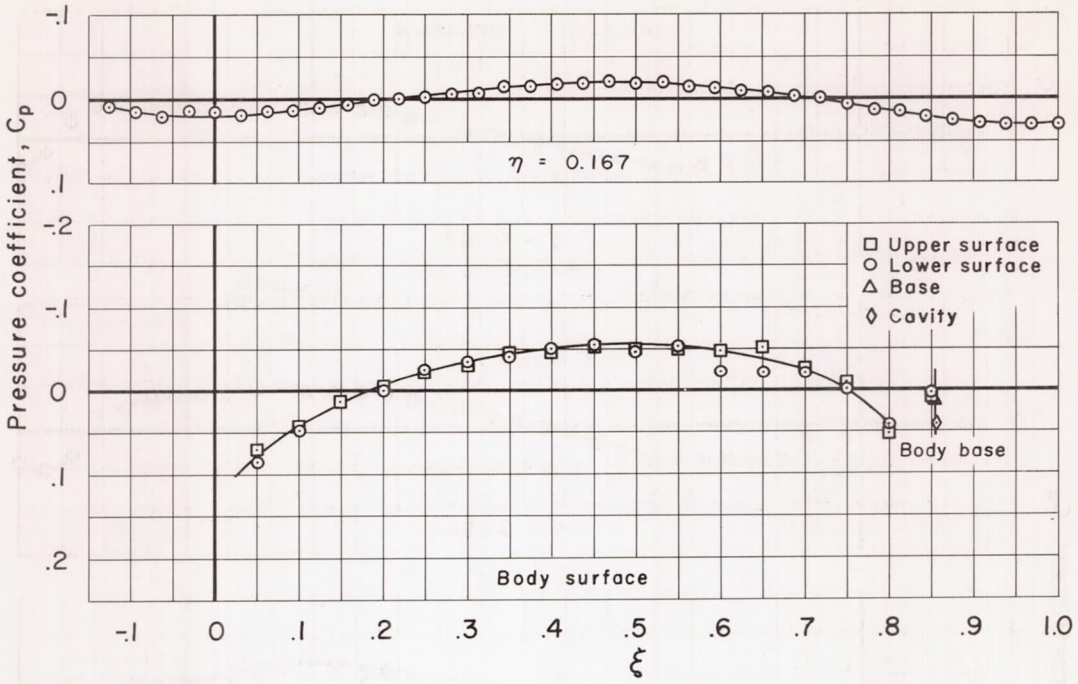

(k) $M_\infty = 0.80$, $\lambda = 3.0$, $\theta = 90^\circ$ and -90°

Figure 10.- Continued.

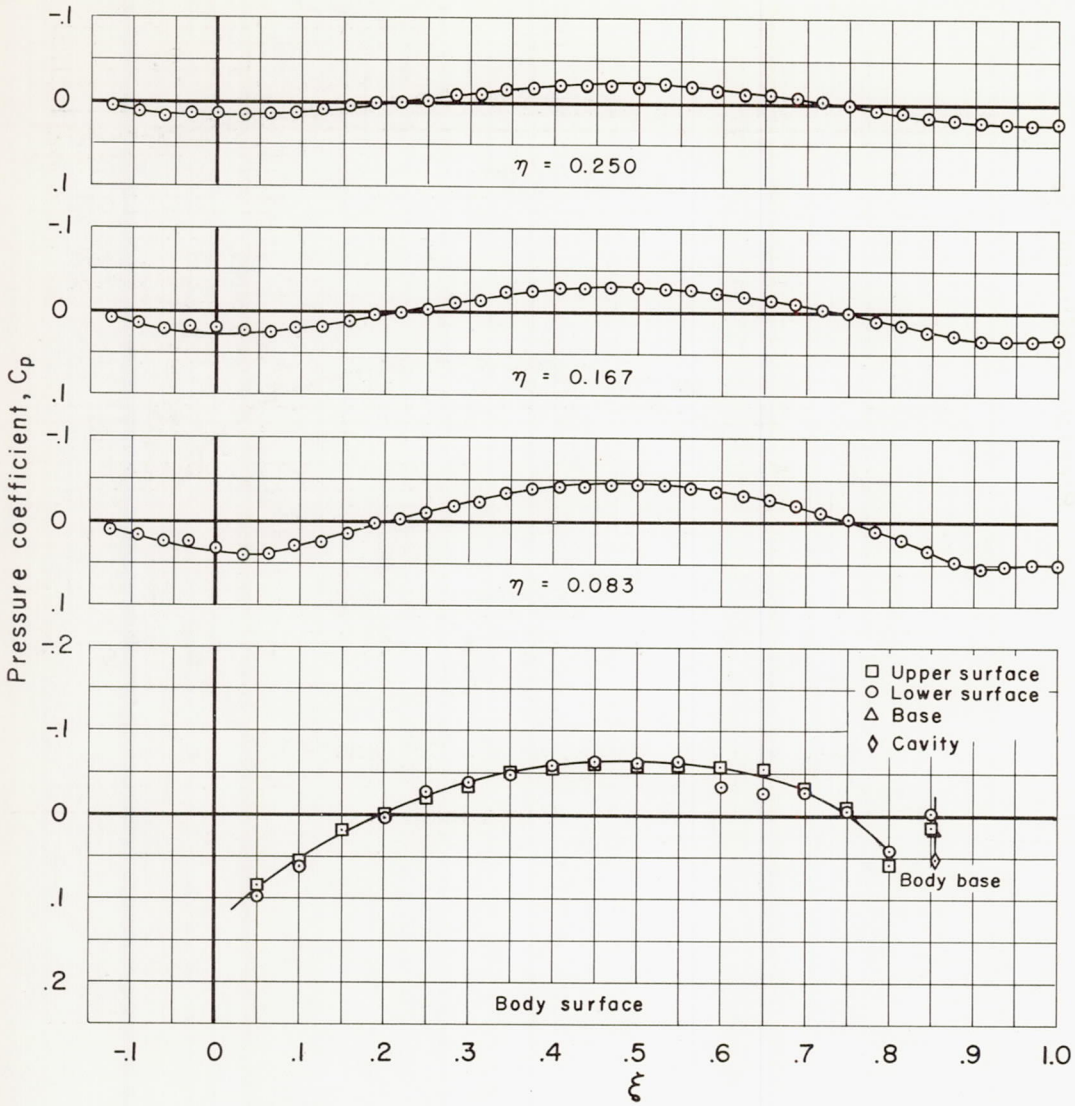

(*l*) $M_\infty = 0.90$, $\lambda = 3.0$, $\theta = 90^\circ$ and -90°

Figure 10.- Continued.

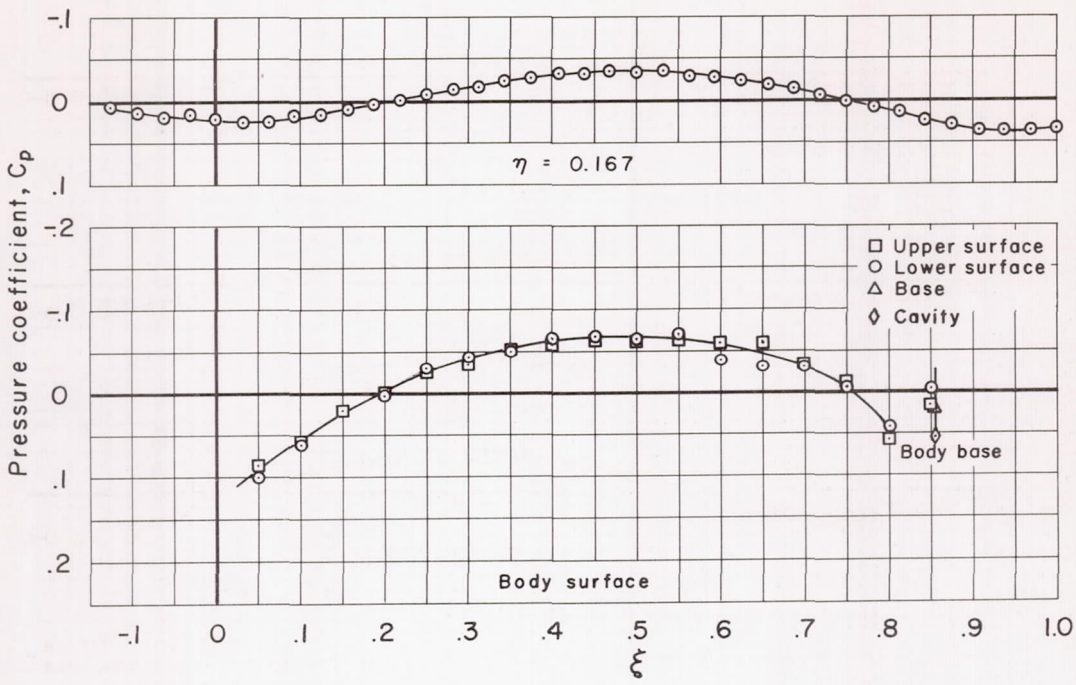

(m) $M_\infty = 0.925$, $\lambda = 3.0$, $\theta = 90^\circ$ and -90°

Figure 10.- Continued.

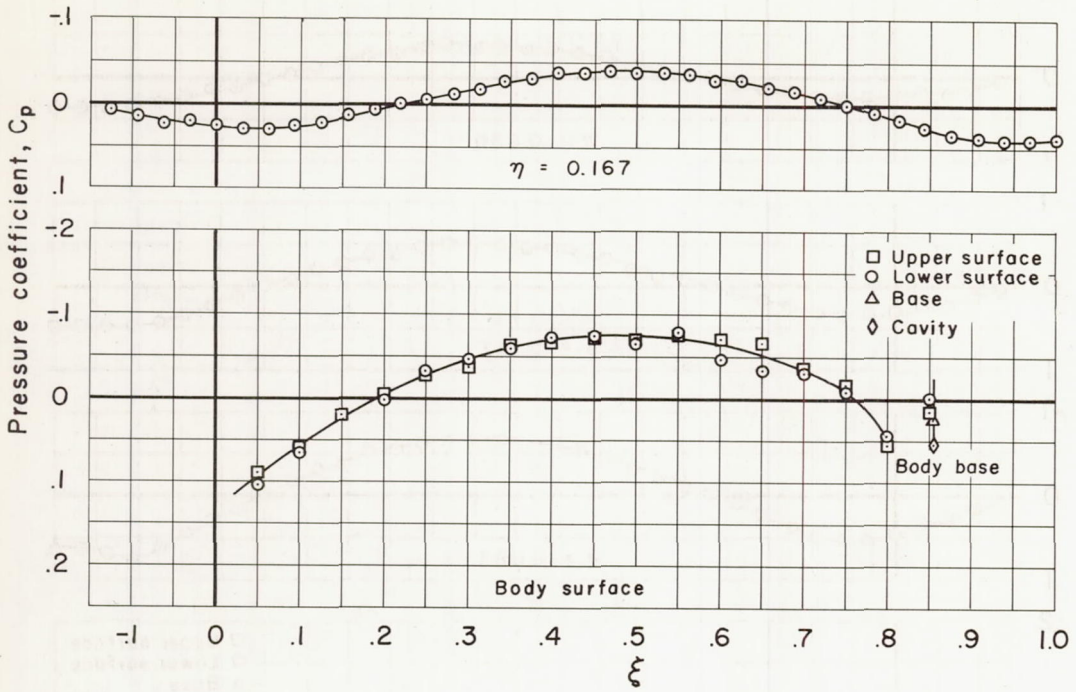

(n) $M_\infty = 0.95$, $\lambda = 3.0$, $\theta = 90^\circ$ and -90°

Figure 10.- Continued.

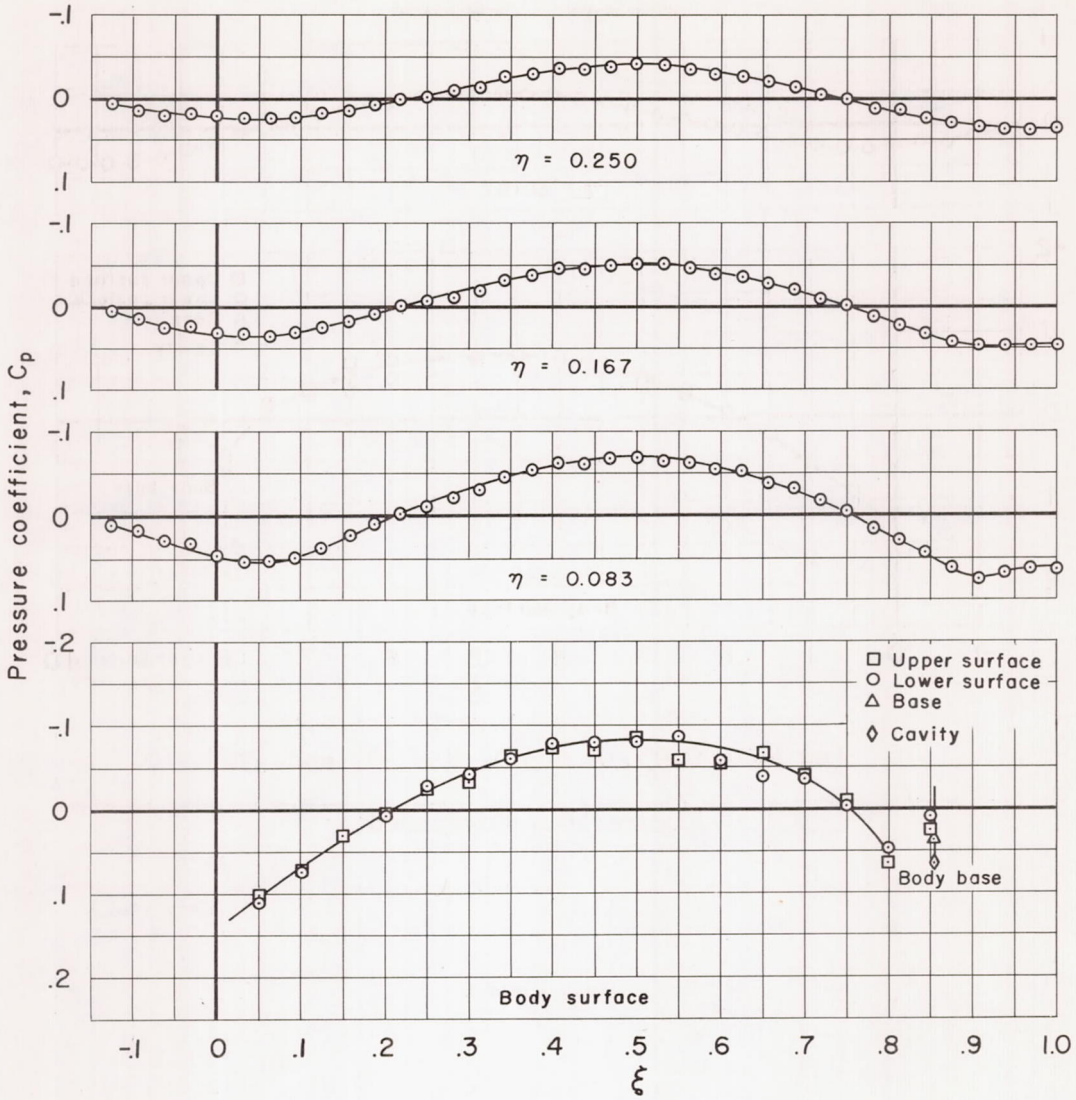

(o) $M_\infty = 0.975$, $\lambda = 3.0$, $\theta = \pm 90^\circ$

Figure 10.- Continued.

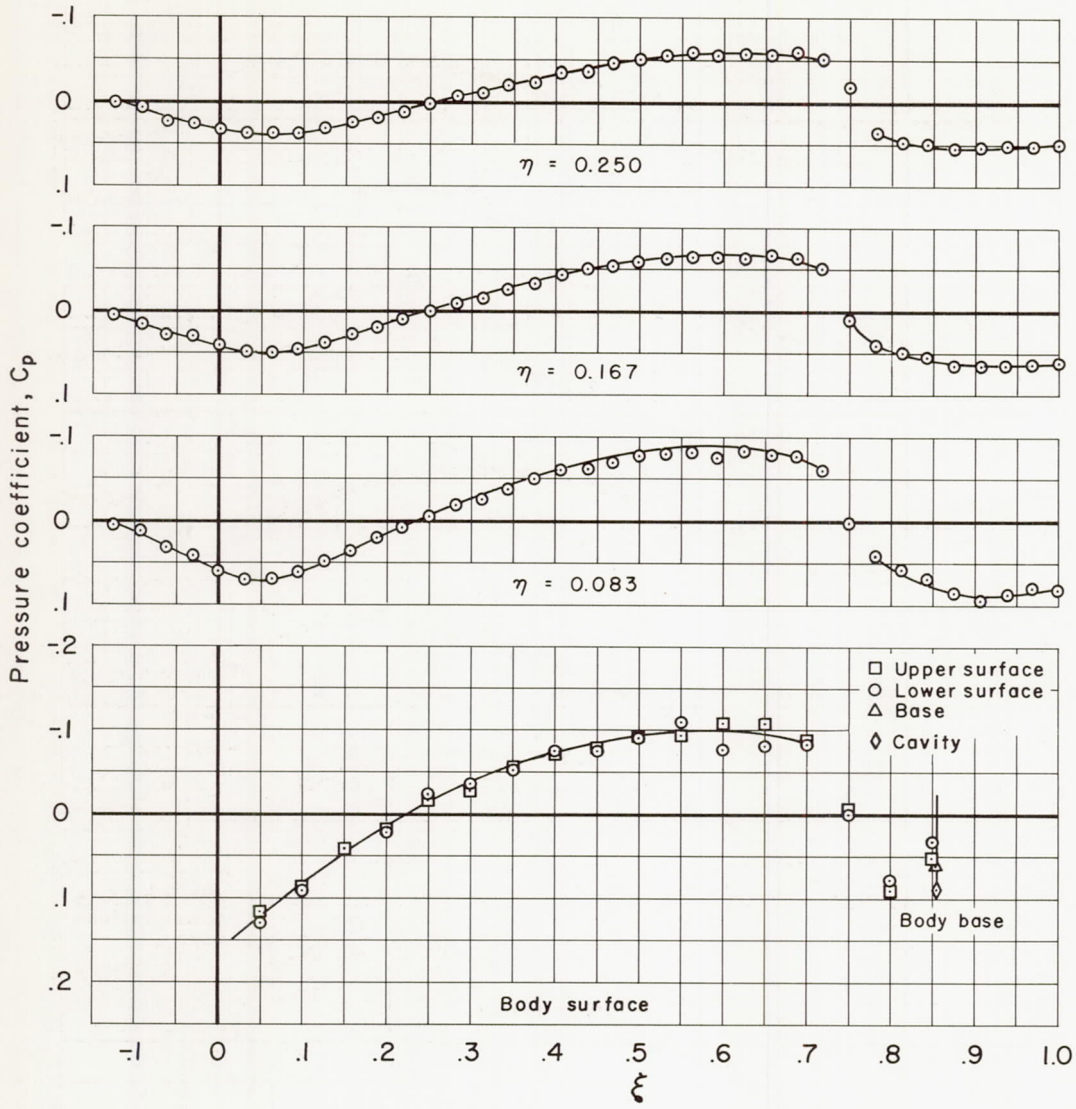

(p) $M_\infty = 1.00$, $\lambda = 3.0$, $\theta = \pm 90^\circ$

Figure 10.- Continued.

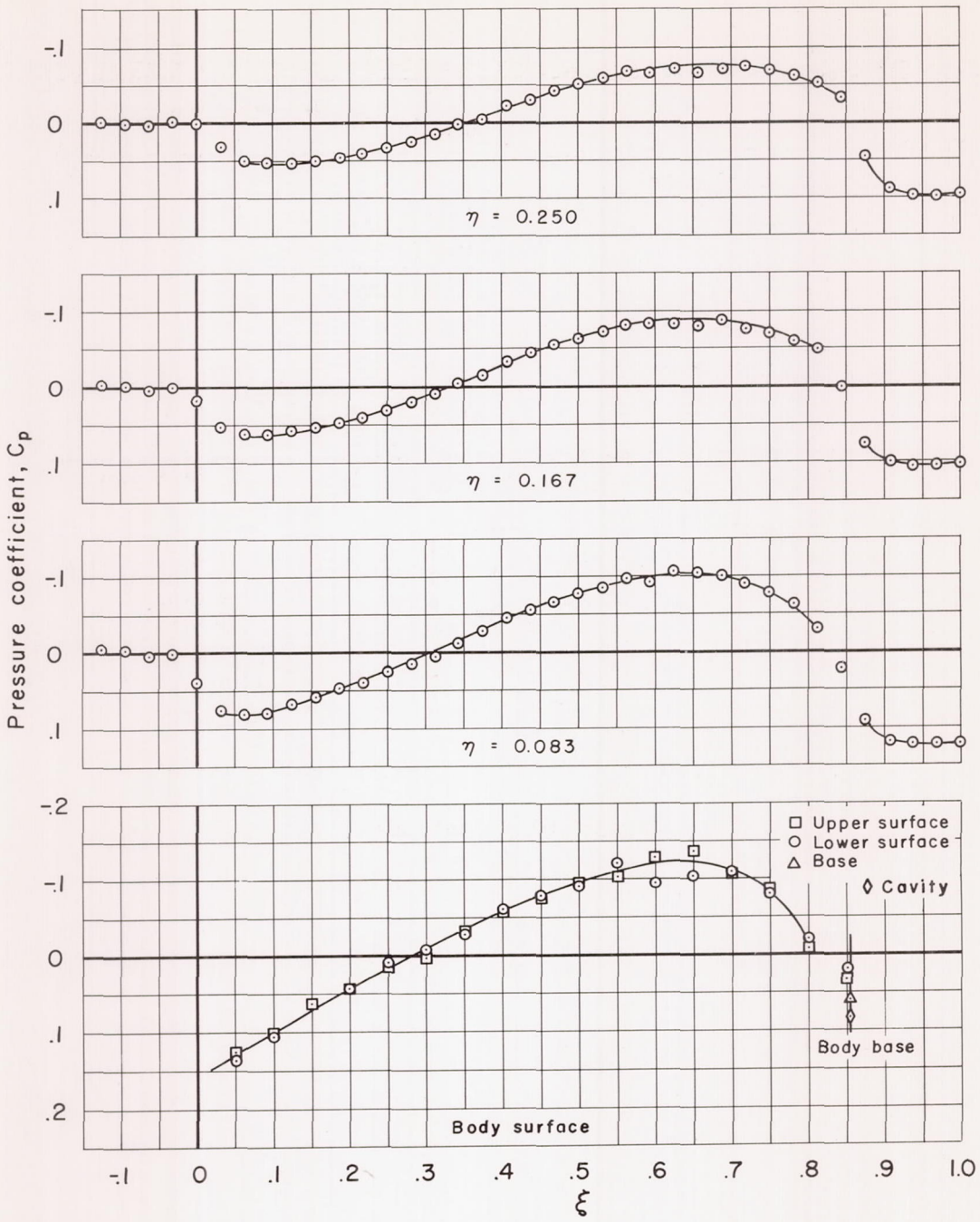

(q) $M_\infty = 1.025$, $\lambda = 3.0$, $\theta = \pm 90^\circ$

Figure 10.- Continued.

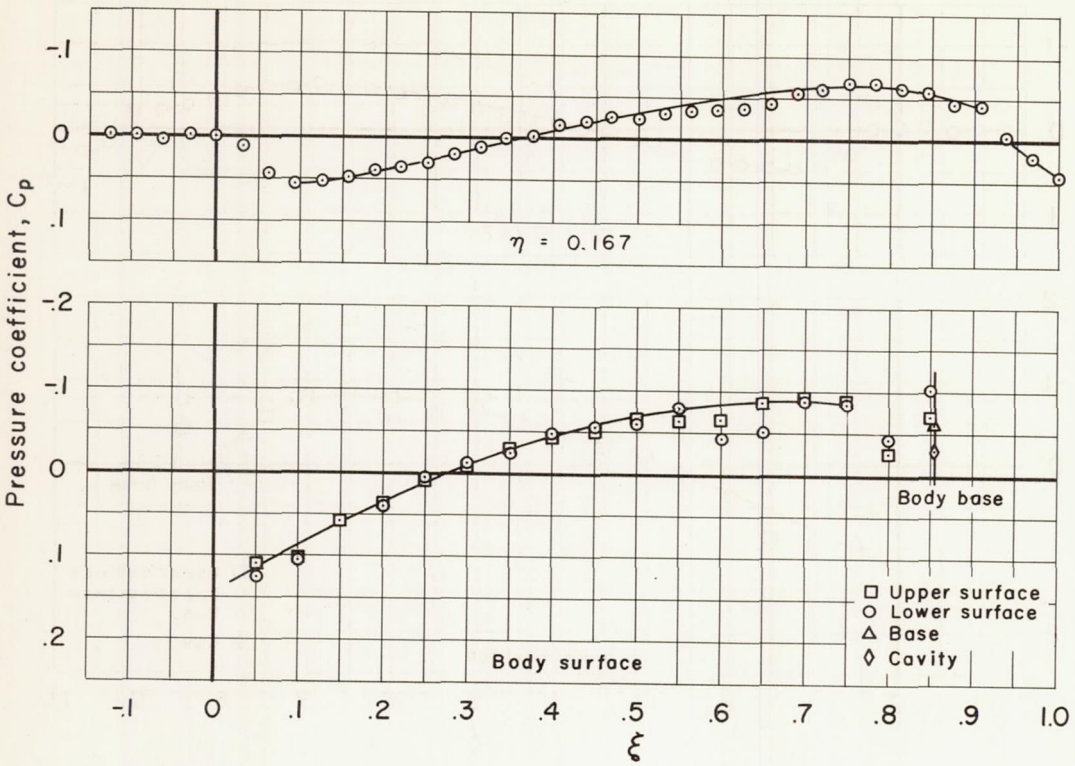

(r) $M_\infty = 1.05$, $\lambda = 3.0$, $\theta = \pm 90^\circ$

Figure 10.- Continued.

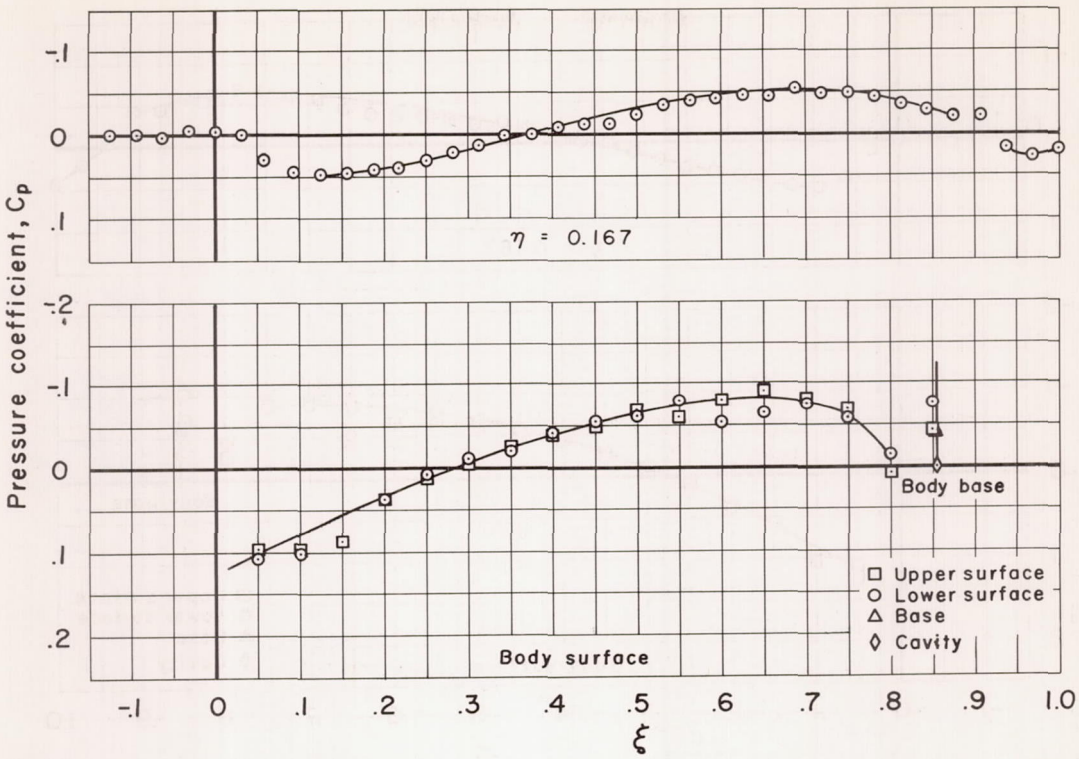

(s) $M_\infty = 1.075$, $\lambda = 3.0$, $\theta = \pm 90^\circ$

Figure 10.- Continued.

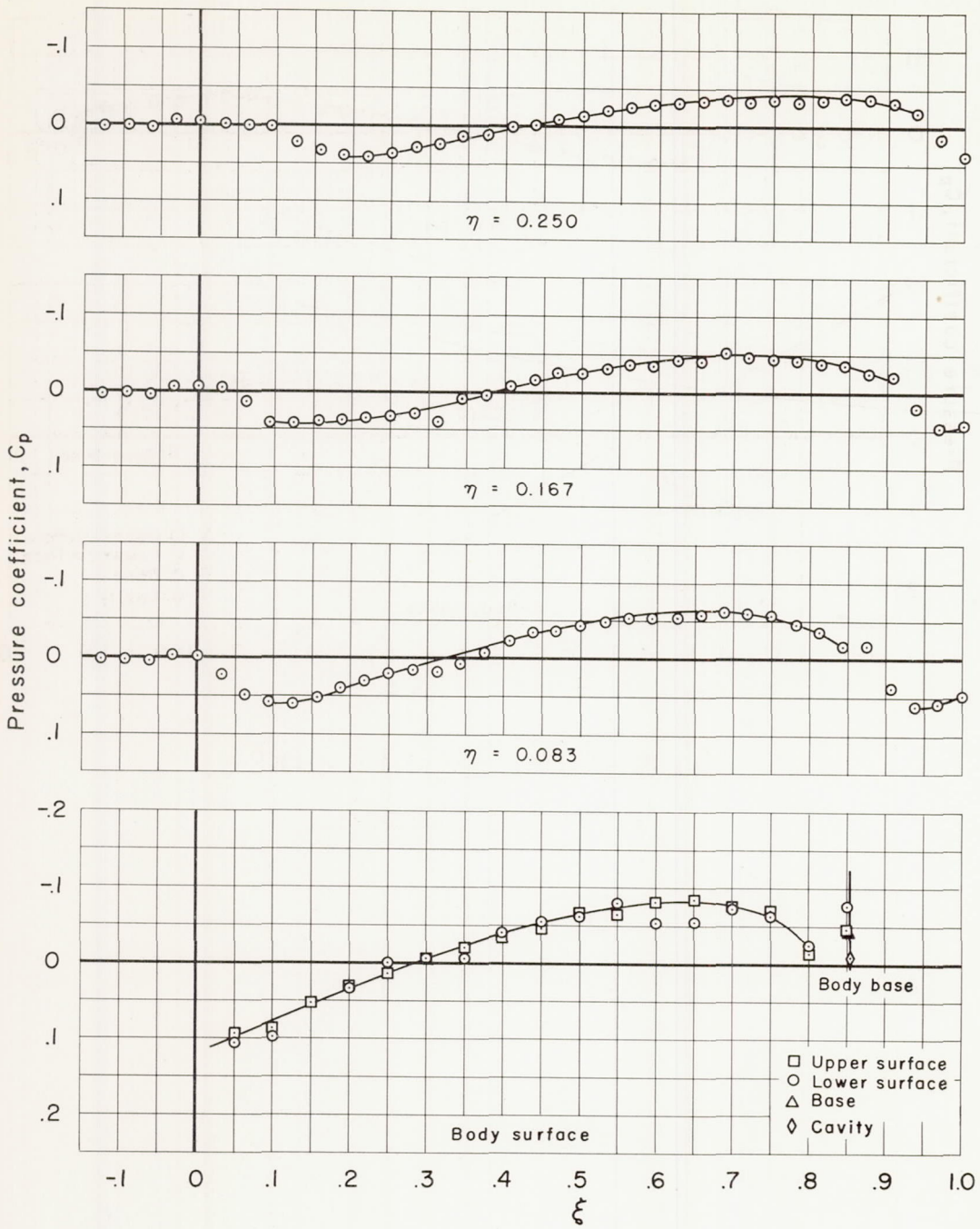

(t) $M_\infty = 1.10$, $\lambda = 3.0$, $\theta = \pm 90^\circ$

Figure 10.- Continued.

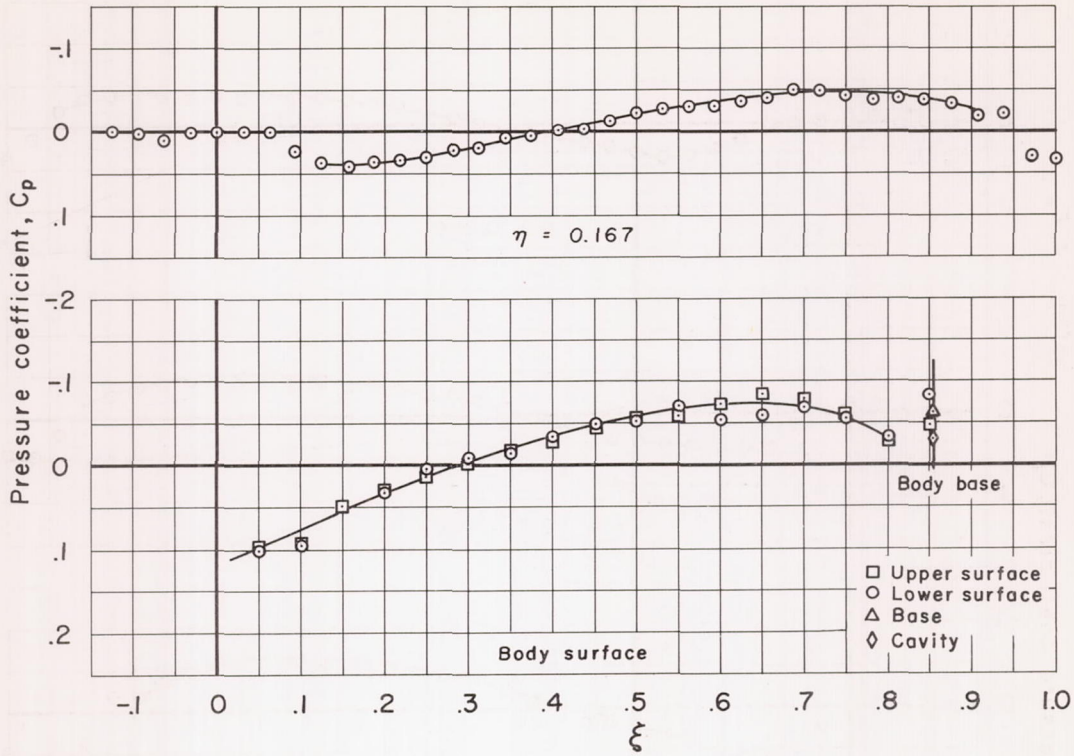

(u) $M_\infty = 1.15$, $\lambda = 3.0$, $\theta = \pm 90^\circ$

Figure 10.- Continued.

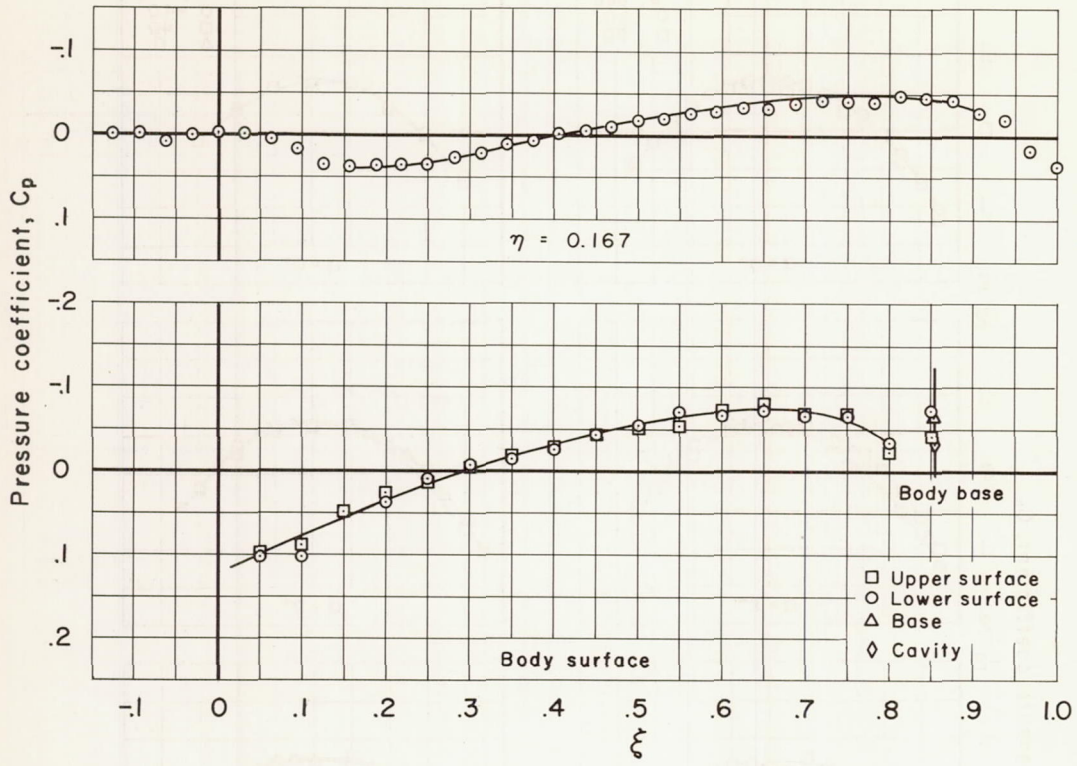

(v) $M_\infty = 1.20$, $\lambda = 3.0$, $\theta = \pm 90^\circ$

Figure 10.- Concluded.

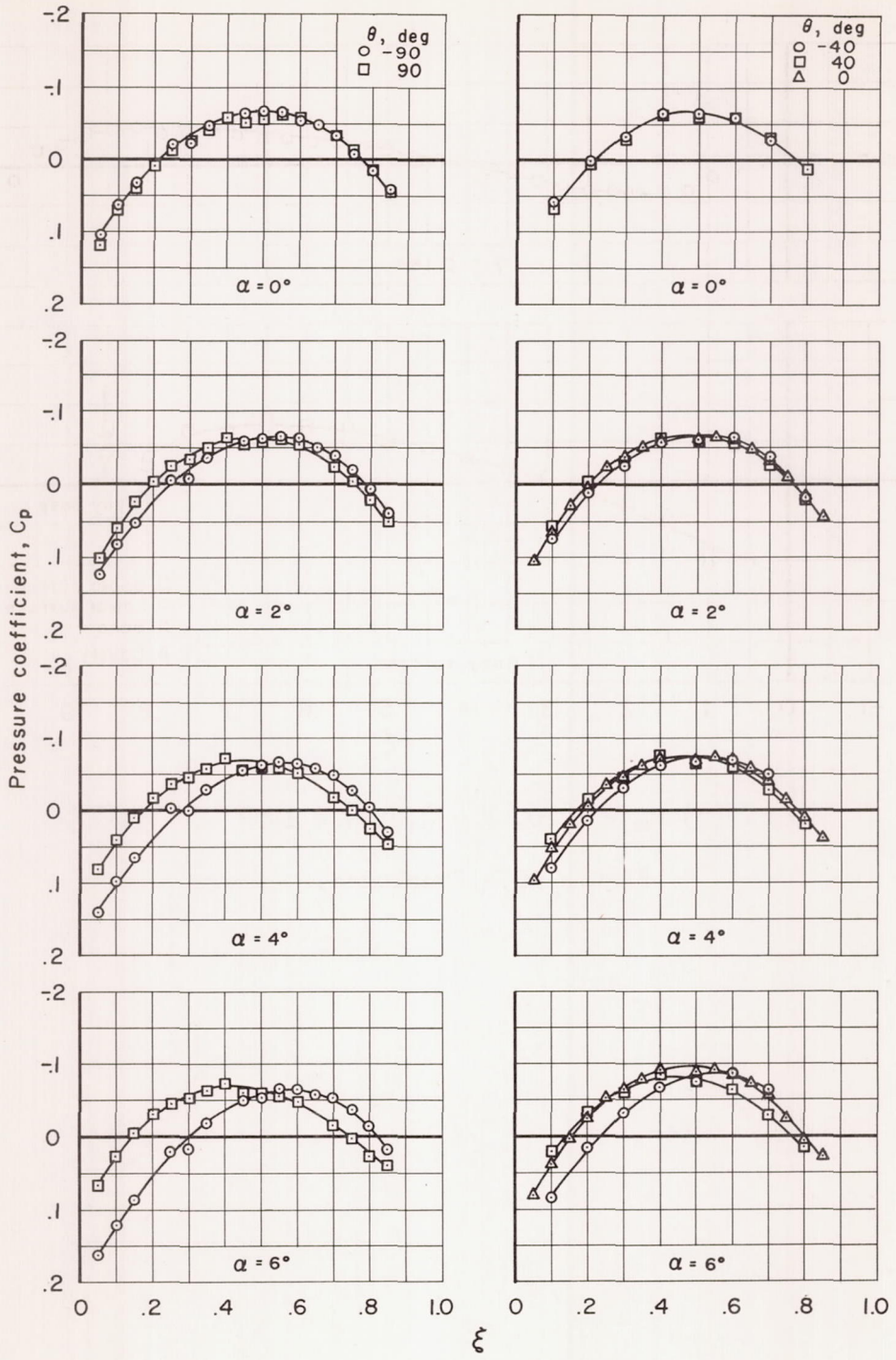

(a) $M_\infty = 0.90$, $\lambda = 1.0$

Figure 11.- Measured pressure distributions at angle of attack for the body having an axis ratio of 1.0.

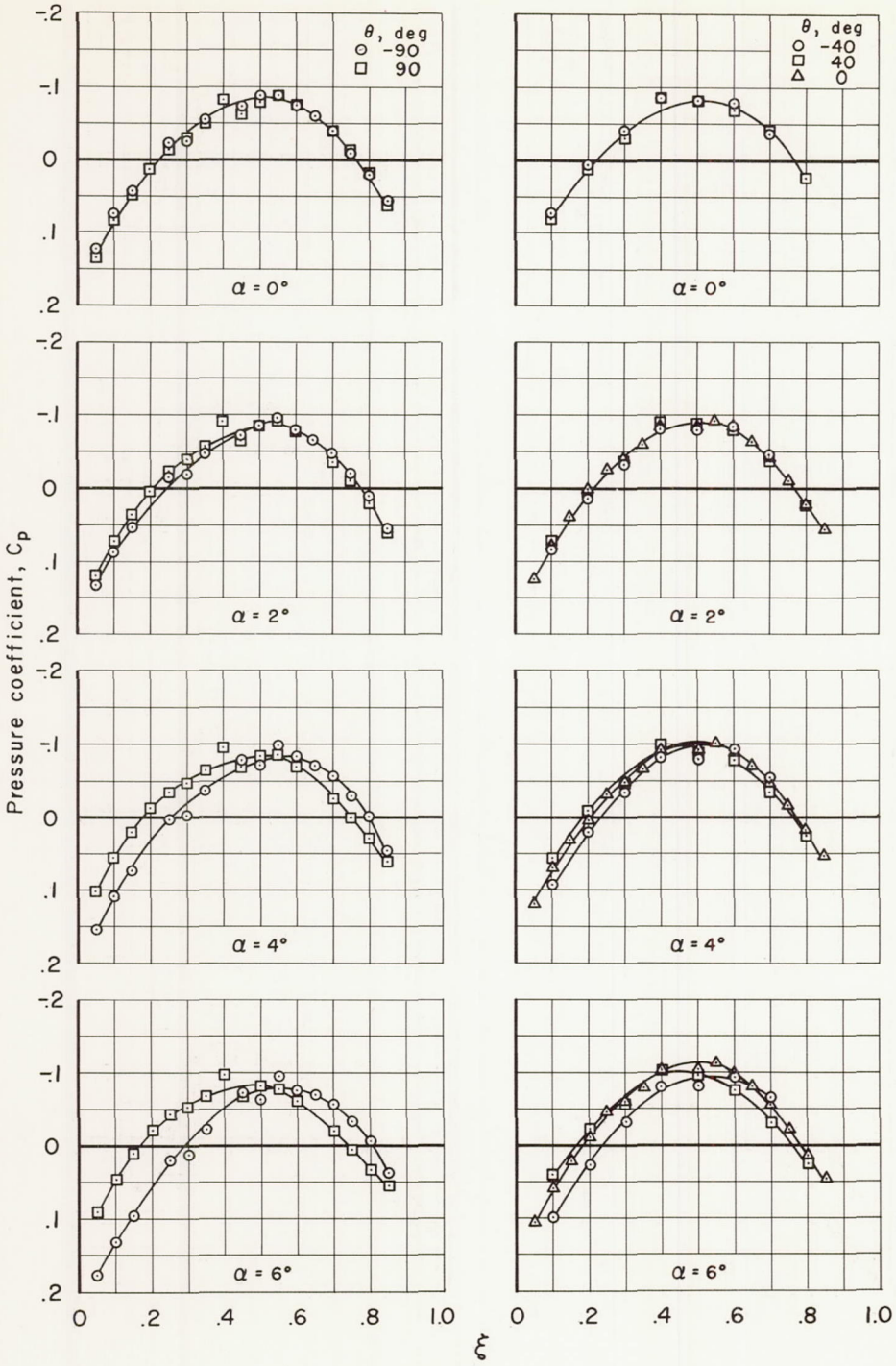

(b) $M_\infty = 0.975$, $\lambda = 1.0$

Figure 11.- Continued.

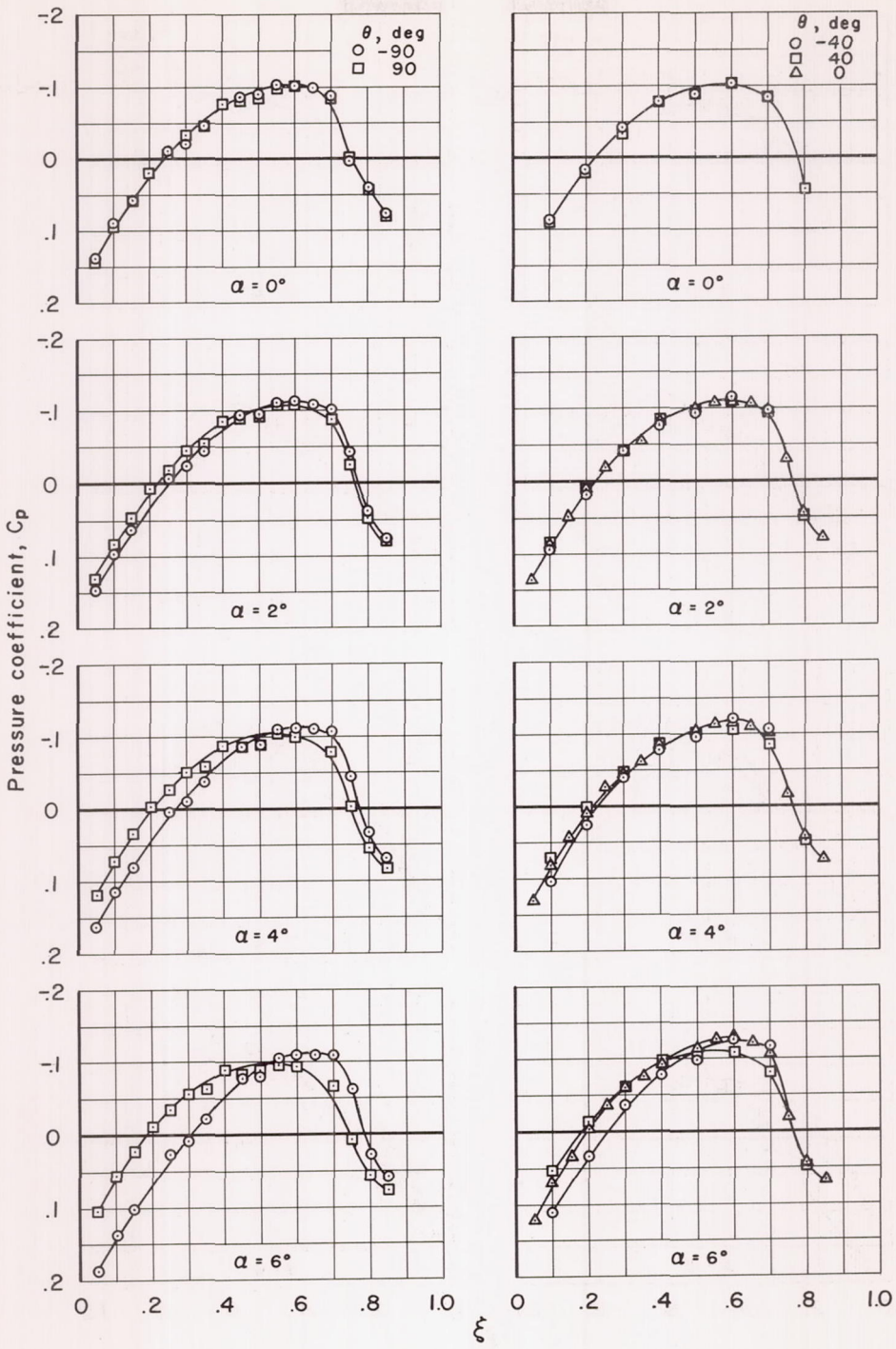

(c) $M_\infty = 1.00$, $\lambda = 1.0$

Figure 11.- Continued.

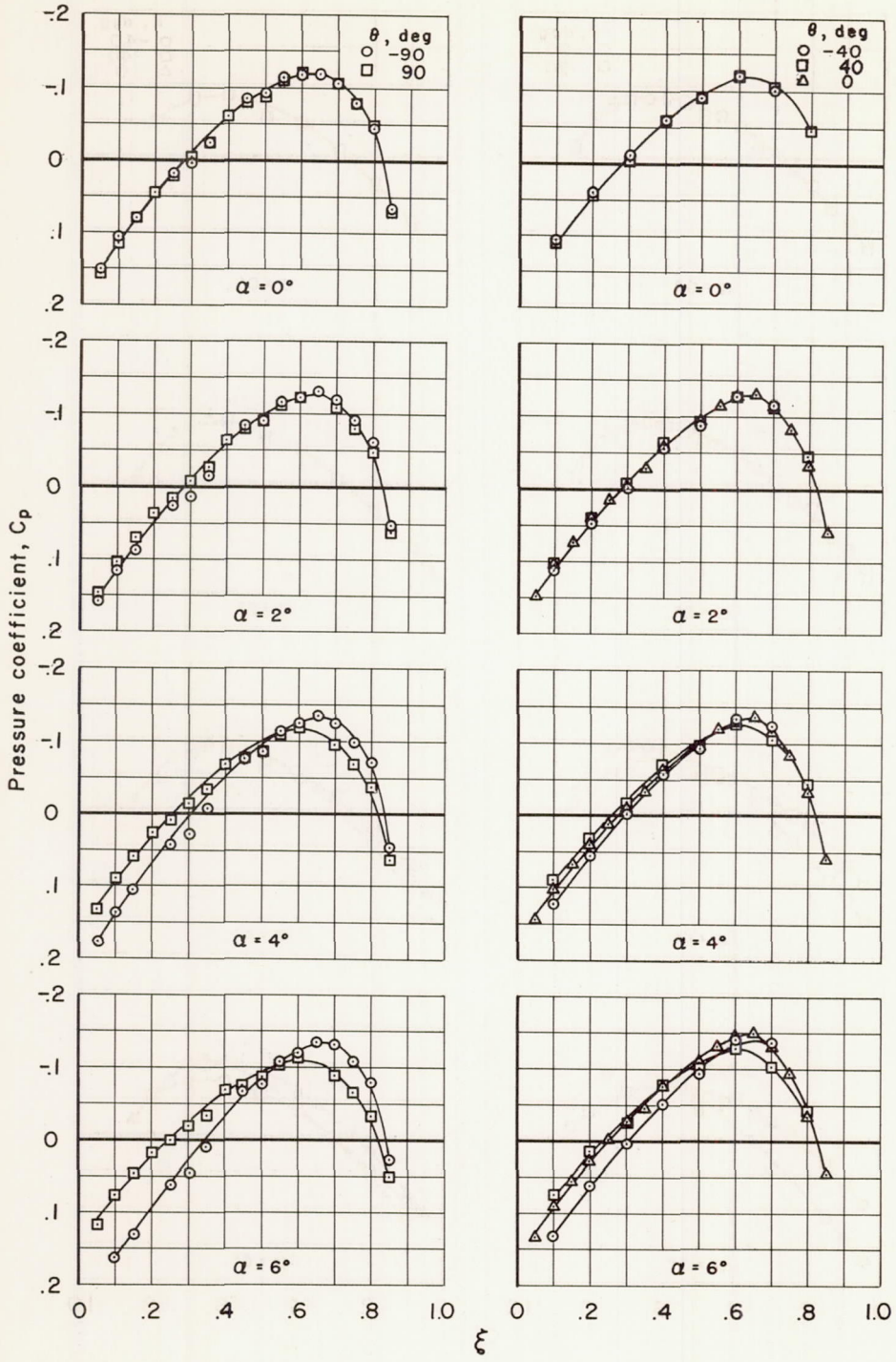

(d) $M_\infty = 1.025$, $\lambda = 1.0$

Figure 11.- Continued.

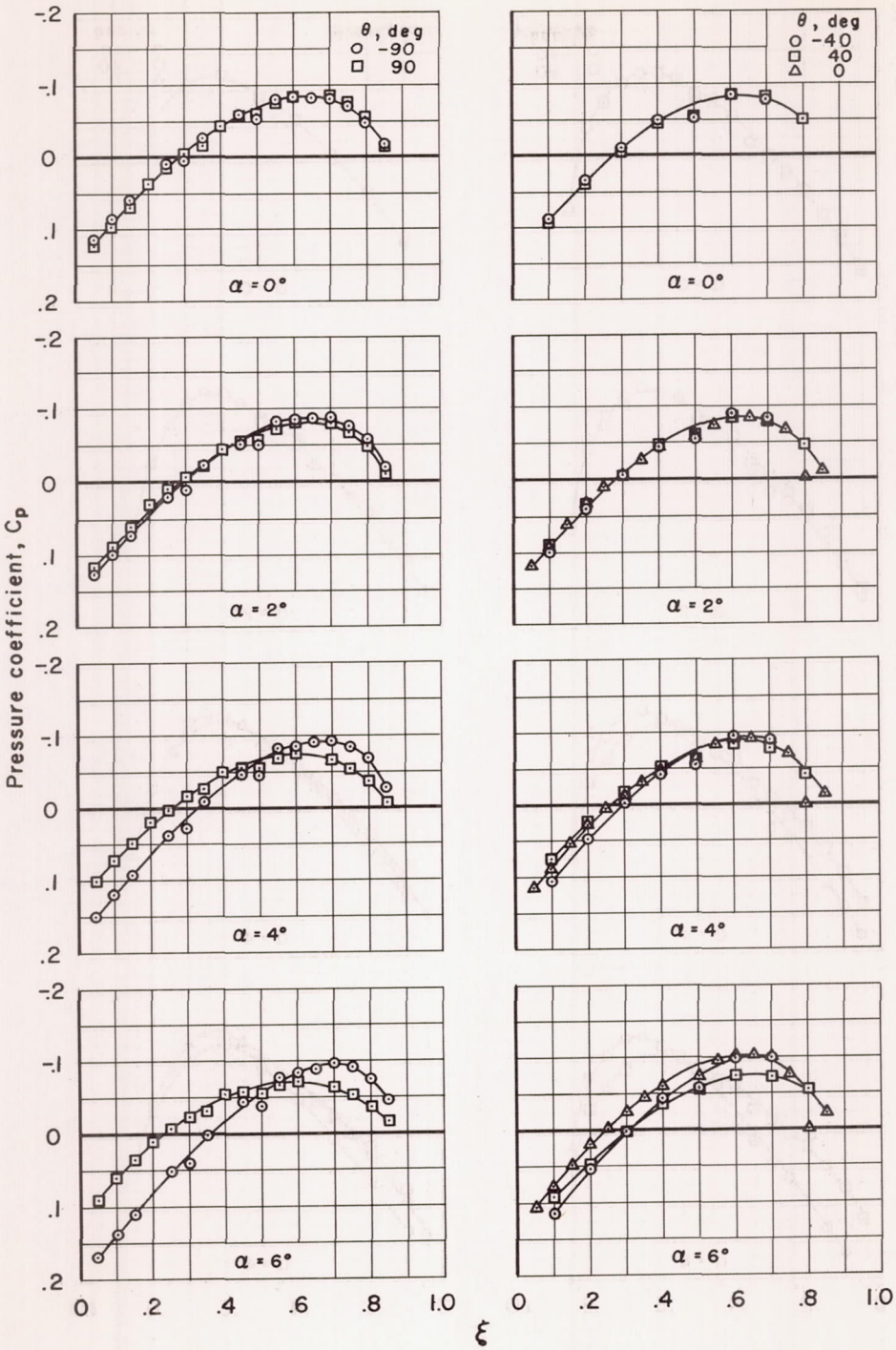

(e) $M_\infty = 1.10$, $\lambda = 1.0$

Figure 11.- Continued.

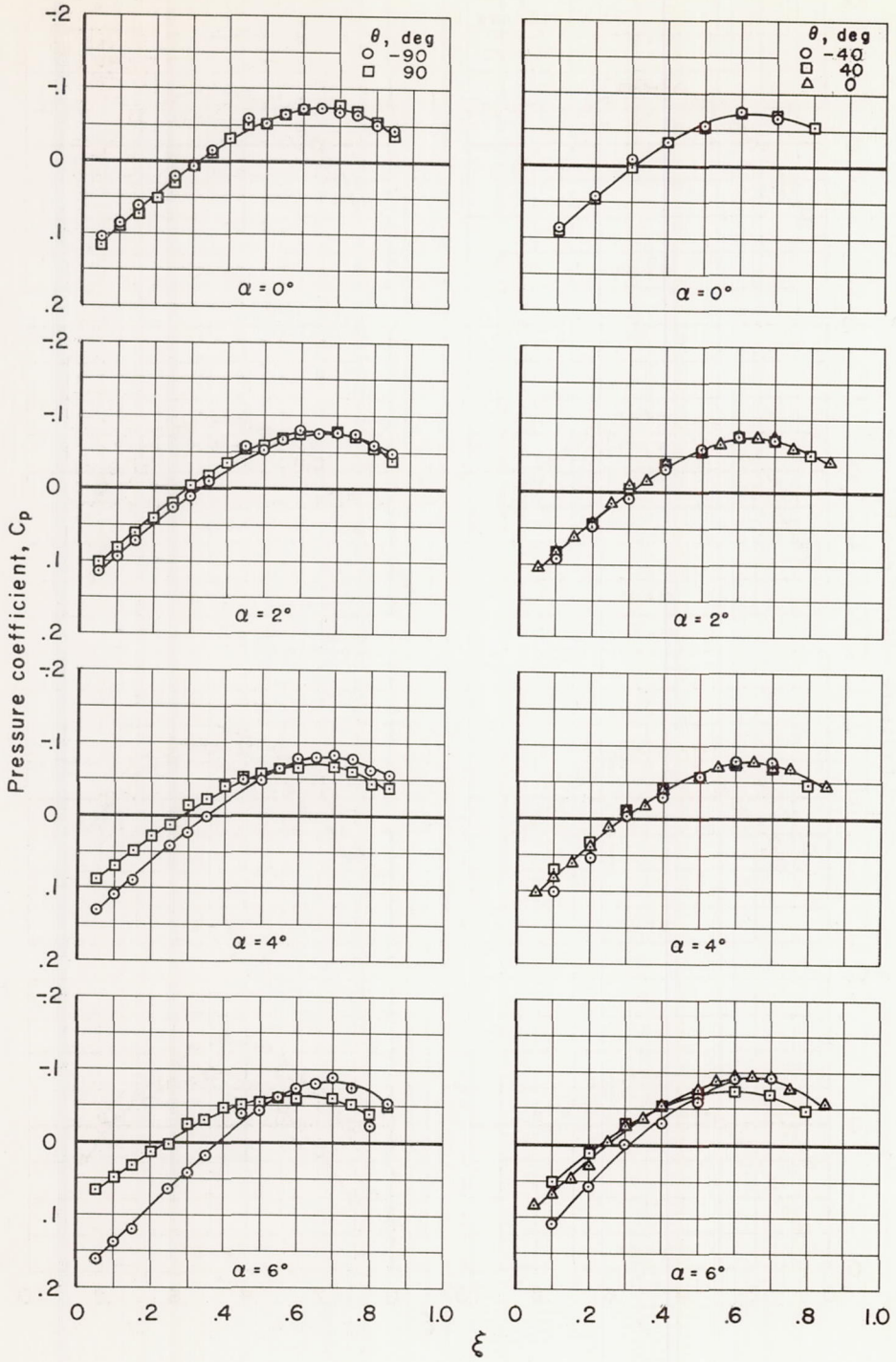

(f) $M_\infty = 1.20$, $\lambda = 1.0$

Figure 11.- Concluded.

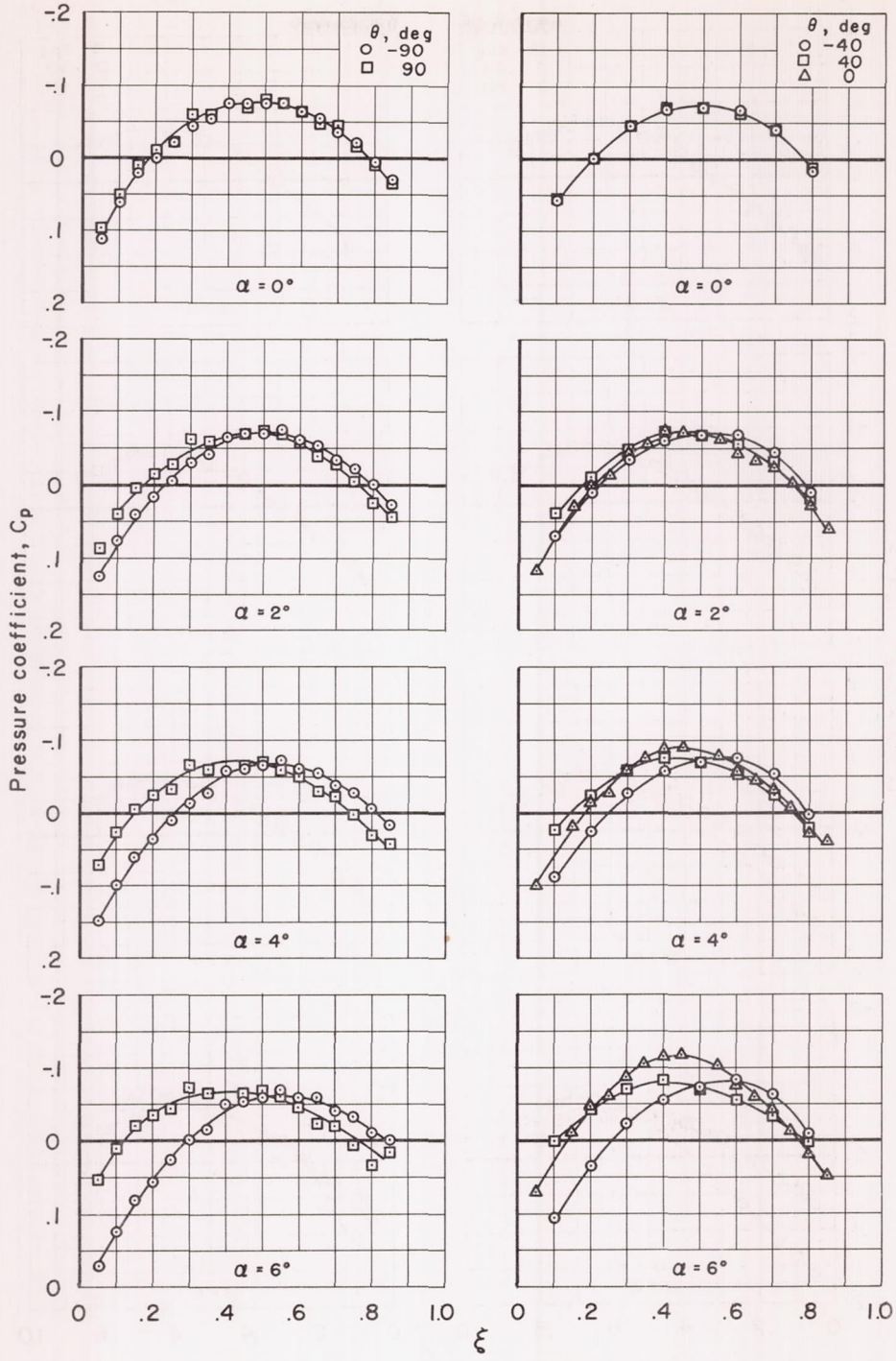

(a) $M_\infty = 0.90$, $\lambda = 1.5$

Figure 12.- Measured pressure distributions at angle of attack for the body having an axis ratio of 1.5.

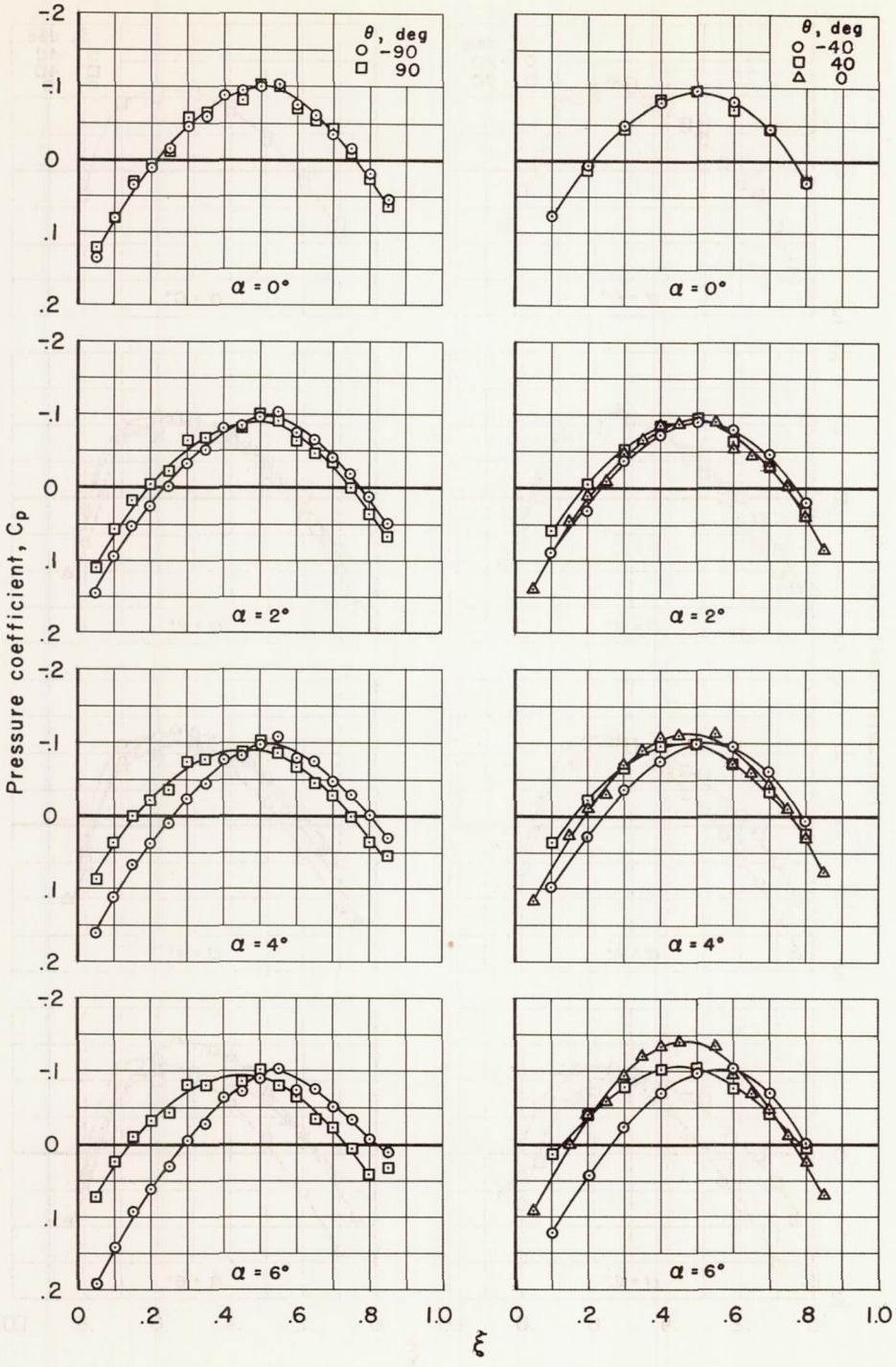

(b) $M_\infty = 0.975$, $\lambda = 1.5$

Figure 12.- Continued.

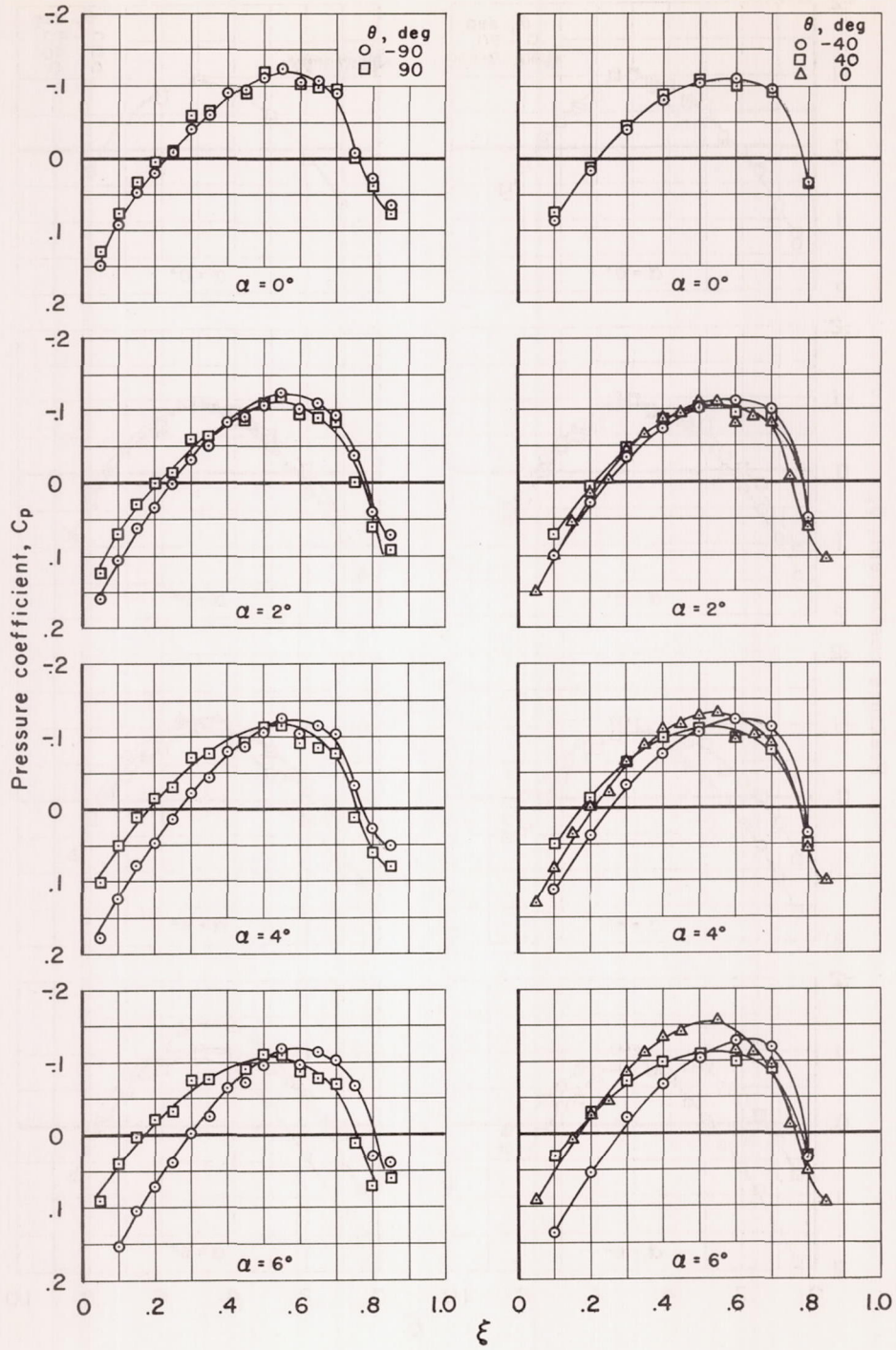

(c) $M_\infty = 1.00$, $\lambda = 1.5$

Figure 12.- Continued.

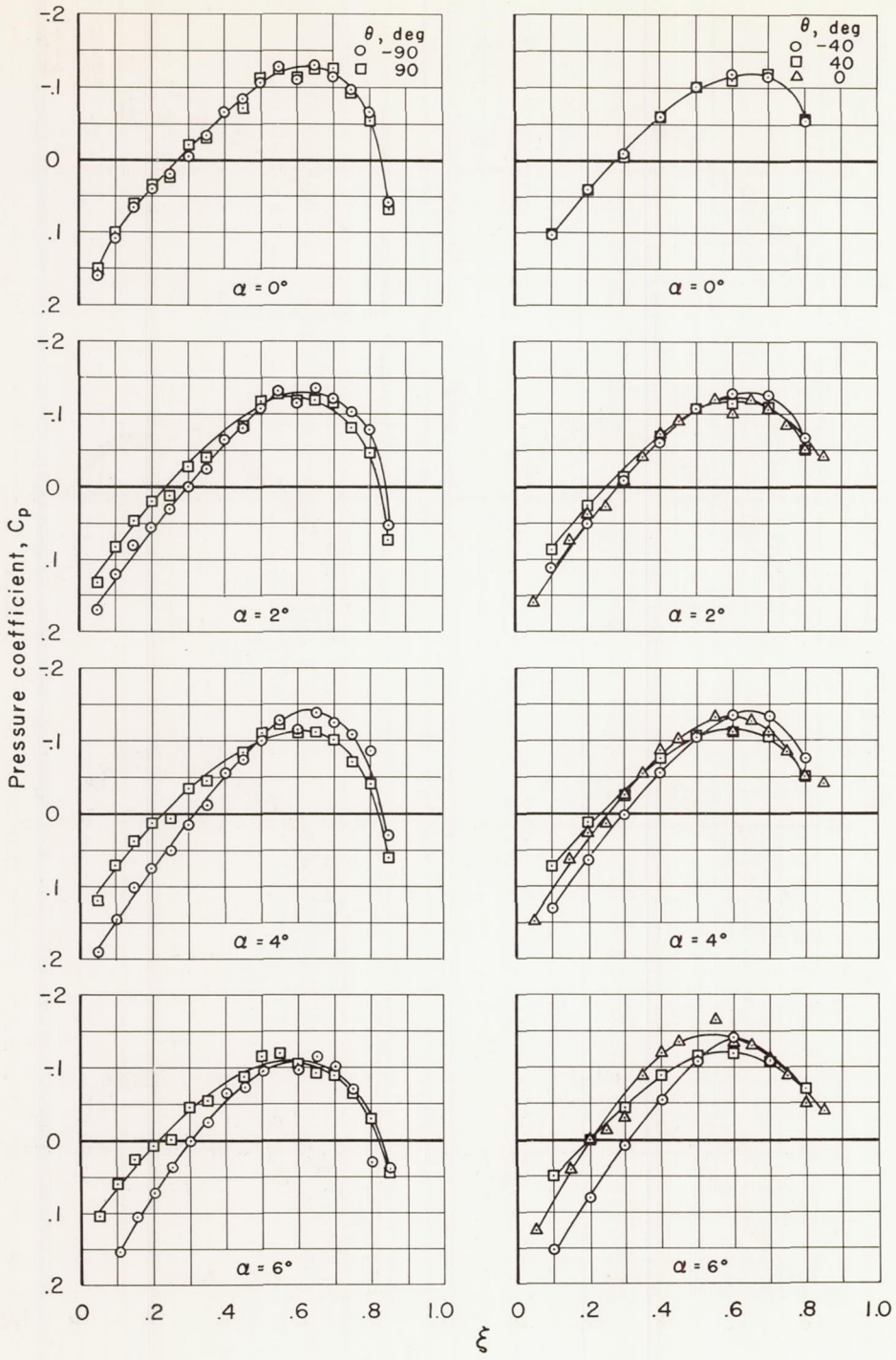

(d) $M_\infty = 1.025$, $\lambda = 1.5$

Figure 12.- Continued.

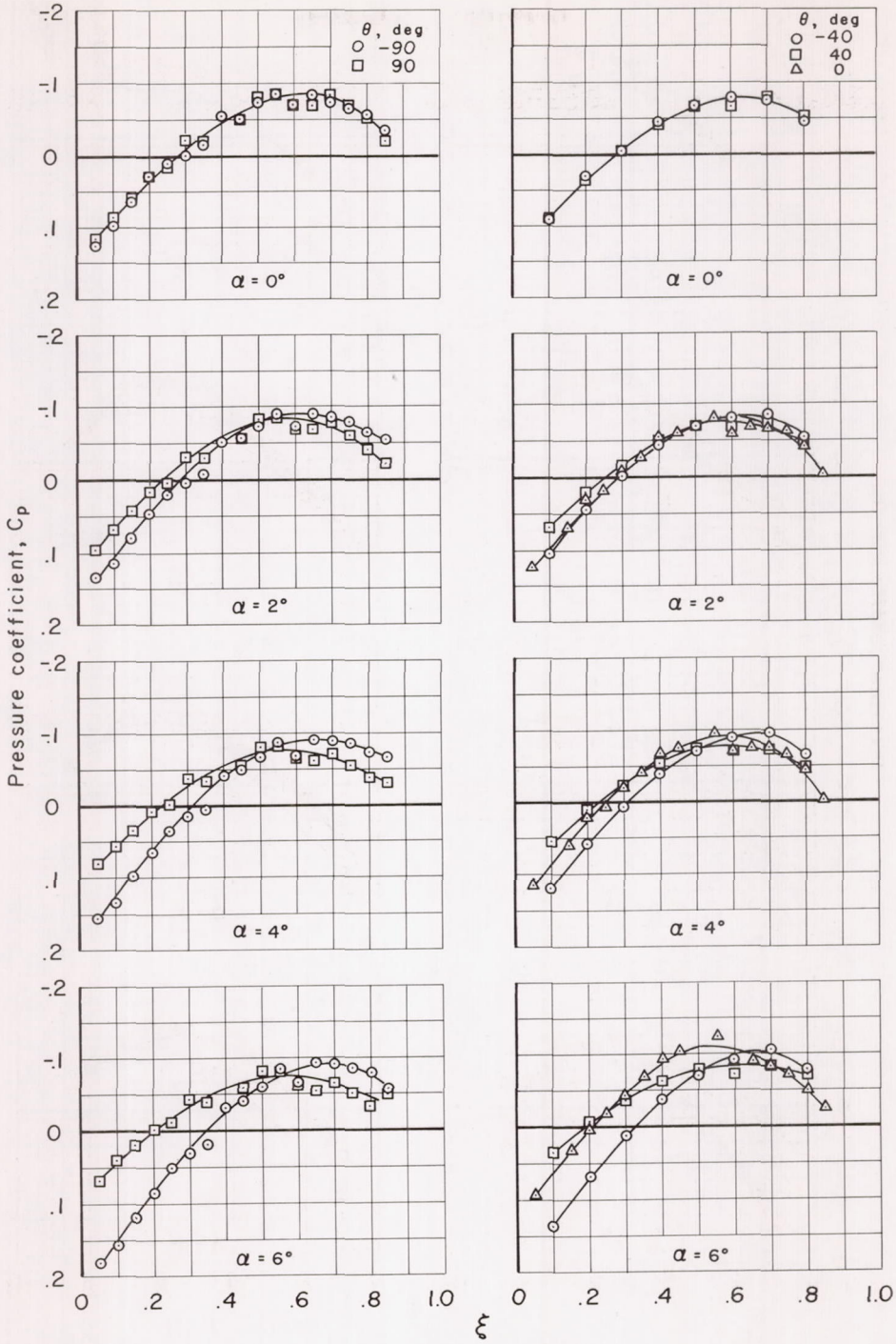

(e) $M_\infty = 1.10$, $\lambda = 1.5$

Figure 12.- Continued.

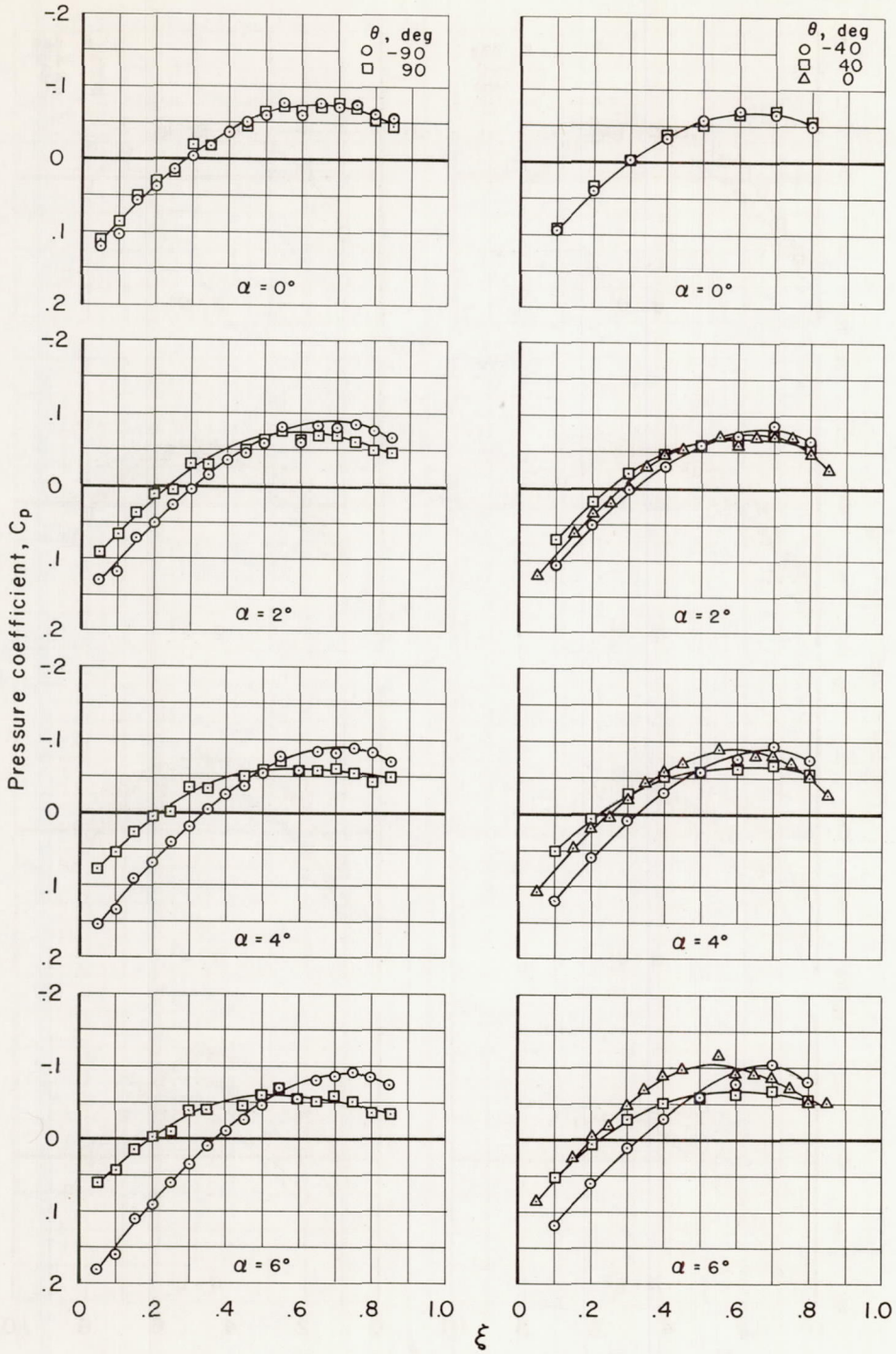

(f) $M_\infty = 1.20$, $\lambda = 1.5$

Figure 12.- Concluded.

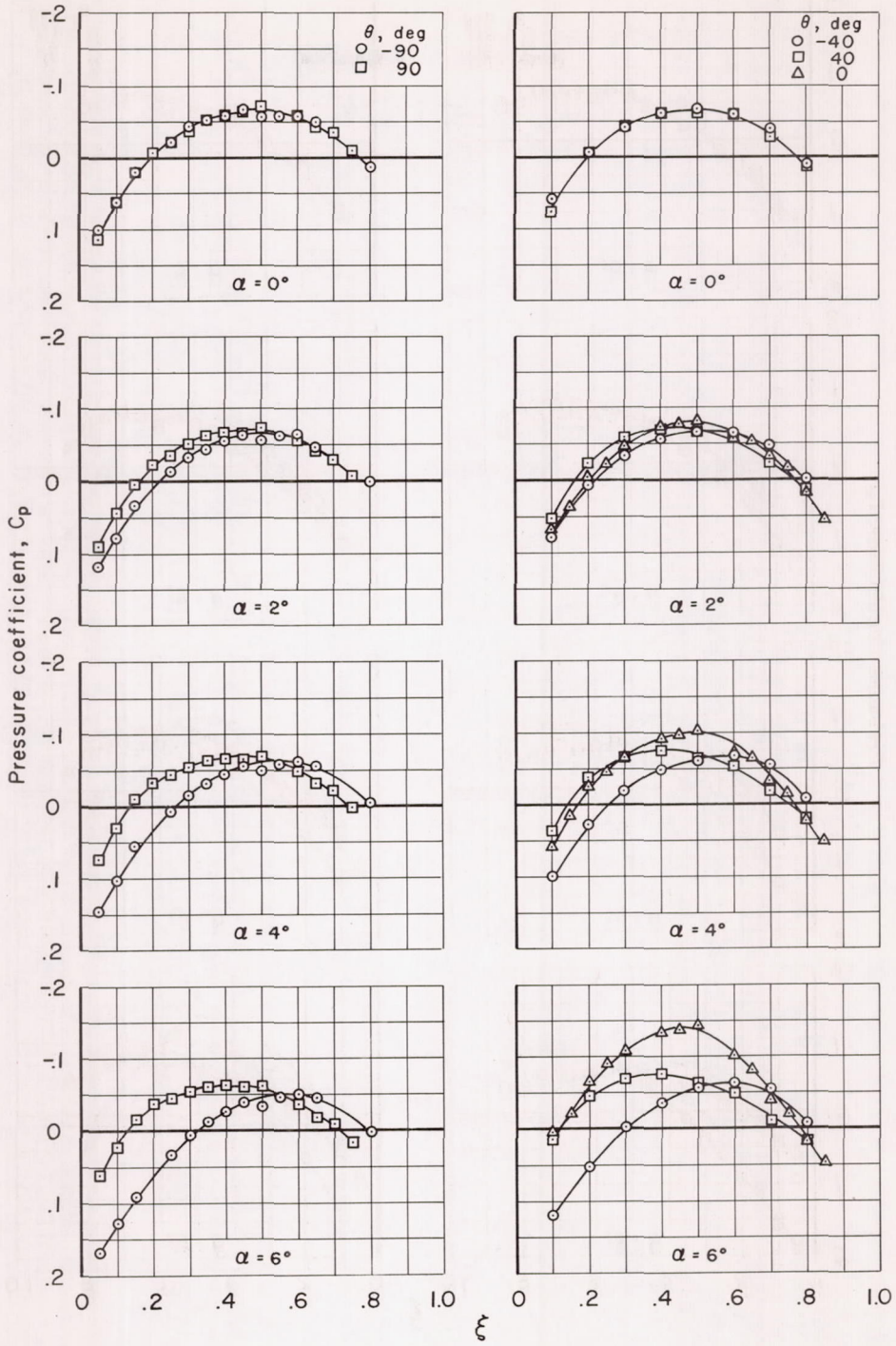

(a) $M_\infty = 0.90$, $\lambda = 2.0$

Figure 13.- Measured pressure distributions at angle of attack for the body having an axis ratio of 2.0.

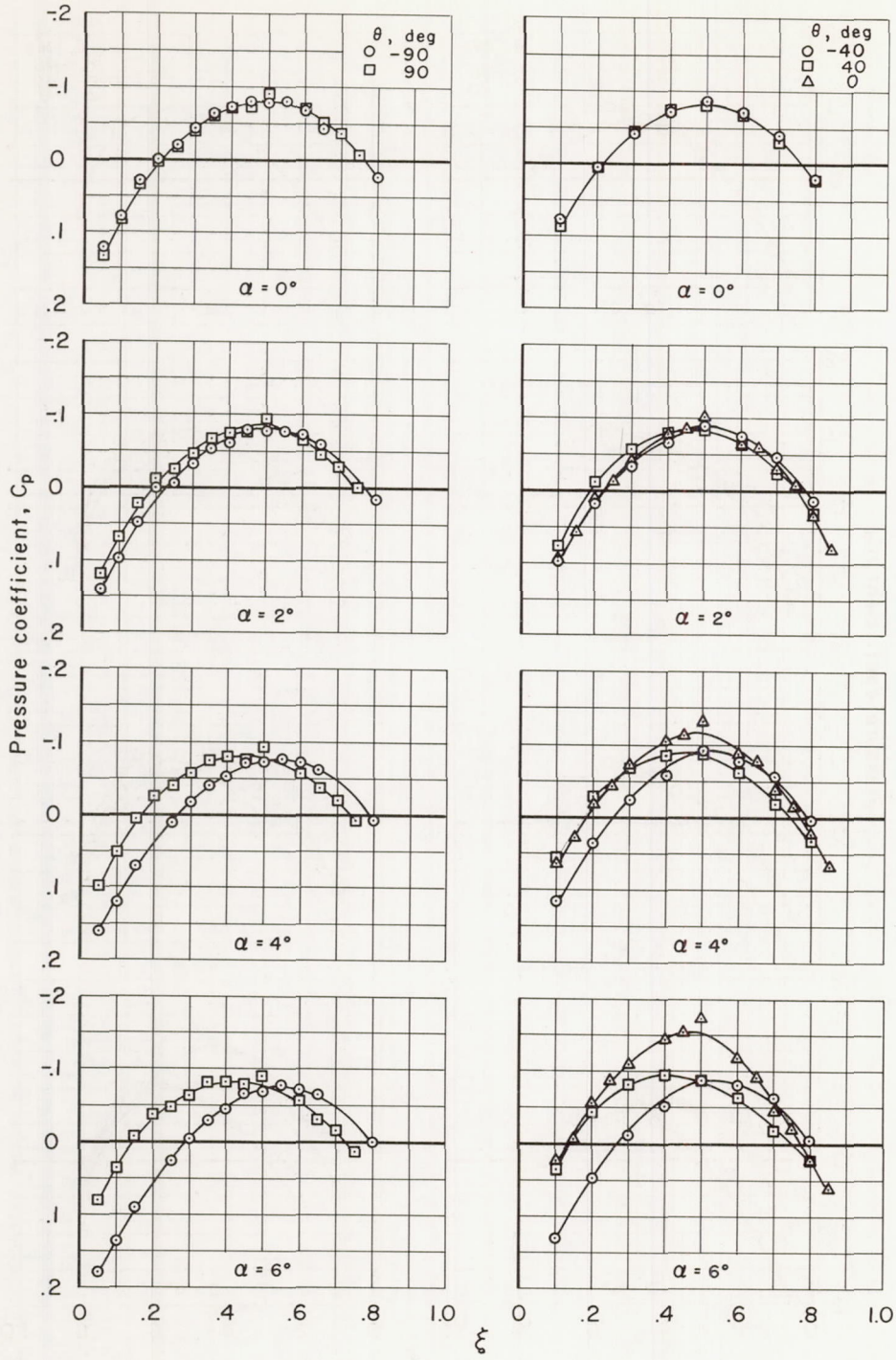

(b) $M_\infty = 0.975$, $\lambda = 2.0$

Figure 13.- Continued.

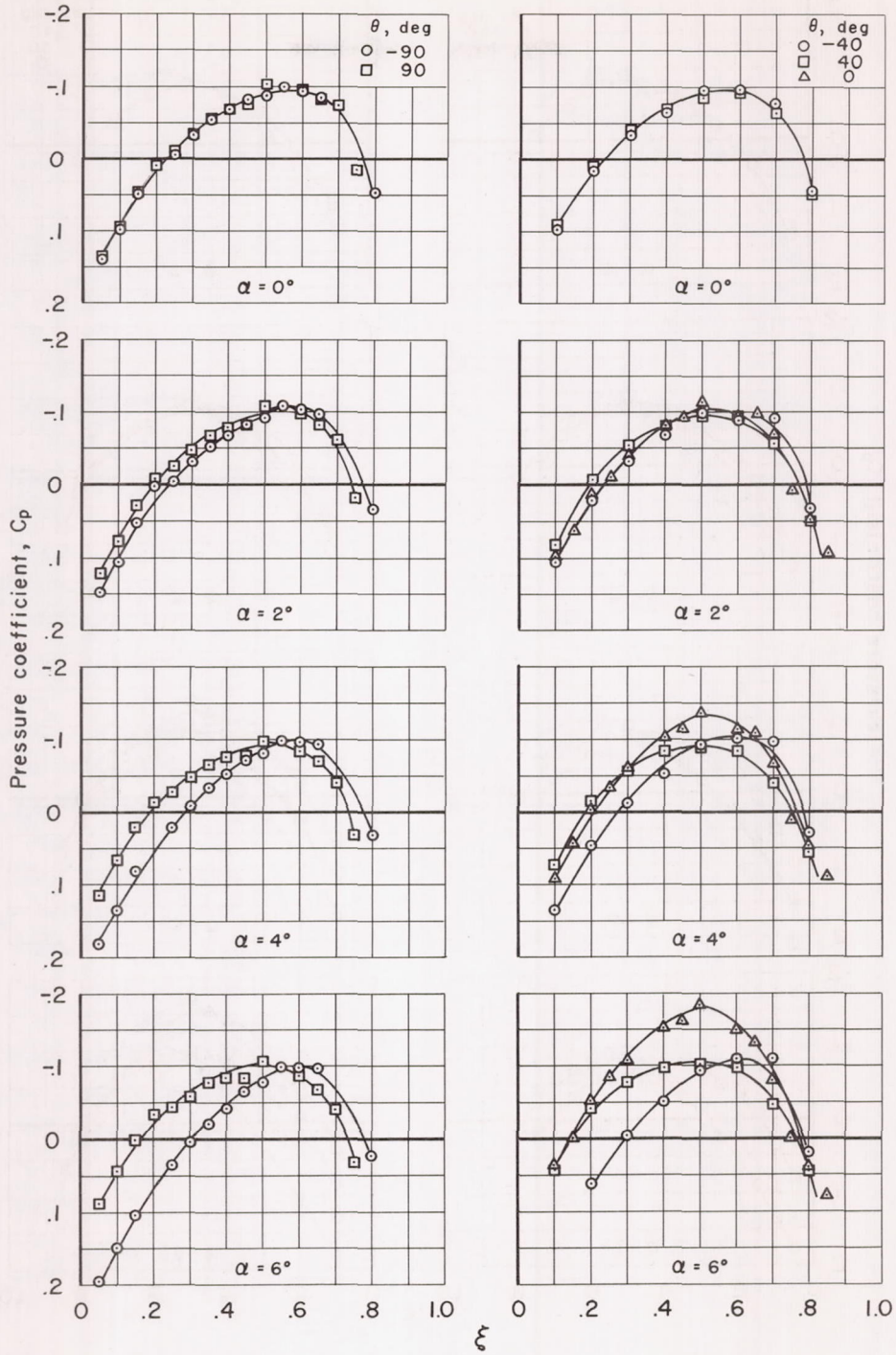

(c) $M_\infty = 1.00$, $\lambda = 2.0$

Figure 13.- Continued.

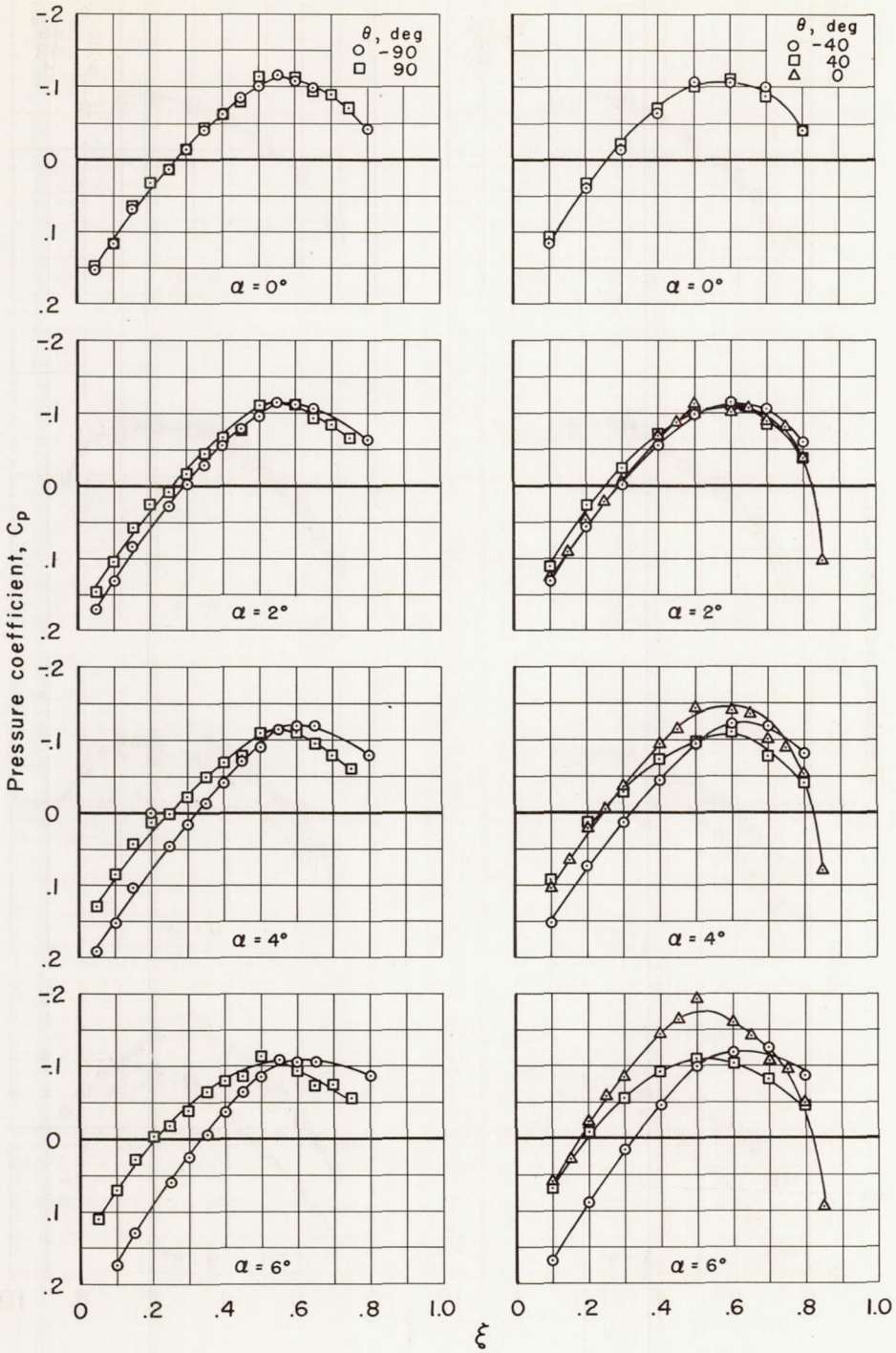

(d) $M_\infty = 1.025$, $\lambda = 2.0$

Figure 13.- Continued.

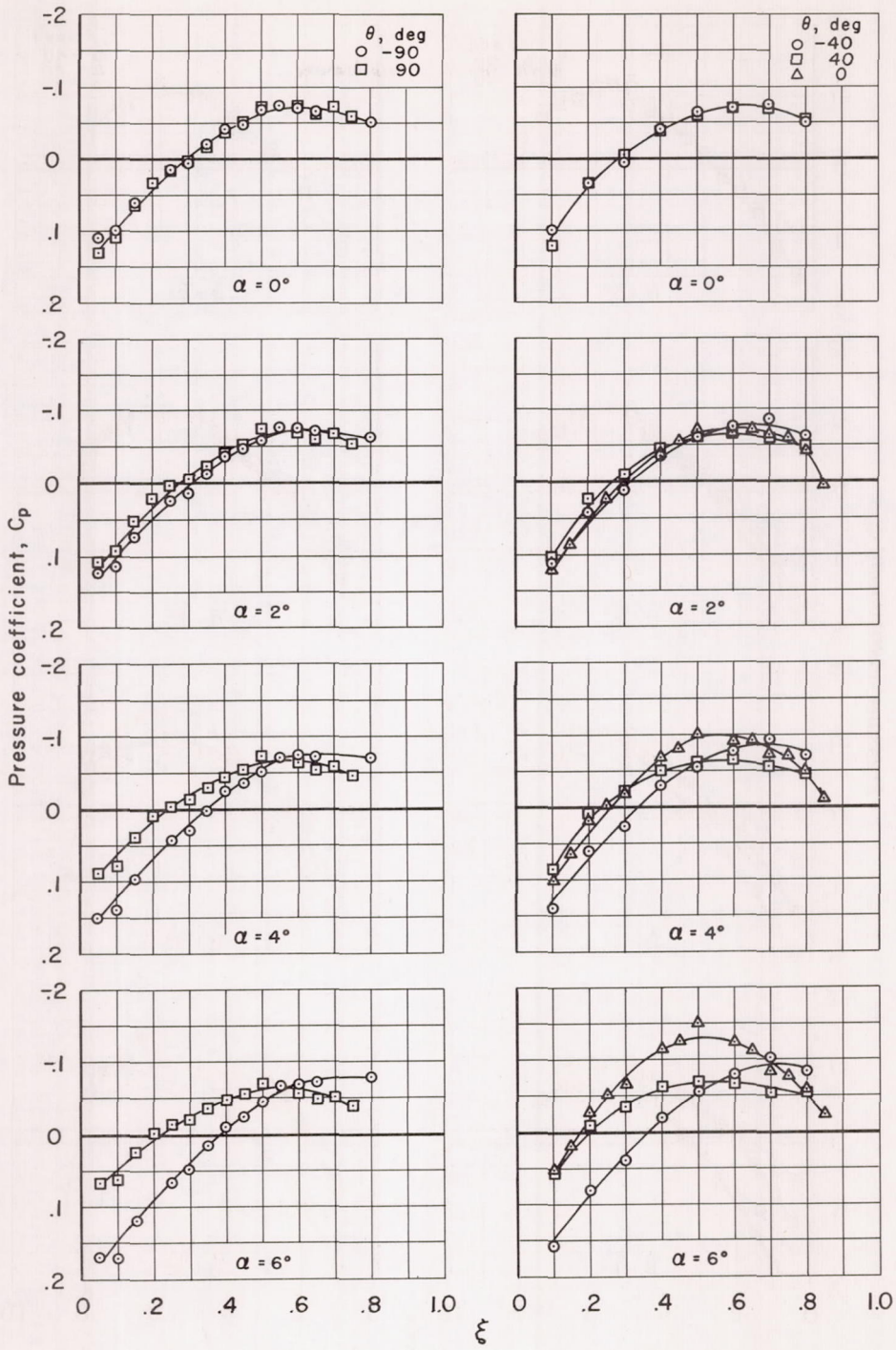

(e) $M_\infty = 1.10$, $\lambda = 2.0$

Figure 13.- Continued.

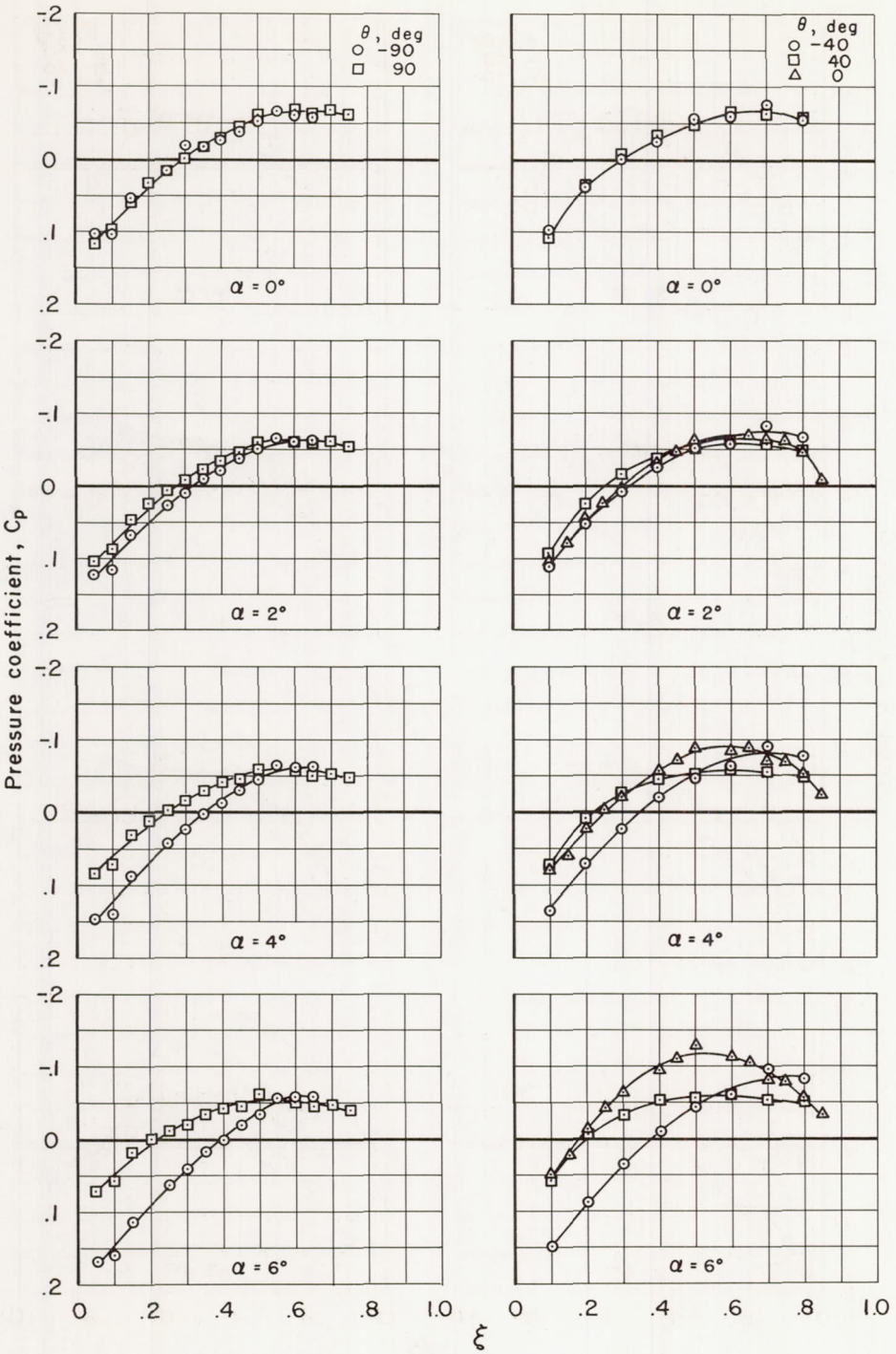

(f) $M_\infty = 1.20$, $\lambda = 2.0$

Figure 13.- Concluded.

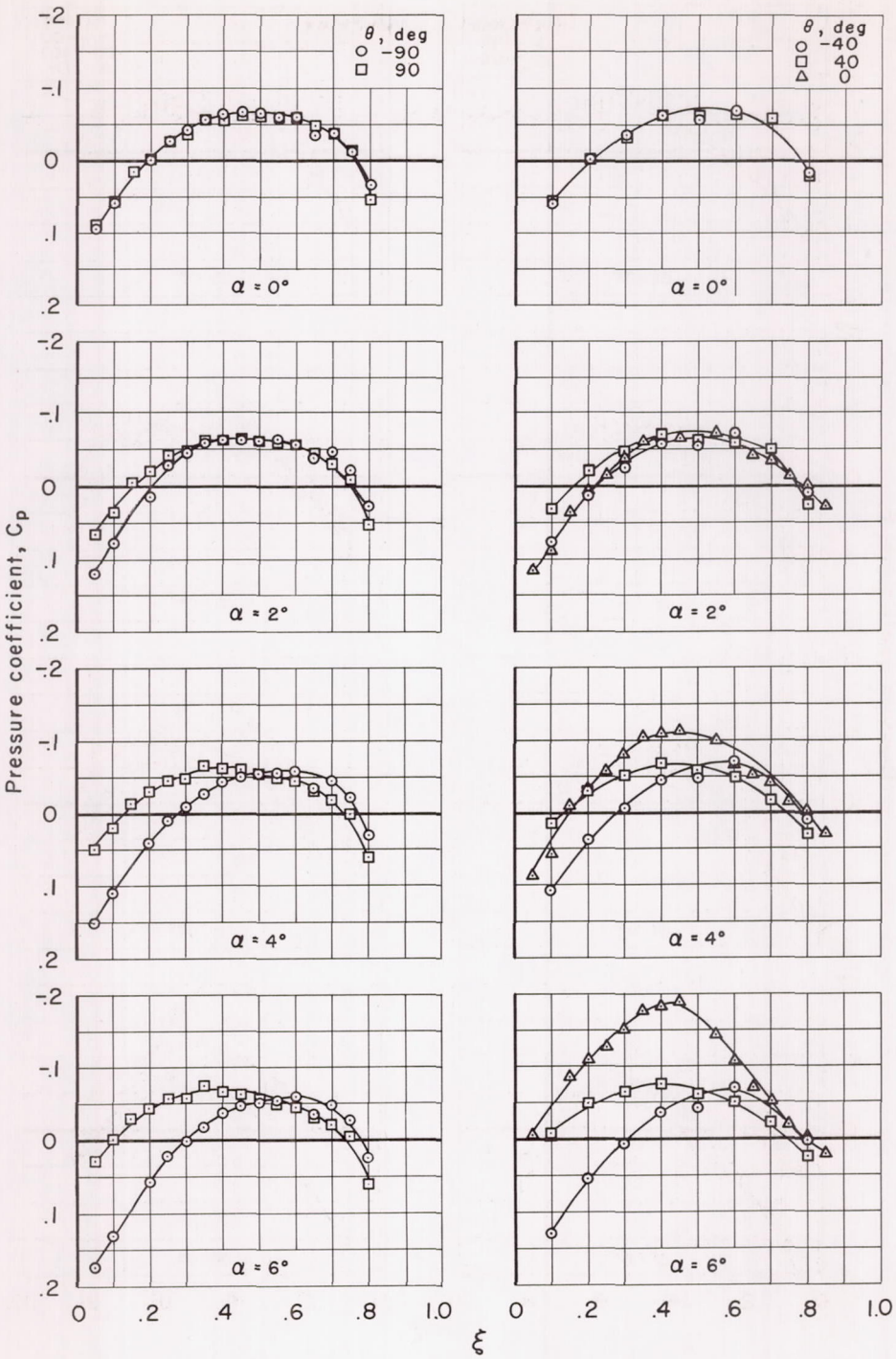

(a) $M_\infty = 0.90$, $\lambda = 3.0$

Figure 14.- Measured pressure distributions at angle of attack for the body having an axis ratio of 3.0.

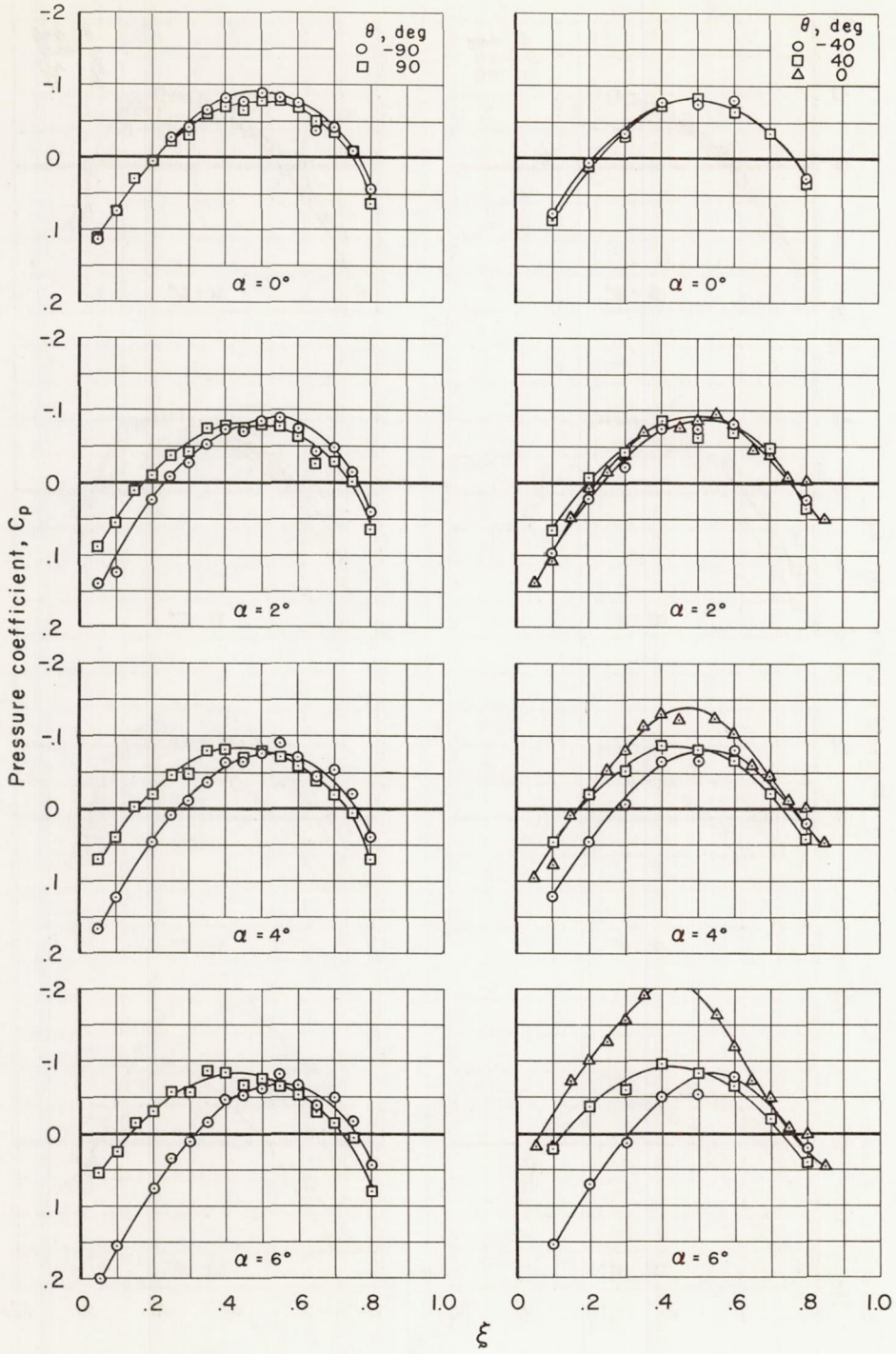

(b) $M_\infty = 0.975$, $\lambda = 3.0$

Figure 14.- Continued.

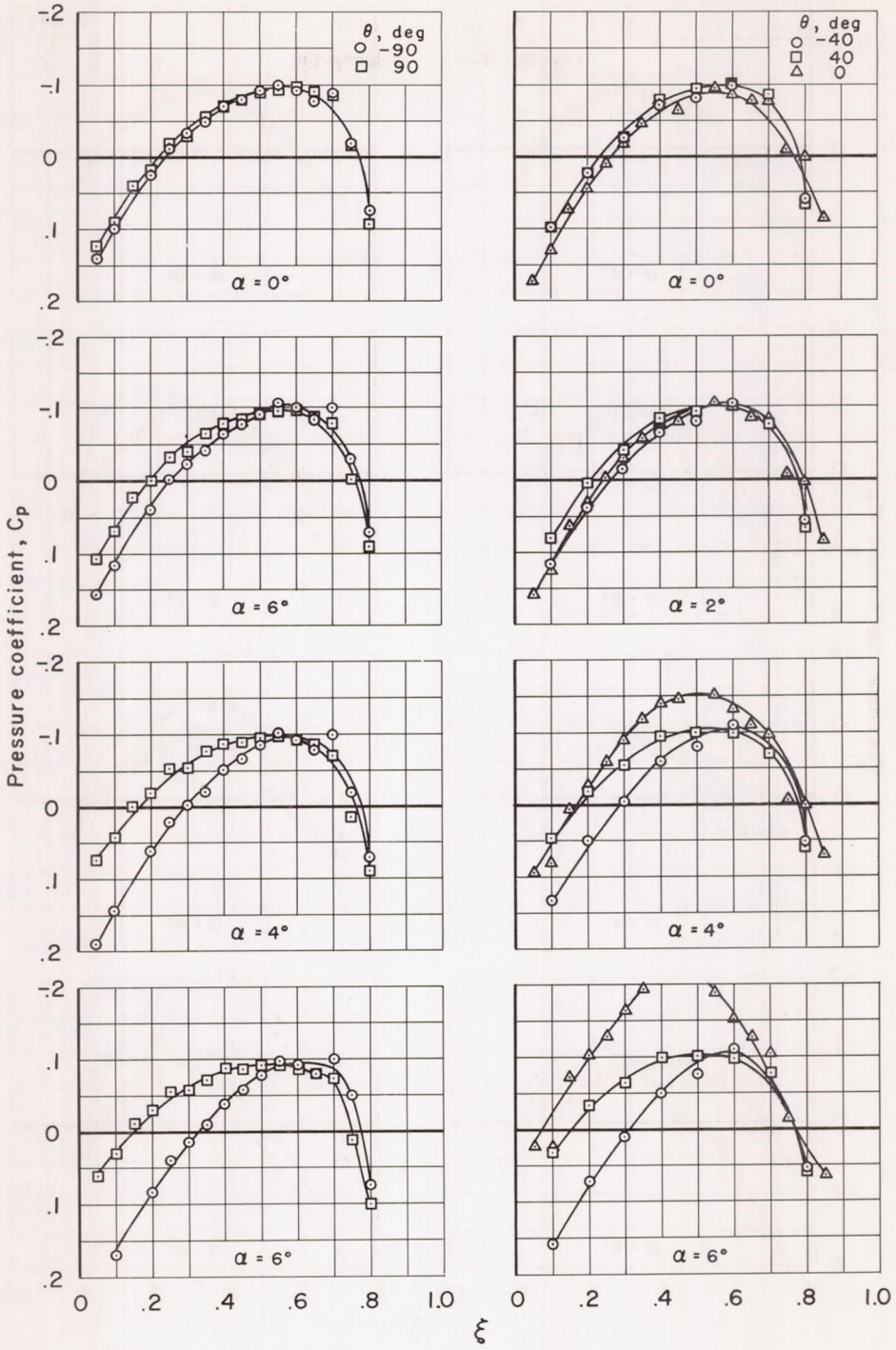

(c) $M_\infty = 1.00$, $\lambda = 3.0$

Figure 14.- Continued.

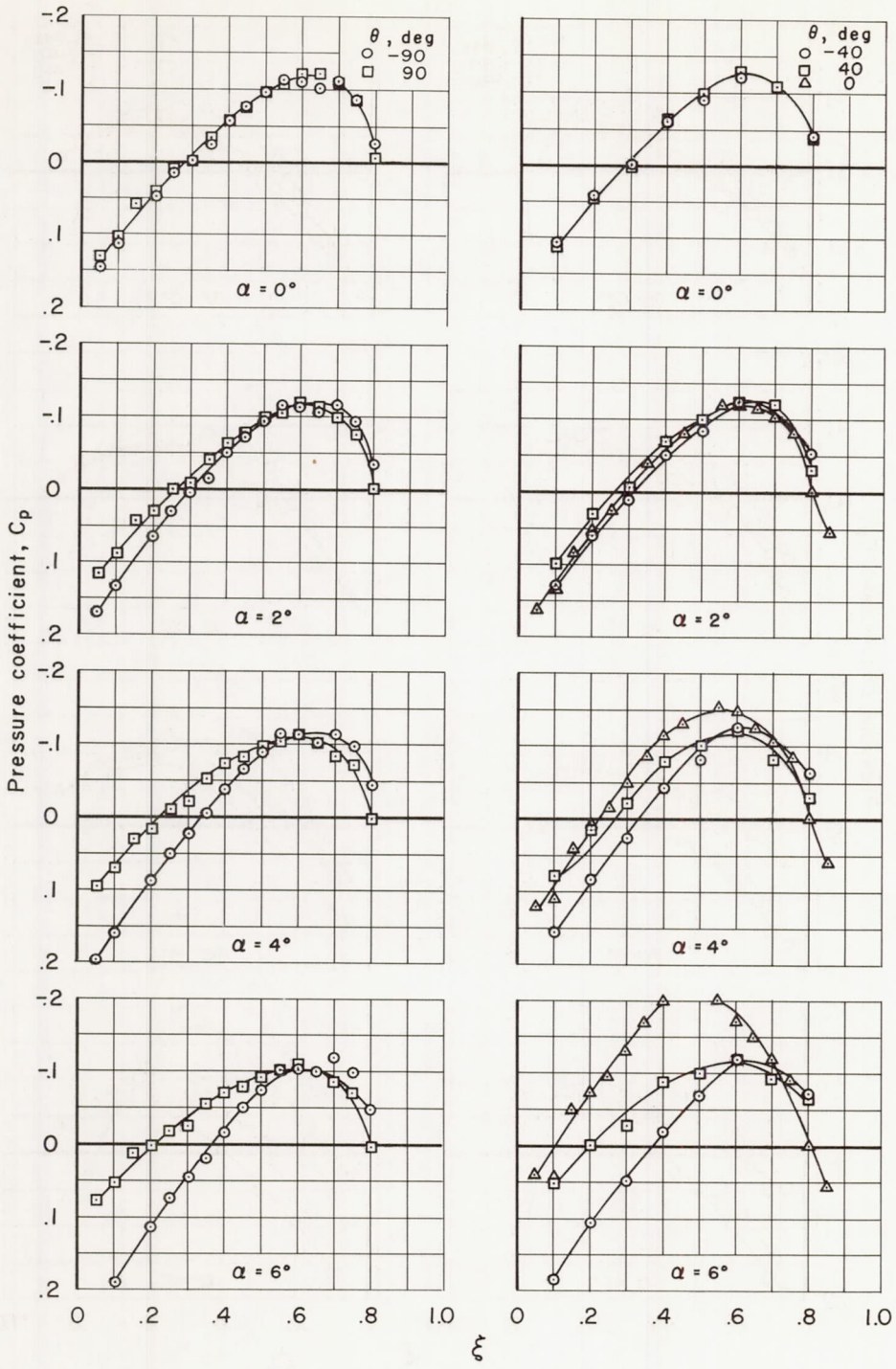

(d) $M_\infty = 1.025$, $\lambda = 3.0$

Figure 14.- Continued.

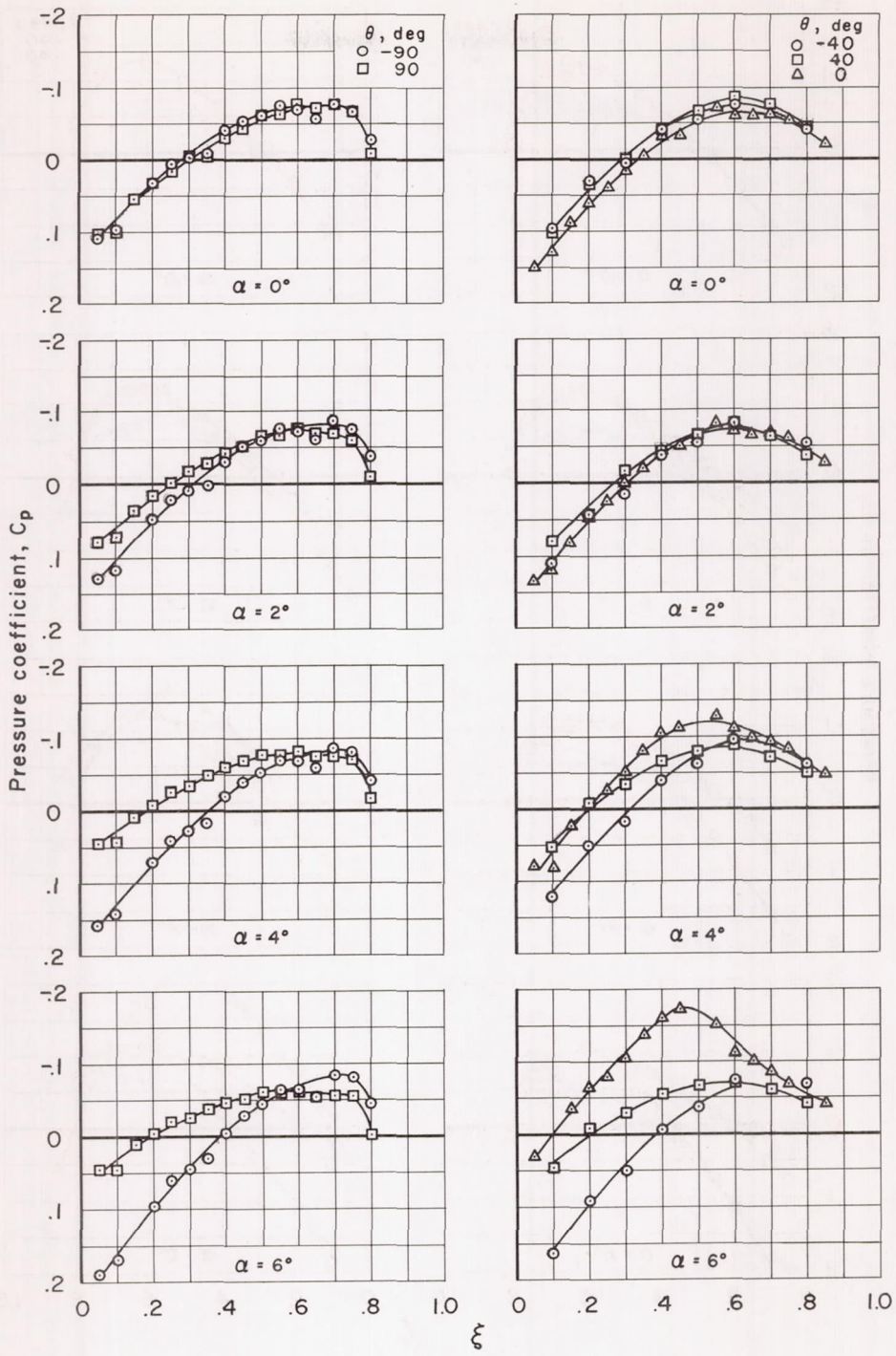

(e) $M_\infty = 1.10$, $\lambda = 3.0$

Figure 14.- Continued.

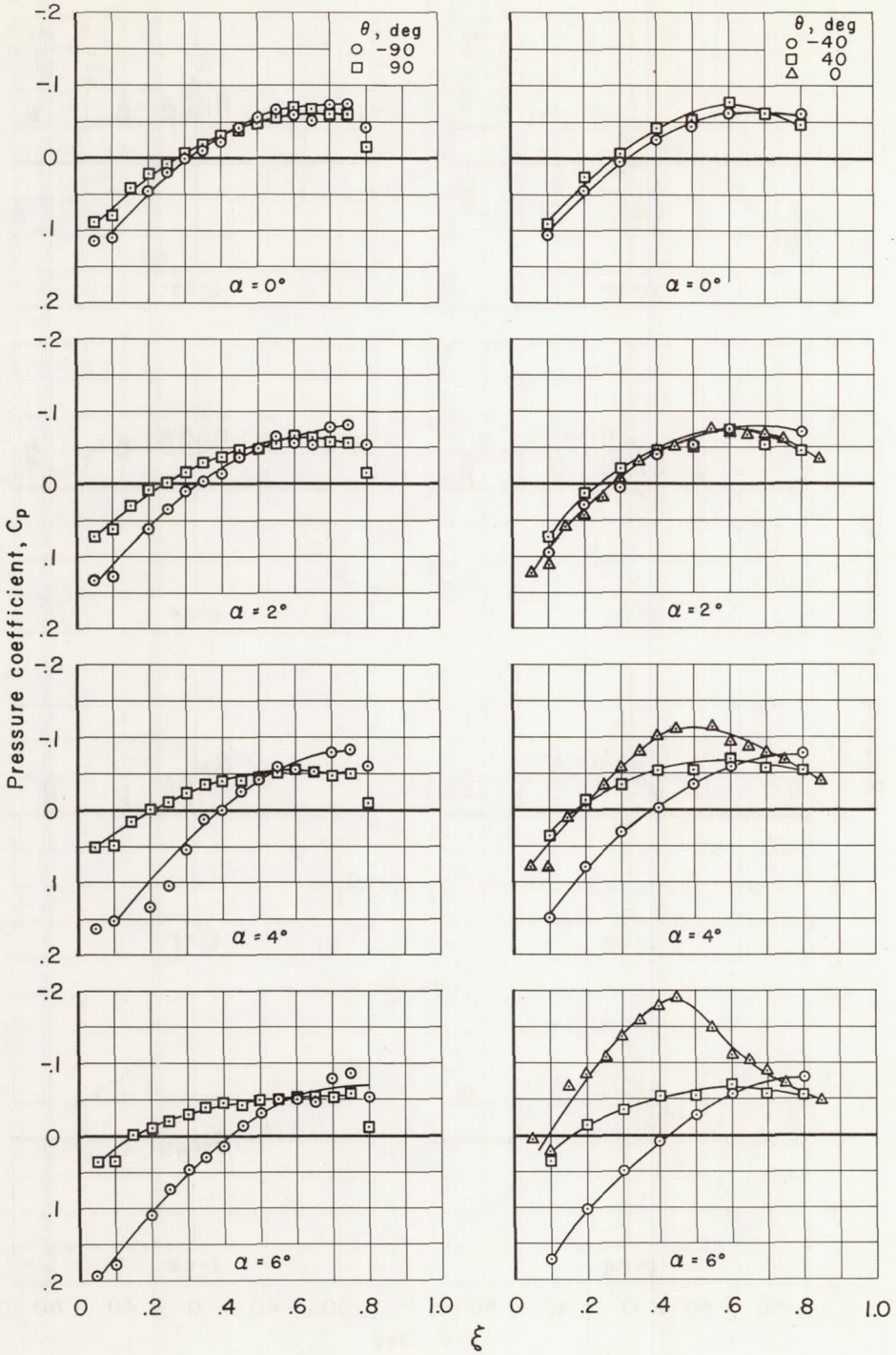

(f) $M_\infty = 1.20$, $\lambda = 3.0$

Figure 14.- Concluded.

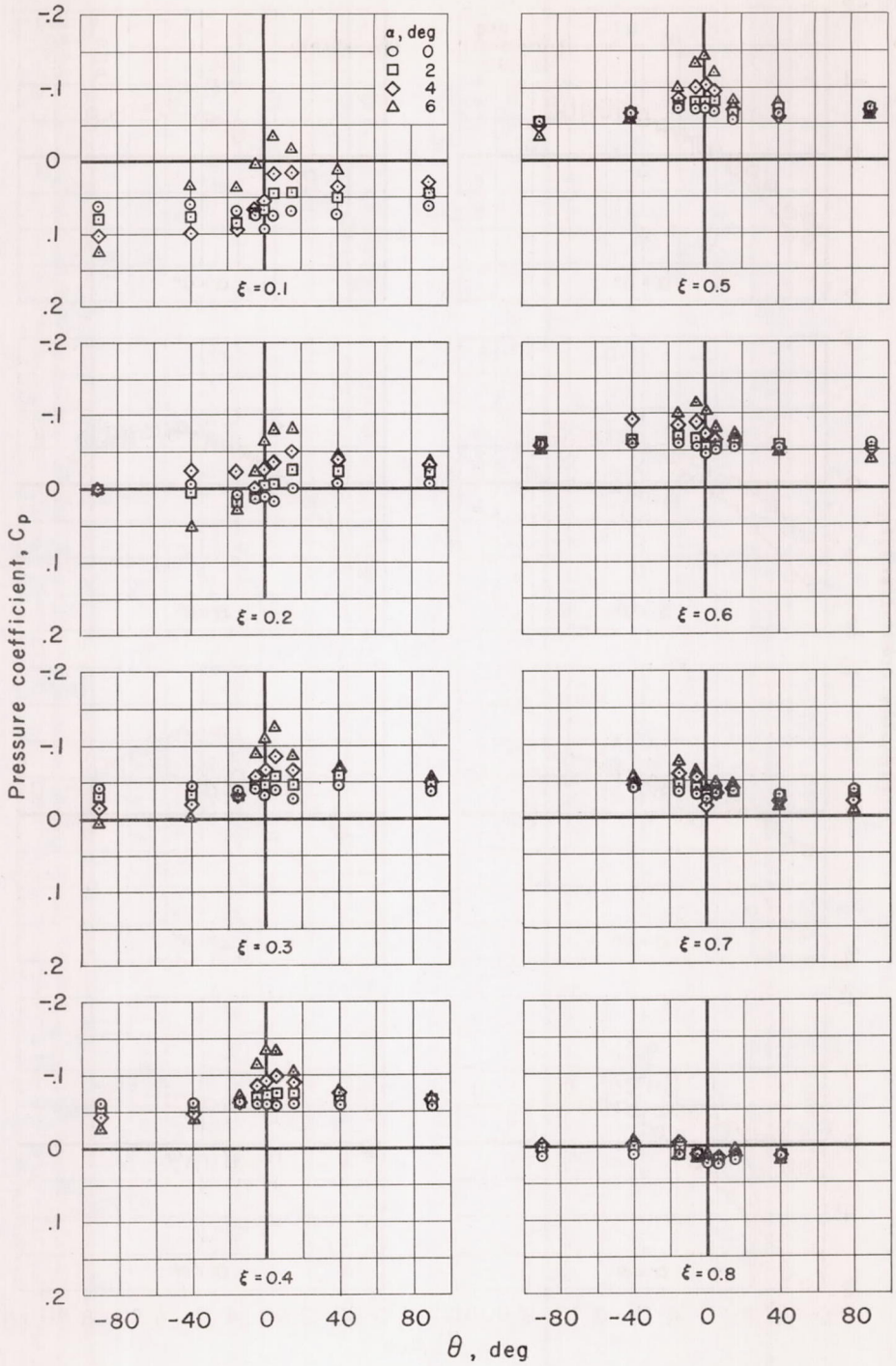

(a) $M_\infty = 0.90$, $\lambda = 2.0$

Figure 15.- Variation of pressure coefficient with meridian angle at different values of ξ for the body having an axis ratio of 2.0.

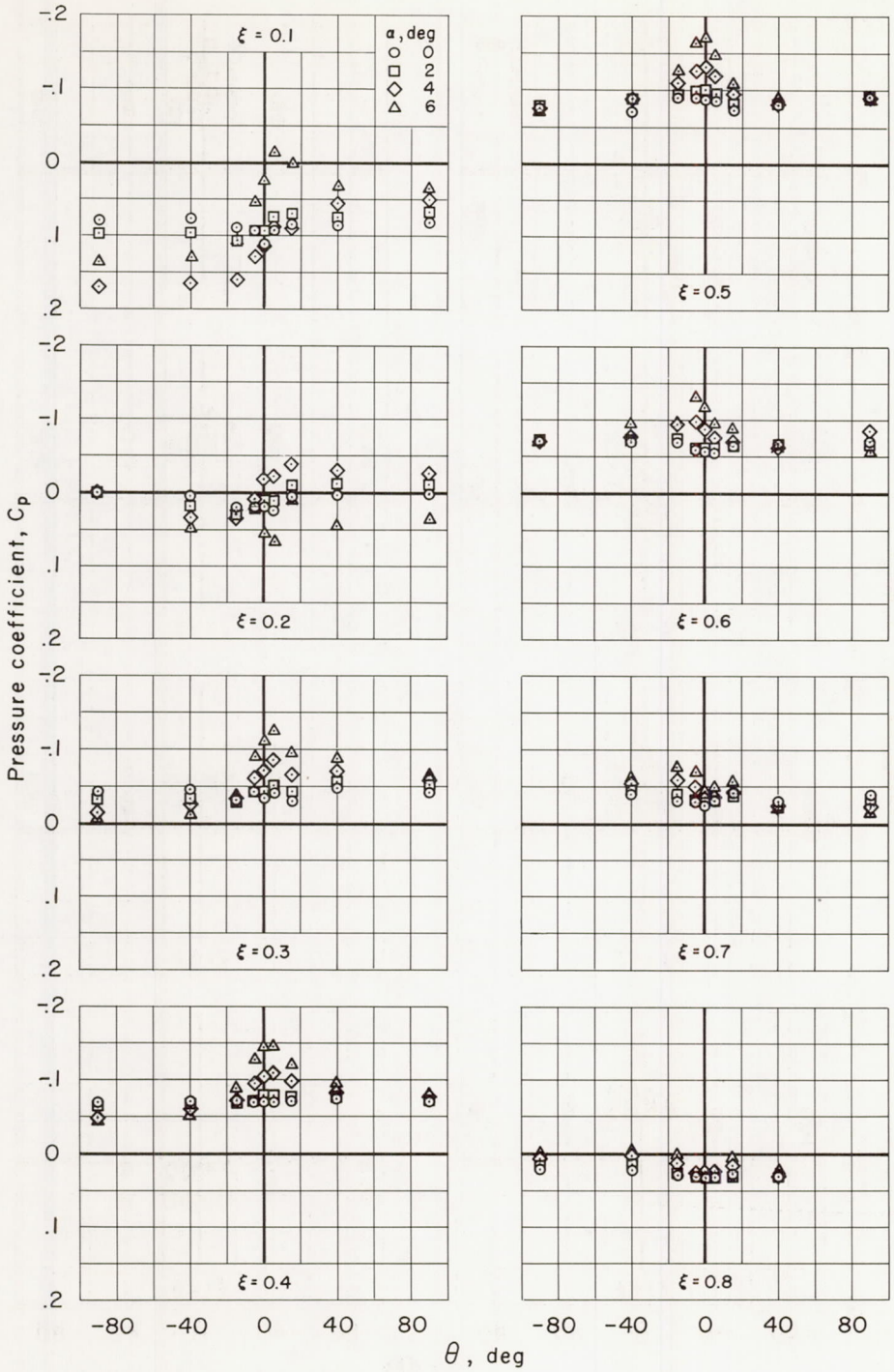

(b) $M_\infty = 0.975$, $\lambda = 2.0$

Figure 15.- Continued.

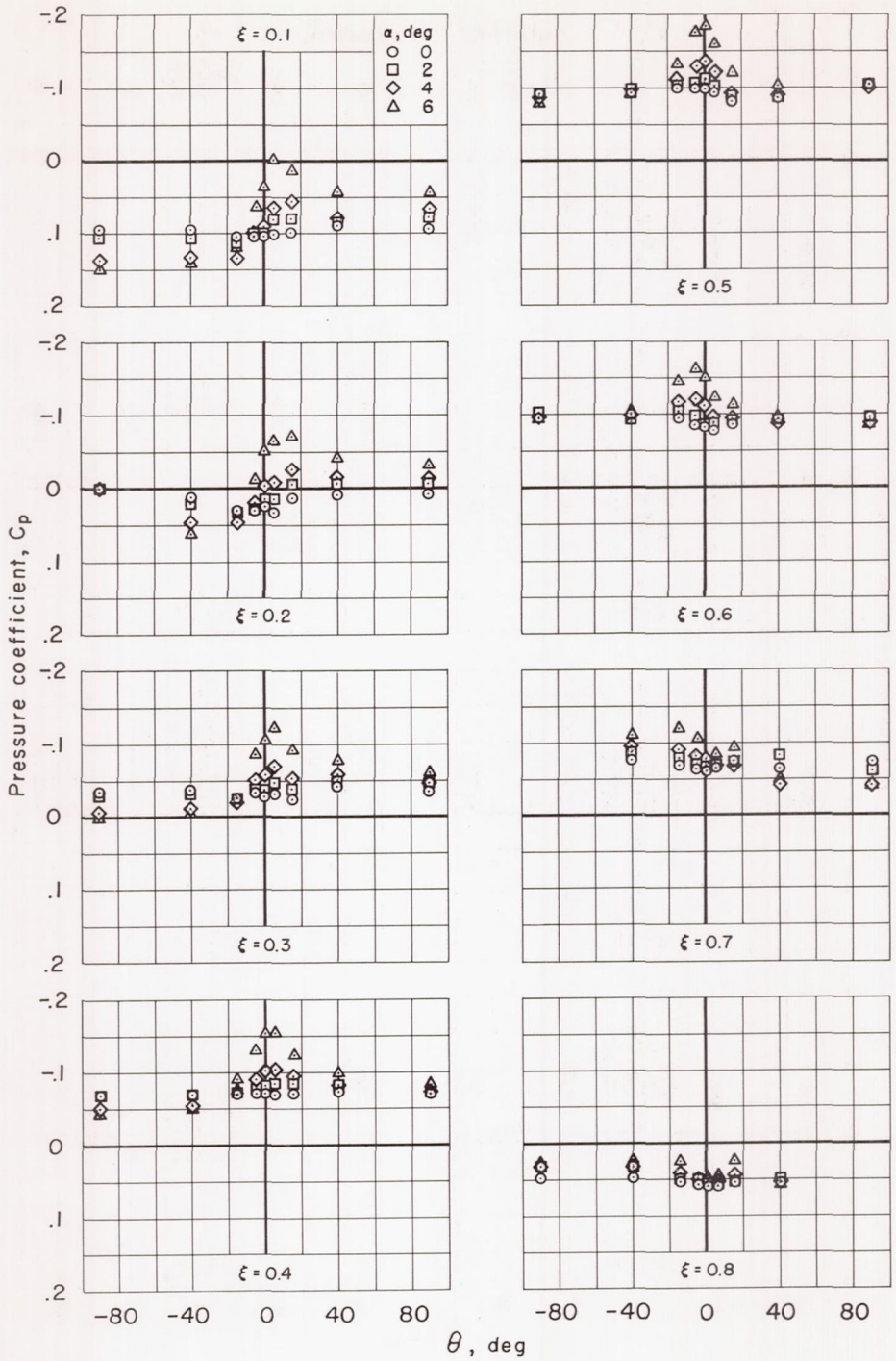

(c) $M_\infty = 1.00$, $\lambda = 2.0$

Figure 15.- Continued.

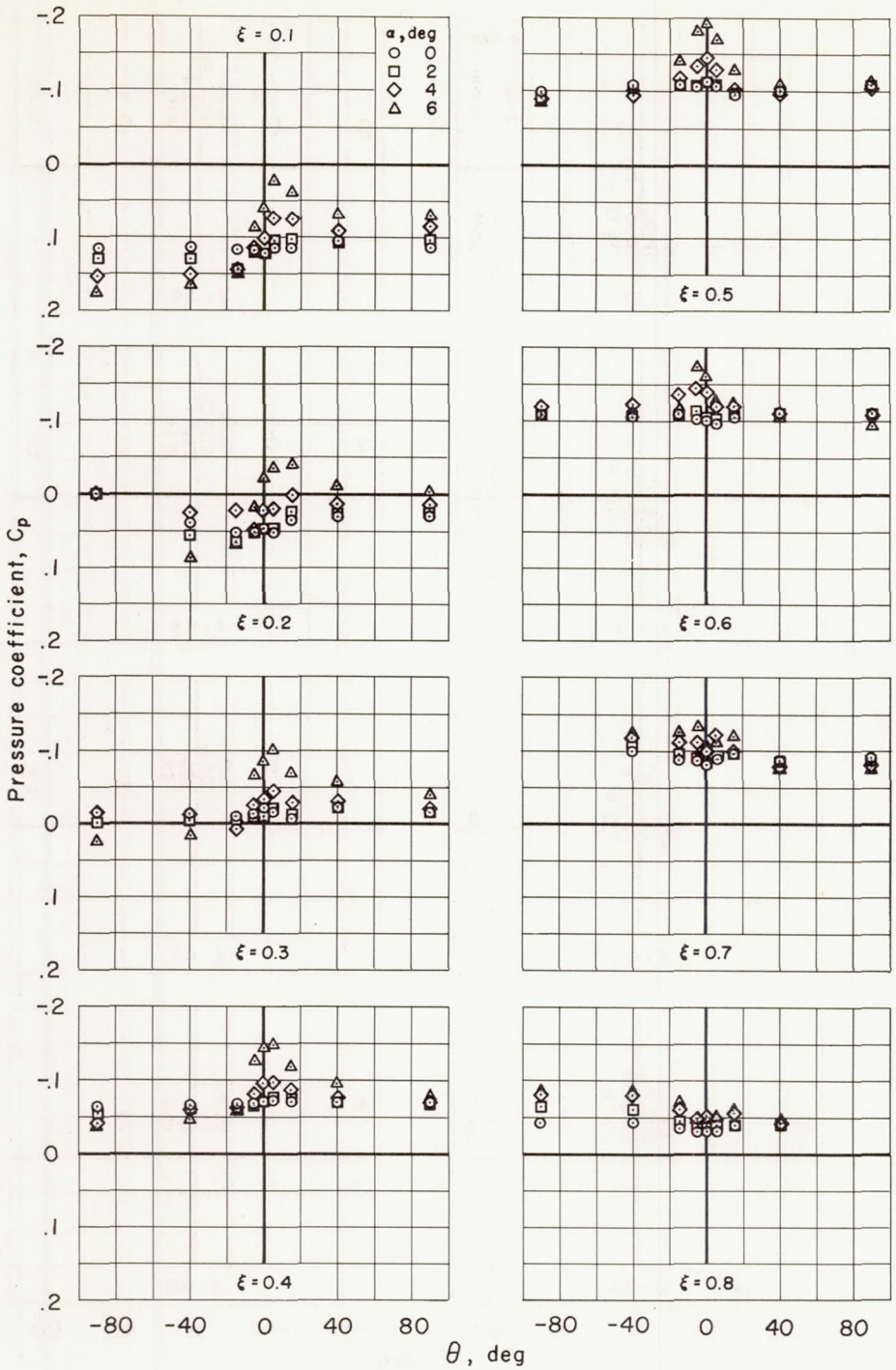

(d) $M_\infty = 1.025$, $\lambda = 2.0$

Figure 15.- Continued.

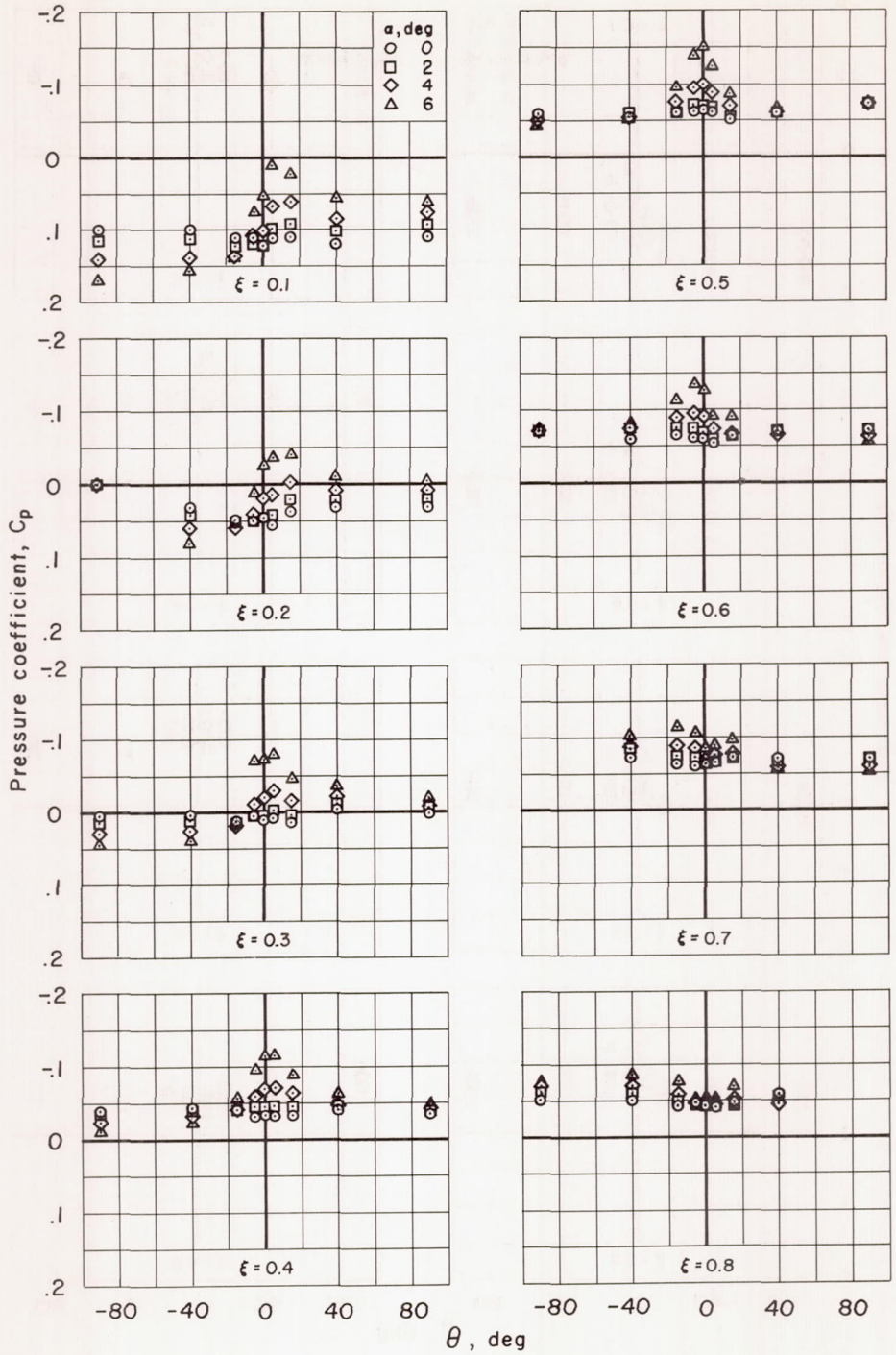

(e) $M_\infty = 1.10$, $\lambda = 2.0$

Figure 15.- Continued.

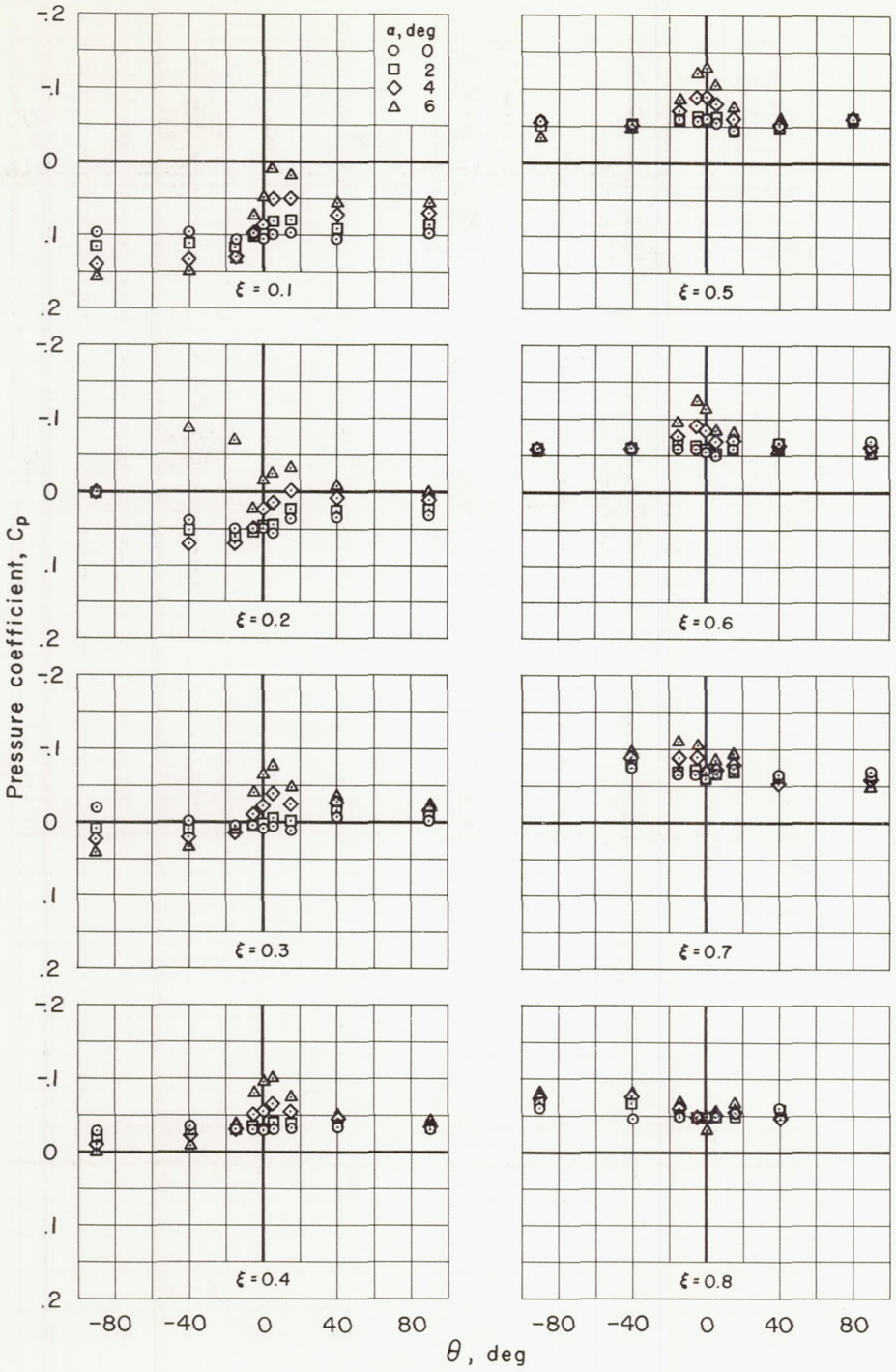

(f) $M_\infty = 1.20$, $\lambda = 2.0$

Figure 15.- Concluded.

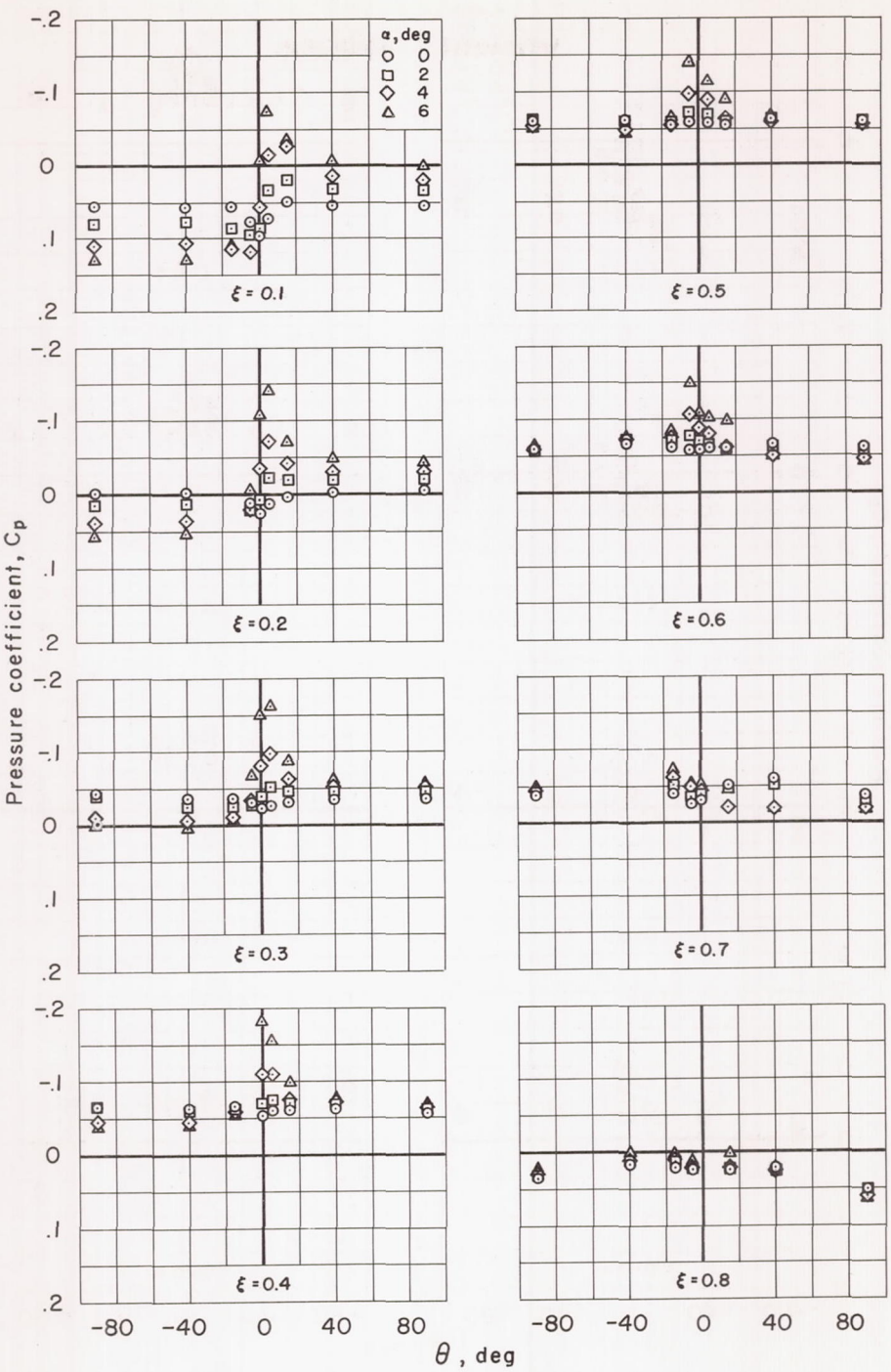

(a) $M_\infty = 0.90$, $\lambda = 3.0$

Figure 16.- Variation of pressure coefficient with meridian angle at different values of ξ for the body having an axis ratio of 3.0.

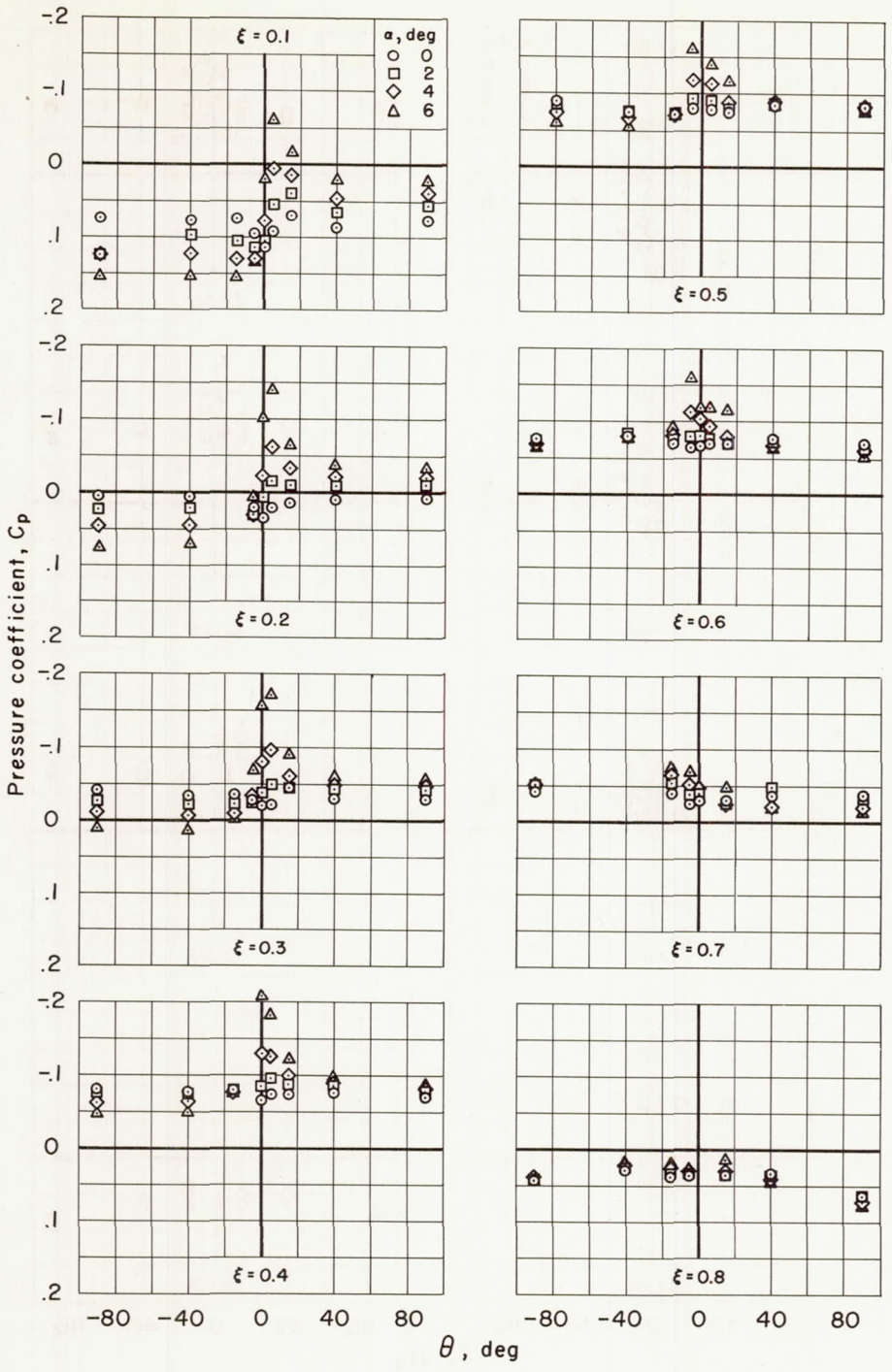

(b) $M_\infty = 0.975$, $\lambda = 3.0$

Figure 16.- Continued.

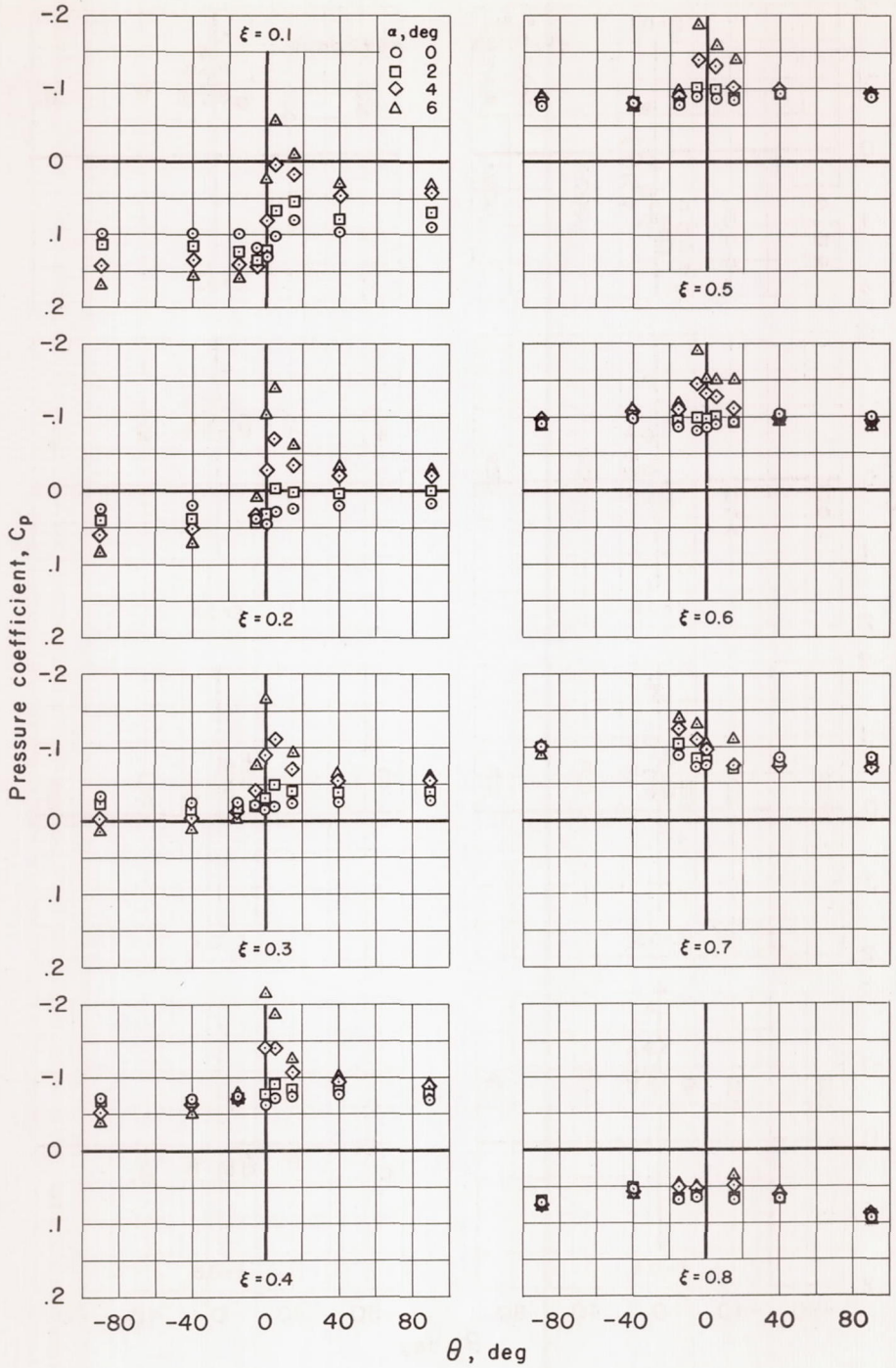

(c) $M_\infty = 1.00$, $\lambda = 3.0$

Figure 16.- Continued.

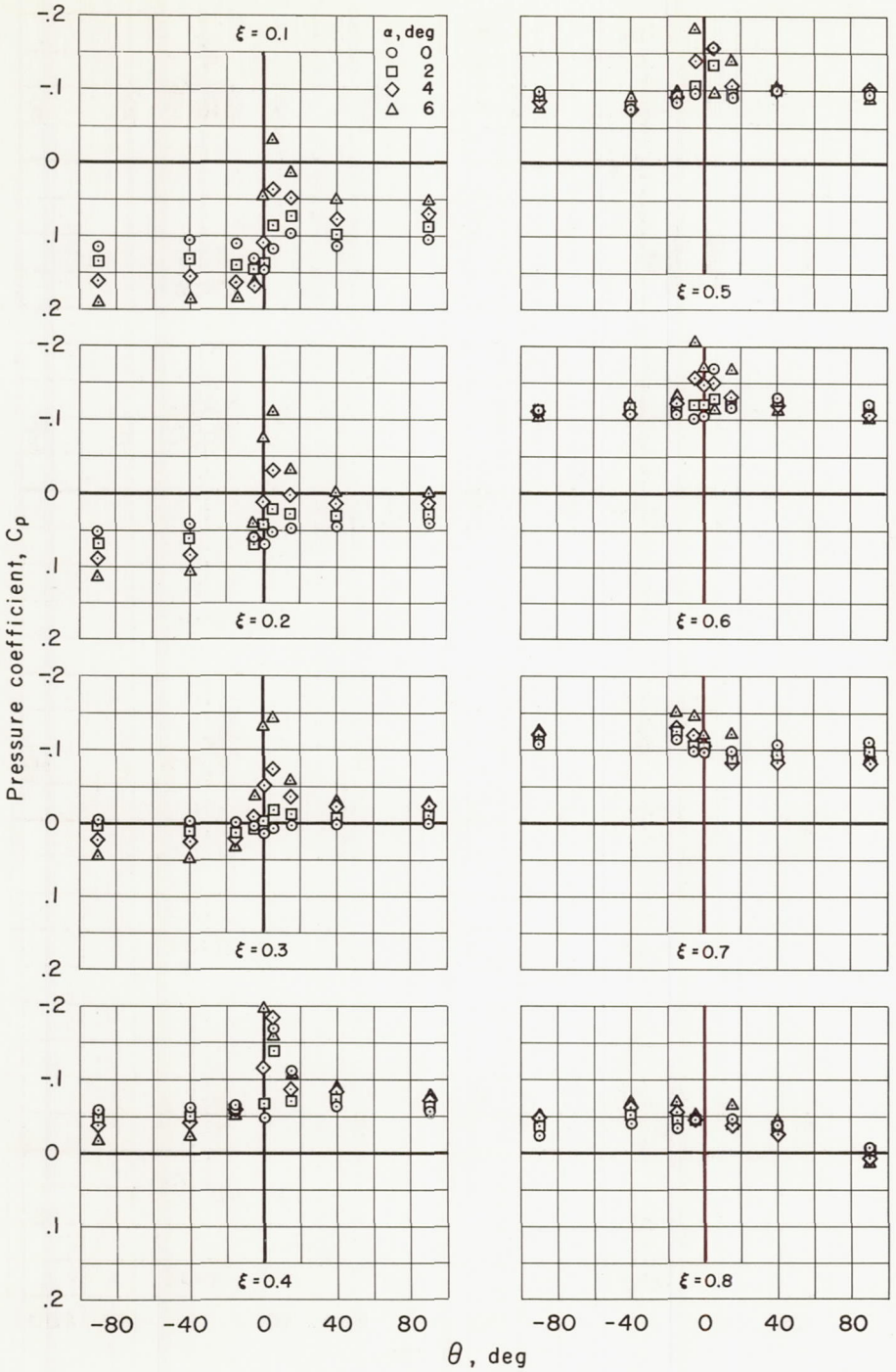

(d) $M_\infty = 1.025$, $\lambda = 3.0$

Figure 16.- Continued.

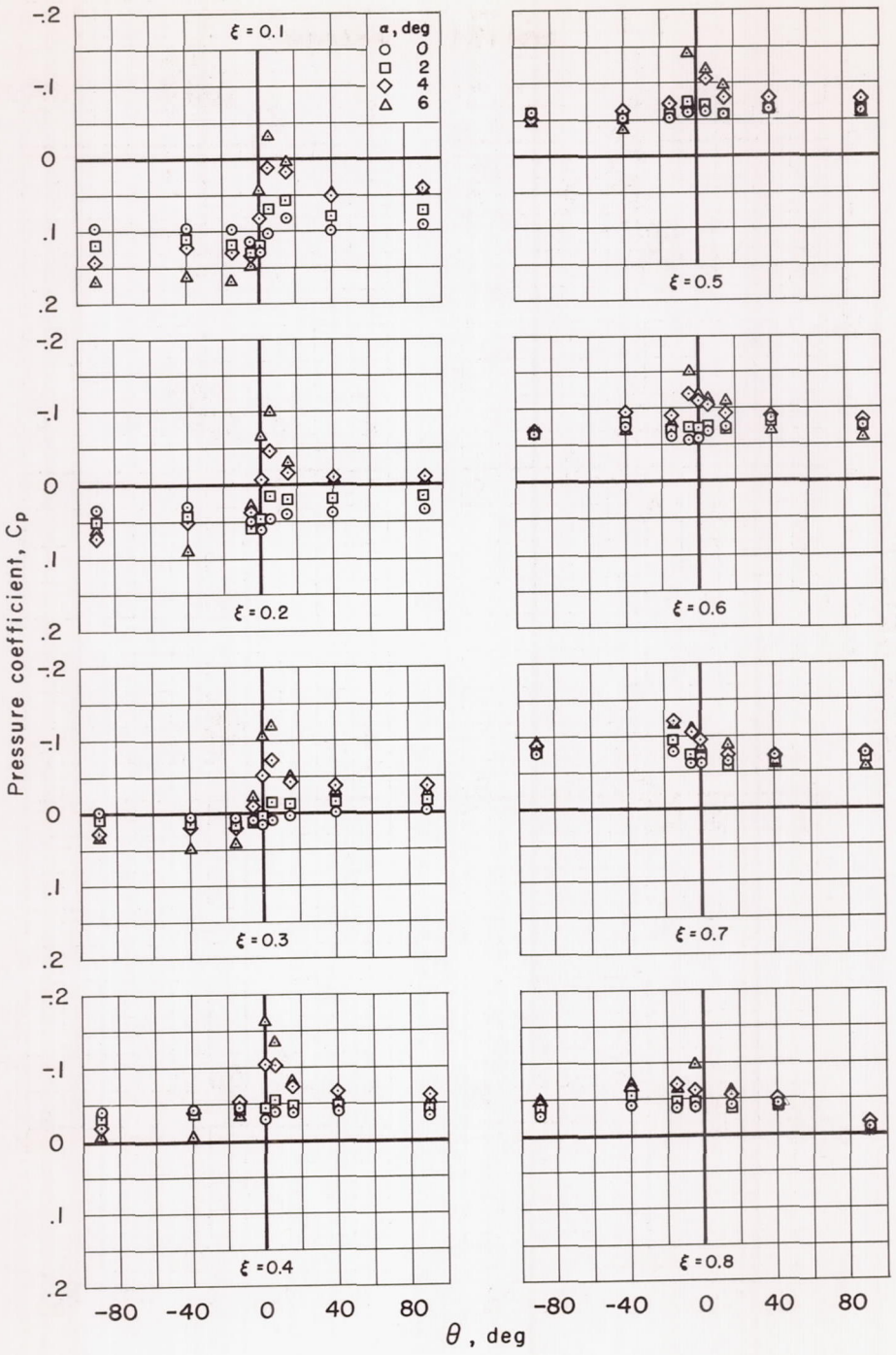

(e) $M_\infty = 1.10$, $\lambda = 3.0$

Figure 16.- Continued.

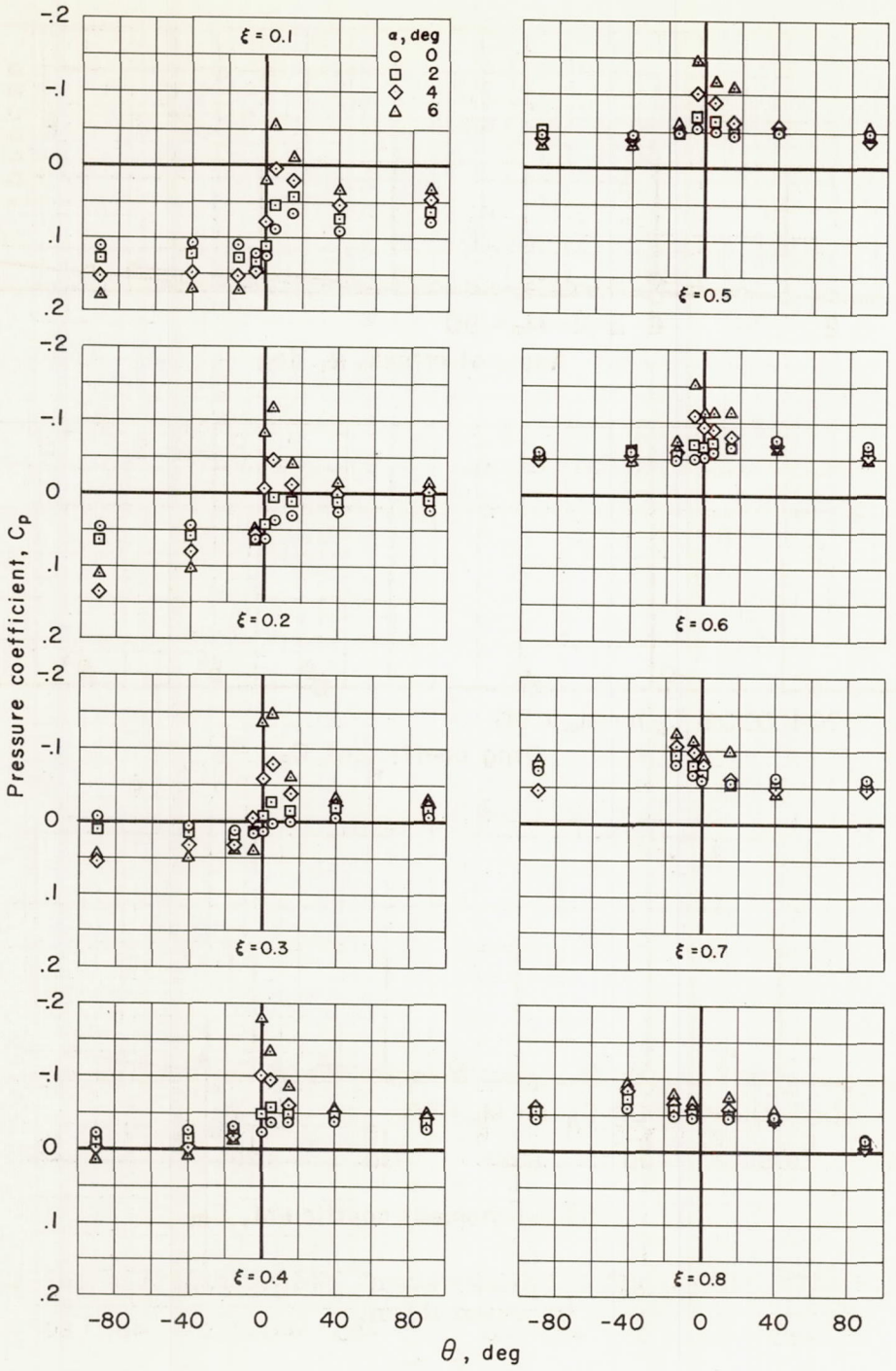

(f) $M_\infty = 1.20$, $\lambda = 3.0$

Figure 16.- Concluded.

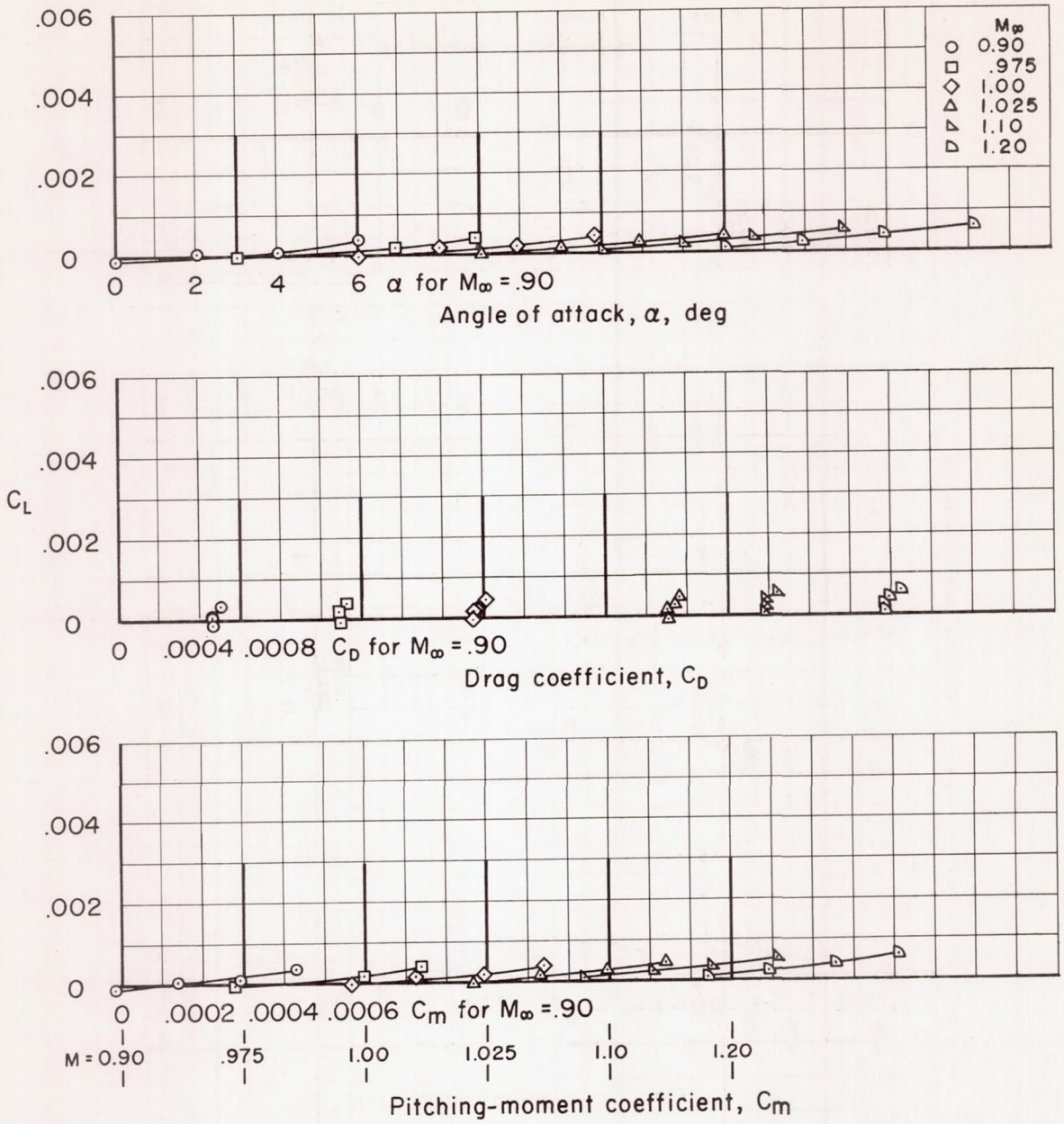

Figure 17.- Lift, drag, and pitching-moment characteristics for the body of revolution.

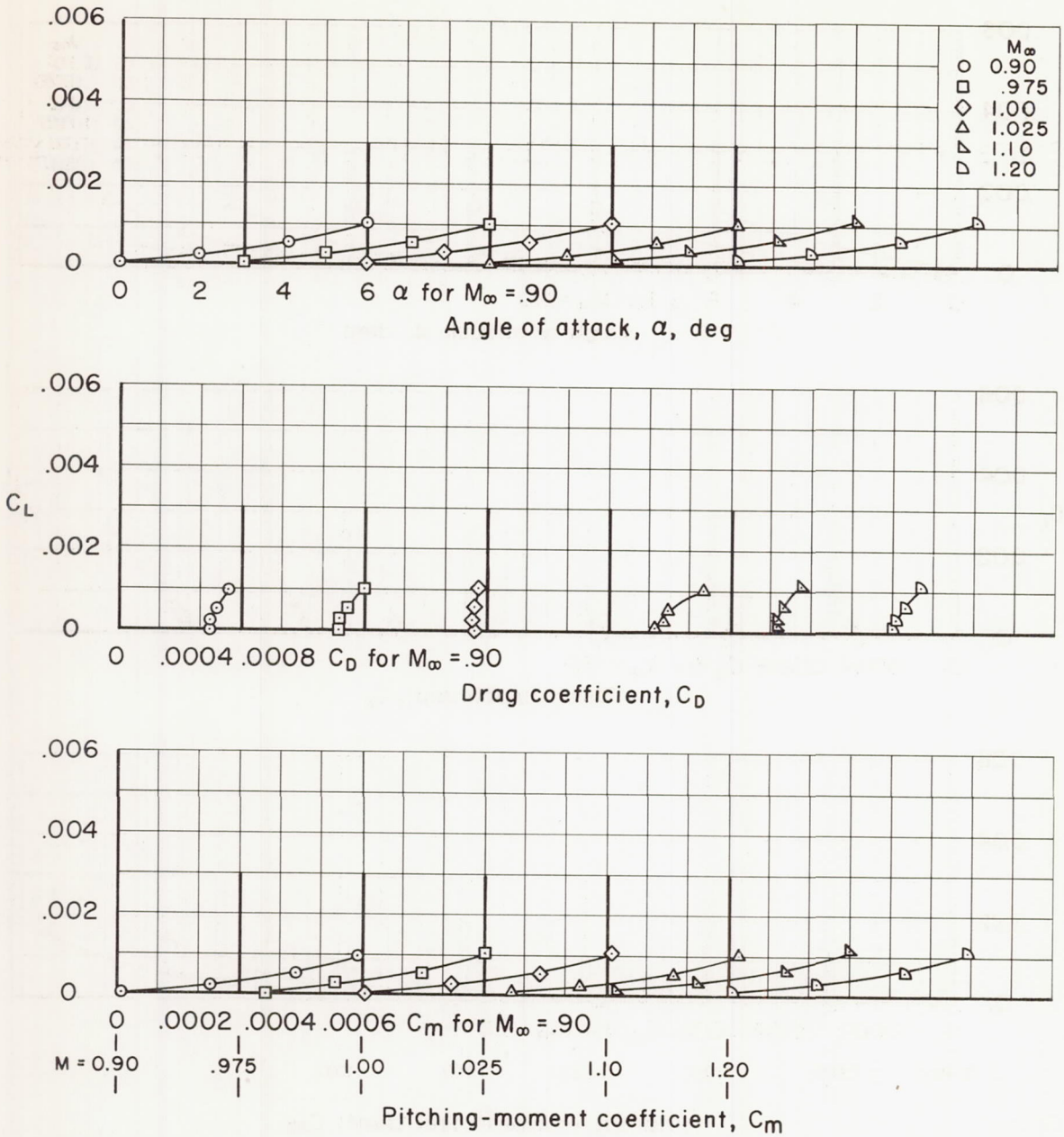

Figure 18.- Lift, drag, and pitching-moment characteristics for the body having an axis ratio λ of 1.5.

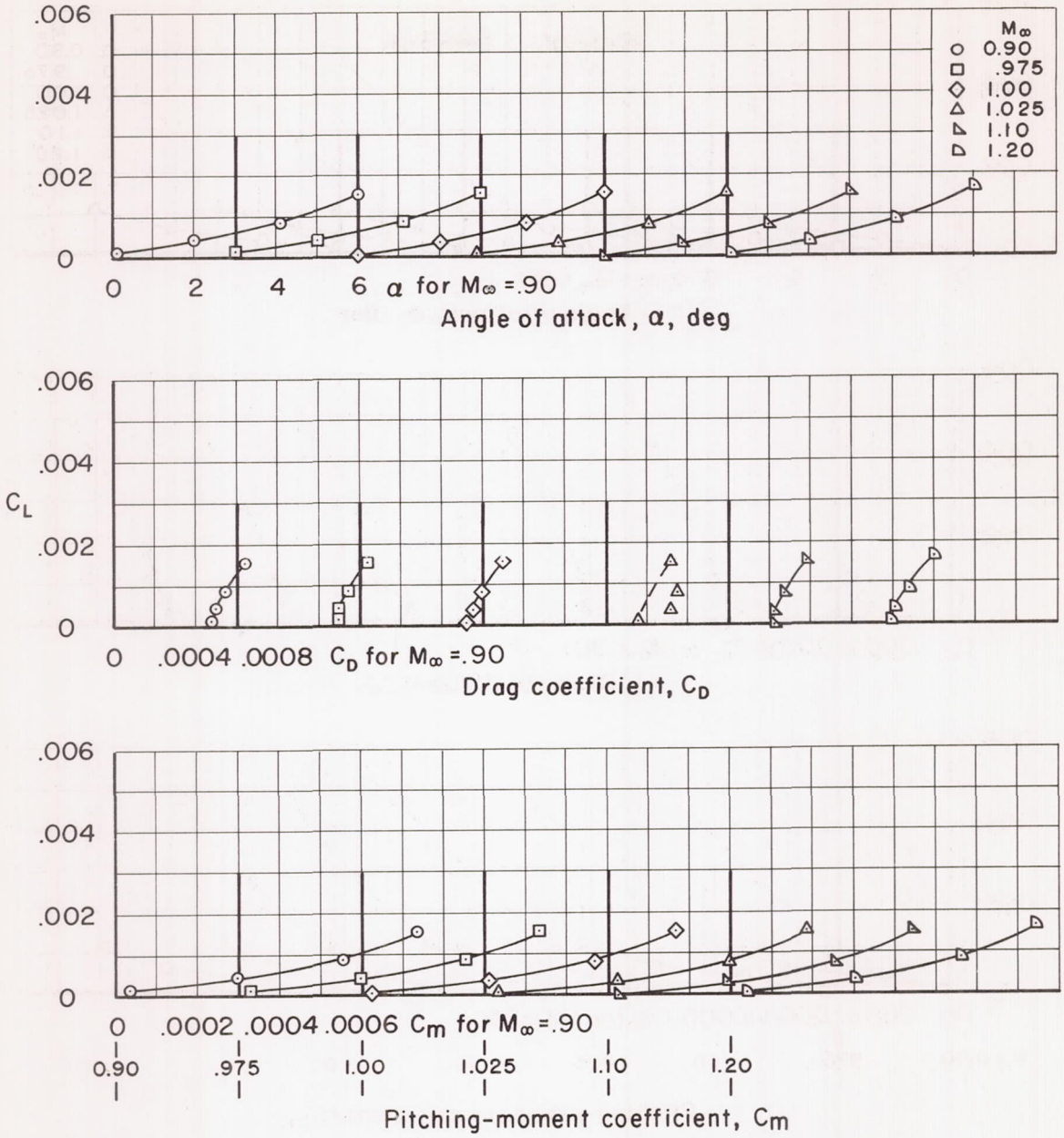

Figure 19.- Lift, drag, and pitching-moment characteristics for the body having an axis ratio λ of 2.0.

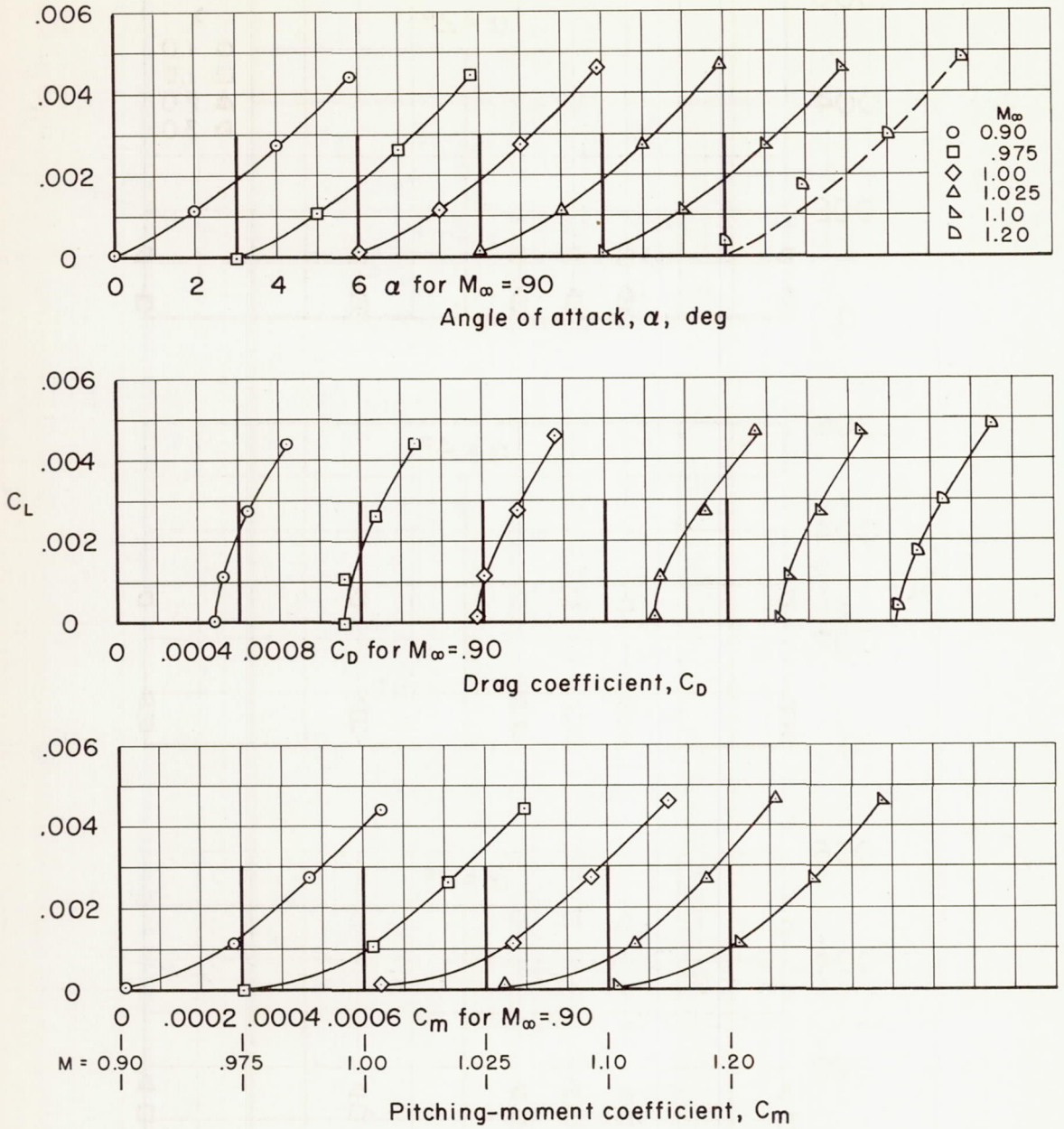

Figure 20.- Lift, drag, and pitching-moment characteristics for the body having an axis ratio λ of 3.0.

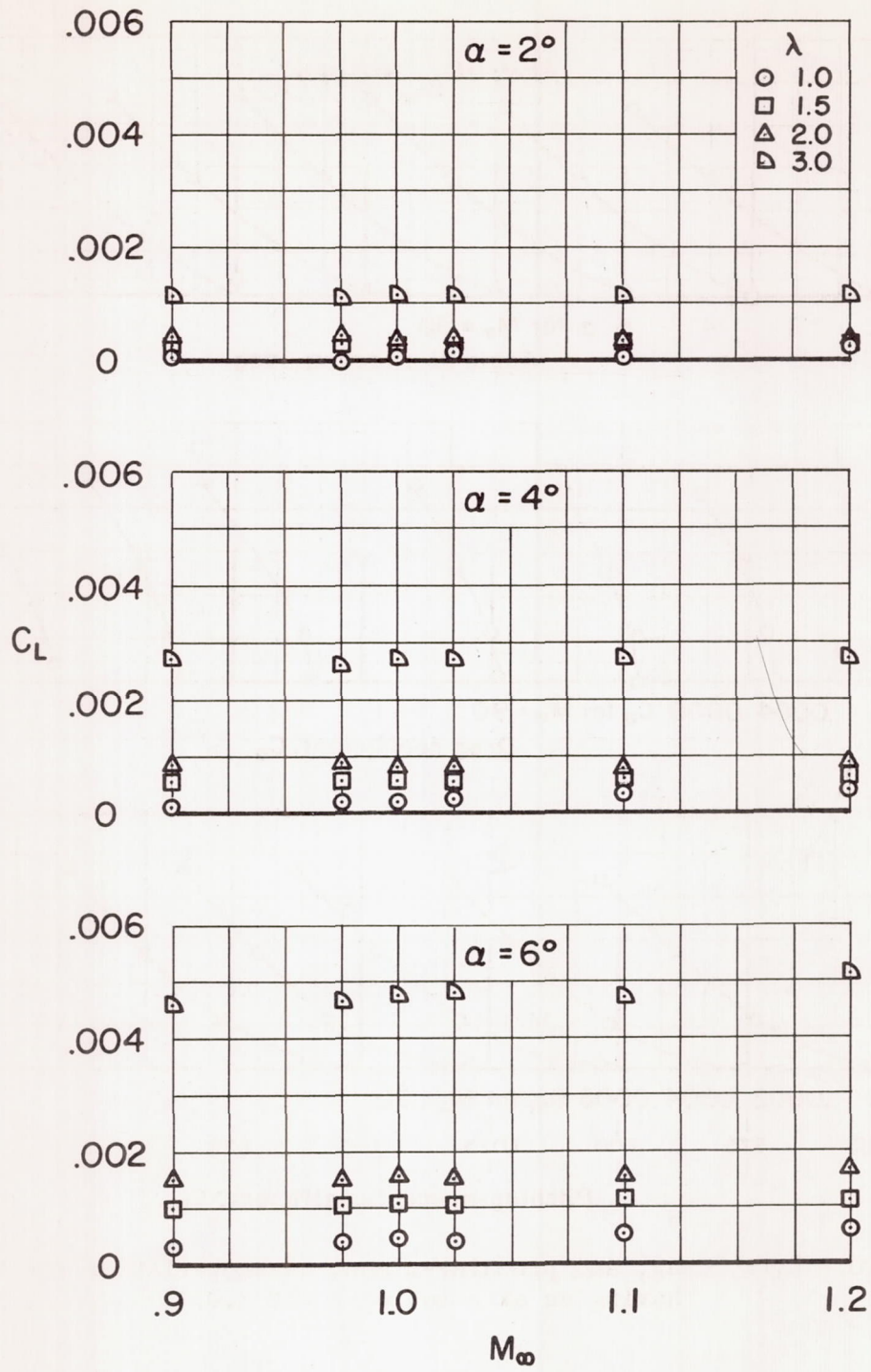

Figure 21.- Variation of lift coefficient with Mach number at angle of attack.

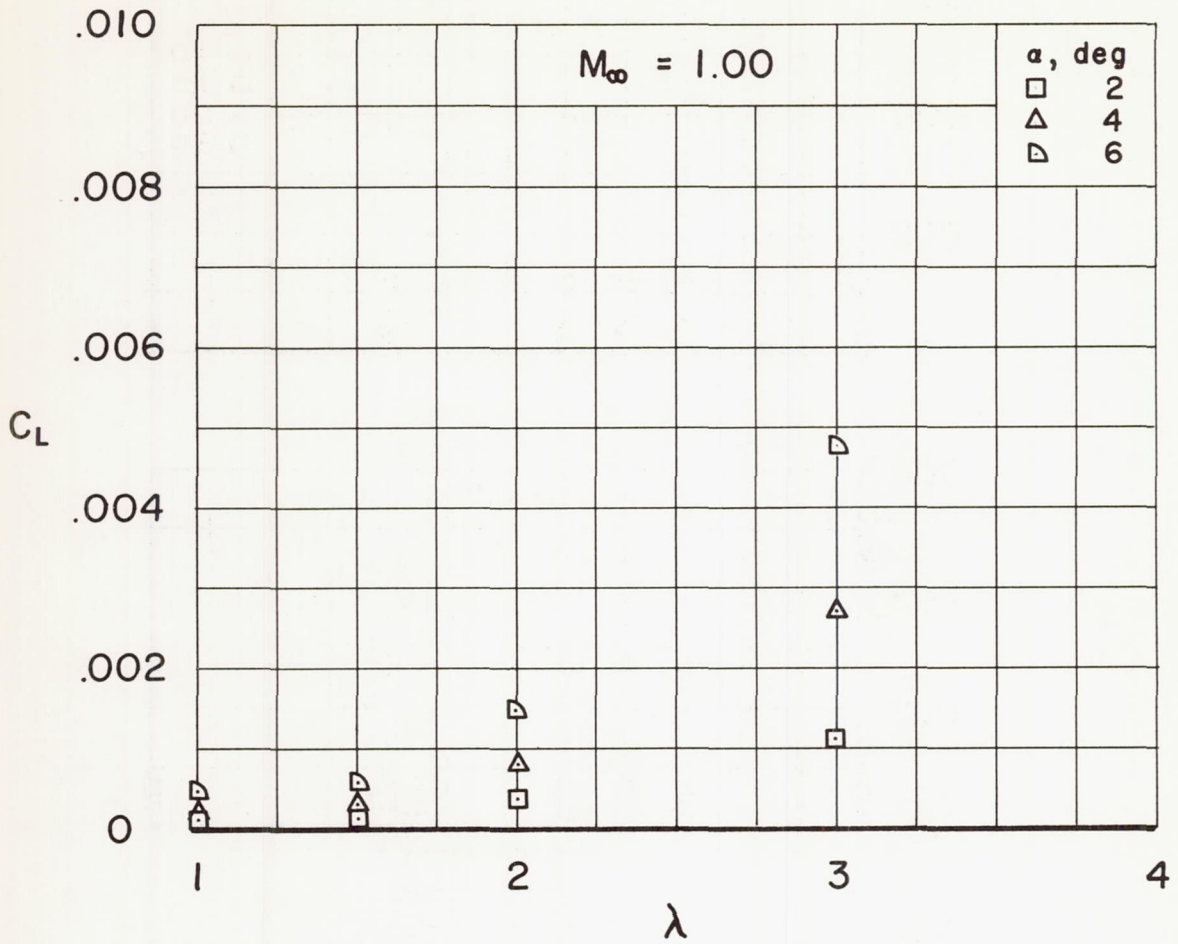

Figure 22.- Variation of lift coefficient with axis ratio λ at a Mach number of unity.

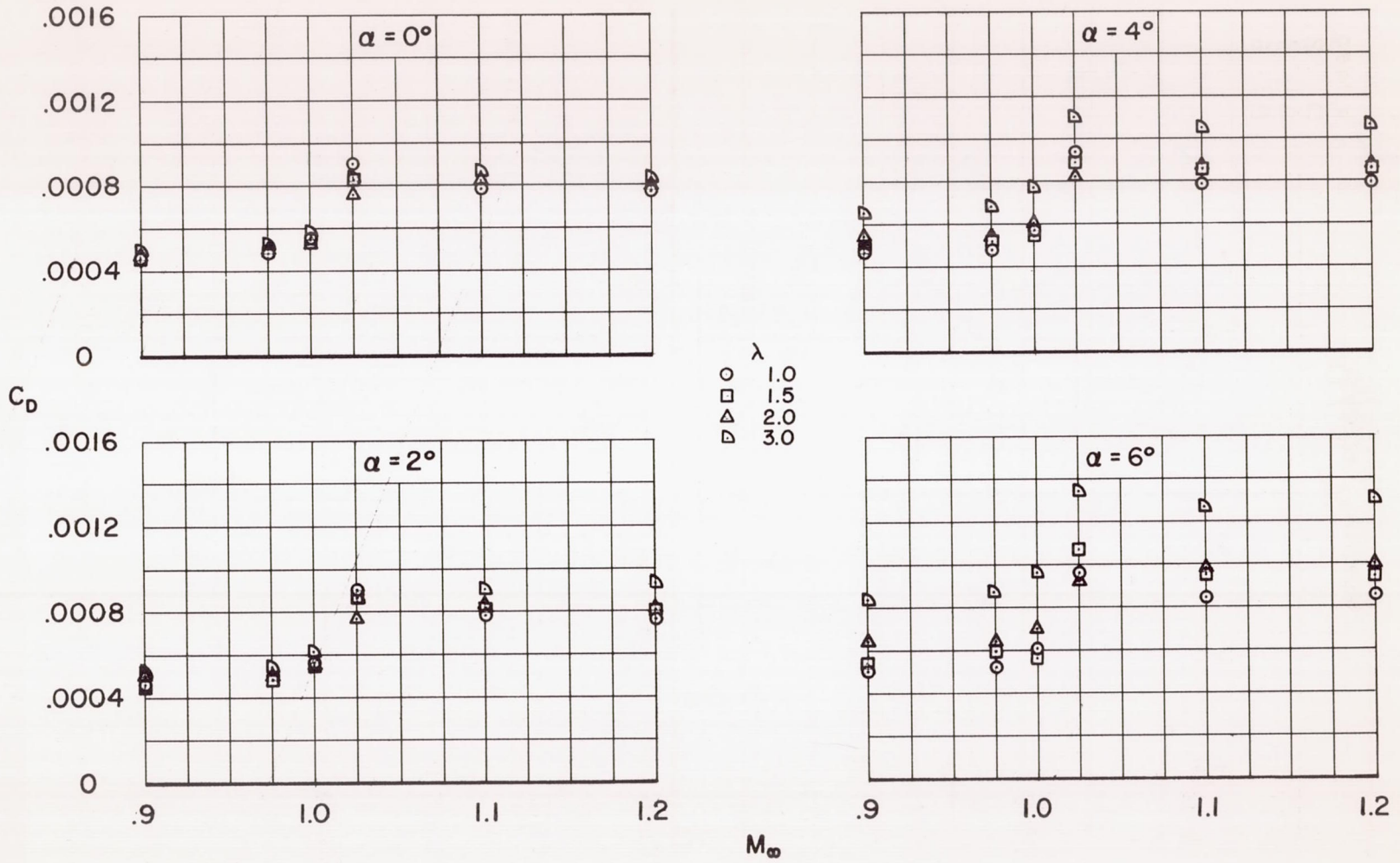

Figure 23.- Variation of drag coefficient with Mach number at angle of attack.

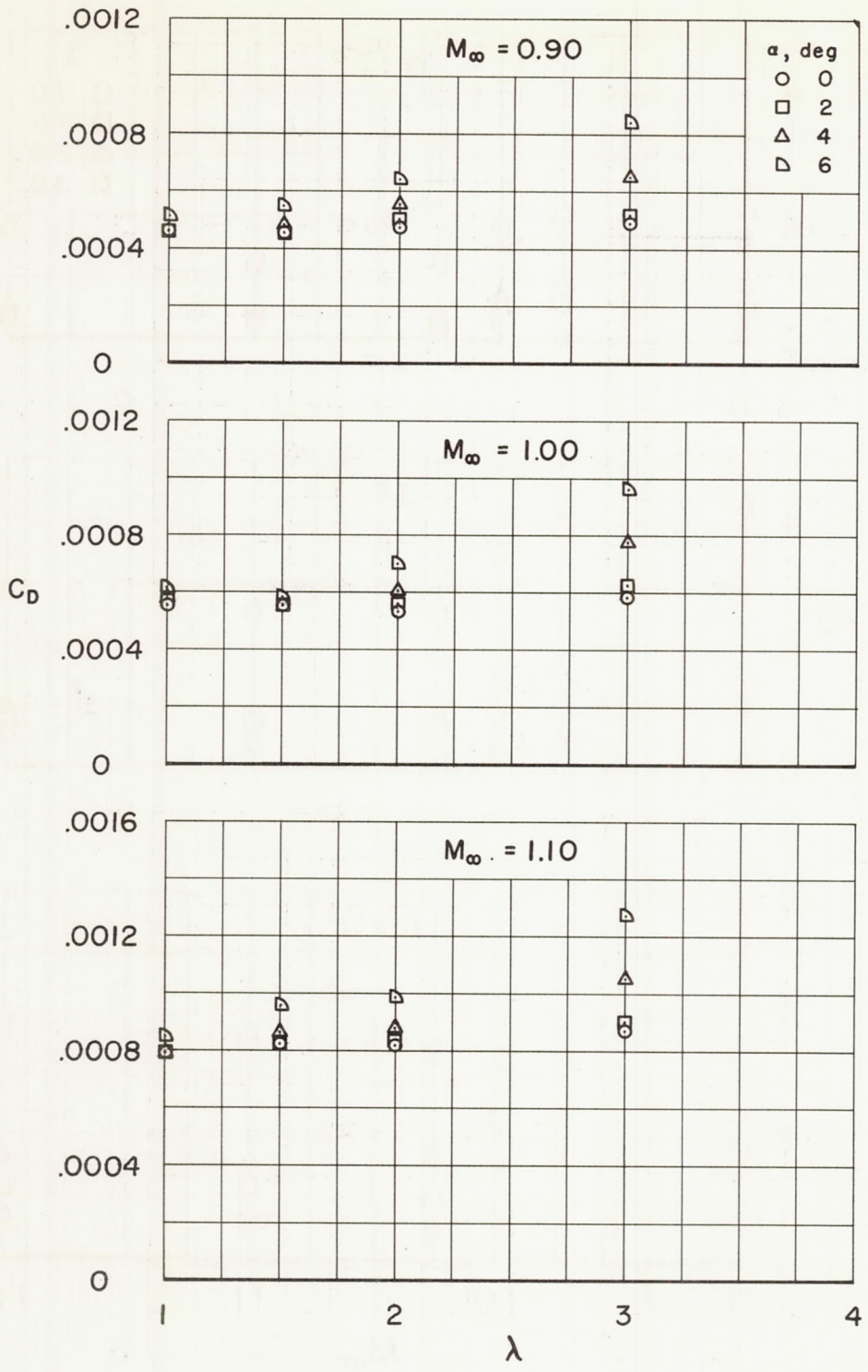

Figure 24.- Variation of drag coefficient with axis ratio λ at several Mach numbers.

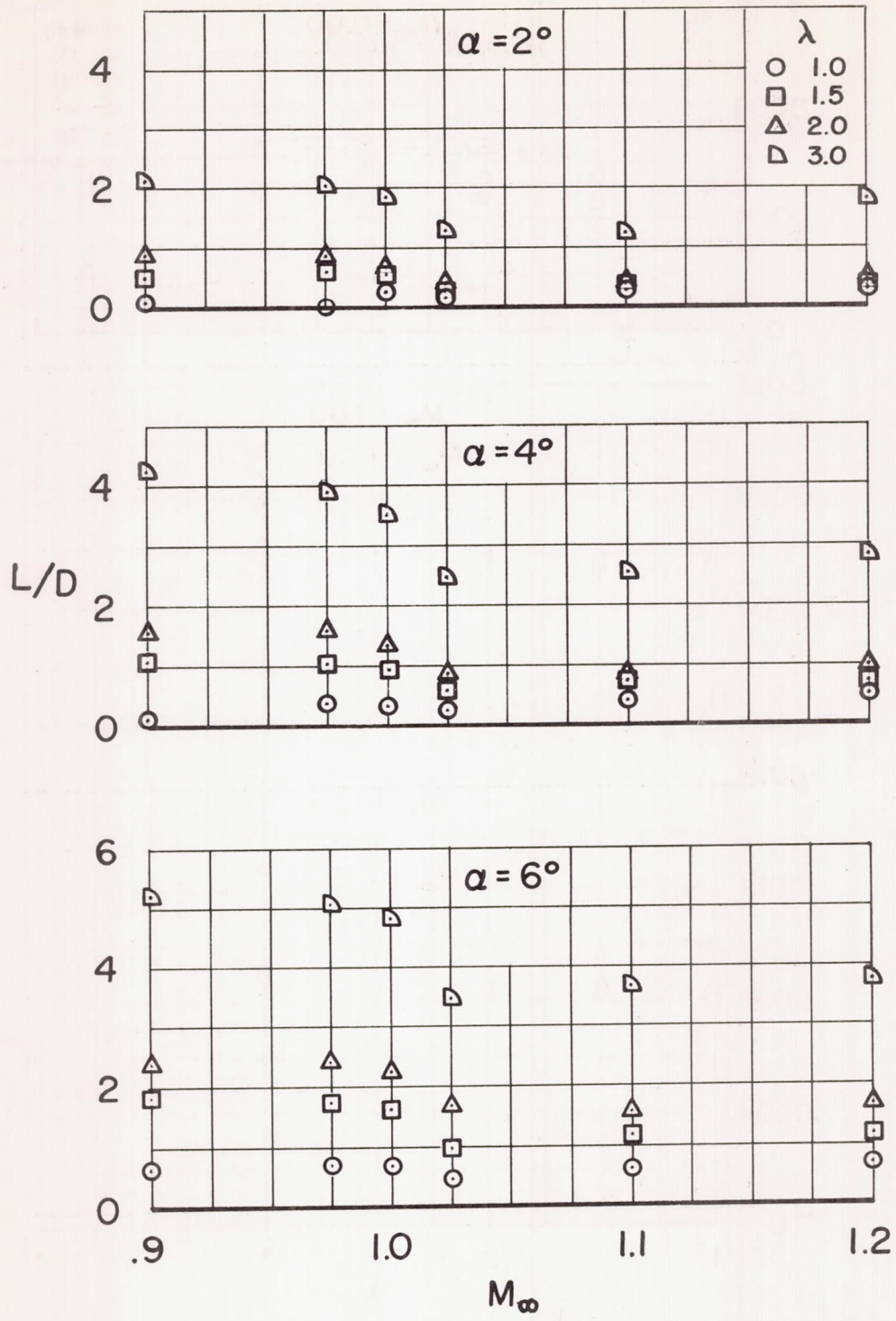

Figure 25.- Variation of lift-drag ratio with Mach number at angle of attack.

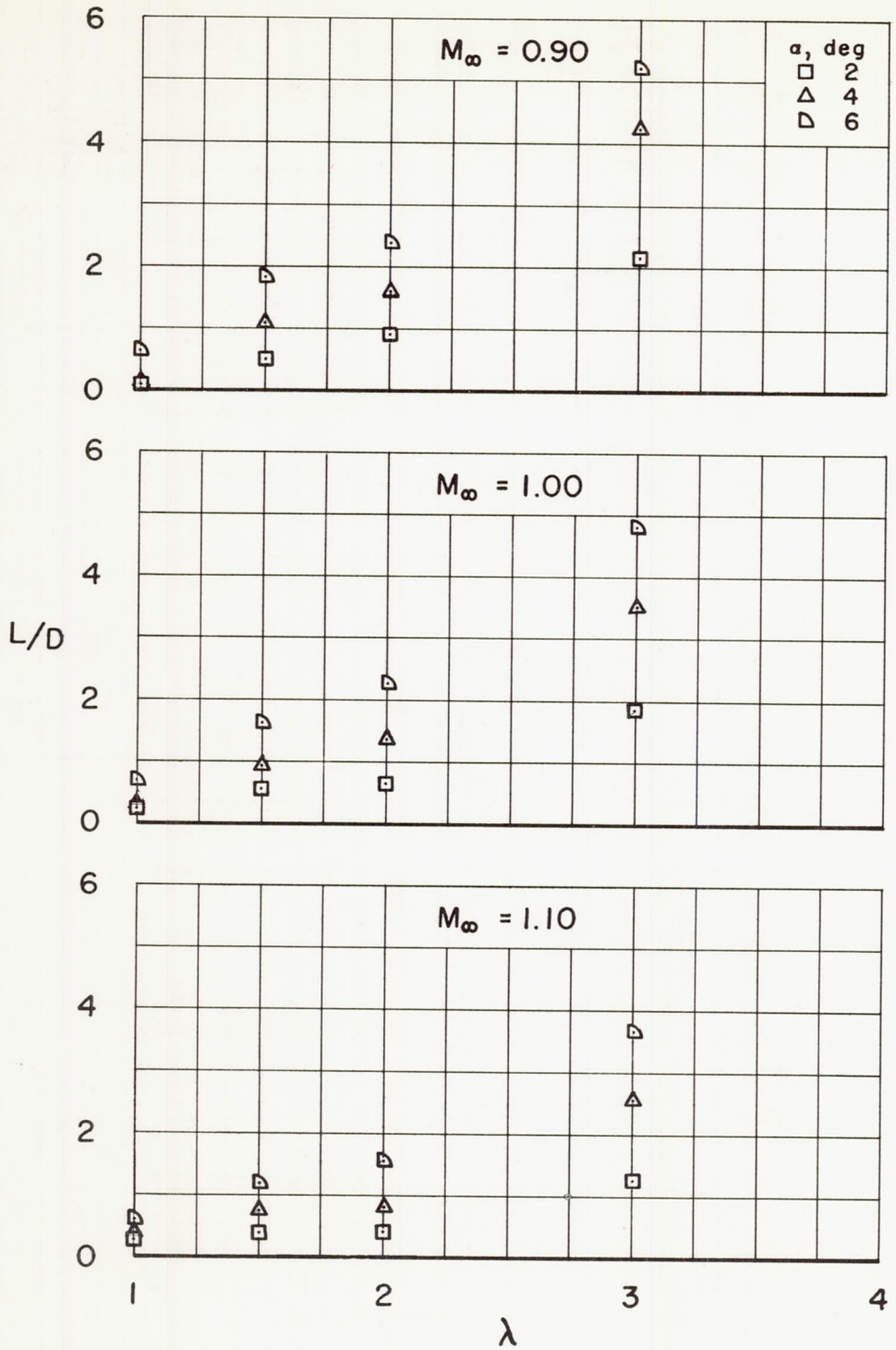

Figure 26.- Variation of lift-drag ratio with axis ratio λ at several Mach numbers.

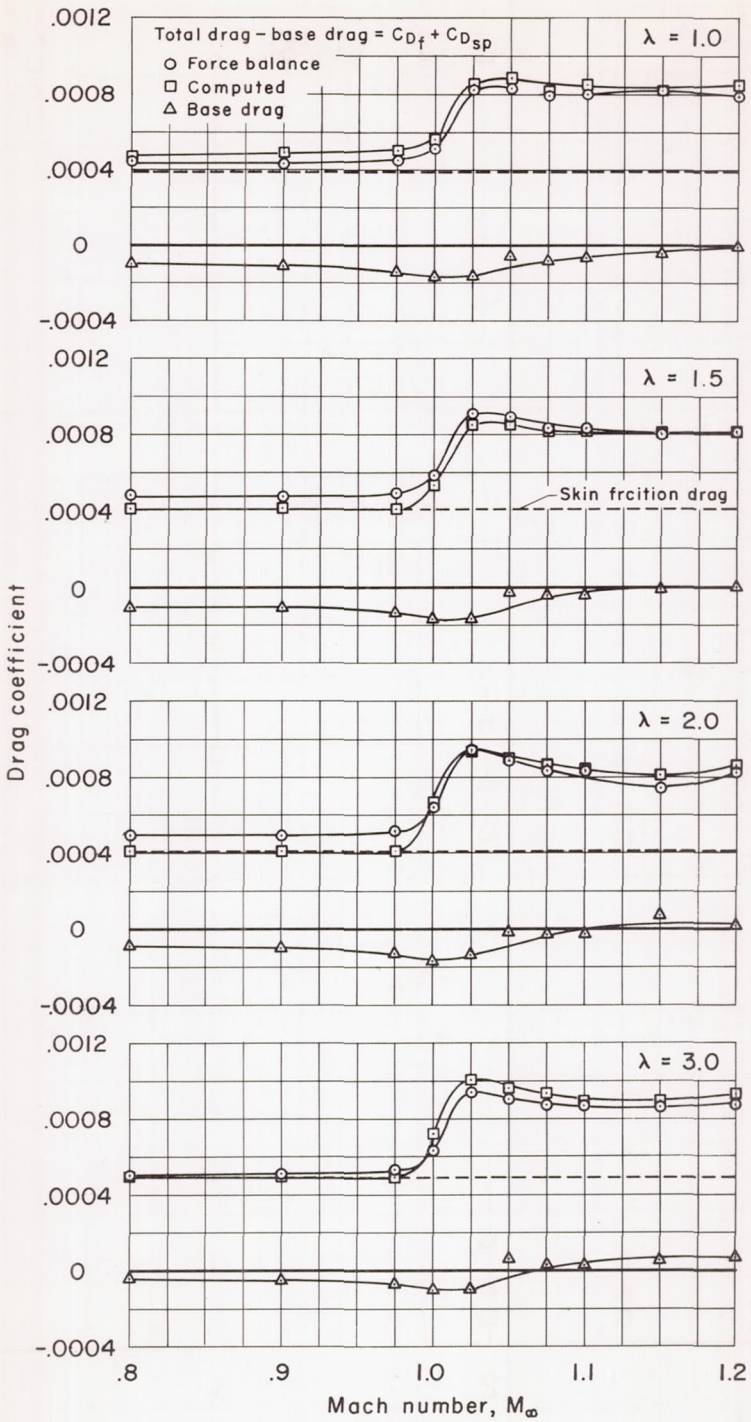

Figure 27.- Variation of drag coefficient with Mach number at zero angle of attack.

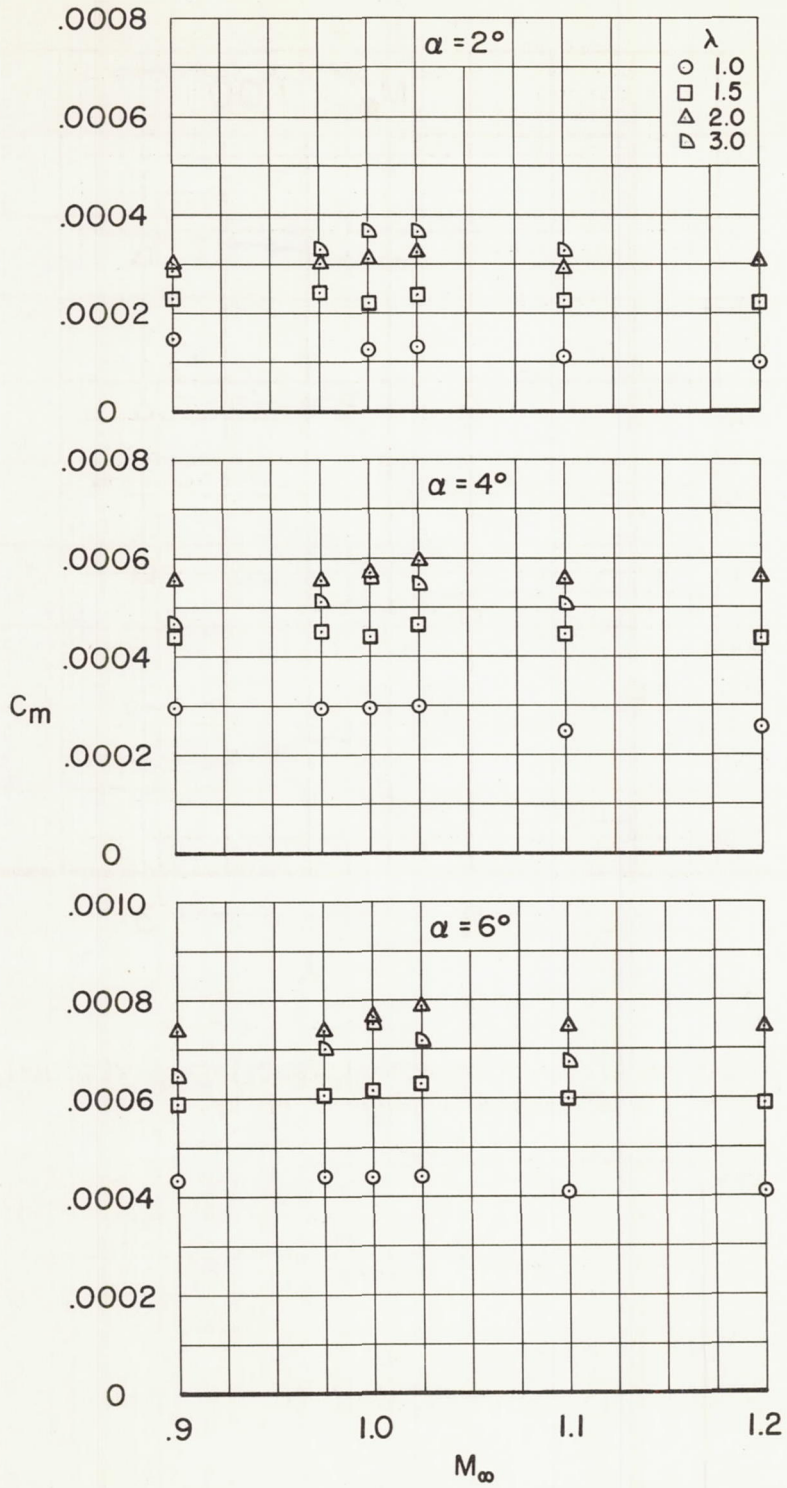

Figure 28.- Variation of pitching-moment coefficient with Mach number at angle of attack.

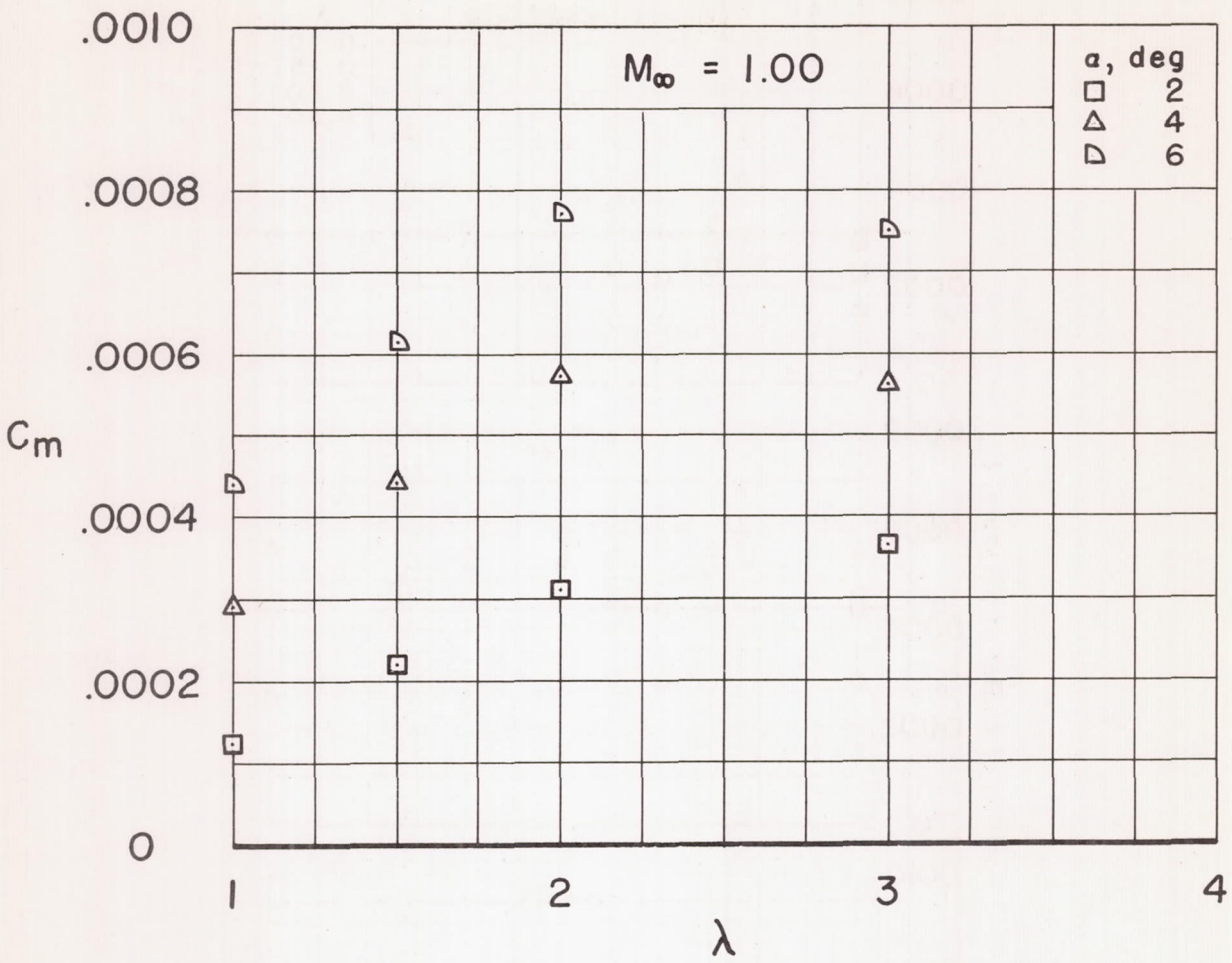

Figure 29.- Variation of pitching-moment coefficient with axis ratio λ at a Mach number of unity.

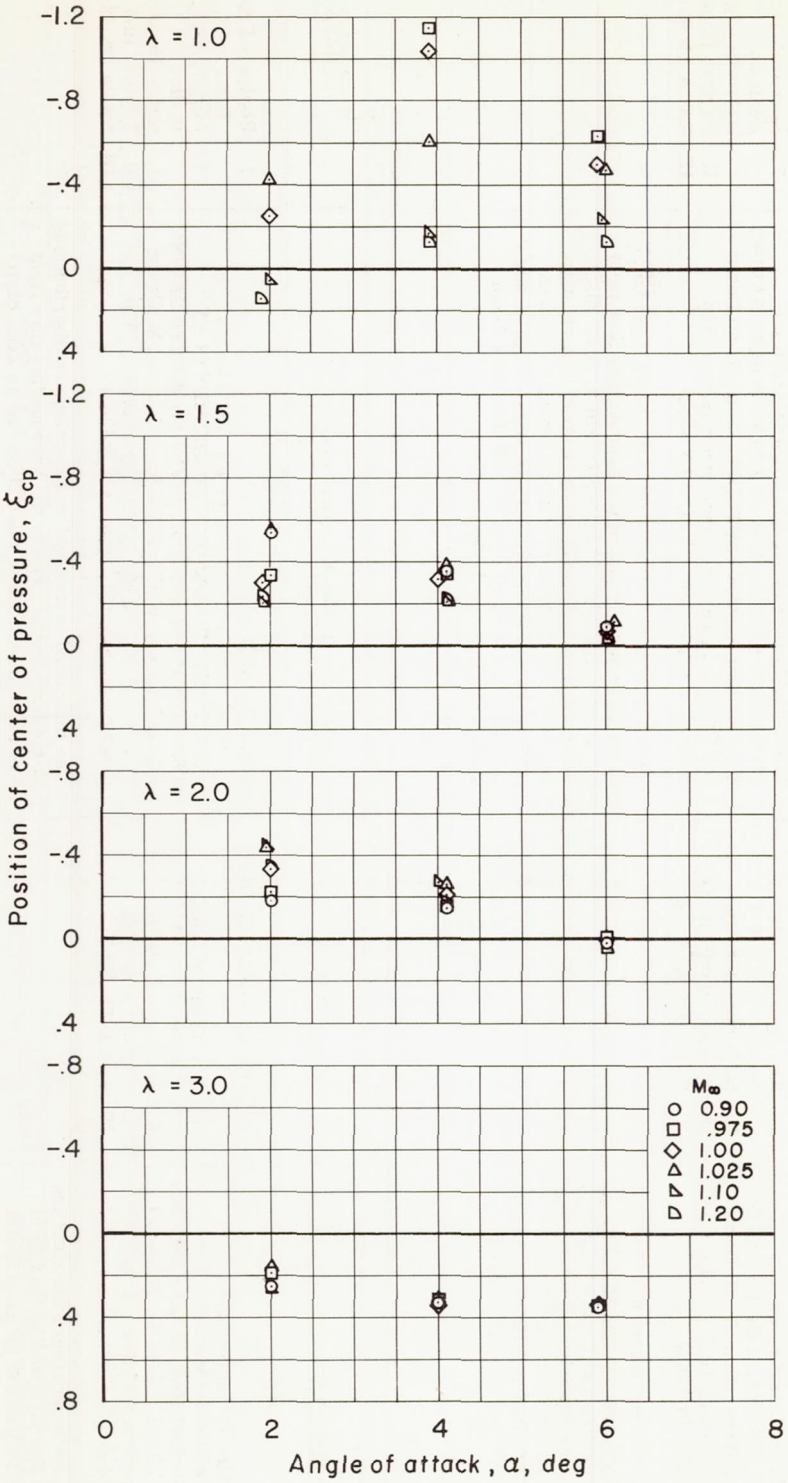

Figure 30.- Variation of center of pressure location with angle of attack at several Mach numbers.